Modelling Wind Turbine Inflow: The Induction Zone

Meyer Forsting, Alexander Raul

Link to article, DOI:
10.11581/DTU:00000022

Publication date:
2017

Document Version
Publisher's PDF, also known as Version of record

Modelling Wind Turbine Inflow

The Induction Zone

DTU Wind Energy PhD

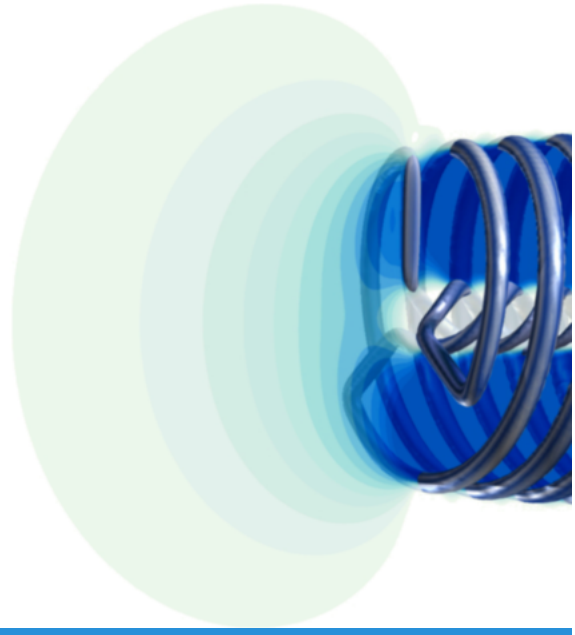

Alexander R. Meyer Forsting

DTU Wind Energy PhD-0078(EN)
DOI: 10.11581/DTU:00000022

August 2017

DTU Wind Energy
Department of Wind Energy

ALEXANDER RAUL MEYER FORSTING

MODELLING WIND TURBINE INFLOW

Author: Alexander Raul Meyer Forsting
Title: Modelling Wind Turbine Inflow: The Induction Zone
Department: DTU Wind Energy (Risø Campus)

This thesis consists of two parts - a synopsis and a collection of journal articles. It is submitted to the Danish Technical University in partial fulfilment of the requirements for the degree of Doctor of Philosophy in Engineering. The work was carried out at the Aerodynamic Design section of the Department of Wind Energy, located at the Risø campus of the Technical University of Denmark. It was co-funded by The Innovation Fund Denmark as part of the UniTTe project under grant number 1305-00024B. The external stay at the École de technologie supérieure (ETS) in Montréal was additionally supported by the Otto Mønsteds Fond.

Principal supervisor:
Dr. Niels Troldborg, DTU Wind Energy
Co-supervisors:
Dr. Andreas Bechmann & Dr. Pierre-Elouan Réthoré, DTU Wind Energy
Examiners:
Prof. Jens N. Sørensen, DTU Wind Energy
Prof. Rebecca J. Barthelmie, Cornell University
Dr. David Schlipf, University of Stuttgart

DTU WIND ENERGY *is a globally leading centre for wind energy with internationally recognized technical-scientific competences through the unique integration of research, education and public/private sector consulting. The department is centred at Risø and has more than 250 staff members, including 150 academic staff and nearly 40 PhD students.*

DTU Wind Energy
PhD-0078(EN)
August 2017

DOI:
10.11581/DTU:00000022

Sponsorship:
Innovation Fund Denmark
1305-00024B

Pages:219
Figures:60
References:55

Technical University of Denmark
DTU Wind Energy
Frederiksborgvej 399
DK-4000 Roskilde
Denmark
alrf@dtu.dk
www.vindenergi.dtu.dk

MODELLING WIND TURBINE INFLOW

ALEXANDER RAUL MEYER FORSTING

The Induction Zone

Principal supervisor:

Niels Troldborg

Co-supervisors:

Andreas Bechmann & Pierre-Elouan Réthoré

DTU Wind Energy
August 2017

ABSTRACT

A wind turbine decelerates the wind in front of its rotor by extracting kinetic energy. The wind speed reduction is maximal at the rotor and negligible more than five rotor radii upfront. By measuring wind speed this far from the rotor, the turbine's performance is determined without any rotor bias. However, the measured wind speed decorrelates from the one interacting with the rotor especially in wind farms and mountainous terrain. This is exacerbated by the ever growing rotors, as the physical distance to the measurement location grows equally.

Decorrelation is mitigated by measuring closer to the rotor, but requires exact knowledge of the flow deceleration to estimate the available, undisturbed kinetic energy. Thus this thesis explores, mostly numerically, any wind turbine or environmental dependencies of this deceleration. The computational fluid dynamics model (CFD) employed is validated with velocity measurements from lidars upstream of an operational turbine. A new stochastic validation methodology in combination with extensive uncertainty quantification and propagation allows validating the CFD model under these realistic conditions for an area covering the majority of the decelerating flow upstream. This is the first validation of its kind and it demonstrates the advantage of including uncertainties in the process.

The flow behaviour upstream of a single rotor is largely insensitive to specific rotor designs and operating conditions. In fact the rotor thrust coefficient is the single most significant parameter. Exploiting this singular dependency, a fast semi-empirical model is devised that accurately predicts the velocity deficit upstream of a single turbine. Near-rotor measurements in combination with this model are able to retrieve the kinetic energy available to the turbine in flat terrain. Complex terrain and multiple turbines are more demanding, though, as they enhance non-linear interactions.

DANSK RESUMÉ

En vindmølle opbremser vinden foran sig ved at udtrække kinetisk energi fra luften. Opbremsningen er størst i rotorplanet mens den er ubetydelig for opstrøms afstande større end 5 rotor radier (R). Området foran rotoren hvor opbremsningen er signifikant kaldes for induktionszonen. Vindhastighedsmålinger mere end 5R opstrøms vil således ikke være influeret af vindmøllen. Imidlertid vil vindhastigheden her til dels være dekorreleret med den vind der faktisk rammer vindmøllen, specielt i de tilfælde hvor den er placeret i en vindmøllepark eller i komplekst terræn. For store vindmøller vil denne dekorrelering være endnu mere udtalt. Det er dog nødvendigt at have et eksakt mål af den tilgængelige vindhastighed for at kunne evaluere en vindmølles ydeevne. Dekorreleringen kan mindskes ved at måle tættere på rotoren, men dette vil kræve en bedre forståelse af induktionszonen således at målingerne kan korrigeres for opbremsningen.

Formålet med den foreliggende afhandling er derfor at studere induktionszonen og dens afhængighed af vindmøllen eller de ydre omgivelser. De fleste resultater præsenteret i afhandlingen er fundet vha. Navier-Stokes simuleringer (CFD). Simuleringerne er blevet valideret ved at sammenligne med lidarmålinger opstrøms en fuldskala vindmølle. I forbindelse med valideringen blev der brugt en helt ny stokastisk valideringsmetode kombineret med omfattende usikkerhedskvantificering som viser vigtigheden og fordelene ved at inkludere usikkerhederne i validering af CFD modeller.

Induktionszonen for en isoleret vindmølle er kun lidt følsom overfor møllens specifikke rotor design og de eksterne vindforhold (vindgradient, turbulens etc.), hvorimod den er meget sensitiv overfor ændringer i rotor thrust-koefficienten. Påbaggrund af denne viden er en hurtig og simpel semi-empirisk model blevet præsenteret som kan forudsige hastighedsopbremsningen opstrøms en enkeltstående mølle. Situationer med komplekst terræn eller tætstående møller er dog mere krævende at forudsige. Det bliver vist at den indkommende vind til en række af møller afviger fra den der eksisterer for en enkeltstående mølle ved bl.a. at være mere afhængig af vindretningen. Denne observation udfordrer den nuværende måde hvorpå man evaluerer vindmøllers ydeevne, da dette ofte foregår på flade områder hvor møllerne står på række.

ACKNOWLEDGMENTS

From the first time I met my supervisor Niels Troldborg, I knew he is someone I would like to work with the next couple of years. I am truly grateful for his continued support throughout the three years - not only at a work level. His motivation is capturing, he is extraordinarily humble and invested a lot of time in me. He never tried to dictate an agenda, but instead knew exactly how to nudge me in the right direction. Thank you so much Niels! I would also express my gratitude to my co-supervisor Andreas Bechmann for his support regarding complex terrain flows and simulations. He was extremely approachable at all times. Many thanks also to Prof. Christian Masson for hosting me at ÉTS and essentially becoming my supervisor for a few months. Generally, everyone that I was involved with in the UniTTe project was tremendously helpful and happy to support me - in particular Antoine Borraccino, Ameya Sathe, Nikolas Angelou and Andrea Vignaroli. Rozenn Wagner was a great project leader to have. I also need to thank my fellow PhD students and colleagues at DTU Wind - in particular Mac Gaunaa, Paul van der Laan and Niels Sørensen - and in Montréal for creating such a great work atmosphere. I sincerely enjoyed collaborating with my PhD colleagues and friends Juan-Pablo Murcia Leon, Emmanuel Branlard and Jörn Nathan (ÉTS) and am extremely grateful for incorporating me in their work.

A big thank you also to my footballing friends in Copenhagen and those at my home airport EDWN in Klausheide, especially to my gliding club LSV Lingen, for allowing me to forget about my PhD every now and then. Finally, I would like to thank my parents, brother and grandparents on both sides of the Atlantic for their moral support. And of course thank you Bryony for coming to Copenhagen and making life so much better.

Im Grunde sind es doch die Verbindungen mit Menschen, die dem Leben seinen Wert geben.
—Wilhelm von Humboldt

To my fellows

CONTENTS

LIST OF FIGURES

LIST OF TABLES

ACRONYMS

CFD	Computational Fluid Dynamics
RANS	Reynolds-averaged Navier-Stokes
LES	Large-eddy simulation
DES	Detached-eddy simulation
AD	Actuator disc
AL	Actuator line
BEM	Blade element momentum
pdf	Probability density function
TI	Turbulence intensity

Part I

SYNOPSIS

This part summaries all work constituting the thesis. It sets the investigated topics into perspective and only focuses on major findings. It is self-contained, which also applies to each of its chapters. The motivation and problem approach are presented in chapter 1, followed by an introduction to the numerical model in chapter 2 and its validation via a newly developed stochastic framework in chapter 3. Chapter 4 gives a detailed account of the flow physics in the induction zone and its dependency on certain parameters. Based on those findings a simple model is devised in chapter 5. Finally, chapter 6 summarises the remaining challenges in connection with the induction zone and provides an outlook how to tackle them. Aside for chapter 2 only a general basis of fluid mechanics and physics is required by the reader.

1 INTRODUCTION

A wind turbine rotor converts the wind's kinetic energy into rotation, driving a generator that produces electrical power. Hence, wind speed and power production are intrinsically linked. Each wind turbine has a specific *power curve* relating wind speed to electrical power output, which allows turbine operators to predict power production at a site or control whether a turbine is performing as promised by the manufacturer. However, where should the wind speed be measured to asses the power curve? After all, it needs to be representative of the power provided by the wind to the turbine. Industrial standards[1] require wind speed measurements at turbine hub height and at least 5 rotor radii (R) in front of the rotor. The latter requirement might be startling, but is related to the presence of the turbine itself. The lift generated at the turning blades creates a reaction force, called thrust, opposing the incoming wind. The thrust distribution

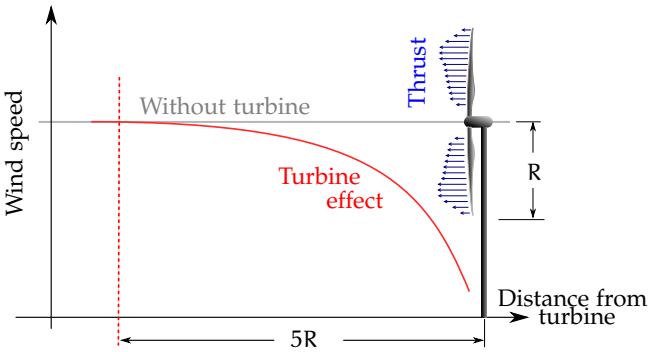

Figure 1: The influence of turbine thrust on the upstream wind speed.

over a rotor is schematically shown in fig. 1 and shows the effect it has on the wind speed (–). The flow deceleration is strongest at the turbine, but diminishes moving upstream until it recovers to the *free* wind speed at 5R.[2] Here *free* refers to the wind speed that would be measured at the rotor position in absence of the turbine (–). The region in which this deceleration is noticeable is commonly referred to as the *induction zone*[3] and the effect as *turbine blockage*.

1 IEC 61400-12-1:2005 [1]

2 The limit is based on predictions by *vortex sheet theory* introduced by Joukowski [2] as early as 1912.

3 Induction zone, as the rotor's aerodynamic forces *induce*/cause negative velocities over the region upstream.

MEASURING POWER CURVES Conventionally the reference wind speed is measured with a cup anemometer installed on a met mast (fig. 2). Considering the small turbine sizes and installation sites a few

Figure 2: Conventional 80m met mast with instrumentation at several heights.

decades back, this approach seems practical and inexpensive. Nowadays though, turbines are exceeding 160m in rotor diameter - coming with towers of similar height - and are more often installed offshore or in mountainous regions. This requires very tall and thus expensive met masts; if an installation is at all possible[4].

Further to the practical limitations of met masts, there are issues emerging from measuring far from the turbine. In fig. 1 the wind speed is shown as constant in absence of the rotor, which is a strong simplification. The real wind field evolves moving along the surface, due to many constantly changing forces in the atmosphere and the terrain itself. At a rotor diameter of 160m and a realistic wind speed of 8m/s it would take 50 seconds for air passing a met mast 5R away to reach the turbine! Measuring further from the rotor thus decorrelates the measured wind field from the one ultimately interacting with the rotor. This flow evolution is exacerbated in mountainous terrain, forests and wind farms, as the wind speed becomes a function of the measurement location. The shape and roughness of the terrain dictates the wind speed, leading to increasing flow

4 Onshore planning permission is hard to obtain and offshore platforms make it prohibitively expensive.

velocities towards hill summits (see fig. 3), whereas neighbouring wind turbines act as additional obstructions to the wind. Reducing uncertainty

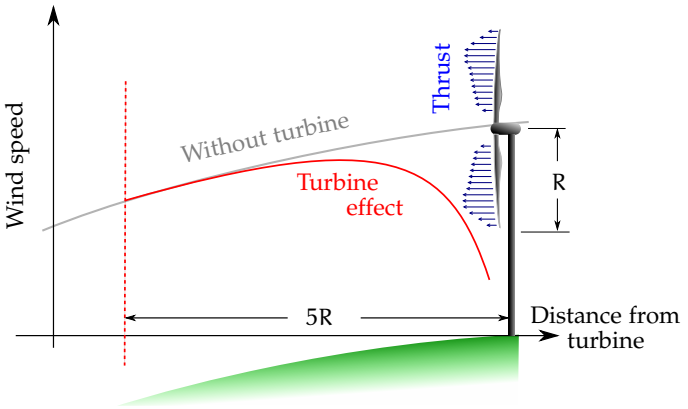

Figure 3: Wind speed evolution upstream of a turbine erected on a hill top. The turbine free wind speed evolves with the distance from the rotor.

from flow evolution would require measurements closer to the rotor, moving them inside the rotor induction zone. Met masts would obstruct the incoming wind and influence the turbine's performance. Lidars [5](wind velocity measuring lasers) on the other hand can be mounted on top of the turbine nacelle and remotely measure at different distances upstream of the turbine, making met masts obsolete. Figure 4 shows two lidars, installed accordingly, performing such inflow measurements. The viability

Figure 4: Two vertically aligned lidars mounted on a Siemens SWT-2.3-93 nacelle facing the wind - ready to measure the inflow.

5 Acronym for Light Detection and Ranging. For an introduction to the measurement principle see [3].

of lidars for power curve assessment has been proven in multiple studies [4, 5]. They even outperform met masts in terms of power curve uncertainty and acquisition time, as they track the wind direction and probe velocities over the entire rotor[6]. Their measurements can additionally become an input to preview-based control strategies, enabling the turbine to dynamically adapt to the incoming wind field [6].

Nevertheless, measuring closer to the rotor and thus inside the induction zone requires a key element: a validated, fast and accurate prediction tool of the wind speed deficit upstream of the rotor (i. e. the shape of – in figs. 1 and 3). This tool could then remove the turbine bias from inflow measurements, such that they remain representative of the kinetic energy contained in the wind.

INDUCTION ZONE PHYSICS The induction zone is ultimately driven by the interaction between the wind turbine and its surrounding environment. Developing a model necessitates understanding this interaction and identifying the major parameters driving it. In this context the following topics need to be addressed:

1. Wind turbine
    - Rotor design
    - Turbine control
    - Operating conditions
2. Environment
    - Neighbouring turbines
    - Atmospheric conditions
    - Topography

LITERATURE REVIEW All of these subjects individually have received considerable attention from the aerospace, meteorology and wind energy research communities over more than a century, however the induction zone was seldom the focus. This is not surprising considering that for rotor (or propeller) design mostly the wind speed in the rotor plane is of interest. Therefore only a relationship between free and rotor plane velocity was of interest, not the velocity evolution in-between.

A first quantitative account of the flow velocities upstream of a rotor was given by Castles and De Leeuw [7] in 1954. Their work was purely theoretical - based on vortex methods[7] - and considered helicopter rotors, which was of more interest during that period[8]. Another theoretical investigation, though this time for wind turbines, followed in 1979

6 Currently, commercial nacelle lidars can measure at multiple distances and locations off the rotational axes.

7 See [8] for a comprehensive introduction.

8 Helicopter theory formed the basis of wind turbine research.

by Modarresi and Kirchhoff [9]. They showed the expansion of the flow approaching the rotor and its acceleration around the nacelle[9]. The expansion was attributed to rapid flow deceleration beyond 2R approaching the rotor.

With the emergence of lidars and their potential application to inflow measurements, the induction zone has received renewed interest from the beginning of this decade. Medici *et al.* [10] performed measurements of the flow upstream of various model turbines in a wind tunnel and compared them to model predictions. The models included simple, analytical predictions based on classical actuator disc vortex theory [2] and high-fidelity Computational Fluid Dynamics (CFD)[10]. Measurements and models show negligible deceleration 6R from the rotor, but already 2.5% and 1% velocity deficit at 4R, respectively. The deceleration rapidly intensifies approaching the rotor and with it the discrepancy between measurements and models. At 1R the velocity deficit lies around 9% for the models versus 13% for the measurements. The reason for this offset remained unanswered. Spurred on by the increasing deployment of lidars, manufacturers started using their products to measure the blockage effect [11, 12] on commercially deployed wind turbines. Their conclusions remained qualitative, but proved that lidars reliably pick up the deceleration in the induction zone. Howard and Guala [13] performed similar measurements and compared them to the same analytical model Medici *et al.* used. They found strong disagreement between the model predictions and the full-scale measurements. Simley *et al.* [14] expanded this work by taking lidar measurements away from the rotor axis of symmetry, showing the induction zone over one side of a real wind turbine rotor (similar measurements are shown in fig. 5, covering the entire rotor instead). They also started a preliminary investigation into the evolution of atmospheric turbulence in the induction zone. Again, they compared with the simple analytical model and found agreement regarding the progression of the deceleration, but strong divergence regarding its magnitude.

Ultimately, all recent studies reported the deceleration of the incoming wind in front of turbines, however its magnitude remains uncertain. Full-scale and wind tunnel measurements showed larger and smaller velocity deficits relative to the same model predictions. Taking the measurements as *truth* the model error would thus lie at about $\pm 100\%$ 4R from the rotor and only drop to $\pm 40\%$ at 1R.[11] Of course the actual *true* induction zone is unknown and with the large variation in the measurements the models' validity can simply not be assessed. Curiously however, high- and low-fidelity model results match, which raises the question as to whether these models, no matter which fidelity, are missing physical phenomena

9 Interestingly they referred to it as *leakage*, as some flow escapes the blades.

10 Solving the fluid flow governing Navier-Stokes equations computationally.

11 The absolute difference increases more quickly than the absolute error approaching the rotor.

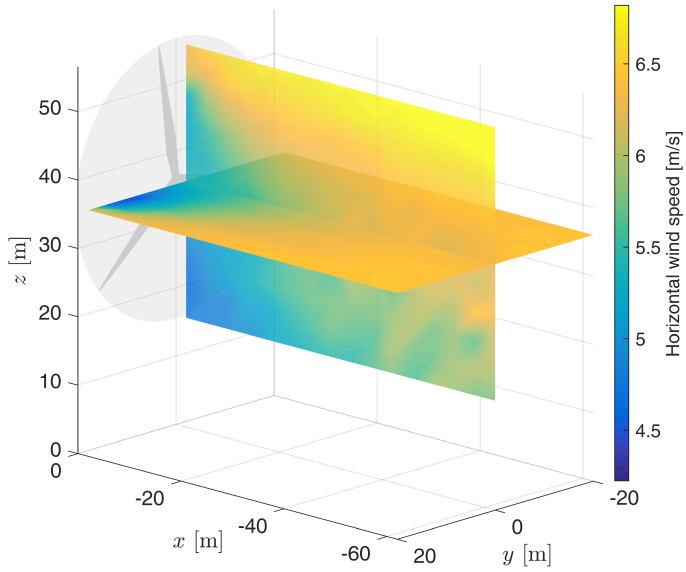

Figure 5: Three-dimensional lidar measurements of the wind turbine inflow [15] in both vertical and horizontal planes, which are analysed in connection with the CFD model validation in article 9. The turbine has a rotor diameter of 41 m.

or inputs detrimental in predicting the induction zone. Or if alternatively the inter-comparison itself is flawed?

GOALS & SCOPE By answering these questions this thesis aims at developing a validated, fast predictive tool for the turbine blockage, which ultimately enables the application of nacelle lidars for power curve measurements. To ensure the universal applicability of such a predictive tool, the induction zone is further studied with respect to all topics presented previously - concerning the turbine itself and its interaction with the environment. This investigation is performed predominantly with CFD simulations, which are validated by full-scale field and wind tunnel measurements. The validated high-fidelity fluid dynamics model consequently serves as a basis for a simple semi-empirical induction zone model.

1.1 NOTATION AND DEFINITIONS

The synopsis attempts to use minimal wind energy terminology and notation, however there are some fundamentals that cannot be avoided. The following quantities are used multiple times throughout the thesis:

γ	Yaw angle	[°]
ϕ	Tilt angle	[°]
λ	Tip speed ratio $\frac{R\Omega}{V_\infty}$	[-]
ρ	Air density	[kg/m^3]
$\sigma_\bullet$	Standard deviation of $\bullet$	[-]
Ω	Rotational speed	[rad/s]
x, y, z	Cartesian coordinates	[m]
u, v, w	Velocity components in Cartesian coordinates	[m/s]
r, ϕ, z	Polar coordinates	[m,rad,m]
$f(\bullet;\bullet)$	Probability density function, semi-colon separates sample-space and function variables	[-]
h	Hub height	[m]
v_r	Radial velocity $\sqrt{v^2 + w^2}$	[m/s]
v_t	Tangential velocity	[m/s]
A	Area covered by rotor (πR^2)	[m^2]
D	Rotor diameter	[m]
P	Power	[W]
R	Rotor radius	[m]
T	Rotor thrust force	[N]
TI	Turbulence intensity $\frac{\sigma_u}{V_\infty}$	[%]
V	Velocity magnitude or wind speed	[m/s]
$\bullet_\infty$	Free-stream value of $\bullet$ i.e. unaffected by the turbine	
$\bullet'$	Ground based reference frame	

In relation to the induction zone, and wind turbines in general, there are additionally some important non-dimensional parameters:

$$C_T = \frac{T}{\frac{1}{2}\rho_\infty V_\infty^2 A} \quad \text{Thrust coefficient}$$

$$C_P = \frac{P}{\frac{1}{2}\rho_\infty V_\infty^3 A} \quad \text{Power coefficient}$$

$$a = 1 - \frac{u}{u_\infty} \quad \text{Axial induction factor}$$

Figure 6 defines the principal coordinate system, centred about the rotor disc, and its relation to the ground fixed ($\bullet'$) and polar system.

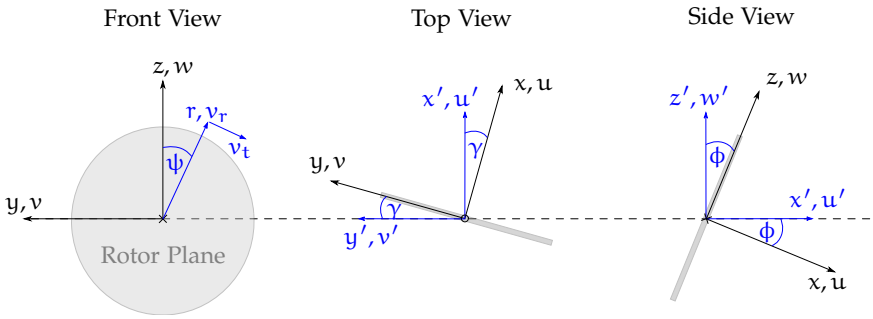

Figure 6: Coordinate system used throughout the thesis. For each dimension the corresponding velocity component is given after the comma.

2 NUMERICAL METHODS

This chapter summarises the major numerical efforts supporting the thesis and details the numerical setup of the CFD simulations. It is purposely very technical to allow the numerical findings to be reproduced, and requires specialist knowledge in this field. The following chapter 3 presents the validation of this particular CFD model, which consequently serves as reference in the development of a simple induction zone model in chapter 5.

2.1 GENERAL MODELLING APPROACH

All CFD simulations are performed following best practice established at DTU Wind Energy over several decades of research in this field. For steady problems the maximum velocity residuals are converged to 10^{-6}. In unsteady flows velocities show strong fluctuations and instead the rotationally averaged thrust serves as convergence measure. Once the thrust residual reaches 10^{-5}, turbulence is injected. The rotor-based Reynolds number is at least 10^5 for all simulations, as proposed by Troldborg *et al.*[16].

2.2 SOLVER

The finite-volume solver, EllipSys3D, discretises the incompressible Navier-Stokes equations over a block-structured domain [17, 18, 19]. The code is parallelised using the MPI library and applies a multi-grid approach to accelerate the computations. The flow is iteratively solved at each time instant by the SIMPLE algorithm [20]. In each sub-iteration it predicts the velocity field by solving the momentum equations, which are subsequently corrected by determining the pressure field (continuity equation). Four sub-iterations are maximally used. The solution is advanced in time by an iterative, implicit second-order scheme. Depending on the turbulence model either the third-order accurate QUICK [21] scheme (RANS) or a fourth-order CDS scheme (LES) discretises the convective terms. EllipSys collocates variables[1], which in combination with a second-order scheme leads to pressure - velocity decoupling. This is avoided by a modified Rhie-Chow algorithm [22]. Its modification additionally avoids numerical wiggles in the pressure field from applying discrete body forces inside the domain.

1 All flow variables are stored at the cell centre.

2.3 TURBULENCE MODELLING

2.3.1 *Reynolds-averaged Navier-Stokes (RANS)*

The RANS equations are closed using two-equation eddy viscosity methods. Despite assuming isotropic turbulence, they perform well within a wind energy context, as they are extremely stable, accurate and need relatively low spatial and temporal resolution.

For all ground-free simulations Menter's k-ω shear-stress transport closure [23] is used. However, as the rotor is represented by forces and not its actual geometry (see section 2.4) the turbulence is in fact closed by a k-ϵ formulation, since Menter's model switches to this model away from the boundary layer. For simulations including terrain, a modified k-ϵ model is used [24], which introduces a length scale limiter to avoid the common issue of non-physical dissipation in the wind turbine wake. Conventional eddy viscosity models assume a single turbulent length scale throughout the entire flow domain, which is non-physical for realistic wind turbine flows, as atmospheric scales are much larger than those in the rotor wake. Therefore the model lowers the eddy viscosity in regions of large shear like the rotor wake. The model is calibrated for the fully turbulent log-law of the wall and multiple offshore/near-shore wind sites [24].[2]

2.3.2 *Detached-eddy simulation (DES)*

DES is a hybrid method solving the Navier-Stokes equations in the far-field with Large-eddy simulation (LES) and only in near-wall regions with RANS. LES solves for the larger turbulent scales directly, whereas those below grid size are modelled with an isotropic sub-grid scale (SGS) turbulence model. Close to the wall, scales diminish beyond a LES realisable dimension and RANS is used instead. Switching between LES and RANS is achieved by a limiter function as defined by Strelets [25].

2.3.3 *Sensitivity of the induction zone to the turbulence model*

Figure 7 shows the influence the k-ω SST closure has on the velocities in the induction zone compared to inviscid flow[3]. Generally, the blockage is reduced. The change in the velocity becomes larger approaching the rotor and is greatest in the shear layer at the wake edge. In this region the turbulence model dissipates energy and starts breaking down the tip vortex. The dissipation continues to grow further downstream in the wake, yet the induction zone is not much affected by the turbulence model. The

2 Offshore roughness is extremely small and thus the model might be invalid for roughness lengths exceeding $z_0 = 0.1\text{m}$.

3 Inviscid flow is characterised by the absence of viscosity.

reduced blockage is directly related to the changes in the near-wake and arises from the reduced strength of the wake vorticity caused by turbulent dissipation. Overall the significance of the turbulence model in the induction zone is very limited.

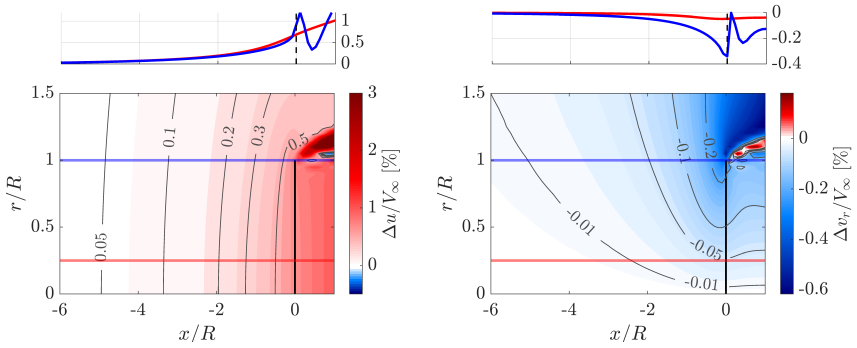

(a) Axial velocity (b) Radial velocity

Figure 7: Difference in velocities upstream of a rotor using the k-ω SST closure in RANS simulations relative to invisicid flow simulations (e.g. $\Delta u = u_{(k\text{-}\omega)} - u_{(inviscid)}$) with an uniformly loaded AD at $C_T = 0.89$ and uniform inflow V_∞. Contours are shown for the difference in axial a) and radial b) velocity components, normalised by the free-stream velocity V_∞.

2.4 WIND TURBINE

To determine the velocities upstream of the rotor it is unnecessary to resolve the full rotor geometry [26], as the blade boundary layer only impacts the velocities locally on the blade. Only large scale three-dimensional effects, like massive separation, that influence the thrust over extensive parts of the blade would make fully resolved blade geometries necessary.[4] Instead, it is common to represent rotors as actuator discs (AD) or lines (AL) as they require far lower spatial and temporal resolution. These models essentially represent the rotor with discrete body forces. The forces are computed like in a BEM approach by extracting the local velocity vector at each blade section and computing lift and drag with the help of the two-dimensional airfoil polars over the entire blade. As the forces themselves impact the velocity field, this process is iterative. It is also possible to prescribe the forces directly. Troldborg *et al.* [27] showed that the actuator representation of the rotor produces wakes nearly equivalent to full rotor simulations in terms of the time-averaged velocity field. As wake

4 Catching separation and transition remains a challenge even with fully resolved CFD.

and induction zone are inherently linked, this conclusion is transferable to the induction zone. Both tower and nacelle are not modelled, because their contribution to the induction zone is negligible in face of the lifting surfaces [27].

2.4.1 *Actuator disc (AD)*

An AD is equivalent to an infinitely fast rotating turbine, such that forces are applied over a disc (the swept area of a rotor) and vorticity is shed as sheets. The AD model developed by Réthoré *et al.* [28] discretises the disc by a polar grid and allows for spatial force variation. By calculating the intersectional grid between disc and flow mesh, disc forces and flow velocities are coupled. The polar disc grid is discretised by 16 radial and 180 azimuthal cells, which is sufficiently fine [29].

2.4.2 *Actuator line (AL)*

The AL model [30] follows the implementation by Mikkelsen [31]. It is conceptually similar to the AD model except that the blades are represented as infinitely thin lines with their forces smeared over neighbouring cells by a three-dimensional Gaussian regularisation kernel[5]. As proposed by Troldborg *et al.* [16] the Gaussian distribution parameter is set to twice the grid spacing. By representing the distinct blades by lines, the blade tip vortices, helical wake vorticity and the periodicity of the flow are captured. The lines are discretised by 41 radial points. This resolution has shown to reproduce experimental data accurately [26].

2.4.3 *The impact of the rotor model on the induction zone*

The major advantage of the AD over the AL model is its rotational independence and low requirement on time resolution, which makes it very suitable for RANS simulations. The flow-field about a disc can essentially be seen as the temporal average of a time-resolved AL solution, which does not disqualify an AD from being used in unsteady simulations [27].

However, the question remains whether missing distinct tip vortices using the AD model impacts the prediction of the induction zone. Figure 8 addresses this by presenting the difference in the average axial velocity field between an AD and AL induction zone either using airfoil data fig. 8a or prescribed forces fig. 8b both with $C_T = 0.78$. Here $\Delta u = u_{AD} - u_{AL}$, thus the contours indicate that the blockage is minutely larger for the AD simulation. The difference between prescribed and airfoil data lies in the sensitivity of the computed forces to the location of the velocity

5 Different force smearing concepts exist, however the Gaussian is the most established and validated.

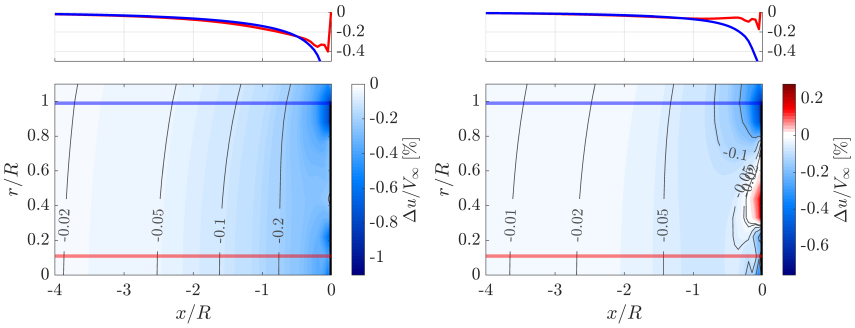

(a) Forces from airfoil data.

(b) Prescribed forces.

Figure 8: Difference in the axial velociy field upstream of a rotor when using an AD instead of an AL representation of the rotor (e.g. $\Delta u = u_{AD} - u_{AL}$). The Mexico rotor [32, 33] is used with uniform inflow $V_\infty = 15$ m/s resulting in $C_T = 0.78$. The AL velocity field is azimuthally averaged over three rotations. In a) the rotor forces are computed from airfoil look-up tables, whereas in b) the forces from the AL simulations are prescribed over the AD.

extraction. That the same thrust results in higher induction for the AD is related to the differing methods for introducing the blade forces inside the flow domain. Smearing the forces in the AL model reduces the blockage [34]. Nevertheless the differences in the induction zone are minor and essentially nil for the other velocity components not shown here. The decision between disc and line thus depends on whether each blade needs to be distinctly resolved.

2.4.4 *Prescribed thrust control*

The induction zone is governed by the rotor thrust. Thus the comparability of different flow scenarios is driven by applying exactly the same thrust coefficient, C_T, in each simulation. This condition is met by an actuator disc representation of the rotor with prescribed forces. The normal force acting over a sectional area ΔA of the disc is given by

$$F_{\{N,\Delta A\}} = \frac{1}{2}\rho_\infty V^2_{\{\infty,\Delta A\}} C_T \Delta A \tag{1}$$

Here the free-stream velocity $V_{\{\infty,\Delta A\}}$ acting over the area ΔA is determined by extracting the velocity at ΔA from a rotor-less simulation as shown in Figure 9.

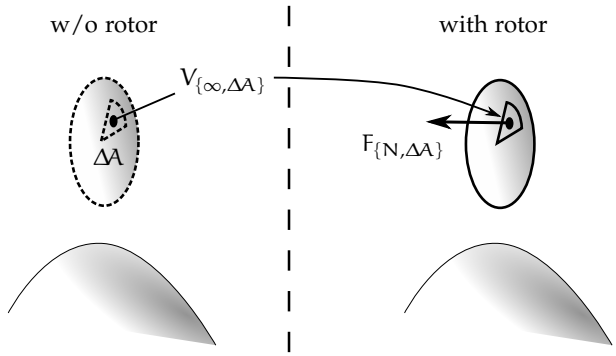

Figure 9: Method for determining the axial force, $F_{\{N,\Delta A\}}$, for each section of the actuator disc by extracting velocities from a rotor-less simulation.

2.5 COMPUTATIONAL DOMAINS

All meshes are uniform, block-structured and equispaced around the rotor. This avoids any flow distortion from cell stretching in the region of interest. Furthermore the grid spacing around the rotor is maximally R/32, which has been shown to yield sufficiently accurate results [29, 27].

2.5.1 *Boundary free and flat terrain*

The domain size is at least $25R^3$, which minimises the impact of domain blockage ($\pi/25^2 = 0.5\%$). The refined mesh region around the rotor is a tenth of the total domain size. In the following sections the domains for different simulations are schematically laid out and the respective boundary conditions given.

BOUNDARY FREE (see fig. 10)

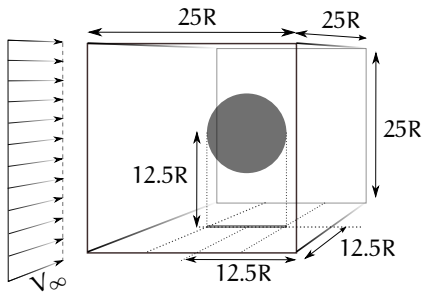

Figure 10: Domain layout for boundary-free simulations with the rotor disc at its centre and uniform inflow.

- Sides + Top + Bottom: Symmetry - normal flux is zero
- Front: Inflow/Dirichlet - fixed velocity
- Back: Outflow/Neumann - zero-gradient

To investigate yaw and tilt, the rotor is angled about its centre.

FLAT TERRAIN (see fig. 11)

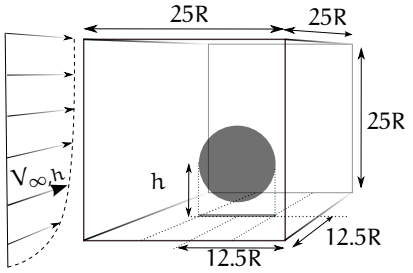

Figure 11: Domain layout for flat terrain simulations with the rotor disc at hub height, h, and sheared inflow following the log-law.

- Sides: Symmetry - normal flux is zero
- Front + Top: Inflow/Dirichlet - fixed velocity defined by log-law
- Bottom: Wall/No-slip - zero normal and tangential velocity
- Back: Outflow/Neumann - zero-gradient

The wall cell size is 0.05m.

2.5.2 *Complex terrain*

The mesh generated for complex terrain follows the WasP-CFD methodology [35], whilst obeying the limitation on the grid size in vicinity of the rotor. The mesh is of an O-type with a centrally located cubic refined region, which allows varying the wind direction without changing the mesh. To include sufficient topographic features surrounding the wind turbine the mesh has a radius of 17 km. The refined mesh region is relatively large with a 32R side length to avoid ignoring small terrain irregularities and the surface map is subsequently smoothed with respect to the grid resolution. The total domain height is 10 km, whereas the refined region extends 5R vertically above the hill surface. The mesh grows upwards in layers normal to the surface, starting from a wall cell size of 0.05 m and expands vertically. A demonstration of the usual mesh layout in complex terrain is given in fig. 12, which shows height contours

of Perdigão (eastern Portugal). Further to the height, the terrain surface roughness is also included in the simulations by estimating the characteristic roughness length z_0 - used in the log-law - from measurements. The wall cell is placed at z_0.

Note that the exact definition of the mesh might vary, as it is site specific!

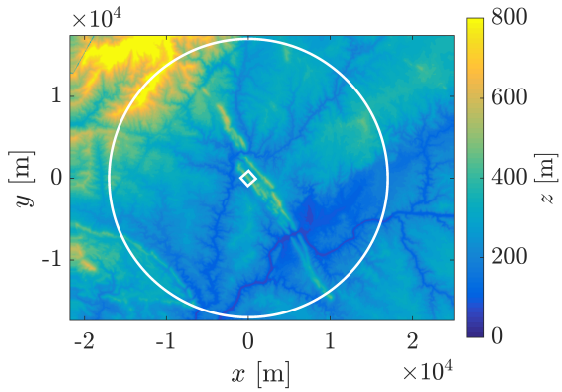

Figure 12: O-mesh in complex terrain with height contours of Perdigão (eastern Portugal). The mesh is centred and refined around the position of an Enercon E-82 (squared region) located on a ridge.

BOUNDARY CONDITIONS The in- and outflow boundaries are applied circumferentially to the O-mesh. The outflow region is defined as the arc resulting from a 90° sector centred about the inflow direction.

- Inlet: Inflow/Dirichlet- fixed velocity defined by log-law
- Outlet: Outflow/Neumann - zero-gradient
- Bottom: Wall/No-slip - zero normal and tangential velocity
- Top: Inflow/Dirichlet- fixed velocity defined by log-law

2.6 INFLOW TURBULENCE

Atmospheric turbulence is generated using the Mann model [36, 37] in accordance with the IEC standards [38]. It is based on rapid distortion of isotropic turbulence under linear shear and applies an eddy lifetime model for estimating the three-dimensional turbulent spectrum. It thus treats longitudinal and vertical velocity components as correlated, as implied by the Reynolds stress tensor. The discrete incompressible turbulent

box is generated on an equispaced mesh and is anisotropic, homogeneous and stationary. By inferring Taylor's frozen turbulence hypothesis the spatial box is advected by the mean wind speed through the flow domain. The fluctuations are simply superimposed on the mean velocities. The cross section of the turbulent box covers an $8R \times 8R$ plane and is centred on the rotor. The resolution of the turbulent box is lowered to a quarter of the flow mesh.

Any physical theory is always provisional: you can never prove it — Stephen W. Hawking

3 MODEL VALIDATION & VERIFICATION

This chapter summarises article 9. Articles 4 and 6 are also associated with the validation, as they concern certain data post-processing challenges.

The results of this thesis rely on the validity of the computational method presented in chapter 2. Validation and verification has been an accompanying effort within the development of EllipSys since its release in the 90s. Comparisons with measurements acquired in wind tunnels and from operational wind turbines have proven the accuracy and precision of the simulations. Nevertheless, full-scale measurements of the flow-field around rotors were missing until recently, which prevented the validation for realistic environmental conditions. Nowadays synchronised lidar systems [39] are providing these measurements, by acquiring 3-D velocity vectors with high temporal and spatial resolution over extensive flow volumes. Such a synchronised triple-lidar system was measuring the inflow region of a 500 kW wind turbine [15, 40] in the summer of 2014 as part of the UniTTe project. Over 11 days it acquired 5 hours of usable data, which proved invaluable in model validation.

3.1 ANALYSING TRIPLE-LIDAR VELOCITY MEASUREMENTS

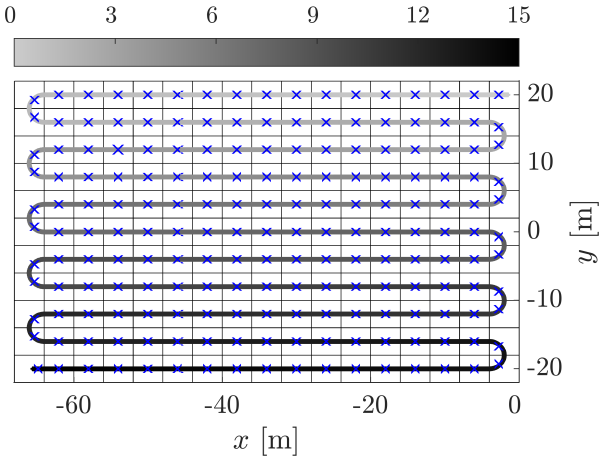

Figure 13: Triple-lidar measurement grid and sampling path (grey tones). x = Cell-averaged points.

A triple-lidar captures complex flow patterns over large areas, bringing with it added complexity in its data analysis, especially in terms of uncertainty quantification. The measurements were taken in front of the Nordtank NTK 500 wind turbine (R = 20.5m) located at the southern edge of the DTU Risø campus. They covered the entire rotor diameter and extended 3.1R upstream. The measurement pattern itself was fixed, such that the rotor and measurement region were not always aligned. The horizontal pattern is shown in fig. 13, where crosses denote the locations of the available velocity vectors. The spatial resolution was 4×4m, which allowed capturing the flow upstream in 15s. There are several processing challenges associated with these triple-lidar measurements, especially with incorporating the various uncertainties into the data processing chain:

- INFLOW VARIABILITY: Wind is highly heterogeneous in space and time during a summer day, resulting in strong fluctuations in the inflow velocity during the measurement acquisition. These natural velocity fluctuations easily surpass the velocities induced by the rotor upstream, thus obscuring the decelerating effect the turbine has on the flow. A graphical representation of this is given in fig. 14. Furthermore, inflow velocity and turbine thrust are intrinsically linked, such that any variability in the wind field is reflected in the thrust and consequently the induction zone.

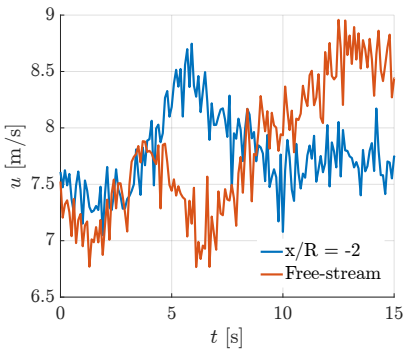

Figure 14: Representative velocity signals extracted from LES simulations in the free-stream (x/R = -6) and the induction zone (x/R = -2) along the rotor centreline (r/R = 0). These signals exclude volume averaging, but random noise is added as seen in actual measurements. Despite the wind's moderate TI of merely 10% the spatial decorrelation and instationarity suffice to obscure the deceleration induced by the rotor.

- MEASUREMENT AND TURBINE COORDINATE SYSTEM MISALIGNMENT: The misalignment uncertainty propagates to the probe location of the velocity vectors and its components.

- FREE-STREAM ESTIMATE FROM TRIPLE-LIDAR DATA: Estimated from measurements in the horizontal plane and inside the induction zone, therefore requiring a thrust correction. This estimate additionally needs to reflect the inflow variability.
- VOLUME-AVERAGING: Unlike conventional wind measuring instruments, lidars measure velocities over a volume and not in a point (see article 6).
- SPATIO-TEMPORAL AVERAGING: As shown in fig. 13 the lidars in fact sample the flow continuously (grey background pattern) and not at distinct locations. Measurements falling in each square are averaged to reduce signal noise, thereby introducing some spatio-temporal averaging.
- MEASUREMENT NOISE: Atmospheric conditions, hard targets, electrical noise and perturbations in the optical system heavily influence measurement quality. The velocity vectors therefore require filtering (see article 4).
- LIDAR MEASUREMENT LOCATION: Lidar beam angles are needed to determine the velocity vector and its location, but are not known for certain.

Except for the last point, all these challenges are tackled in the data analysis, including the estimation of the uncertainties associated with each of them.

To preserve the authenticity of the measurements the data itself is not altered by any of the processing steps, but instead the CFD flow-fields are processed to mimic the triple-lidar measurements. This essentially leads to the measurement uncertainties propagating through the model, as they become an input to the CFD simulations.

3.2 A STOCHASTIC VALIDATION METHODOLOGY

Perfect knowledge about the atmospheric conditions, the free wind field and the terrain would possibly allow reproducing the lidar measurements deterministically with a CFD model at any instant in time. Despite measuring more of the wind field than ever before with a triple-lidar, velocities are just known in a single point at any one time. Everywhere else in space only measurements taken earlier are available. Even estimating the variation of the free-stream velocity from the lidar measurements is challenging as the velocities are a function of time and space and should exclude any rotor induction. Essentially, the sole possible input remaining for the CFD model is thus the free-stream velocity, which is estimated from a heavily fluctuating quantity and thereby uncertain.

Usually in wind energy the fluctuations and noise in the measurements are filtered out by time-averaging all data over 10 to 30 minutes, depending on their variability[1]. A comparison with a model is then performed by inputting the average free-stream velocity to the model. Following this approach the results presented in fig. 15 are obtained with the triple-lidar measurements and a RANS-AD model.[2] A LES-AL approach is unnecessary in this case as only a time-averaged solution is needed. As the flow

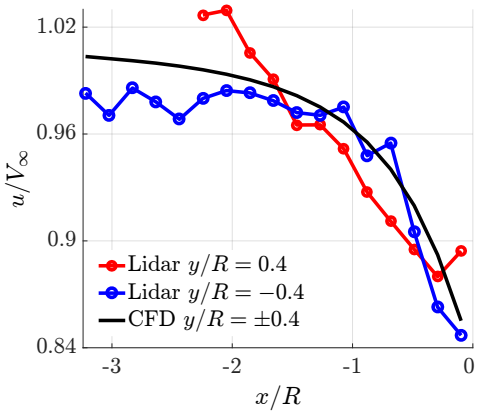

Figure 15: Axial velocity evolution upstream of wind turbine along two lines perpendicular to the rotor. The lidar data are averaged over a 30 minute period with a mean free-stream velocity of 10.3m/s. This velocity is set as inlet condition to the steady-state RANS simulation. The agreement between measurements and model results is equally weak across the remaining dataset.

approaches the turbine ($x \to 0$) the axial velocity component (u) diminishes, due to the turbine-induced blockage. However, even though the line y/R = -0.4 appears to match the numerical simulations[3], the other line shows strong disagreement with regards to the nature of this deceleration. In fact almost any kind of *model* could be fitted to this data. This figure only serves as an example of a phenomenon registered across all measurements and is not limited to temporal averages. Any kind of sorting and averaging introduces some bias into the model validation, by making the validation space a function of the sorting process. This encourages tuning the sorting parameters and limiting the validation space, which jeopardises proper model validation. Additionally, with little data as in this particular measurement campaign, short averaging periods cannot eliminate noise either.

1 The more noise or fluctuations in the signal, the longer the averaging periods need to be.
2 This particular 30 minute period is shown, as it contains most lidar data and presents relatively good agreement.
3 The induction zone is symmetric with horizontally uniform inflow.

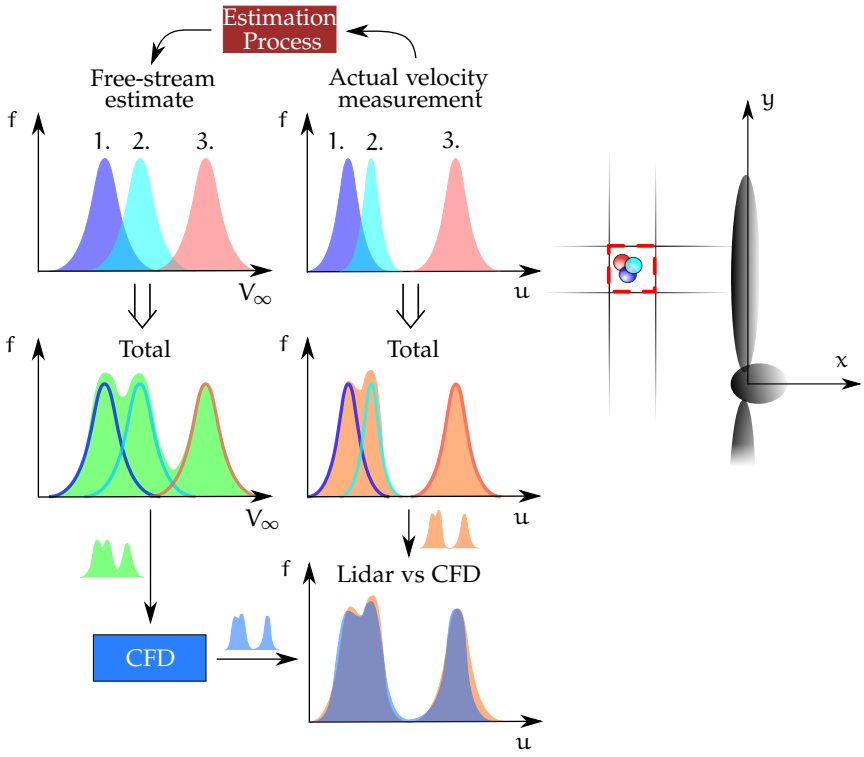

Figure 16: Each triple-lidar measurement has a free-stream velocity estimate further to the actual measured velocity vector. Both the uncertainty and natural variability is accounted for by a probability distribution f. Here three lidar measurements and their free-stream estimate are falling into the same spatial averaging window, contributing towards the final free-stream and measured velocity distribution in this grid cell. The CFD block stands for all numerical processing and uncertainty propagation associated with generating a final model pdf.

So why not avoid sorting data all together and include the variability in the wind field seen by the measurements? A deterministic approach cannot include the uncertainty in the inflow. A stochastic method, however, allows combining all measurements without disregarding any information contained within them. Figure 16 shows schematically how three distinct measurements falling into the same spatial averaging window are treated following this approach. Each data point has not only the actual measured velocity associated with it but also a corresponding free-stream velocity estimate[4]. Both velocity measures are uncertain and therefore are expressed with probability distributions. As a next step all probabilities are combined, giving an aggregated probability distribution in this grid

4 How to estimate the free-stream velocity is detailed in article 9.

cell. The total free-stream velocity distribution then acts as an input to the CFD model producing a numerically generated velocity distribution, which is compared to the lidar measurements. This is a very simplified description of the stochastic approach, as it only details how to treat the inflow variability, but integrating all uncertainties presented previously in section 3.1 is readily accomplished via this stochastic framework. All other uncertainties and their integration in the validation process are given in article 9, but due to its significance the uncertainty associated with the coordinate system misalignment needs special mention.

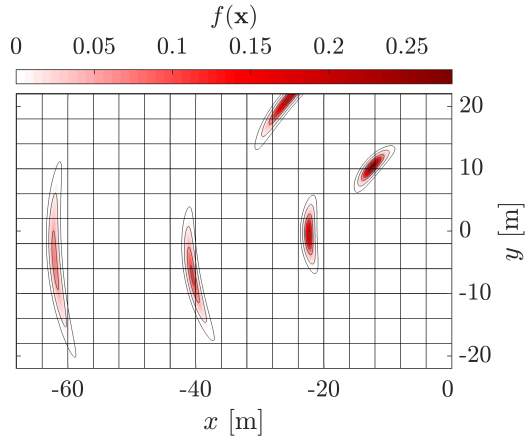

Figure 17: Heat map of the probability associated with the position of five randomly chosen, independant triple-lidar measurements in the rotor coordinate system. Note that the pdf of each triple-lidar point fulfills $\int_{\mathbf{x}} f(\mathbf{x})\, d\mathbf{x} = 1$. The spatial averaging grid is overlayed.

The yaw motion of the turbine with respect to the triple-lidar measurement grid *smears* the velocity vectors out in space. This smearing effect over the horizontal plane of the rotor coordinate system is demonstrated for five independent triple-lidar measurements in fig. 17 by visualising the pdfs of their spatial location. The further from the axis of yaw rotation (orthogonal to the plane through $(0, 0)$), the more smeared the probabilities in space. Here two-dimensional[5] normal distributions describe the probability of each velocity vector's position. The actual spatial averaging grid is overlaid and demonstrates how distinct measurements contribute to several spatial averaging windows. This does not change the fundamental validation methodology of fig. 16, but only signifies that each measurement point contributes differently to each spatial averaging cell.

5 The distribution is defined in the radial coordinate system.

THE VALIDATION The stochastic validation approach in fig. 17 is applied to all 197×10^3 triple-lidar data points - the complete 5 hour dataset - in combination with extensive uncertainty propagation/quantification. As a result, each spatial averaging cell is associated with velocity pdfs computed from triple-lidar measurements and the CFD model. Note that pdfs exist for each velocity component. Figure 18 compares the axial velocity pdfs in form of their respective mean and standard deviation along the line $y/R = -0.4$. The agreement is nearly perfect; only in the rotor's vicinity ($x/R > -0.1$) do the results diverge slightly. Comparing with the previously shown deterministic results in fig. 15 reveals the vast benefits coming with this novel stochastic approach to validation. Here only the results along a single line are shown, but this favourable agreement between measurements and model continues across the entire induction zone and the other velocity components.[6] In fact the maximal difference between

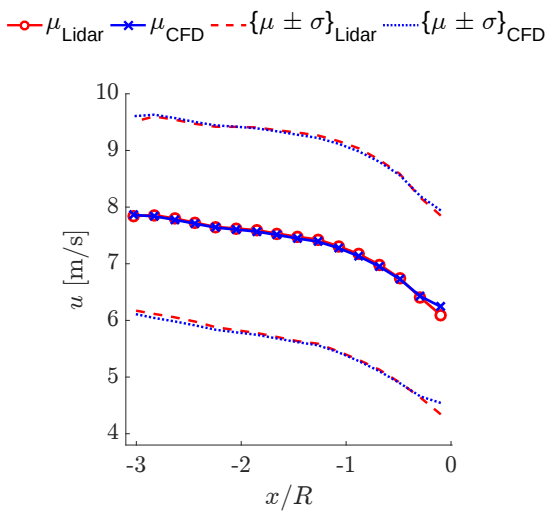

Figure 18: Comparison of triple-lidar (o-) and CFD (x-) probability density functions in form of mean and standard deviation along the line $y/R = -0.4$. The pdfs are a result of the sotchastic validation process.

mean and standard deviations - normalised by the mean free-stream velocity magnitude - stays below 4.5%[7] up to half a radius upstream of the turbine for all three velocity components. For the axial component it even remains below 1.6% for $x/R < -0.8$, which translates into a maximal nominal difference of 0.11m/s. Setting this figure into perspective with some potential measurement errors truly reveals how well triple-lidar and CFD agree: The minimal recorded variability in the free-stream velocity during a triple-lidar measurement period of 30 minutes was more than double

6 Refer to pages 1495-1496 of article 9.

7 Percentage difference is here defined as: $\Delta\bullet = \left| \frac{\bullet_{\text{Lidar}} - \bullet_{\text{CFD}}}{(V_\infty)_{\text{Lidar}}} \right| \times 100$

this value at 0.26m/s. Furthermore the Doppler spectral resolution of the lidars lies at 0.15m/s and a 1° error in the lidar beam angle would incur the same velocity difference. Essentially this renders model and measurement errors indistinguishable, validating the model within the measurement error bounds. Nevertheless, its validity is more questionable close to the rotor, as both model and measurements are suffering from errors in this region. The validation conducted herein increases the confidence in the CFD model, but only over a limited parameter space. Obviously, further validation with different parameters related to the wind turbine and the environment would be beneficial.

4 FLOW PHYSICS OF THE INDUCTION ZONE

This chapter summarises how different parameters affect the induction zone by investigating each of them in isolation. Each parameter has its own section. Results are almost exclusively obtained with the numerical approach detailed in chapter 2. Hence, unless specifically stated, model solutions are presented. An overview of the parameter specific numerical configuration is given at the end of each section. If the content of a section is related to an academic publication the article is cross-referenced in the heading and should be consulted for more detailed information.

4.1 INTRODUCTION

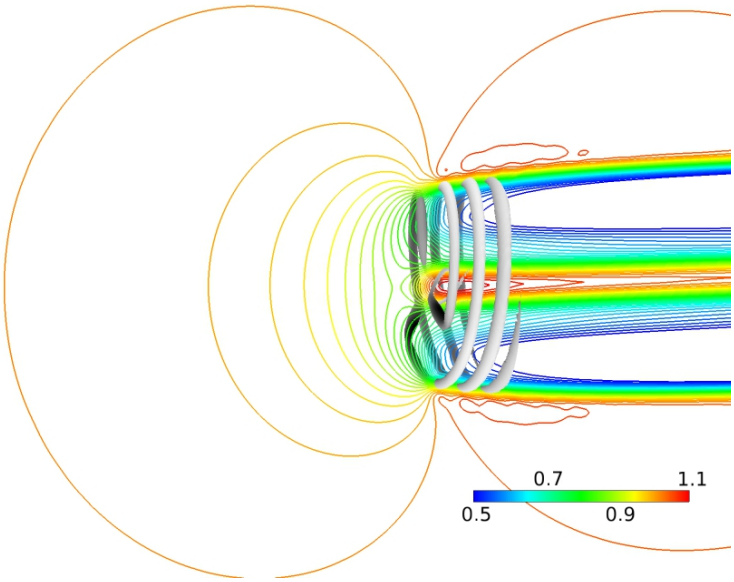

Figure 19: Instantaneous flow-field in front of a rotor: contours of axial velocity, normalised by the inflow wind speed. An iso-surface of voritcity magnitude shows the rotor vortex system.

Figure 19 demonstrates the instantaneous velocity field developing around a wind turbine rotor.[1] Contours of the axial velocity normalised by the inflow wind speed, show the continuous deceleration of the flow approaching the turbine. Passing the turbine, the flow has lost energy to the tur-

1 Vorticity magnitude is a measure of local flow rotation.

bine, leading to a pronounced velocity deficit in its wake. The blockage from the blades and their wake also cause the flow to accelerate around the wake edge and through the rotor core[2]. The contours additionally demonstrate the symmetry of the induction zone about the rotational axis of the turbine.

4.2 WIND TURBINE

4.2.1 *Thrust* [article 2]

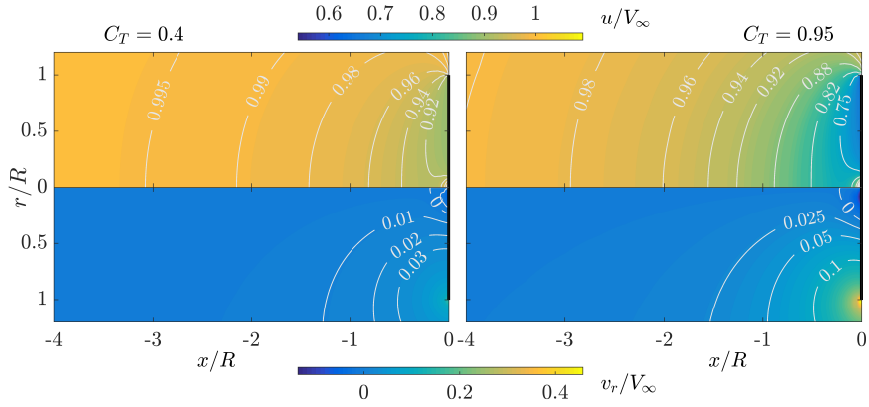

Figure 20: Contours of the upstream axial (top) and radial (bottom) velocity components normalised by the free-stream velocity magnitude for $C_T = 0.4$ (left) and $C_T = 0.95$ (right) in the induction zone. Note that the induction zone is axisymmetric about the centreline.

The thrust exerted by the turbine on the flow causes the formation of the induction zone and thus strongly correlates with the flow deceleration. In fig. 20 normalised axial (top) and radial (bottom) velocity contours are depicted for thrust coefficients of $C_T = 0.45, 0.95$ in the induction zone. The inflow is homogeneous and thus the blockage is axisymmetric. The iso-lines highlight that the reduction in the axial velocity (u) is strongest along the centreline for a given distance from the rotor. The further from the rotor, the lower and more homogeneous is the velocity reduction in the radial direction. By mass conservation a drop in the axial flow rate is accompanied by an increase in the radial component, forcing flow around the rotor and intensifying towards the rotor tips. However, the change in the radial velocity is smaller and occurs closer to the rotor than for the axial component. As the core of the turbine is not occupied by any lifting

2 The flow-field does not include the nacelle or tower, however it is still a realistic representation as both only exert a negligible force on the flow in comparison to the blades [27].

surfaces[3], no thrust is exerted on the flow. The rotor blockage forces flow through this core - represented by a negative radial velocity ($v_r < 0$) - forming a high velocity jet. An increase in the thrust coefficient leads to a clear decrease in the axial velocity: whereas for $C_T = 0.45$ the rotor blockage is negligible beyond -3R it still leads to a 2% drop in the axial velocity at $C_T = 0.95$. A more quantitative representation of this change is given in fig. 21. The impact of thrust becomes more dominant the closer to the rotor, manifesting itself in a 5% difference in the normalised axial component between the two thrust levels at $x/R = -1$, compared to 2.5% at $x/R = -2$. The higher reduction in the axial velocity leads to larger radial velocities. Clearly, the induction strength is predominantly governed by thrust and not the radial position. This is especially true further from the rotor.

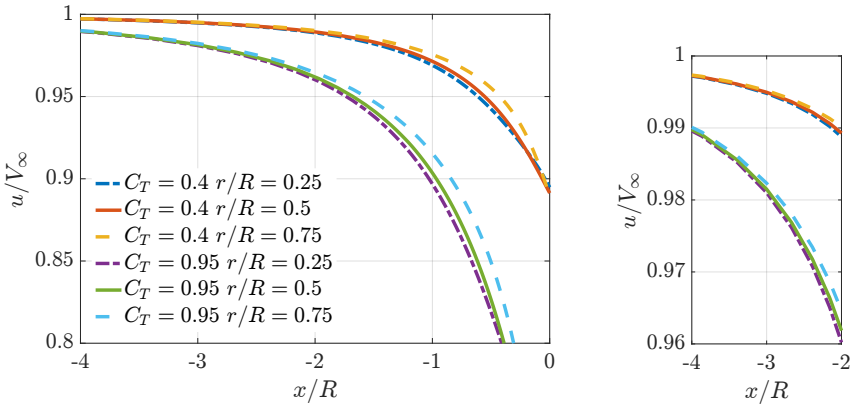

Figure 21: Axial velocity evolution through the induction zone at different radial positions and thrusts. Velocities are normalised with the free-stream velocity magnitude.

SENSITIVITY TO THRUST CHANGES The relationship between the rotor induced velocities and thrust coefficient is non-linear. Vortex sheet theory allows to approximate the velocity along the centreline:

$$\frac{u}{V_\infty} = \tilde{u} = 1 - \overbrace{\left(\frac{1}{2} - \frac{\sqrt{1 - C_T}}{2}\right)}^{a} \underbrace{\left[1 + \frac{\tilde{x}}{\sqrt{1 + \tilde{x}^2}}\right]}_{K(\tilde{x})} \tag{2}$$

3 The inner parts of the blades are cylindrical, generating a drag force that is limited in comparison to the blade lift. This also applies to the nacelle.

Differentiating with respect to C_T provides the sensitivity as a function of $\tilde{x} = x/R$ and C_T:

$$\frac{d\tilde{u}}{dC_T} = \frac{K(\tilde{x})}{\sqrt{1 - C_T}} \tag{3}$$

Contours of this function are shown in fig. 22. Clearly, a change in thrust

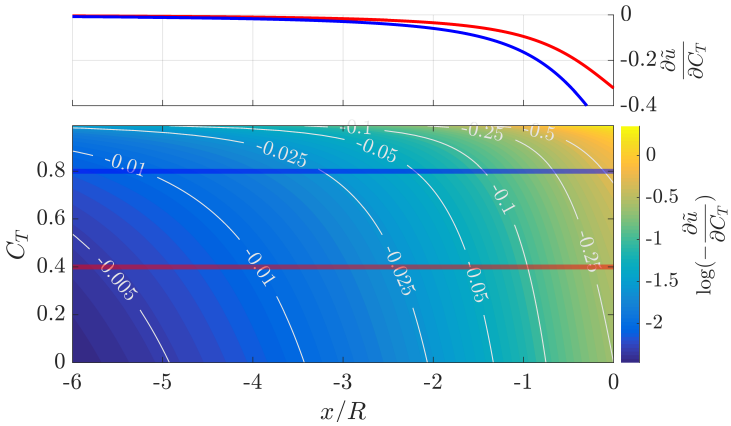

Figure 22: Sensitivity of the normalised axial velocity along the centreline ($r/R = 0$) to a change in thrust.

is felt more strongly closer to the rotor. At moderate thrust levels ($C_T < 0.5$) the sensitivity increases tenfold from x/R = -3 to x/R = -1. The increased curvature of the iso-lines in the region $x/R <$ -3 and $C_T > 0.6$ indicates a more pronounced response in the induced velocities to a thrust change, tending towards infinity beyond $C_T > 0.9$.

COMPUTATIONAL METHOD	
State	Steady
Flow equations	RANS
Turbulence model	k-ω SST
Turbine model	AD, loading from [41]
Inflow	Uniform
Domain	Boundary free

4.2.2 *Blade rotation*

The blade forces - resulting from the extraction of energy from the flow - cause the appearance of the induction zone. The blades are rotating,

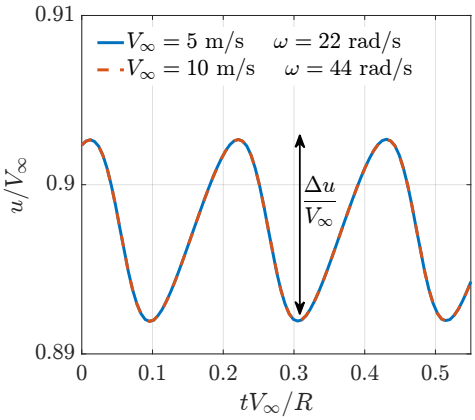

Figure 23: Periodic variation of axial velocity at the point $x/R = -1, y/R = 0.75$ with rotating blades and constant $\tilde{t}_p$ (see eq. (5)). Free-stream velocity and rotational speed are varied such that $\tilde{t}_p = 1.88$ in both cases.

such that the forcing/blockage experienced upstream changes periodically with the location of the blades. The corresponding oscillation in the velocity at a single point is shown in fig. 23. The time period needed for the same blade force to act at a certain point in space can be expressed as:

$$t_p = \frac{2\pi}{n_B \Omega} \tag{4}$$

Here n_B defines the number of blades and Ω is the rotational speed of the turbine. Unsurprisingly, with either rotational speed or the number of blades tending towards infinity the periodicity entirely disappears. This measure of periodicity is furthermore normalised by the free-stream velocity and the rotor radius, which sets it into perspective with respect to the advection velocity of wake vorticity:

$$\tilde{t}_p = \frac{\frac{2\pi}{n_B \Omega} V_\infty}{R} = \frac{2\pi}{n_B \lambda} \tag{5}$$

where $\lambda = \frac{\Omega R}{V_\infty}$ is the *tip speed ratio*. Figure 23 demonstrates the consistency of this normalisation.

Wind turbines are usually designed with three blades, as it yields the best compromise between performance, structural dynamic behaviour and costs and are operated at tip speed ratios λ between 6 and 10. Figure 24 investigates the effect of λ on the variation in the axial velocity over the induction zone. Results are shown for tip speed ratios at the extremes of the operating regime of commercial turbines with $C_T = 0.74$. Generally, blade rotation only gains importance close to the rotor $x/R >$ -2. By

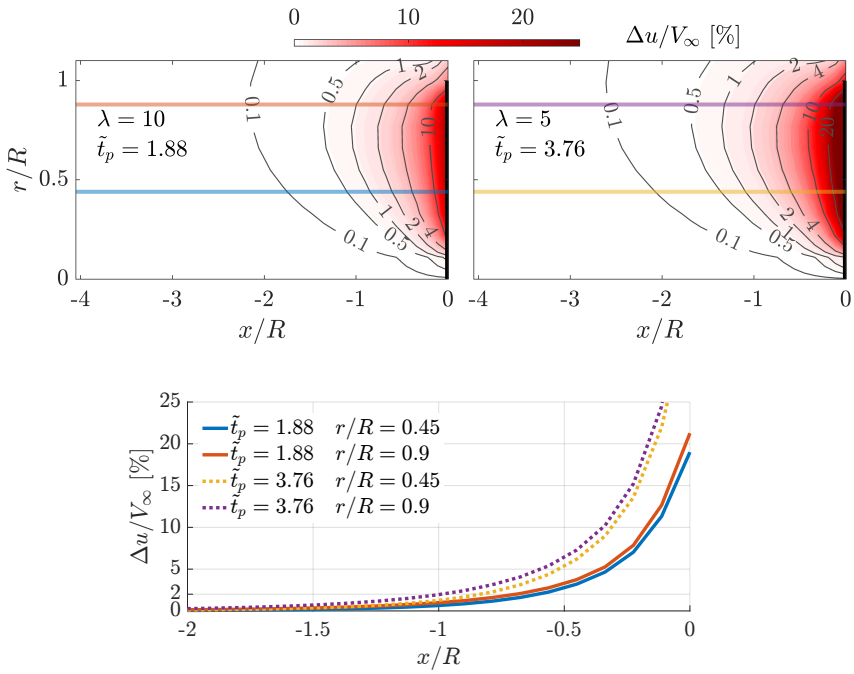

Figure 24: Amplitude of axial velocity variation $\Delta u/V_\infty$ (see fig. 23) over the induction zone with changing tip speed ratio λ and $n_B = 3, C_T = 0.74$.

doubling $\tilde{t}_p$ larger oscillations arise in the velocity, mostly taking effect under 1R upstream. The induction zone is mostly insensitive to blade rotation, as the rotating blades act jointly as a partially permeable disc further upstream and not as individual blades. This is connected to the wake vorticity, emanating from the blades (see fig. 19) continuously inducing velocities upstream whilst being advected away from the rotor. The velocity induced by a vortex source quickly diminishes with distance[4], explaining why strong velocity variations are only found close to the rotor.

COMPUTATIONAL METHOD	
State	Unsteady
Flow equations	LES
Turbine model	AL, scaled MEXICO rotor [32] loading at $V_\infty = 15$ m/s, C_T & C_P constant
Inflow	Uniform
Domain	Boundary free

4 For a vortex line the induced velocity $\propto \frac{1}{\text{distance}}$.

4.2.3 *Wake rotation* [article 2]

The incoming flow forces the turbine to rotate, resulting in an equal and opposite reaction force. Downstream of the turbine the flow thus rotates opposite to the direction of the rotor. A measure of the swirl or wake rotation is the *tip speed ratio* $\lambda = \frac{R\Omega}{V_\infty}$, where Ω is the turbine's rotational speed. For $\lambda \to \infty$ the wake rotation tends to zero and conversely it is maximised for $\lambda \to 0$.[5] The impact on the velocity field moving from a

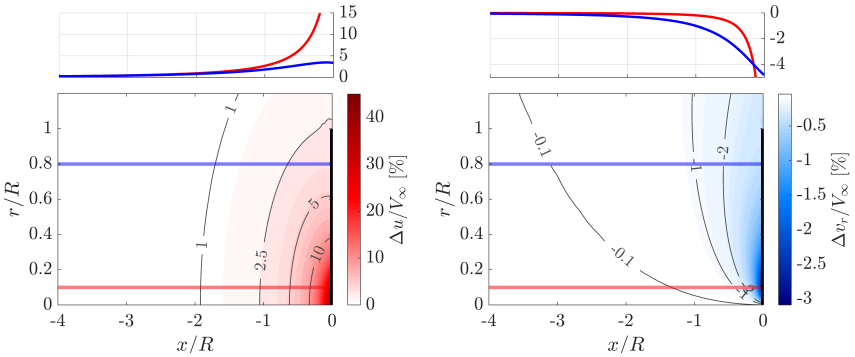

(a) Axial velocity (b) Radial velocity

Figure 25: The influence of wake rotation on the axial a) and radial b) velocity components in the induction zone. Difference in velocities ($\Delta\bullet = \bullet_\lambda - \bullet_{(\lambda=\infty)}$) for $\lambda = 2$ to non-rotational flow ($\lambda \to \infty$) with $C_T = 0.95$.

non-rotational ($\lambda \to \infty$) to a strongly rotational wake ($\lambda = 2$) is shown in fig. 25. The axial component shows a large increase towards the centre and in vicinity of the rotor, signifying a reduction in blockage with wake rotation in this region. However, the impact is very local and drops to 1% at $x/R = -2$. A drop in the radial component is noticeable even closer to the rotor (see fig. 25b), where any significant changes are confined to the region $x/R > -0.5$. The sign of Δv_r reveals that rotation introduces radial flows towards the core, which hints at the formation of root vortices. They lower the pressure in this region, resulting in lower blockage and hence larger axial flow [41]. The two major parameters governing the influence of wake rotation are the thrust coefficient, C_T, and the tip speed ratio, λ. Therefore their influence on the velocity field is examined by comparing the average difference in velocities to non-rotating wake flow in the region bounded by $-3 < x/R < 0$ and $r/R \leqslant 1$. The results are shown in fig. 26. The strongest changes are found in the axial velocity component and towards larger thrust levels. Higher loading leads to stronger root vortices and lower pressure in the rotor core region, introducing greater changes

5 Consider the paths of the rotor tip vortices in the wake and their dependence on λ for a physical interpretation.

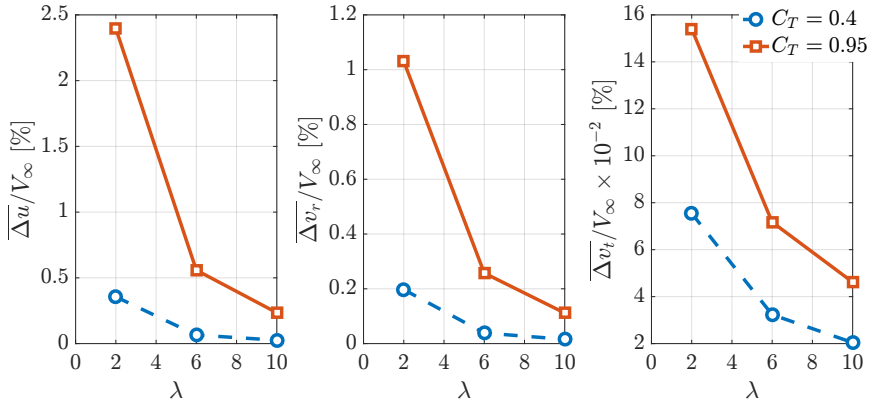

Figure 26: Average change in the velocity components relative to non-rotational wake ($\lambda \to \infty$) over the region -3 < x/R < 0, r/R ⩽ 1.

in the velocity field. With increasing λ the difference rapidly converges asymptotically towards zero. Keeping in mind that most commercial turbines operate in the region $6 < \lambda < 10$, the effect of wake rotation on the induction zone is minute and limited to a region in close proximity to the rotor.

COMPUTATIONAL METHOD	
State	Steady
Flow equations	RANS
Turbulence model	k-ω SST
Turbine model	AD, loading from [41]
Inflow	Uniform
Domain	Boundary free

4.2.4 *Rotor design* [article 10]

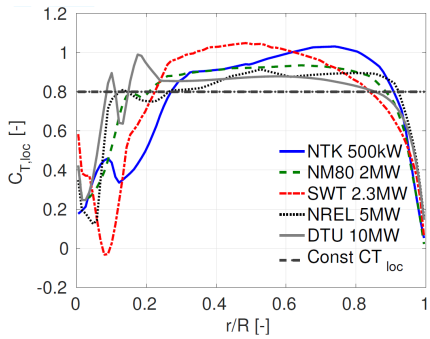

Figure 27: Local thrust distributions along different rotor blade designs, all with integral thrust $C_T = 0.8$.

The influence of rotor design on the induction zone is linked to the thrust exerted by the respective turbine model on the flow. The thrust distribution along a wind turbine blade follows from the lift and drag distributions, which can vary significantly between models. With respect to the induction zone, the influence of rotor design thus translates into the influence of the specific blade thrust distribution. Figure 27 shows the local thrust coefficient $C_{T,loc}$[6] along five different blades[7] all with the same global thrust coefficient of $C_T = 0.8$. These blades represent designs over the last three decades and were thus conceived with different design philosophies and power requirements. This clearly shows in the distributions, with some conserving a constant load over most of the blade, whereas others are strongly curved and have pronounced peaks. In fig. 28 the corresponding axial velocity profiles are shown at four distances upstream. The profiles originating from a constant thrust distribution serve as reference. There is a clear difference in the peak velocity deficit that decreases with distance from the rotor, however the profiles are of similar shape. Considering the thrust distributions in fig. 27, the largest blockage corresponds to the rotors with greatest $C_{T,loc}$, namely the SWT and NTK turbines. Rotors with fairly constant $C_{T,loc}$, such that $C_{T,loc} \approx C_T$, approach the axial velocity profiles of the constantly loaded blade. In fig. 29 these profiles are statistically summarised. Even for the fairly large C_T of 0.8 [8] the standard deviation is low with respect to the mean, but increases approaching the rotor. This signifies that the blade design, or equivalently the local thrust distribution, manifests itself in the velocity field only in the rotor's vicinity (x/R > -2). Further upstream it is only the

6 $C_T = \frac{2}{R^2}\int_0^R r C_{T,loc}\,dr$

7 NTK = Nordtank; NM = NEG Micon; SWT = Siemens Wind Power; NREL and DTU are reference wind turbines.

8 The upper operational thrust limit of these turbines.

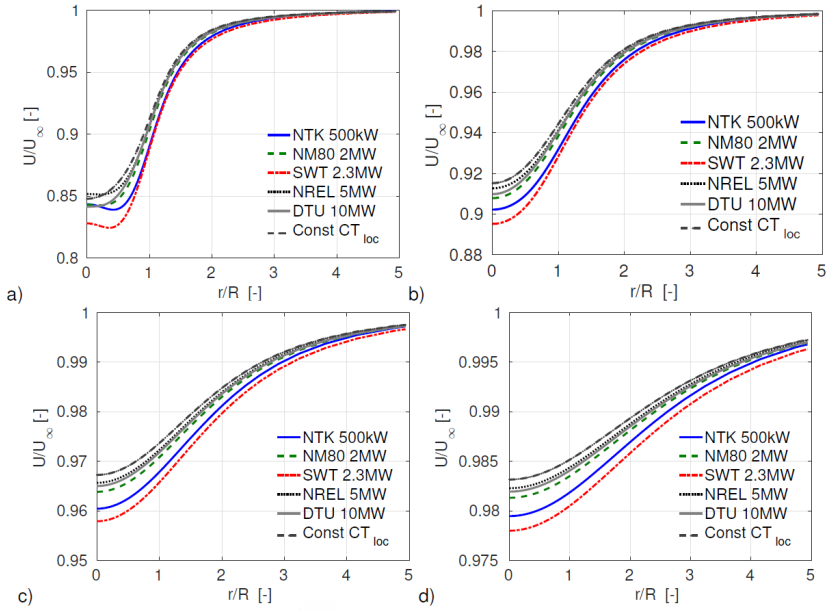

Figure 28: Axial velocity (u) profiles along the radial direction, normalised by the free-stream velocity magnitude, upstream of different rotors operating at $C_T = 0.8$: a) x/R = -0.5R b) x/R = -1R c) x/R = -2R d) x/R = -3R.

global thrust coefficient determining the blockage, signifying that a disc with the same C_T as an actual operational rotor would lead to the same induction.

COMPUTATIONAL METHOD	
State	Unsteady
Flow equations	RANS
Turbulence model	k-ω SST
Turbine model	AL, airfoil data + controller
Inflow	Uniform
Domain	Boundary free

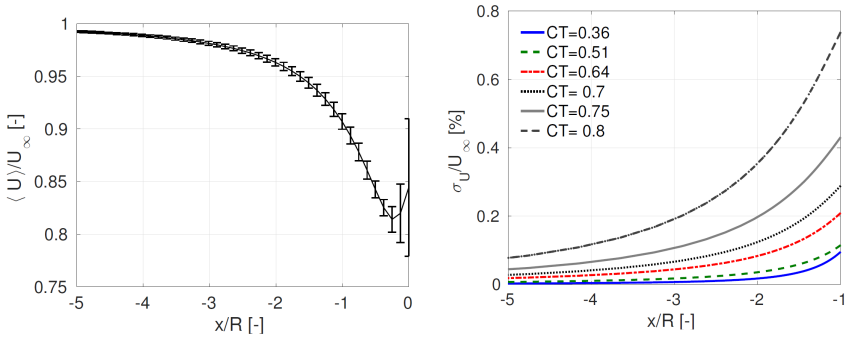

(a) Mean

(b) Standard deviation

Figure 29: Statistics of the axial velocities of five different rotors along the centreline ($r/R = 0$) and $C_T = 0.8$.

4.2.5 *Yaw and tilt* [article 9]

The stochastic nature of wind does not allow a turbine to follow the wind direction at all times. Instantaneously the wind direction can in fact vary significantly across the rotor area, particularly for the large rotors installed nowadays. Therefore wind turbines always operate under some yaw misalignment. Only if a significant and lasting change in the wind direction is detected does a turbine yaw.[9] The exact turbine yaw response depends on the specific turbine control system, however measurements on real turbines [42, 40] suggest that the yaw misalignment over a ten minute period follows a normal distribution. Without a systematic bias in the yaw control, the distribution has zero mean. The standard deviation or width of the distribution positively correlates with the turbulence level. At a relatively high turbulence intensity of 18% the standard deviation is about 5°. The final distribution is shown in fig. 30. This distribution in fig. 30 demonstrates that a turbine rarely exceeds ±10° misalignment.[10] Surpassing these bounds the blade and tower loads quickly escalate and the turbine would lose power in excess of 5% [42].

In the vertical plane the equivalent of yaw is *tilt*. Commercial turbines usually are tilted about 5° above the horizon to achieve greater blade-tower clearance. The fluctuation in tilt misalignment is far lower than in yaw, though. In the following passages yaw is used to describe inflow misalignment, yet it is interchangeable with tilt.

In fig. 31 the change in the velocity field with respect to non-yawed inflow is shown for a yaw misalignment of $\gamma = 8°$ and a relatively large thrust coefficient of $C_T = 0.85$. To make the velocity fields at different yaw

9 Yawing less reduces yaw actuator fatigue and hence costs.

10 This might change with wake steering, as then large yaw misalignments are needed to influence the wake trajectory.

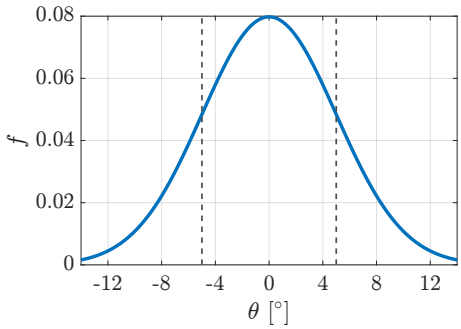

Figure 30: Probability distribution of yaw misalignment on an operational turbine over a ten minute period, following a Gaussian with zero mean and standard deviation of 5°. Estimated from measurements [40] at large turbulence intensity (18%).

misalignments comparable, the velocity components are normalised with respect to the rotor projected far-field wind speed (coordinate system: fig. 6):

$$\tilde{u}(\gamma) = \frac{u(\gamma)}{V_\infty \cos(\gamma)} \qquad \tilde{v}(\gamma) = \frac{v(\gamma) - V_\infty \sin(\gamma)}{V_\infty \cos(\gamma)} \tag{6}$$

The difference is then given by $\Delta u = \frac{\tilde{u}(\gamma) - \tilde{u}(0)}{\tilde{u}(0)}$ with an equivalent expression for Δv. Figure 31a shows that the change in the axial velocity is confined to a region in close proximity to the rotor $x/R >$ -2. At the blade tip facing the inflow the induction is reduced, whereas at the opposite tip it increases. This is connected to the wake trajectory: The angle between turbine centreline and wake, χ, is roughly proportional to the inflow direction $\chi \approx (0.6a + 1)\gamma$; here a is the induction factor and a function of C_T. Thus in fig. 31 the wake centre is advected towards $y/R > 0$, such that the upper rotor tip is closer and the lower one further from the wake than in the non-yawed case. In simple terms, this change in the distance from the rotor wake determines the change in axial induction.[11] In fig. 31b a reduction in the radial component is noticeable over the entire rotor, though again only in its vicinity. This can be attributed to some of the thrust force acting normal to the inflow direction, leading to blockage in the radial direction.[12] The changes in both velocity fields result in a change in the local flow angles $\Delta\theta$, where θ is given by:

$$\theta = \arctan\left(\frac{v}{u}\right) - \gamma \tag{7}$$

11 For a detailed explanation see [43] and [44] for the relationship between wake vorticity and induced velocities.

12 With $\gamma = -8°$ the results would be reflected in y.

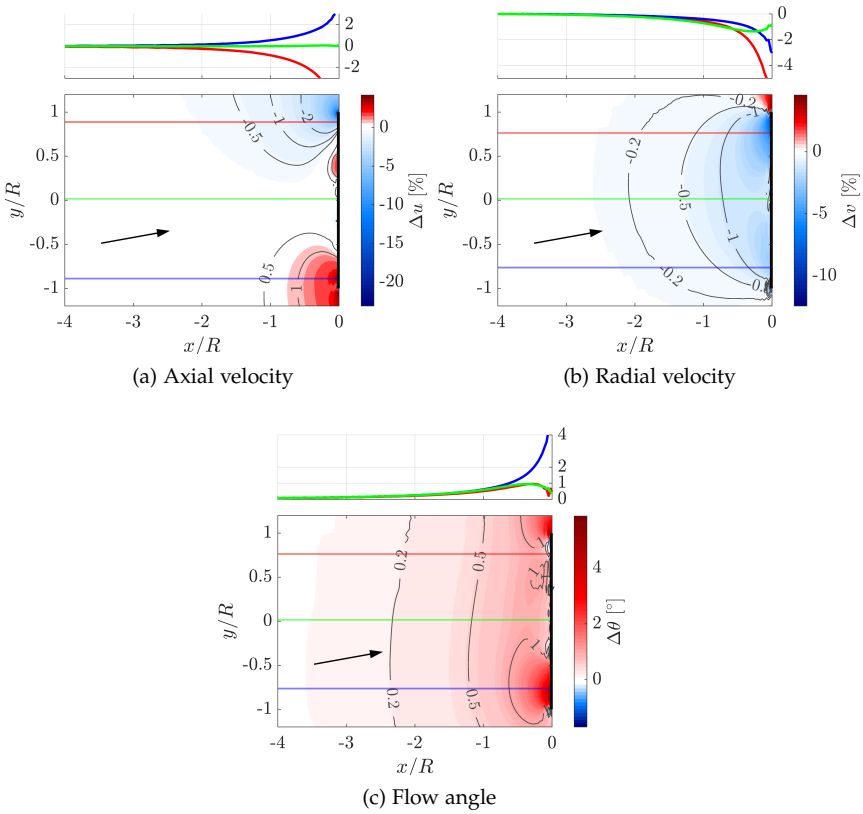

(a) Axial velocity

(b) Radial velocity

(c) Flow angle

Figure 31: Change in velocity and flow angle with yaw misalignment $\gamma = 8°$ and $C_T = 0.85$ over non-yawed inflow. The arrow indicates the free-stream flow direction.

Figure 31c shows that the flow is deflected upwards relative to a non-yawed turbine, as the angle increases approaching the turbine. At the rotor disc itself the inflow angle is thus larger than upstream, signifying that the flow turns away from the rotor. Stronger rotor loading leads to stronger induction and consequently the phenomena developing under yaw misalignment are also more pronounced. For lower thrust values the change in the axial component is unaffected by γ. Generally, the change in the radial component dominates and linearly increases for yaw angles below $\pm 10°$.

Finally, what would be the error from ignoring yaw misalignment all together when measuring velocities inside the induction zone? Referring

back to the yaw misalignment distribution in fig. 30 the total error can be estimated by weighting the errors for each γ:

$$\epsilon = \frac{\int_{0^\circ}^{8^\circ} f(\gamma)\max(u(\gamma))\,d\gamma}{\int_{0^\circ}^{8^\circ} f(\gamma)\,d\gamma} \tag{8}$$

Instead of using the average, the maximum difference is determined over -6 $\leqslant x/R \leqslant$ -1, $r/R \leqslant 1$, to give an upper estimate of the error. Even at $C_T = 0.85$ it remains below 0.15% for the axial and 0.56% for the radial component.

COMPUTATIONAL METHOD	
State	Steady
Flow equations	RANS
Turbulence model	k-ω SST
Turbine model	AD, uniform loading
Inflow	Uniform
Domain	Boundary free

4.2.6 *Dynamic load changes [article 5]*

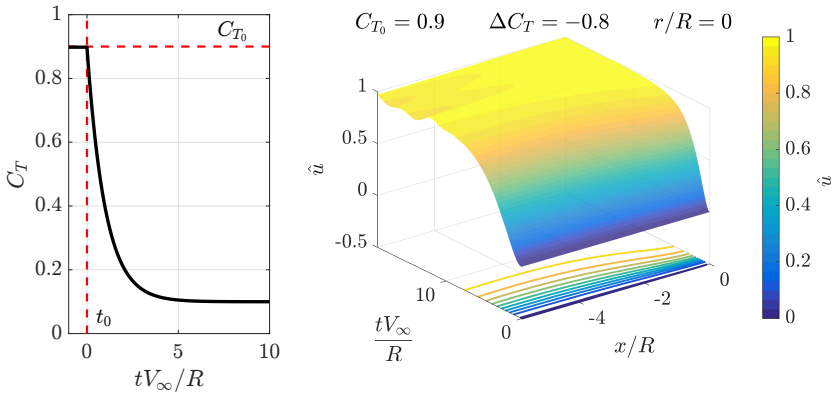

(a) Thrust change

(b) Flow response

Figure 32: The transient response of the axial velocity to a sudden drop in thrust with $\hat{\tau}_T = 1$. a) shows the time evolution of the thrust over the rotor and b) the corresponding flow response along the centreline.

The load on a rotor fluctuates as the inflow velocity is constantly changing in a turbulent wind field. Furthermore wind shear - the change of velocity with height - leads to a cyclic behaviour of aerodynamic forces on

the blade during rotation. Wind turbines indirectly control the blade loading, as they act upon the generator speed by pitching the blades and/or regulating the generator torque. Their objective is to optimise power production below rated wind speed and keeping power and rotational speed constant above rated. Under normal operating conditions the turbine controller thus limits variations in loading, but strong gusts and emergency situations lead to very rapid changes in the angle of attack, which cannot be counteracted, and hence introduce strong load variations. Depending on the pitch system, the blades can pitch towards feather during an emergency shut-down in no more than 10 s, shedding all load from the rotor in a similar time frame. What is the effect of such changes in load on the induction zone and where are they most noticeable?

To assess the change in velocity and its response time to a change in thrust, the response itself is normalised for each point in space:

$$\hat{u}(t) = \frac{u(t) - u(t_0)}{u(t_\infty) - u(t_0)} \tag{9}$$

Here t_0 denotes the instant just before a load change and t_∞ the time at which the velocity field reaches a steady-state under the new loading. This analysis focuses on the axial component u, as it is the one predominantly influenced by load changes.

As laid out in section 4.2.1 the induction is maximal along the axis of rotation for constant x/R. Figure 32b demonstrates the flow response to a sudden drop in thrust from an initial value of $C_{T_0} = 0.9$ to $C_T = 0.1$ (see fig. 32a). Here the thrust change is assumed to follow the step response of a first order system[13]:

$$C_T(t) = \begin{cases} C_{T_0} & \text{for} \quad t \leqslant t_0 \\ C_{T_0} + \Delta C_T \left(1 - e^{-\frac{t-t_0}{\tau_T}}\right) & \text{for} \quad t > t_0 \end{cases} \tag{10}$$

The time constant τ_T determines the speed of the thrust change: the smaller τ_T the faster changes the thrust. It is usually normalised by the free-stream velocity and rotor radius: $\hat{\tau}_T = \frac{\tau_T V_\infty}{R}$. In fig. 32b the response of the velocity field is fastest, the closer to the rotor. However the response time converges moving further than $2R$ upstream. The response of the velocity is similar to that of a first order system [45], allowing time constants, τ, to be determined over the induction zone.[14] They vary with respect to the initial thrust level C_{T_0}, the corresponding change ΔC_T, the speed of the change $\hat{\tau}_T$ and on the location as shown in fig. 33a. Decreasing $\hat{\tau}_T$ unsurprisingly leads to lower response times in the velocity field. However, for $\hat{\tau}_T < 0.1$ there are virtually no noticeable changes. For the same

13 For simplicity the elasticity of real blades is ignored, despite having some impact during large pitch changes on the loads.

14 Essentially fitting $y = 1 - e^{-(t-t_0)/\tau}$ to the velocity response $\hat{u}(t)$ to determine τ.

absolute change in thrust the response is quicker for a drop in thrust. Sørensen and Madsen [45] attributed this to the actual wake velocity. As the rotor is unloaded the wake velocity increases with decreasing induction. This signifies that the vorticity in the wake is advected more quickly leading to quicker changes in the induction zone. The opposite is true for increasing loading. Subsequently they applied the near-wake velocity[15] in the normalisation of the time constants instead:

$$\hat{\tau}^{\star} = \tau \frac{V_{\infty}\left(1 - \frac{3}{2}a\right)}{R} \quad \text{with} \quad a = \frac{1}{2}\left(1 - \sqrt{1 - C_{T_{\infty}}}\right) \tag{11}$$

Figure 33b shows that following this approach the time constants become nearly independent of the sign of the thrust change. With increasing distance from the rotor the time constants start to diverge, hinting towards a normalisation that is a function of space.[16] Close to the rotor this normalisation performs consistently well regardless of C_{T_0} and $\hat{\tau}_T$. A spatially more consistent normalisation might provide a vortex-based approach. It could potentially even demonstrate the self-similarity of the flow response.

COMPUTATIONAL METHOD	
State	Unsteady
Flow equations	RANS
Turbulence model	k-ω SST
Turbine model	AD, uniform loading
Inflow	Uniform
Domain	Boundary free

15 The average of disc and far-wake velocity predicted by momentum theory.

16 Sørensen and Madsen [45] applied this normalisation to estimating time constants in the rotor plane, where this approach works best.

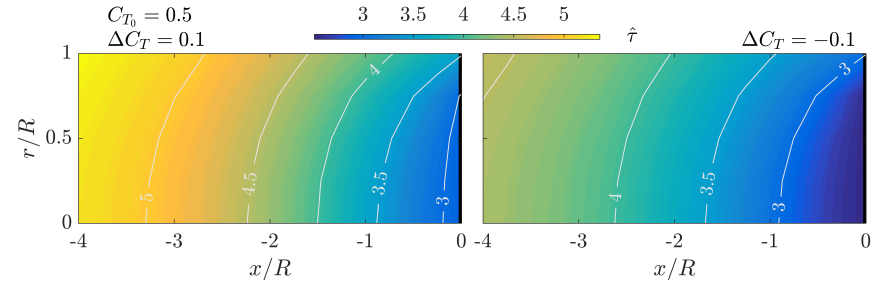

(a) Standard normalisation

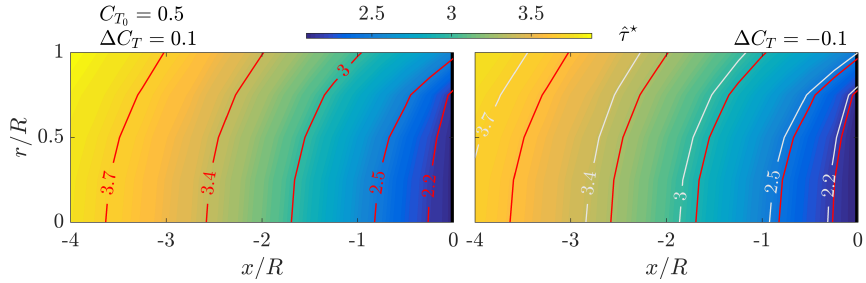

(b) Normalisation with near-wake velocity

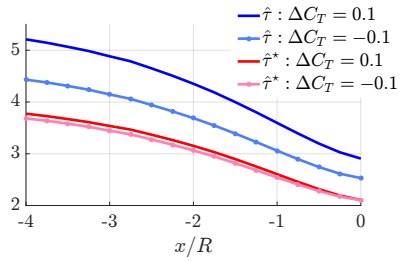

(c) Comparison of normalisations in a) and b) along centreline

Figure 33: Time constants in the induction zone for a rise and fall in thrust $\pm\Delta C_T = 0.1$ from intial thrust $C_{T_0} = 0.5$ and $\hat{\tau}_T = 1$, following different normalisation approaches.

4.3 ENVIRONMENT

4.3.1 *Multiple turbines* [article 8]

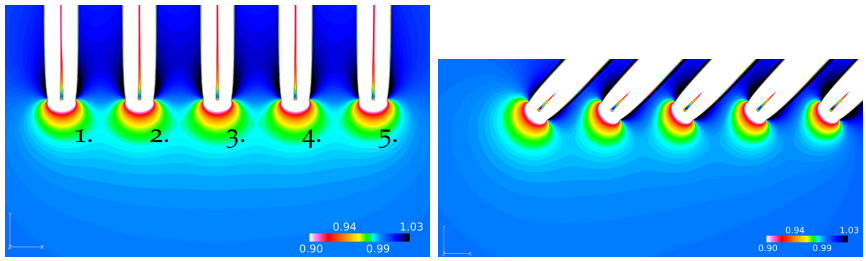

(a) $\theta = 0°$ (b) $\theta = 45°$

Figure 34: Contours of the normalised axial velocity in the horizontal plane at hub height at two different inflow angles. The turbines are numbered from left to right and velocities are shown in the local rotor coordinate system (see fig. 6).

It is well known, that rotor wakes play a crucial role in turbine power production and loading in wind farms, however do they also interact upstream, inside the induction zone? Do neighbouring turbines influence the inflow sufficiently to impact power production? This is investigated in connection with the DTU wind turbine test site in Høvsøre, where five turbine test stands are located about 300m apart. With the rotors commonly installed and tested nowadays the stands are 6R apart. The line of rotors is perpendicular to the prevailing wind direction. In fig. 34a con-

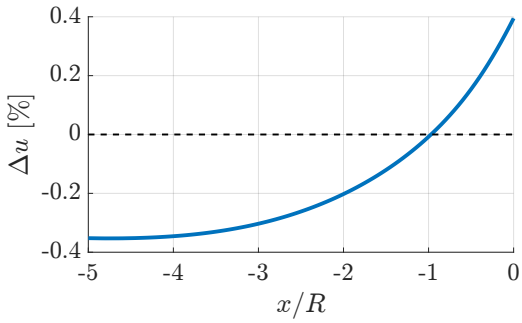

Figure 35: Change in the axial induction along $r/R = 0$ of turbine 3 relative to a single rotor.

tours of the axial flow (u) are shown for this inflow direction and five identical wind turbines with $R = 63$m (turbines are numbered for reference). The induced velocities are similar close to the rotors, except for the outer two (turbines 1 and 5). The turbines act together as one large ob-

struction to the flow, thus reducing the flow speed further than a single isolated turbine. Figure 35 shows this difference relative to the induced velocities from a single turbine along $y/R = 0$ of turbine 3. The change is small ($\approx$ -0.3%) furthest from the rotor and disappears approaching it. Now increasing the inflow angle and yawing the rotors correspondingly, leads to largely different induction zones as seen in fig. 34b. There is an

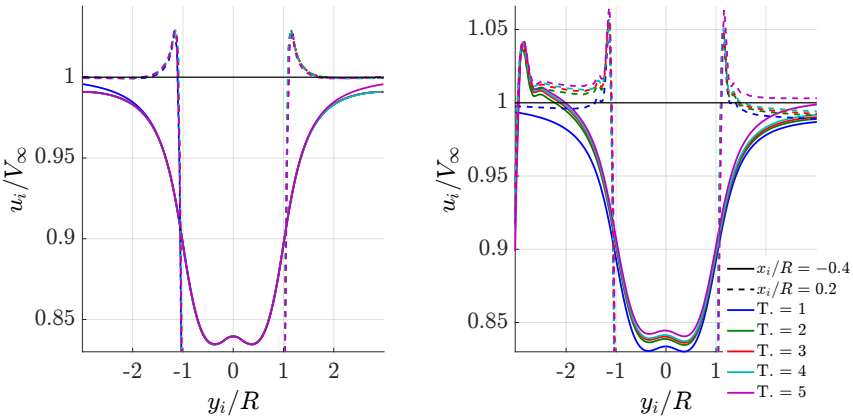

(a) $\theta = 0°$ (b) $\theta = 45°$

Figure 36: Axial velocity profiles along two lines (up- and downstream of rotor) parallel to the respective rotor planes in the local rotor coordiante system.

acceleration of the flow down the row of turbines (1. $\rightarrow$ 5.). The first rotor shows the largest induction zone, whereas the 5th has the smallest. This is also represented in the velocity profiles extracted parallel to rotor planes, which are presented in fig. 36 for the two inflow directions. At $\theta = 0°$ differences are only visible for $y/R > 1$, whereas for $\theta = 45°$ they are apparent across the entire region. Here the progressive acceleration along the row from turbine 1 to 5 becomes noticeable, as well as the acceleration in between the turbines and the neighbouring wake (- -). Turbine 1. is subjected to the strongest induction. The acceleration along the row is related to the induced velocity field of each rotor. Upstream of the rotor plane velocities are negative, whereas they turn positive downstream. Conceptually regarding the flow-field of the five turbines as linear combination of single velocity fields, the induced velocities become more negative towards the first and positive towards the 5th turbine.[17] Finally the change in the induction zone impacts the velocity at the rotor disc and thus the available kinetic energy. Figure 37 shows the change in power production

17 A more extensive explanation is given in article 8 with additional visual content supporting it.

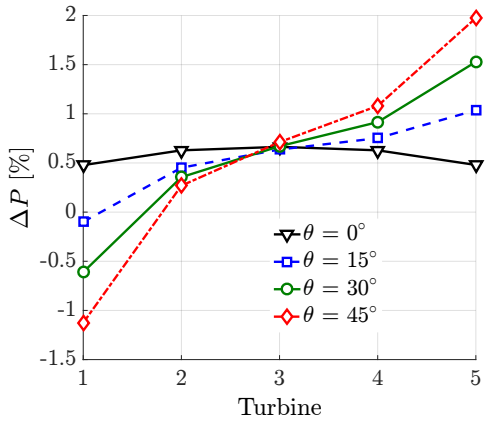

Figure 37: Change in the power production along the turbine row with varying inflow angles θ relative to an isolated turbine.

for varying inflow angles relative to an isolated turbine. The change in the axial velocity along the turbine row is directly reflected in the power production and becomes more pronounced the greater the inflow angle. Interestingly the average change across the row is positive and about constant with θ at around $\approx$ 0.57%.[18] This might have some implications regarding power measurements in wind turbine arrays, especially considering the large region over which they impact the surrounding flow-field and thus the reference wind speed[19]. Under certain conditions the difference in power can reach up to 9% [47], when measuring in an array according to the IEC standards[1].

COMPUTATIONAL METHOD	
State	Steady
Flow equations	RANS
Turbulence model	k-ω SST
Turbine model	AD, NREL 5MW [48]
Inflow	Uniform
Domain	O-mesh, boundary free

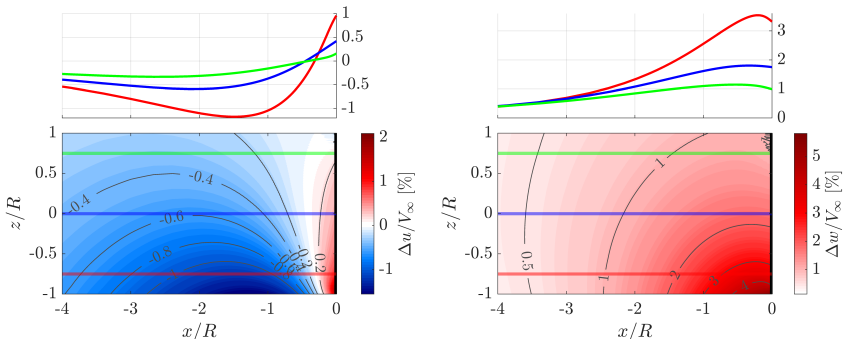

(a) Axial velocity (b) Radial velocity

Figure 38: Change in flow-field for a hub height of $h = 1.5R$ and $C_T = 0.89$ relative to a ground-free induction zone in the vertical plane ($y/R = 0$). Here $\Delta\bullet = \bullet_h - \bullet_{(h=\infty)}$.

4.3.2 *Hub height/Bounded flow*

The hub height of wind turbines is nowadays reaching up to 160m, which especially onshore yields greater power output, as the rotor leaves the lower velocity region close to the ground affected by surface friction. In non-dimensional terms the hub height is reaching 2.5R onshore and 1.5R offshore. Towers are shorter offshore, due to lower surface friction and additional technical constraints.

However, hub height not only determines to which extent the rotor thrust interacts with surface friction - it also dictates the impact of the flow obstruction from the ground. In this section surface friction is excluded, helping to isolate the ground effect. Surface friction is dealt with in section 4.3.3.

To quantify the ground effect all following results are given with respect to the induction zone developing upstream of a rotor far from the surface. In fig. 38 the change in the axial and radial velocity components upstream of a rotor at a hub height, h of 1.5R and thrust of $C_T = 0.89$ is shown. The effective blockage increases away from the rotor, reducing the axial flow especially close to the ground. In the vicinity of the rotor itself, the flow is accelerated axially.[20] The presence of the ground unsurprisingly increases the tendency of upward flow as shown in fig. 38b.

18 The change in power is in fact a function of the inter-turbine spacing [46].

19 The reference wind speed is still measured only 5R away from each wind turbine and the neighbouring turbines impact the velocity at this location - to which extent depends on the location and the inflow angle.

20 This is also observed for multiple turbines and increases the available power (refer to section 4.3.1)

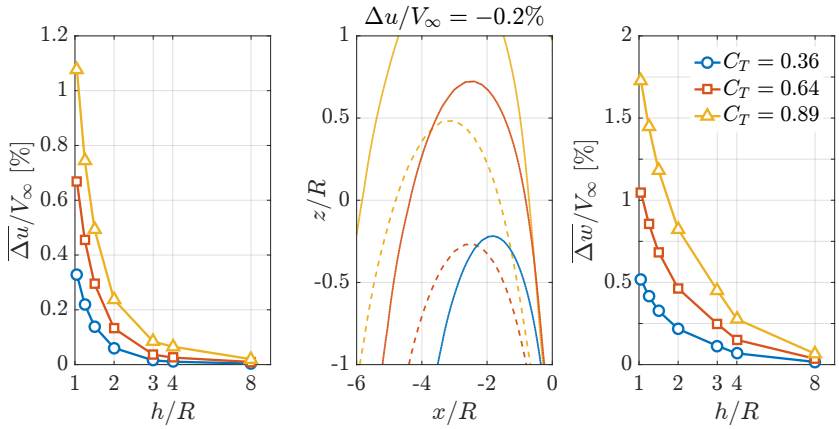

Figure 39: Average change in the induction zone ($0 \leqslant x/R \leqslant$ smt4, $r/R \leqslant 1$) relative to boundary-free flow. Left: axial velocity; Middle: iso-line for $\Delta u/V_\infty$ = -0.2 and - $h/R = 1.5$, - - $h/R = 2$; Right: vertical velocity.

Figure 39 summarises the effect of hub height in combination with thrust. The mean change in the the axial (left) and vertical (right) velocities over the induction zone are shown relative to a boundary free flow. The larger the thrust the stronger the blockage leading to larger reductions in the axial and increased vertical flow[21]. The impact on the flow seems exponentially linked to hub height, such that for the axial velocity it becomes negligible past $h = 2R$. Conversely, at an offshore site with $h = 1.5R$ it may play a more significant role. In the middle graph of fig. 39 isolines for $\Delta u/V_\infty$ = -0.2 are shown for two hub heights and different thrust levels. Note that towards the inside of each isoline the deficit in u is larger (compare with fig. 38a) and indicates the region of the induction zone that is most strongly affected. A step up in hub height of 0.5R has a stronger impact than a decrease in thrust from 0.89 to 0.64. Even with a relatively large C_T of 0.64 the region in which a significant change is seen for $h = 2R$ is limited to the lower section of the the induction zone.

THE GROUND AND ITS REPRESENTATION WITH A MIRROR ROTOR

The reason for the exponential increase in blockage with diminishing hub height becomes clearer when representing the flow close to the wall with a vortex system. The ground induced flow singularity can then be represented by a mirror vortex system, which ensures zero flow through the boundary without adding any surface friction. Figure 40 shows this equivalent representation, which practically adds a neighbouring turbine. Therefore the flow-field detailed in section 4.3.1 developing in front of multiple turbines is comparable to this one. The closer the rotor gets to

21 Conversation of mass in incompressible flows.

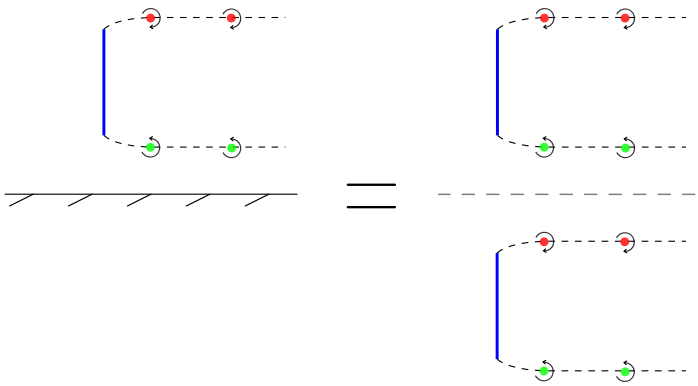

Figure 40: Simplified vortex system of a wind turbine wake and the representation of the ground by a mirror image of the rotor.

the ground the greater the induction, as the real and mirror image of the rotor start to act as one single obstruction to the flow, forcing flow around the rotors away from the wall. For a quantitative description refer to Branlard *et al.* [8].

COMPUTATIONAL METHOD	
State	Steady
Flow equations	RANS
Turbulence model	k-ω SST
Turbine model	AD, uniform loading
Inflow	Uniform
Domain	Flat, excluding wall friction

4.3.3 *Wind shear* *[article 3]*

Wind shear describes a velocity gradient with height and is mainly a result of surface friction, which forces the velocity at the ground's surface to zero. If the flow is only subjected to this mechanical friction the wind speed increases with height. The velocity gradient and the surface friction interact with the rotor induced blockage. The extent depends on the ratio between rotor hub height and surface friction. This is easily shown assuming the mean velocity gradient to be in balance with surface friction in neutral homogeneous flow:

$$\frac{du}{dz} \propto \frac{1}{z+h}\sqrt{\frac{\tau}{\rho}} \tag{12}$$

Here τ denotes the surface friction and ρ air density. The greater the hub height, h, the smaller the variation in u over the rotor disc for constant

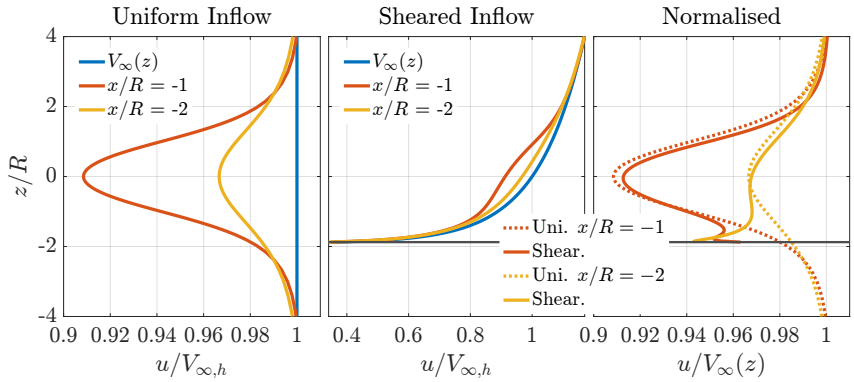

Figure 41: Axial velocity profiles extracted along the vertical axis at two distances from the rotor for uniform and sheared inflow. Left: uniform inflow profiles normalised by the free-stream velocity at hub height $V_{\infty,h}$; Middle: same as to the left but with sheared inflow ($z_0 = 0.1$m); Right: both uniform and sheared inflow normalised by the respective free-stream profile $V_\infty(z)$. The black horizontal line at z/R = -1.9 indicates the ground.

friction. Different land use results in varying friction - a forest causes more drag than an open field for instance - which is usually characterised by a specific roughness length z_0 (the greater the larger the friction).

Figure 41 compares the axial velocity profiles in the induction zone at two different distances from the rotor: for free flow (left) and wall-bounded flow (middle) normalised by hub height wind speed $V_{\infty,h}$. For the former the inflow is uniform across the rotor, whereas it is sheared for the latter. The roughness length here is $z_0 = 0.1$m corresponding to *farmland with closed appearance* [49]. Clearly, the rotor induced velocities are extremely limited relative to the underlying shear profile. In uniform inflow the induction zone is symmetric about $z/R = 0$. However, normalising by the respective free-stream velocity profile $V_\infty(z)$[22] leads to very similar profiles, especially approaching the rotor. Further upstream the influence of the boundary layer is more visible, as the profiles diverge below hub height ($z/R < 0$). The limited effect of wall friction on the induction zone is further supported by fig. 42, which shows the contours of axial velocity for the entire region upstream. For reference selected contours are highlighted and compared to those resulting from shear-free and nearly shear-free flow (uniform, smooth). Only some distance below hub height is a clear divergence from uniform inflow apparent. Again, the difference diminishes approaching the rotor and the induction zone becomes axisymmetric about $r/R = 0$. Measurements in the induction zone of an operating full-scale turbine in fig. 43 show the same qualitative be-

22 Here the free-stream velocity changes with height.

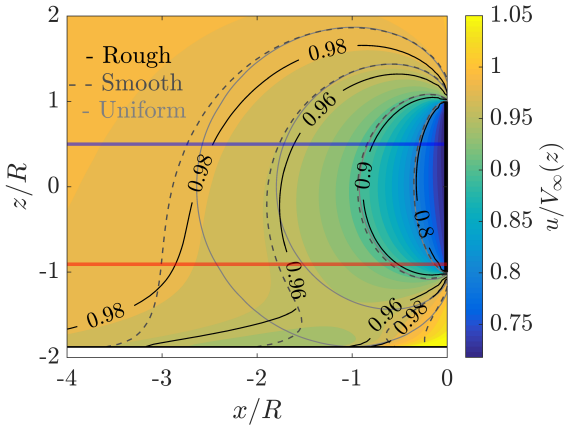

(a) Normalised axial velocity contours for a rough wall and superimposed contours for smooth and unbounded flow.

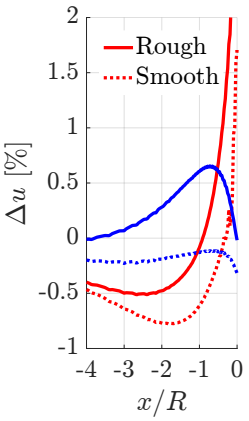

(b) Difference in axial velocity relative to unbounded flow along the two lines in a).

Figure 42: Comparison of the axial velocities for two surface frictions (rough: $z_0 = 0.1$ m, smooth: $z_0 \approx 0$ m) and boundary-free flow (uniform), normalised by their respective free-stream velocity profile $V_\infty(z)$. In b) $\Delta u = u_{\{\text{rough,smooth}\}} - u_{\{\text{uniform}\}}$).

haviour as the numerical results presented before. On the left, contours of the average axial velocity are presented, making the dependence of u with height obvious. When normalising with $V_\infty(z)$, however, the symmetric shape of the induction zone is recovered.[23] This has also been shown by Simley *et al.* [14] with similar measurements.

COMPUTATIONAL METHOD	
State	Steady
Flow equations	RANS
Turbulence model	k-ϵ-f_P
Turbine model	AD, V_∞ scaled loading
Inflow	Sheared
Domain	Flat

23 A direct comparison with the numerical results should be avoided, due to the large averaging period for the measurements and approximating $V_\infty(z)$ from data inside the induction zone at $x/R = -3$.

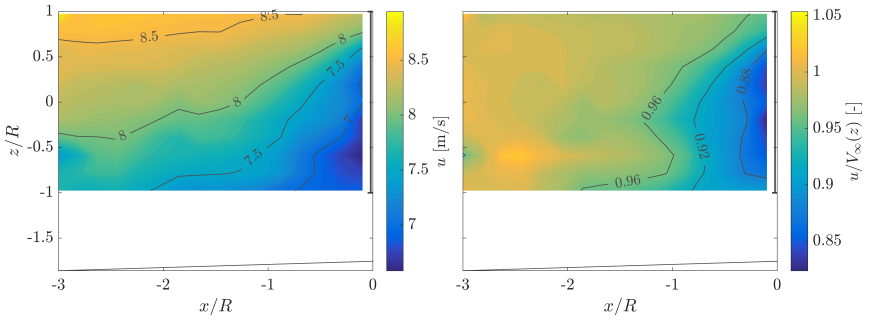

Figure 43: Average axial velocity from triple-lidar measurements [article 9] in the vertical plane through the rotor centre (11 half hour periods of data taken over 6 days). Left: average; Right: average normalised by vertical wind speed profile.

4.3.4 *Atmospheric turbulence*

Everyone has experienced the intermittent nature of the wind, expressing itself in chaotic changes in velocity and pressure. The so called atmospheric turbulence interacts with wind turbines and is mostly the product of surface friction and thermal convection. In wind energy the time scales of turbulence with significance lie in the region of minutes, where the larger ones contain most energy. Stochastic measures are confined to these time scales as statistical stationarity[24] is violated exceeding them. Therefore mean and standard deviation in wind energy are usually determined over 10 to 30 minute periods.

The turbulence is of course also present throughout the induction zone, such that an instantaneous snapshot shows spatial variations in the velocities. Figure 44a compares the instantaneous axial velocity field with (left) and without rotor (right). The turbulent structures are visibly similar and clearly surfacing in the wake deficit. Only closely upstream and in the wake of the rotor is significant energy extracted. The instantaneously induced velocity field[25] for this snapshot is given in fig. 44b; the turbulent footprint of the flow remains. This is related to the rotor thrust balancing differently with the momentum contained within the various turbulent

24 A stationary time series has constant statistical measures (mean, variance etc.) over time.

25 Here the instantaneous induced velocity directly follows from fig. 44a by dividing the rotor flow snapshot with the one without rotor. It could be argued, though, that in turbulent flow no instantaneous free-stream exists, as the transport velocity of the turbulent eddies is changed by the turbine itself. The same turbulent eddy is thus - at the same instant in time - located differently in the flow with than without rotor. The flow-fields $u(\mathbf{x}, t)$, $u_\infty(\mathbf{x}, t)$ are thus decorrelated, disallowing the computation of instant induced velocity. As their decorrelation is limited, however, the induced velocity can be obtained from the time-averaged flow fields instead e.g. $u_i = \left(\frac{1}{T}\int_{t_1}^{t_2} u(t)\,dt\right) / \left(\frac{1}{T}\int_{t_1}^{t_2} u_\infty(t)\,dt\right)$, $T = t_2 - t_1$. By definition induced velocities thus always represent time-averages.

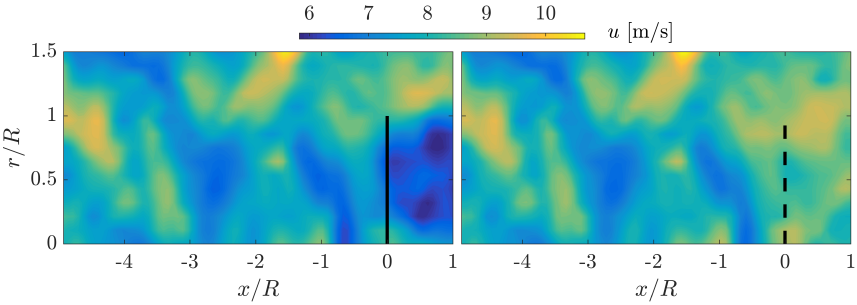

(a) Instantaneous axial velocity contours in turbulent flow with (left) and without rotor (right).

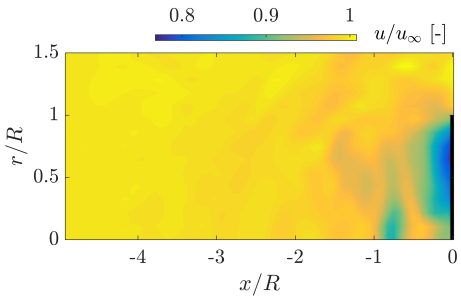

(b) Axially induced velocities upstream.

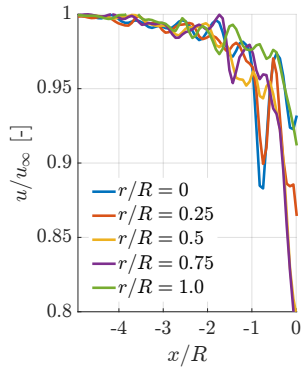

(c) Lines across b).

Figure 44: Instantanous axial flow-field with a turbulence intensity of 15%.

structures. The question thus arises whether turbulence fundamentally changes the induced velocities upstream of the rotor. A measure of turbulence in wind energy is *turbulence intensity* (TI) and is defined as[26]:

$$\mathrm{TI} = \frac{\sigma_{u_\infty}}{\overline{V}_\infty} \tag{13}$$

Here standard deviation and mean are commonly determined over 10 minute periods. Taking 10 minute averages of the induced velocity field for three common turbulent intensities and taking the difference to non-turbulent flow shows the impact turbulence has on the induction zone in fig. 45. Generally, the difference is very limited, but increases with turbulence intensity. This is related to the turbulent fluctuations increasing with TI. They lead to a quicker break-down and dissipation of the rotor wake vorticity, which is expressed in the flow-field by an increase in velocity

26 This measure oversimplifies turbulence, as it assumes heterogeneity and gives no indication of energy distribution over the turbulent scales. However, it is the wind energy standard.

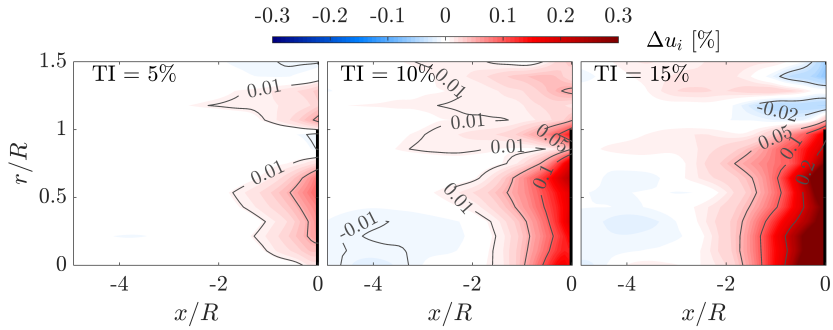

Figure 45: Influence of turbulence intensity on the time-averaged (10 minute period) axially induced velocity ($u_i = \left[\int u(t)\,dt\right] / \left[\int u_\infty(t)\,dt\right]$), expressed as difference to non-turbulent inflow e.g. $\Delta u_i = u_i^{TI} - u_i^{(TI=0)}$.

(reduced blockage) in the rotor's vicinity. Equally the acceleration outside the wake ($r/R > 1$) is diminished. The variation in the rotor thrust also increases with TI.[27] The convergence of the induced velocity fields with averaging period is shown in fig. 46. Once the averaging period surpasses 5 minutes the induced velocities converge in turbulent inflow.

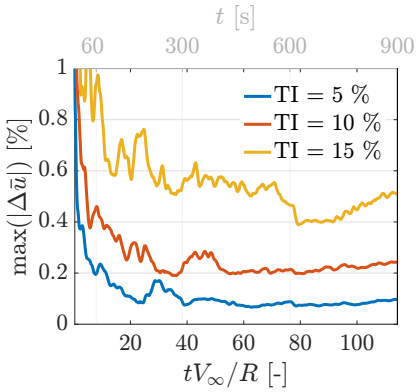

Figure 46: Convergence of the induced axial velocity residual (maximum absolute difference) in the induction zone ($0 \leqslant x/R \leqslant -4$, $r/R \leqslant 1$) reltive to non-turbulent flow.

THE EVOLUTION OF TURBULENCE The mean flow in the induction zone is mostly insensitive to the turbulence, however what about the influence of the rotor on inflow turbulence? Is there any energy exchange

27 $\sigma_{C_T} = [1.55, 2.83, 4.05] \times 10^{-2}$ for TI = [0.05, 0.1, 0.15]

with certain frequencies of turbulence as the turbulent eddies are distorted by the alterations in the mean flow throughout the induction zone? By determining the spectra of the fluctuations inside the induction zone, the distribution of energy with frequency is established. Here frequency f is interchangeable with a length scale $x = V_\infty t = V_\infty / f$.

In fig. 47a the spectra for two turbulent intensities are shown and compared to their rotor-free counterparts. The turbine is operating at constant pitch and rotational speed. The energy contained at higher turbulence intensity is substantially larger over the entire frequency range. The spectra are affected by blade rotation, as they are taken relatively close to the rotor ($x/R = -0.5, r/R = 0.5$). This is represented by pronounced peaks at the rotational frequency ($\Omega = 0.96$ rad/s) and its harmonics. Except around the

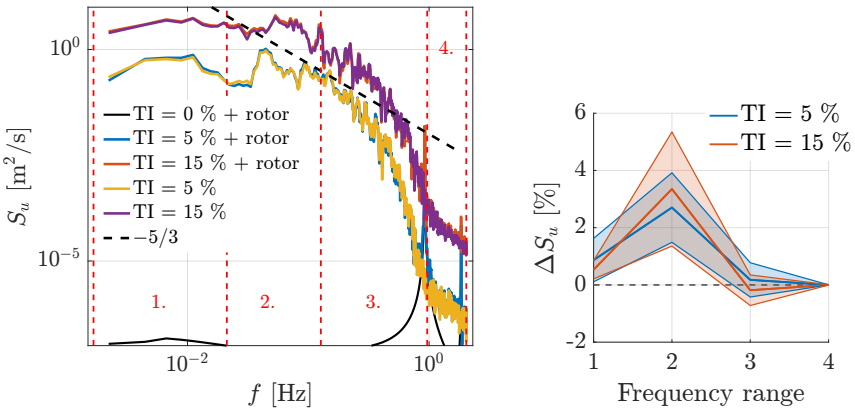

(a) Spectral energy density at $\psi = 0°$ with and without rotor.

(b) Relative change in energy density in regions 1. to 4. Shading represent the azimuthal variation.

Figure 47: Spectral energy density close to the rotor at $x/R = -0.5, r/R = 0.5$. The rotor operates at constant pitch and rotational speed.

rotational frequency, there seems to be little influence of the rotor on the turbulence. However, by comparing the energy contained over certain frequency bands ($\int_{f_i}^{f_{i+1}} S_u \, df$) even small differences in energy are revealed. Here four frequency bands are chosen:

$$\left(\frac{1}{10 * 60}\right) \leftarrow 1. \rightarrow \left(\frac{V_\infty}{6R}\right) \leftarrow 2. \rightarrow \left(\frac{V_\infty}{R}\right) \leftarrow 3. \rightarrow (\Omega) \leftarrow 4. \rightarrow \left(\frac{V_\infty}{\Delta x}\right) \quad (14)$$

The first boundary represents the common averaging time period of 10 minutes, followed by the scale of the induction zone[28], rotor scale and the rotational speed. The final boundary represents the smallest turbulence

28 Assuming the induction zone extends $6R$ upstream.

scale captured accurately.[29] Here the induction zone scale is of special importance, as it is the limit of the quasi-steady behaviour of the induction zone [50]. Smaller scales (faster fluctuations) result in an unsteady interaction between rotor and upstream flow.

Figure 47b shows the change in energy over each of these regions relative to the total energy contained in the rotor-less flow.[30] The shading represents azimuthal variation in form of the standard deviation. The turbulent energy seems to notably increase in the second region - in scales larger than the rotor radius - which is reinforced by larger turbulence intensity. A reduction in energy is not seen at greater scales (smaller frequencies), as this is captured by the mean flow; here only the fluctuations about the mean are investigated. The method to quantify ΔS_u in fig. 47b

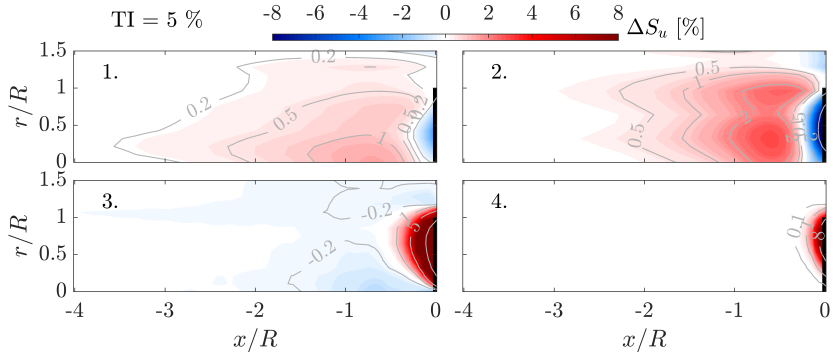

Figure 48: Change in turbulent energy density induced by the rotor and aggregated over the frequency bands defined in (14). Here TI = 5% and the change in S_u is computed relative to a rotor-less flow with the same TI.

is subsequently applied to the entire induction zone to reveal spatial dependencies in fig. 48. Each graph represents the azimuthally averaged change in energy for one frequency region. Below the rotor scale (3. - 4.) considerable energy is added, but only in close proximity to the blades ($x/R > -0.2$). This is accompanied by a drop in energy at greater scales (1. - 2.), hinting towards some transfer of energy to smaller scales close to the rotor. The increase in energy seen in fig. 47b for frequency region 2 in fact extends laterally over the entire rotor span and peaks close to the rotor. Overall the influence of the induction zone on turbulence is minor, except at the rotor itself, which is also supported by Graham's theoretical work [51]. However, Mann *et al.* [50] stress the importance of thrust

29 Here Δx is the grid spacing of the LES simulations. Scales below this size are not directly resolved, but modelled.

30 $\Delta S_u = \frac{(S_u)_{rotor} - S_u}{\int S_u \, df}$

changes above rated wind speed[31] on the energy content of frequencies in the quasi-steady regime (these thrust variations are not modelled here). They find a maximum increase in energy over the lower frequencies in the order of 10% one radius upstream.

COMPUTATIONAL METHOD	
State	Unsteady
Flow equations	LES
Turbine model	AL, NREL 5MW [48]
	$\Omega = 0.96$ rad/s, constant pitch of 4°
	$\Rightarrow C_T = 0.56$ and $C_P = 0.47$, average
Inflow	Uniform ($V_\infty = 8$ m/s) + turbulence
Domain	Boundary free

4.3.5 *Topography [article 3]*

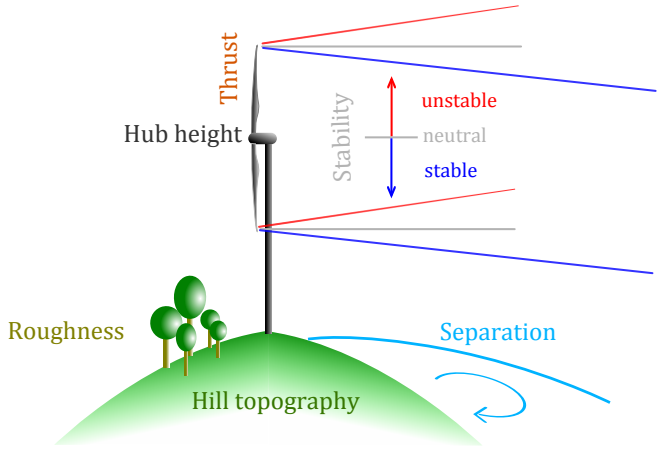

Figure 49: Major parameters and phenomena possibly affecting the induction zone in mountainous regions.

Ever more often wind turbines are installed in mountainous regions, especially on ridges as the wind accelerates uphill. However, the mountain climate is highly complex and not fully understood. Especially its impact on wind turbines is largely unexplored. There are a multitude of factors potentially impacting the induction zone in complex terrain (see fig. 49):

31 Above rated wind speed the power output is kept constant by pitching the rotor blades, lowering the thrust coefficient.

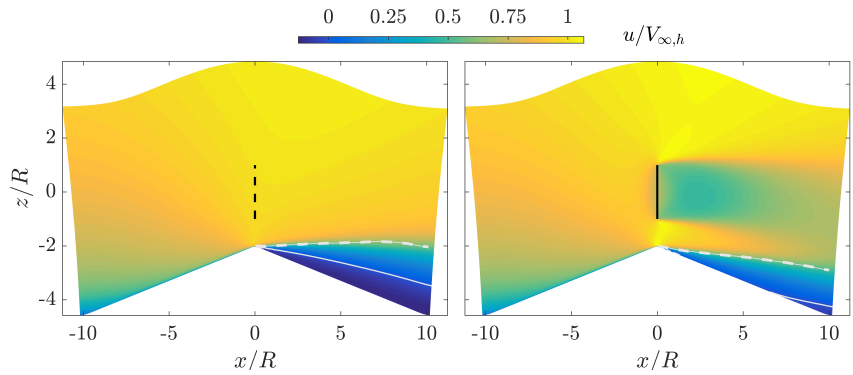

Figure 50: Average axial velocity field through the rotor centre without (left) and with rotor (right), normalised by the free-stream velocity at hub height. Shear layers are indicated by dashed and separated flow by solid lines. Hill with upstream slope of 15°, downstream -15° and surface roughness of $z_0 = 0.05$m. The rotor thrust is $C_T = 0.89$ and hub height above the crest is 2R. The atmosphere is neutrally stratified and surface is heating is excluded.

- HILL TOPOGRAPHY: The shape of the terrain surface directly impacts the flow. A hill accelerates the flow towards the crest, as does a gap in a mountain ridge, which funnels the flow.
- ROUGHNESS: Largely impacts the flow close to the ground, as it introduces mechanical friction and breaks down turbulent eddies. It thus increases dissipation near the surface, which facilitates separation in the hill's lee[32]. Furthermore it helps detach hot pockets of air from the surface increasing convection, particularly in regions of large roughness changes.
- STABILITY: The temperature profile of the ambient air determines whether an air parcel rises (unstable), falls (stable) or remains (neutral) in its initial position. It influences the wind turbine's wake by moving it vertically (refer to fig. 49 for the direction) and breaking it up more quickly in case of unstable stratification, due to increased mixing.
- SURFACE HEATING: Mountain flanks facing the sun are heated more than the surrounding terrain, introducing large temperature gradients and thus enforcing convection.
- SEPARATION: In the wake of the hill or lee a recirculation area might form, which changes the aerodynamically effective shape of the hill. Its formation depends on all factors above and locally even on the rotor thrust.

32 The wind facing side of a hill is termed windward, the other leeward.

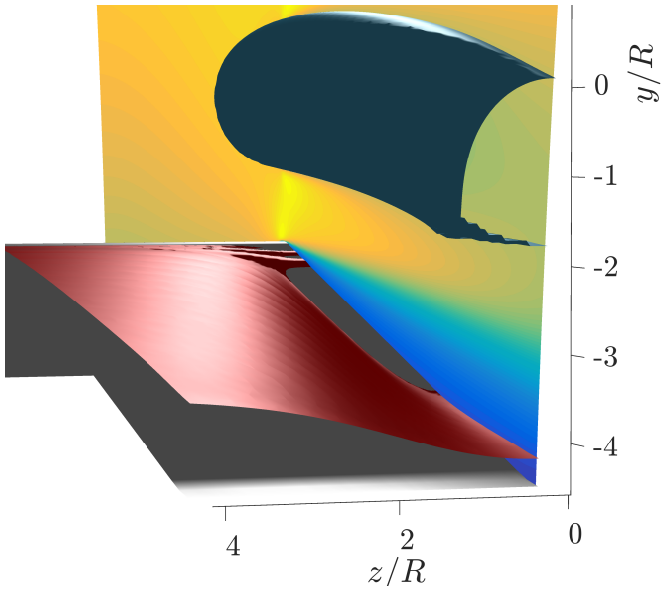

Figure 51: Three-dimensional visulisation of the separated flow in fig. 50. Isosurfaces of the separation line and the rotor wake deficit are shown. The flow is symmetric about the contour plane (x-y).

- HUB HEIGHT: The closer the rotor to the crest, the more it influences the local flow-field, as it eventually acts together with the hill as a single obstruction to the incoming flow.
- ROTOR THRUST: Increasing the thrust increases the blockage and wake deficit, thus amplifying the effect the rotor has on the flow-field. The wake interacts more strongly with the leeward flow.

As already seen from the short description of each factor, none can be analysed in isolation, as they influence each other and interact non-linearly. Figure 50 compares the time-averaged axial velocity fields developing over a ridge with (right) and without rotor (left). The contours are normalised by the free-stream velocity at hub height and the rotor is strongly loaded ($C_T = 0.89$) with its hub is located $h = 2R$ above the crest. Surface heating is excluded and the atmosphere is neutrally stratified. Starting with the flow-field without a rotor: The strong adverse pressure gradient on the hill's backside decelerates the flow to such an extent, that the flow detaches from the hill's surface at its crest. A region of separated flow develops downstream and grows vertically with distance, as indicated by the solid line. Here the axial velocity is in fact negative and flow is recirculating. The strong adverse pressure and ensuing early flow detachment stop the flow in fact from following the hill shape. A marked shear layer thus develops between high speed flow passing over the crest

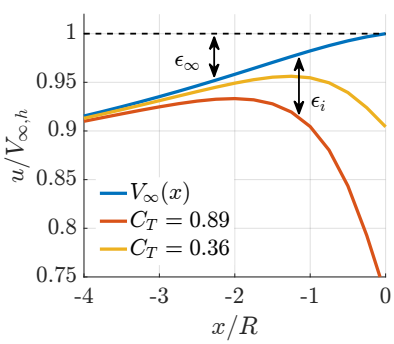

(a) Axial velocity normalised by free-stream velocity at hub height.

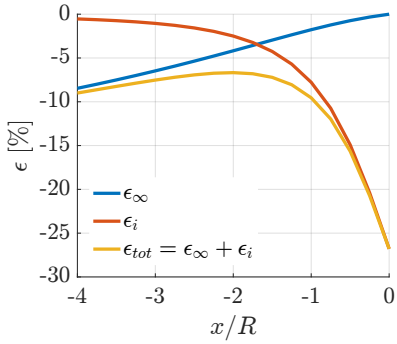

(b) Velocity difference to hub-height velocity incurred by free-stream evolution ϵ_∞ and induction ϵ_i for high loading $C_T = 0.89$.

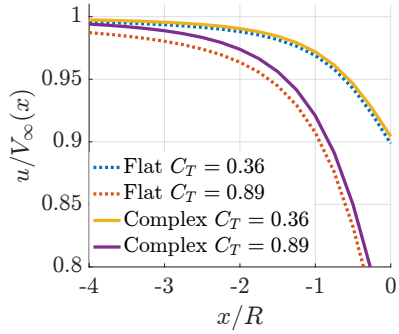

(c) Induction in complex and flat terrain.

Figure 52: Axial velocity evolution along the centreline ($r/R = 0$) for the complex terrain flow-field in fig. 50 with different rotor loading.

and the recirculating, low speed flow below (dashed line in fig. 50). The rotor restricts mass flow as it extracts energy and thus leads to higher velocities above and below the rotational plane. The high speed flow developing above the crest re-energizes the near-wall flow, hence delaying separation - now occurring at $x/R = 6$. The shear-layer is also clearly pushed down. This effect diminishes moving laterally away from the rotor centreline, eventually resembling the rotor-free flow-field. This three-dimensionality of the interaction between rotor wake and separation is visualised in fig. 53 by iso-surfaces. The wake follows the hill shape and forces the separation laterally outwards. The deceleration in the induction zone is noticeable only in the rotor's vicinity.

The axial velocity evolution along the rotor centreline ($r/R = 0$) of the flow-field presented in fig. 50 is compared in fig. 52a with the addition of the evolution at lower rotor loading. As stated in chapter 1 the free-

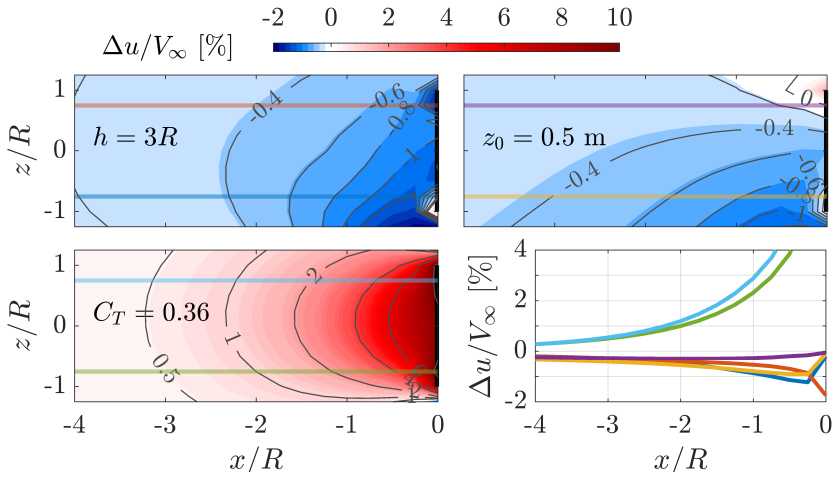

Figure 53: Change in the normalised axial velocity shown in fig. 50 ($z_0 = 0.05$m, $C_T = 0.89$, $h = 2R$) from altering single parameters. Top left: increase in hub height; Top right: increase in roughness; Bottom left: decrease in thrust; Bottom right: comparison along the lines shown in the other frames.

stream velocity becomes a function of space, due to the terrain $V_\infty(x)$ and accelerates towards the crest of the ridge. Thus determining the hub-height free-stream velocity with measurements anywhere upstream of the rotor always results in underestimating the velocity. This effect is shown in fig. 52b, where the difference to the hub-height free-stream velocity is split into a free-stream evolution component ϵ_∞ and one due to the rotor induction ϵ_i. In the absence of the rotor only ϵ_∞ would remain. Determining the free-stream with lidars on an operating turbine the combination of both components needs to be considered. Despite the blockage effect from the rotor it would be beneficial to measure about $2R$ upstream of the turbine, as the error in the free-stream estimate is mostly caused by flow evolution. With lower loading the optimum moves closer to the rotor, as the turbine blockage is reduced, whilst the flow evolution caused by the hill remains unchanged.

Does complex terrain fundamentally alter the induction zone or is it solely a question of finding the correct normalisation as for wind shear (see section 4.3.3)? As mentioned in connection with fig. 50 certain non-linearities seem to develop under strong rotor loading, which is supported by fig. 52. Here the induced axial velocities are compared between flat and complex terrain[33] by normalising the latter with the spatially evolving free-stream $V_\infty(x)$. Whereas at $C_T = 0.36$ flat and complex ter-

33 Hill shape, roughness and hub height are still those of fig. 50.

rain are nearly indiscernible, a clear gap is present at greater loading. In complex terrain the blockage seems to be lowered.

Figure 53 explores the effect of roughness, hub height and thrust on the induction zone in complex terrain. Each frame presents the impact of a single parameter change on the induction zone with respect to the flow-field presented earlier in fig. 52. Hub height (top left) and roughness (top right) are increased, whereas thrust is decreased (bottom left). The impact of those parameter changes is indicated by the difference in normalised axial velocity with respect to the reference. Negative values (blue) indicate lower velocities/higher induction for increasing the hub height by 1R and increasing the roughness length by factor 10. Deceleration remains limited below 1% almost everywhere, but is highly asymmetric. A stark drop in thrust, however, results in a equally pronounced increase in the axial velocity. The asymmetry remains. Clearly, thrust remains the single most important parameter!

An increase in velocity following a drop in thrust is expected (see section 4.2.1), but is there also a physical explanation for the deceleration seen from increasing hub height and roughness? One simple explanation connects induced velocities and vorticity with the wake advection velocity. Reverting to a vortex sheet representation of the wake, the vorticity in the wake can be expressed as:

$$\gamma = \frac{\partial \Gamma}{\partial x} = \frac{\partial \Gamma}{\partial t}\frac{1}{V_c} \tag{15}$$

Here Γ is the total circulation of the rotor, which is proportional to the rotor thrust. With constant thrust (or equivalently, circulation) and vorticity release ($\frac{\partial \Gamma}{\partial t}$) - a fair assumption in steady flow - $\gamma \propto \frac{1}{V_c}$. V_c is the transport velocity of the wake vorticity. Consequently, a decrease in the transport velocity leads to higher vorticity, inducing[34] higher negative velocities upstream. A rise in induction in line with hub height and roughness, thus indicates a drop in the advection velocity. In the case of hub height, this might be related to a reduced jet formation between rotor and hill crest, as the distance in-between is augmented. Thereby separation is no longer suppressed to the same extent as at $h = 2R$. Higher roughness also facilitates flow separation, as it extracts added energy from the wall-adjacent flow.

HILL SHAPE To evaluate the influence of the hill shape on the induction zone, the change in the axial velocity with respect to up- (α_1) and downhill (α_2) slope is shown in form of a heat map in fig. 54. The change is determined relative to unbounded flow.[35] Here the iso-lines are nearly

34 It is acknowledged that vorticity does not really *induce* velocities, but this formulation simplifies the explanation.

35 The average difference is only used for showing correlations. Its actual value is of little importance. The unbounded velocity field is determined by the vortex model presented in chapter 5.

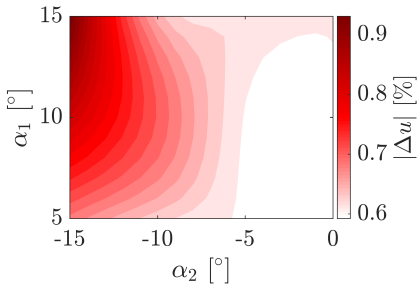

Figure 54: Change in the axial velocities in the induction zone with respect to up- (α_1) and downhill (α_2) slope. Baseline is unbounded flow; disregard the actual value |Δu| it is solely indicative.

vertical indicating that the difference is overwhelmingly changing with downhill slope. For $\alpha_2 < -10°$ the change accelerates. This strong dependence on the downhill slope is partially related to the way it impacts the wake trajectory in the vertical plane. The wake mildly follows the terrain under neutral stratification, such that a larger negative slope on the leeward hill side signifies a more downward pointing wake trajectory. Wake trajectories non-orthogonal to the rotor plane also occur for rotors under yaw misalignment and therefore some changes in the induction zone are similar (see 4.2.5). Additionally, separation is more likely with increasing downward slope. By changing the aerodynamically effective hill shape, separation alters the flow-field substantially as shown earlier in fig. 50. This in turn influences the rotor wake trajectory, wake advection velocity and break-up, as it mixes with the recirculating flow in the hill's lee. Wake trajectory and separation strongly depend on stability [52], thus changes in the induction zone might differ for non-neutral stratification.

COMPUTATIONAL METHOD	
State	Steady
Flow equations	RANS
Turbulence model	k-ϵ-f_P
Turbine model	AD, V_∞ scaled loading
Inflow	Sheared
Domain	Modified flat terrain

5 SIMPLE INDUCTION ZONE MODEL

This chapter summarises article 10 and follows its notation. Therefore γ and λ are simply model constants and should not be mistaken with yaw angle and tip speed ratio.

From an industrial perspective CFD is not feasible for predicting the blockage effect. It is relatively expensive with its need for expert knowledge and substantial computational resources. Instead companies and industry standards prefer analytical models with few parameters that run even on weak processors at least in real-time. As presented in chapter 3 the CFD model accurately predicts the temporally-averaged induction zone, allowing it to serve as reference in the development of a simple analytical model. The CFD model's accuracy is linked to the physical conditions/parameters considered in its validation. Any derived model, thus inherits its conditional validity.

5.1 MODEL DEVELOPMENT

Chapter 4 demonstrates a nearly singular dependency of the induction zone on the thrust coefficient, which is exploited in the model development. The model consists of two parts: one describing the axial and the other the radial evolution, where only the former is dependent on thrust.

$$\tilde{u}(\tilde{x},\tilde{r},C_T) = 1 - \overbrace{a(\tilde{x},C_T)}^{\text{axial}}\underbrace{f(\epsilon)}_{\text{radial}} \tag{16}$$

The model is defined by a number of normalised variables:

$$\tilde{u}(x,r) = \frac{u(x,r)}{u_\infty}, \quad \epsilon = \frac{r}{r_{1/2}(x)}, \quad \tilde{r}_{1/2}(x) = \frac{r_{1/2}(x)}{R}, \quad \tilde{x} = \frac{x}{R}, \quad \tilde{r} = \frac{r}{R} \tag{17}$$

5.1.1 *Axial model*

Branlard and Meyer Forsting [article 2] showed that a vortex cylinder model predicts the upstream flow-field similar to the CFD model. Following this vortex approach, the velocity deficit along the rotor centreline $(x, r = 0)$ is given by an analytical function:

$$a(\tilde{x},C_T) = \frac{1}{2}\left(1-\sqrt{1-\gamma C_T}\right)\left[1+\frac{\tilde{x}}{\sqrt{1+\tilde{x}^2}}\right] \tag{18}$$

Here γ is determined by fitting the curve to RANS simulated induction zones of various wind turbine rotors. Figure 55 shows that the vortex model fits the averaged RANS results with $\gamma = 1.1$.

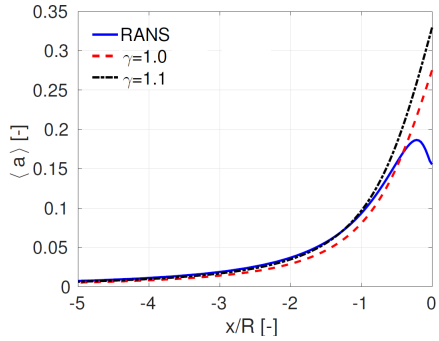

Figure 55: Induction along the centreline at $C_T = 0.8$ predicted by the vortex model eq. (18) for different γ and the average induction of five CFD simulations with different rotor designs.

5.1.2 *Radial model*

Radially the induction zone can be regarded as self-similar, signifying that the shape of the radial velocity profile is independent of the axial distance from the rotor $\tilde{x}$. Scaling the profiles with the centreline induction determined by eq. (18) thus allows representing the radial variation with a single function[1]

$$f(\epsilon) = \operatorname{sech}^{\alpha}(\beta\epsilon) \tag{19}$$

This approximation is inspired by solutions capturing self-similar profiles in turbulent flows and corresponds well with simulations (see fig. 56a). An important normalisation parameter capturing the self-similarity is the characteristic induction half width $r_{1/2}$, where the axial velocity drops to half its centreline value e.g. $a(x, r_{1/2}) = \frac{1}{2}a(x, 0)$. Considering conservation of mass in combination with the CFD solutions the half-width is approximated by:

$$\tilde{r}_{1/2}(\tilde{x}) = \sqrt{\lambda(\eta + \tilde{x}^2)} \tag{20}$$

This function closely follows the simulations, except close to the rotor as shown in fig. 56b.

All constants of the various functions are summarised in table 1. They are obtained by least-squares fitting of the analytical functions to the averaged RANS simulations. With the limited variation observed across these

1 The *hyperbolic secant* is defined as: $\operatorname{sech}(x) = \frac{1}{\cosh(x)} = \frac{2}{\exp(x)+\exp(-x)}$

five simulations for $x/R < -1$ - in terms of maximum standard deviation $\approx 1\%$ for $f(\epsilon)$, 4% for $\tilde{r}_{1/2}(\tilde{x})/R$ and below 1% for $a(\tilde{x}, C_T)$ - the analytical functions seem sufficiently general and accurate. Still, the fits are based on a limited number of rotor simulations in uniform inflow, thus strongly sheared inflow or unconventional turbines might be outside the validity of these functional fits.

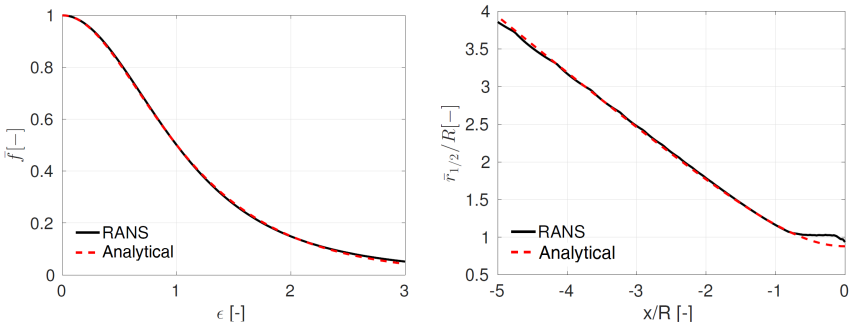

(a) Self-similar profile

(b) Induction half-width

Figure 56: Analytical functions fitted to five averaged RANS simulations. The analytical self-similar radial profile a) is given in eq. (19) with the non-dimensional radial dimension ϵ following from a fit to the induction half width $\tilde{r}_{1/2}(\tilde{x})$ shown in b) (eq. (20)).

CONSTANTS	
γ	1.1
α	$\frac{8}{9}$
β	$\sqrt{2}$
λ	0.587
η	1.32

Table 1: Simple induction zone model constants obtained from least-squares fitting to the averaged RANS solution.

5.2 SIMPLE MODEL PERFORMANCE

Figure 57 compares velocity profiles predicted by the simple model and the averaged CFD solutions from five rotors. The radial evolution of the induction zone and its depth are captured by the simple analytical model. To assess the performance relative to the different wind turbines fig. 58 compares the maximum absolute deviation between simple and CFD model

(-) and the spread in the various CFD simulations (○). The simple model error remains below 0.7% for x < -2R, but grows quickly approaching the rotor. Nevertheless the spread in the simulations follows the same trend and is maximally 0.4% at $C_T = 0.8$ below the model error. As the simple model error cannot fall below the spread in the simulations it is based on, it is considered sufficiently accurate. A first application of the simple model by Borraccino *et al.* [5] to nacelle lidar induction zone measurements confirms its applicability in flat terrain.

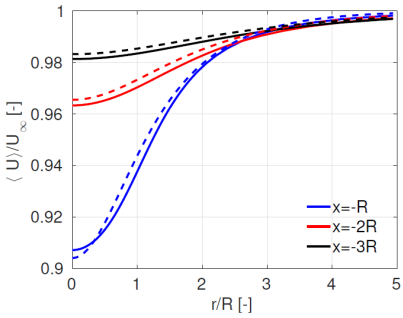

Figure 57: Axial velocity profiles predicted by the simple model (dashed) and five averaged CFD simulations (solid) at $C_T = 0.8$.

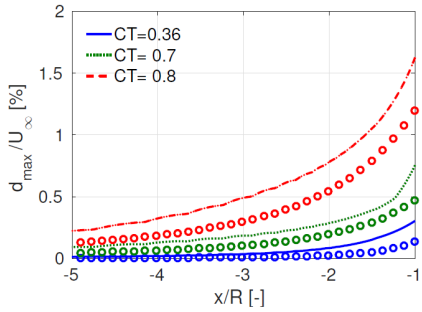

Figure 58: Lines: maximum absolute deviation (d_{max}) between the analytical and five averaged CFD results; ○ d_{max} between mean and individual RANS simulations.

5.3 PRACTICAL/COMMERCIAL MODEL APPLICATIONS

With the thrust coefficient C_T as single input, the new model is extremely simple without losing significantly in accuracy. In fact there are solely two unknowns, namely thrust C_T and the free-stream velocity V_∞. This makes the model extremely suited for practical applications following different strategies:

1. Measure velocities in at least two locations upstream of the rotor to determine C_T and V_∞.
2. Use a known C_T curve and a single velocity measurement to compute V_∞.
3. Measure the total thrust, T (for instance with blade-integrated strain-gauges) and measure the velocity in a single point upstream to arrive at V_∞ and C_T.

6 CONCLUDING REMARKS

SUMMARY The major contributions of this thesis include the development of a novel stochastic model validation methodology and identifying the major turbine and environmental parameters governing the flow deceleration in front of the rotor. By isolating the thrust coefficient as single most important factor enabled the derivation of a simple induction zone model, which is sufficiently accurate for industrial applications. Table 2 gives in overview of the maximal impact each parameter has on the induction zone. Here impact is quantified in terms of the maximal change in the axial velocity once the parameter is included in the computational model. Values in table 2 thus represent upper limits of the influence of each parameter. Of course the importance of each of them ultimately depends on

MAX. IMPACT	PARAMETER
$\leqslant 0.5\%$	Multiple turbines (4.3.1); Hub height (4.3.2); Atmospheric turbulence (4.3.4); Wind shear (4.3.3)
$\leqslant 1.0\%$	Yaw and tilt (4.2.5); Rotor design (4.2.4)
$\leqslant 2.0\%$	Blade rotation (4.2.2); Wake rotation (4.2.3)
$> 2.0\%$	Thrust (4.2.1); Topography (4.3.5); Dynamic load changes (4.2.6)

Table 2: Parameters catagorised by their maximal impact on the induction zone. Their impact is assessed by the maximal difference in axial velocity encountered past one rotor radius upstream ($\max_{(x/R\leqslant -1)} \Delta u/V_\infty$) relative to a flow-field excluding the parameter e.g. wake rotation vs no wake rotation. For Dynamic load changes it is the difference in the time constants relative to the one in the rotor plane.

the application. In power curve assessment, for instance, velocity changes induced by the rotor even below one percent might matter. However, in a real measurement scenario it remains questionable whether differences below 2% are discernible from noise introduced by the natural variability of the wind or the instrument itself. All parameters were studied in isolation and idealised conditions, but in reality they act simultaneously and especially the small effects might balance out. That thrust is the crucial parameter, though, is confirmed by Borraccino *et al.* [5]. They accurately retrieved the free-stream velocity from near-rotor lidar measurements in flat terrain by fitting an induction zone model to the data - solely with the thrust coefficient as variable (see fig. 59a). Preliminary results in complex

terrain, following the same simple approach, are equally favourable and point towards thrust as the crucial factor.

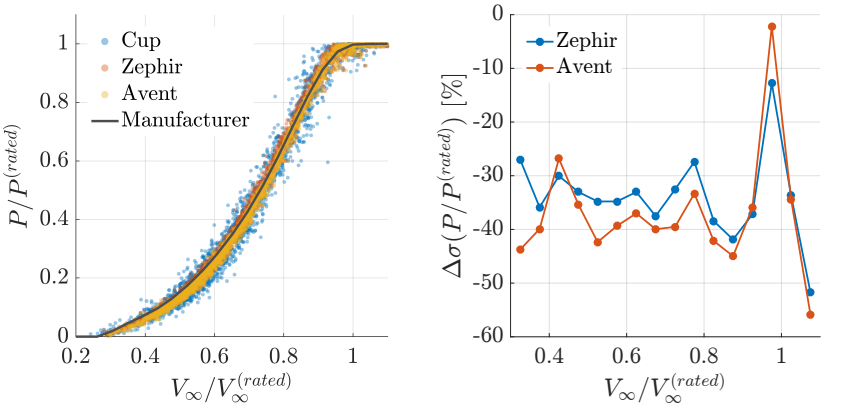

(a) Measured power curves.

(b) Scatter reduction for near-rotor nacelle lidars measurements relative to classic cup approach.

Figure 59: Power curves measured by a cup anemometer on a met mast 5R upstream of rotor and two nacelle lidars (Zephir, Avent). The lidars measure close to the rotor, inside the induction zone, and use a simple model to determine V_∞. For reference the maufacturer's power curve is also shown. Data provided by A. Borraccino [53].

OUTLOOK This thesis tries to cover most aspects influencing the flow upstream of the turbine, though some open questions remain. Most results presented within this document are numerically generated; the computational model is validated, but only for limited parameter ranges and thus further measurements are required to confirm the numerical predictions. Already existing datasets [24, 54] might, at least partially, validate the results presented for Multiple turbines (4.3.1) and Topography (4.3.5) in the future. For this purpose the data first needs to be re-analysed, though. Another possibility to compare with real data would be the development of a computational, virtual counterpart to the real measurement environment. This would combine atmospheric flow, topography, turbine, controller and the specifics of the measurement system. Such a virtual environment was created by Simley *et al.* [55], but more emphasis would be on the effect of topography and atmospheric conditions, like shear and stability. Our knowledge about the evolution of turbulence throughout the induction zone also remains hazy. Mann *et al.* [50] and Graham [51] recently incited a discussion on this topic. Their different models come to

contrary conclusions, but Mann *et al.* suggest that a combination of both might hold the answer.

An extended deployment of nacelle lidars seems ever more likely in the future, as they outperform the classic cup-met mast approach on several counts. Not only are they cost-effective - by avoiding the construction of expensive met masts - they also significantly reduce the scatter in the power measurements when combining near-rotor measurements with a simple induction zone model as shown in fig. 59b. For an industry-wide adoption of this method yet more measurement campaigns covering all sorts of terrain and atmospheric conditions are necessary; only then can the robustness and accuracy of this approach be proven.

Figure 60: The Enercon E-82 in Perdigão (eastern Portugal) which was part of a triple-lidar measurement campaign in 2015 [54] in extremely complex terrain.

BIBLIOGRAPHY

[1] *IEC 61400-12-1:2005, Power performance measurements of electricity producing wind turbines.*

[2] Joukowski NY. Vortex theory of the screw propeller i-iv. *(French translation: "Théorie tourbillonnaire de l'hélice propulsive I-IV" by W. Margoulis, Éditeurs: Gauthier-Villars et Cie. Paris, 1929)* 1912-1918; .

[3] Sathe A, Banta R, Pauscher L, Vogstad K, Schlipf D, Wylie S. *Estimating Turbulence Statistics and Parameters from Ground- and Nacelle-Based Lidar Measurements: IEA Wind Expert Report*. DTU Wind Energy: Denmark, 2015.

[4] Wagner R, Pedersen TF, Courtney M, Antoniou I, Davoust S, Rivera RL. Power curve measurement with nacelle mounted lidar. *Wind Energy* 2014; **17**:1441–1453, doi:10.1002/we.1643.

[5] Borraccino A, Schlipf D, Haizmann F, Wagner R. Wind field reconstruction from nacelle-mounted lidars short range measurements. *Wind Energy Science Discussions* 2017; **2**:269–283, doi:10.5194/wes-2017-10.

[6] Schlipf D, Fleming P, Haizmann F, Scholbrock AK, Hofsäß M, Wrigth A, Cheng PW. Field testing of feedforward collective pitch control on the cart2 using a nacelle-based lidar scanner. *The Science of Making Torque from Wind*, 2012.

[7] Castles W, de Leeuw JH. The normal component of the induced velocity in the vicinity of a lifting rotor and some examples of its application. *Technical Report*, NACA 1954.

[8] Branlard E. *Wind Turbine Aerodynamics and Vorticity-Based Methods*, *Research Topics in Wind Energy*, vol. 7. Springer, 2017, doi:10.1007/978-3-319-55164-7.

[9] Modarresi K, Kirchhoff RH. The flowfield upstream of a horizontal axis wind turbine. *Technical Report*, University of Massachusetts Wind Energy Center, Amherst, MA 1979.

[10] Medici D, Ivanell S, Dahlberg JA, Alfredsson P. The upstream flow of a wind turbine: blockage effect. *Wind Energy* 2011; **14**:691–697, doi:10.1002/we.451.

[11] Asimakopoulos M, Clive P, abd R Boddington GM. Offshore compression zone measurement and visualisation. *Proceedings of the European Wind Energy Assosciation 2014 Annual Event*, 2014.

[12] Slinger C, Leak M, Pitter M, Harris M. Relative power curve measurements using turbine mounted, continous-wave lidar. *Proceedings of the European Wind Energy Assosciation 2013 Annual Event*, 2013.

[13] Howard KB, Guala M. Upwind preview to a horizontal axis wind turbine: a wind tunnel and field-scale study. *Wind Energy* 2015; **19**:1371–1389, doi:10.1002/we.1901.

[14] Simley E, Angelou N, Mikkelsen T, Sjöholm M, Mann J, Pao LY. Characterization of wind velocities in the upstream induction zone of a wind turbine using scanning continuous-wave lidars. *Journal of Renewable and Sustainable Energy* 2016; **8**(013301), doi:10.1063/1.4940025.

[15] Angelou N, Sjöholm M. *UniTTe WP3/MC1: Measuring the inflow towards a Nordtank 500kW turbine using three short-range WindScanners and one SpinnerLidar*. DTU Wind Energy E, DTU Wind Energy, 2015.

[16] Troldborg N, Sørensen J, Mikkelsen R. Actuator line modeling of wind turbine wakes. PhD Thesis, Technical University of Denmark 2009.

[17] Sørensen N. General purpose flow solver applied to flow over hills. PhD Thesis, Risø National Laboratory 1995.

[18] Michelsen J. Basis3d - a platform for development of multiblock pde solvers. *Technical Report*, Dept. of Fluid Mechanics, Technical University of Denmark, DTU 1994.

[19] Michelsen J. Block structured multigrid solution of 2d and 3d elliptic pde's. *Technical Report*, Dept. of Fluid Mechanics, Technical University of Denmark, DTU 1994.

[20] Patanker S, Spalding D. A calculation procedure for heat, mass and momentum transfer in three-dimensional parabolic flows. *International Journal of Heat and Mass Transfer* 1972; .

[21] Leonard B. A stable and accurate convective modelling procedure based on quadratic upstream interpolation. *Computer Methods in Applied Mechanics and Engineering* 1979; **19**:59–98.

[22] Réthoré PE, Sørensen N. A discrete force allocation algorithm for modelling wind turbines in computational fluid dynamics. *Wind Energy* 2012; **15**:915–926, doi:10.1002/we.525.

[23] Menter FR. Zonal two equation $k-\omega$ turbulence models for aerodynamic flows. 23^{rd} *Fluid Dynamics, Plasmadynamics, and Lasers Conference, Fluid Dynamics and Co-located Conferences*, Orlando,FL, 1993, doi:10.2514/6.1993-2906.

[24] van der Laan P, Sørensen NN, Réthoré PE, Mann J, Kelly MC, Troldborg N, Schepers JG, Machefaux E. An improved $k-\epsilon$ model applied to a wind turbine wake in atmospheric turbulence. *Wind Energy* 2014; doi:10.1002/we.1736.

[25] Strelets M. Detached eddy simulation of massively separated flows. 39^{th} *AIAA Aerospace Sciences Meeting and Exhibit*, AIAA Paper 2001-0879, Reno,NV, 2001.

[26] Nathan J, Meyer Forsting A, Troldborg N, Masson C. Comparison of openfoam and ellipsys3d actuator line methods with (new) mexico results. *Journal of Physics: Conference Series (Online)* 2017; **854**, doi:10.1088/1742-6596/854/1/012033.

[27] Troldborg N, Zahle F, Réthoré PE, Sørensen N. Comparison of wind turbine wake properties in non-sheared inflow predicted by different cfd rotor models. *Wind Energy* 2013; **18**:10.1002/we.1757.

[28] Réthoré PE, van der Laan P, Troldborg N, Zahle F, Sørensen N. Verification and validation of an actuator disc model. *Wind Energy* 2014; doi:10.1002/we.1806.

[29] Meyer Forsting A, Troldborg N. The effect of blockage on power production for laterally aligned wind turbines. *Journal of Physics: Conference Series (Online)* 2015; **625**, doi:10.1088/1742-6596/625/1/012029.

[30] Sørensen JN, Shen WZ. Numerical modelling of wind turbine wakes. *Journal of Fluids Engineering* 2002; **124**:393–399, doi:10.1115/1.1471361.

[31] Mikkelsen R. Actuator disc methods applied to wind turbines. PhD Thesis, Technical University of Denmark 2003.

[32] Schepers J, Snel H. *Model Experiments in Controlled Conditions, Final report*. Report, Energy Research Center of the Netherlands, ECN, 2007.

[33] Schepers J, *et al* KB. *Final report of IEA Task 29, Mexnext (Phase 2)*. Report, Energy Research Center of the Netherlands, ECN, 2014.

[34] Martínez-Tossas LA, Churchfield MJ, Leonardi S. Large eddy simulations of the flow past wind turbines: actuator line and disk modeling. *Wind Energy* 2015; **18**:1047–1060, doi:10.1002/we.1747.

[35] Troen I, Bechmann A, Kelly M, Sørensen N, Réthoré PE, Cavar D, Ejsing Jørgensen H. *Complex terrain wind resource estimation with the wind-atlas method: Prediction errors using linearized and nonlinear CFD micro-scale models*. European Wind Energy Association (EWEA), 2014.

[36] Mann J. The spatial structure of neutral atmospheric surface-layer turbulence. *Journal of Fluid Mechanics* 1994; **273**:141–168.

[37] Mann J. Wind field simulation. *Probabilistic Engineering Mechanics* 1998; **13**:269–282.

[38] *IEC 61400-1:2005+AMD1:2010, Design requirements*.

[39] Mikkelsen TK. Windscanner.dk, a new danish remote sensing-based infrastructure for wind energy nd turbulence research: Design, establishment and operation 2009-2014. *Technical Report*, DTU Wind Energy, Technical University of Denmark 2015.

[40] Vignaroli A. *UniTTe- Nordtank Measurement Campaign (Turbine and Met Masts)*. DTU Wind Energy, 2015. DTU Wind Energy-I-0363.

[41] Madsen HA, Bak C, Døssing M, Mikkelsen R, Øye S. Validation and modification of the blade element momentum theory based on comparisons with actuator disc simulations. *Wind Energy* 2010; **13**:373–389, doi:10.1002/we.359.

[42] Kragh KA, Hansen MH, Mikkelsen T. Precision and shortcomings of yaw error estimation using spinner-based light detection and ranging. *Wind Energy* 2013; **16**:353–366, doi:10.1002/we.1492.

[43] Burton T, Jenkins N, Sharpe D, Bossanyi E. *Wind Energy Handbook: Second Edition*. John Wiley & Sons, Ltd: Chichester, United Kingdom, 2011.

[44] Branlard E, Gaunaa M. Cylindrical vortex wake model: skewed cylinder, application to yawed or tilted rotors. *Wind Energy* 2016; **19**(2):345–358, doi:10.1002/we.1838.

[45] Sørensen N, Aagaard Madsen H. *Modelling of transient wind turbine loads during pitch motion (paper and poster)*. European Wind Energy Association (EWEA), 2006.

[46] McTavish S, Rodrigue S, Feszty D, Nitzsche F. An investigation of in-field blockage effects in closely spaced lateral wind farm configurations. *Wind Energy* 2014; doi:10.1002/we.1806.

[47] Meyer Forsting A. Power curves in a wind turbine array: A numerical study. 2016. Poster presented at Wind Europe 2016.

[48] Jonkerman J, Butterfield S, Musial W, Scott G. Definition of a 5-mw reference wind turbine for offshore system development. *Technical Report*, NREL 2009.

[49] Troen I, Petersen EL. *European Wind Atlas*. Risø National Laboratory: Roskilde, Denmark, 1989.

[50] Mann J, Peña A, Troldborg N, Andersen SJ. How does turbulence change approaching a rotor? *Wind Energy Science Discussions* 2017; **2017**:1–13, doi:10.5194/wes-2017-53. URL https://www.wind-energ-sci-discuss.net/wes-2017-53/.

[51] Graham JMR. Rapid distortion of turbulence into an open turbine rotor. *Journal of Fluid Mechanics* 2017; **825**:764–794, doi:10.1017/jfm.2017.400.

[52] Hansen K, Larsen G, Menke R, Vasiljevic N, Angelou N, Feng J, Zhu W, Vignaroli A, Liu W W, Xu C, *et al.*. Wind turbine wake measurement in complex terrain. *Journal of Physics: Conference Series (Online)* 2016; **753**(3), doi:10.1088/1742-6596/753/3/032013.

[53] Borraccino A, Courtney M, Wagner R. Remotely measuring the wind using turbine-mounted lidars: Application to power performance testing. PhD Thesis, DTU Wind Energy, Denmark 2017, doi:10.11581/DTU:00000021.

[54] Vasiljević N, Palma JM, Angelou N, Matos JC, Menke R, Lea G, Mann J, Courtney M, Ribeiro LF, Gomes VM. Perdigão 2015: methodology for atmospheric multi-doppler lidar experiments. *Atmospheric Measurement Techniques Discussions* 2017; **2017**:1–28, doi:10.5194/amt-2017-18.

[55] Simley E, Pao LY, Frehlich R, Jonkman B, Kelley N. Analysis of liight detection and ranging wind speed measurements for wind turbine control. *Wind Energy* 2014; **17**:413–433, doi:10.1002/we.1584.

Part II

PUBLICATIONS

A collection of all journal/conference articles published in connection with the thesis is presented in this part. Each paper is accompanied by a cover page detailing the formation of its content and, if applicable, at which conference it was presented. The papers are available in their original, published format.

ARTICLE 1

THE EFFECT OF BLOCKAGE ON POWER PRODUCTION FOR LATERALLY ALIGNED WIND TURBINES

CONFERENCE JOURNAL ARTICLE

Journal of Physics: Conference Series 625 (2015) DOI

Wake Conference, Visby, Sweden, May 2015

Main author

These are the first published results performed within the PhD project and helped establish a numerical framework from which all following studies benefited. Preliminary work by Niels Troldborg highlighted the issue of lateral blockage in power performance measurements and facilitated this early publication.

The effect of blockage on power production for laterally aligned wind turbines

A R Meyer Forsting[1], **N Troldborg**[1]

[1] DTU Wind Energy, Department of Wind Energy, Technical University of Denmark, Risø Campus, DK-4000 Roskilde, Denmark

E-mail: alrf@dtu.dk

Abstract. This paper studies the change in the individual power coefficients for a laterally aligned row of wind turbines over a single, free turbine in the context of varying inflow directions via numerical simulations. All turbines were rotating in-line with the main flow direction. The problem definition is similar to that of many wind turbine testing sites and wind farms. Hence any changes in the individual turbine power production could have implications regarding power curve validation procedures.These changes are relatively small and therefore the size of the computational domain was identified to be detrimental in avoiding any domain-inflicted blockage. Increasing the misalignment of the main flow direction with the row of turbines led to significant variations in the power production across turbines. At the largest inflow angle of 45° it varied from -1.1 % to 2 %. As a whole, the power production increased by about 0.5 %, almost independent of the inflow direction.

1. Introduction

The lateral spacing between wind turbines is an important parameter in wind farm development, as it limits the number of wind turbines for a given site. Recent technological advances in the wind turbine industry have left many prime wind farm sites underperforming to their power production potential, due to their older, sub-MW turbines. Many wind parks have to undergo extensive modernisation programs in the years to come. These include upgrading to taller towers and larger rotors. In most cases, however the tower positions are fixed under the initial planning permits. As a consequence the lateral distance between blade tips is further reduced. Moving rotors ever more closely together means that the individual blockage effects, that are caused by the pressure jump across turbines, start to interact. Therefore the velocity field upstream is not only altered locally for a single turbine but, also on the global, wind farm scale. One would hence expect significant patterns to emerge in the individual power coefficients. Performance analyses of wind farms, though mainly focusing on wake effects, reveal significant variations along the first row of wind turbines, even if their causation has not so far been identified [1].

Whereas the effect might be negligible over an entire wind farm they can be significant in turbine power curve verification. Wind turbine testing sites normally align several turbines so that they lie on an axis perpendicular to the prevailing wind direction. Representative of this are the DTU sites Høvsøre and Østerild in Denmark. The widely used IEC standard for power curve validation does not include any specifications regarding lateral spacing, instead focusing on the avoidance of wake interaction from neighbouring objects and other turbines. Depending on the layout of the testing site valid wind sectors might include wind directions of up to 45° to the

alignment axis. The underlying assumption is of course that the neighbouring wind turbines are not influencing each other significantly, even at large inflow angles. Evaluating and quantifying the power production under the effect of interacting blockages, thus may proof important for future testing procedures and standards, as these assumptions are tested. In particular the influence on short-range remote sensing technology could be significant as it relies heavily on quantifying the local velocity field upstream.

Blockage has attracted most attention in marine research, as it has been shown experimentally [2] and numerically [3, 4] that it significantly increases the power output of tidal wave turbines. This conclusion is not transferable to wind turbines, which operate in a free domain unrestricted by water depth. In wind energy the focus has been largely on longitudinal spacing and wind farm staggering, as these parameters significantly influence wake interaction. Its impact on overall wind farm power production and turbine lifetime explain the proliferation of papers published on this subject. Previous attempts to quantify upstream blockage in a wind engineering context heavily relied on low Reynolds number experiments and a limited number of flow conditions. This includes work of Medici *et al.*, who used hot-wire anemometry and particle image velocimetry on a single turbine and concluded that blockage was noticeable more than three turbine diameters (D) upstream [5]. McTavish *et al.* studied the effect with similar limitations for three turbines by attempting to reach power maximization through an optimal spatial arrangement [6]. A power increase of 8 % was observed for a lateral spacing of 1.5D during experiments, which was validated by vortex particle simulations.

None of the current literature quantifies the blockage effect to the extent that any conclusions could be drawn for wind turbine testing. All existing experiments' flows were operating at small Reynolds numbers and the flow orientation was at all times perpendicular to the line of turbines. Furthermore the impact of tunnel blockage on results was hastily rejected and not properly assessed. The approach of this paper is more systematic. It employs computational fluid dynamics (CFD) to evaluate any kind of blockage and more specifically its possible effects on power curve measurements, where special attention is given to uncertainty reduction.

1.1. Problem definition

To allow for the conclusions of this paper to be relevant for turbine testing procedures, the arrangement adopted is loosely related to the DTU Høvsøre testing site. As shown in figure 1.1 five turbines are aligned on an axis with a 3D lateral spacing. Taking current measuring procedures as a reference, the angle between the line of wind turbines and the main wind direction (θ) was varied from 0° to 45° in 15° steps and the wind speed set to 8 ms^{-1}. Note that θ will sometimes be referred to as 'yaw' in the following passages. The inflow was set to be uniform and the solution assumed to be time invariant.

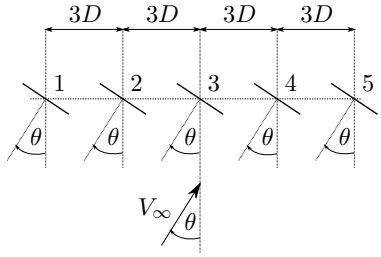

Figure 1. Schematic of the wind turbines' arrangement and reaction to changing inflow directions.

2. Computational method

2.1. Flow solver

The finite volume code EllipSys3D solves the incompressible Reynolds Averaged Navier-Stokes (RANS) equations over a discretised block-structured domain [7–9]. The SIMPLE algorithm [10] solves the pressure-linked terms of the Navier-Stokes equations, while the QUICK scheme [11] is applied to the convective terms. To allow the implementation of discrete body forces without jeopardising the coupling between velocity and pressure a modified Rhie-Chow algorithm has been implemented [12]. Further the Menter $k-\omega$ shear-stress transport modelled the turbulence [13].

2.2. Turbine model

Allowing the computations to be easily reproducible and representative of wind turbines currently employed, the well known NREL 5-MW [14] turbine with a diameter of 126 m was used. At the set wind speed of 8 ms^{-1}, the rotor performs 9.21 rotations per minute (RPM).

In the computational domain the rotor is represented by permeable body forces, which are derived from local velocity and 2-D airfoil data. In this particular simulation the actuator shape model [15] distributed these forces inside the domain by calculating the intersection between the rotor and flow grid.

2.3. Numerical domain

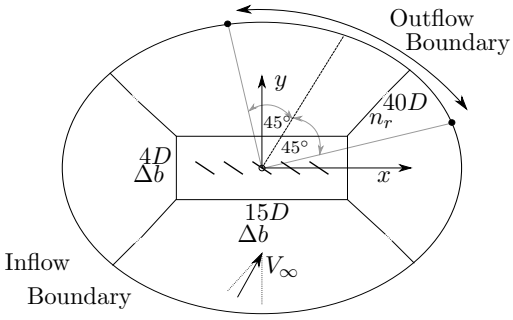

Figure 2. Top view of the numerical domain. All dimensions are scaled by the turbine diameter D. Note that the boundaries are a function of the inflow angle.

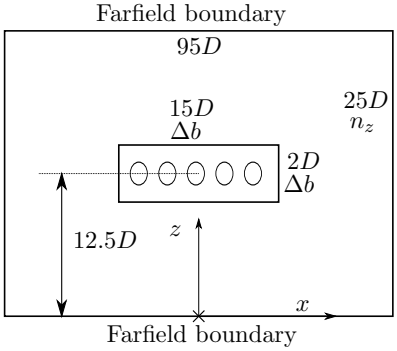

Figure 3. Frontal view of the numerical domain.

2.3.1. Layout The numerical domain was discretised by a structured O-type meshing methodology, containing a centrally located equispaced box mesh. The latter encompassed the row of turbines. Farfield boundary conditions were applied to both, top and bottom of the domain. The inflow and outflow boundaries were applied dynamically to the sides of the O-mesh by the preprocessor, depending on the inflow angle. More specifically the outflow sector is $\pm$ 45° centred around the inflow direction. A schematic layout of the domain and its coordinate system is shown in figures 2 and 3. All dimensions were scaled by D. The spacing inside the central box was fully defined by the inner grid spacing Δb, that resulted from the number of grid points specified per diameter (n_{rot}). From there the mesh grew hyperbolically outwards in the radial and z directions, where the dimension of the first cell connecting to the inner box mesh

was equal to Δb. The number of grid spaces along the radial and z directions were defined by n_r and n_z respectively.

2.3.2. Grid resolution and domain size To allow the conclusions drawn from this paper to be generally applicable, the grid resolution had to be sufficiently fine and the domain large enough to ensure the simulation results to be independent of these two factors.
Preliminary investigations showed that a relatively large domain was needed with respect to other types of investigations, to avoid 'tunnel' blockage influencing the results. 'Tunnel' blockage refers to constriction of the cross-sectional area through an object, leading to flow acceleration, which will hence influence the C_P of each turbine. In fact the equivalent 'tunnel' blockage, if defined as the rotor swept area over the cross-sectional area of the numerical domain, was 0.165 %, much lower than was seen as acceptable in previous investigations [6]. To further reduce the uncertainty deriving from the domain size, an outflow correction can be implemented at the domain boundaries to remove some of the excess mass flow. Koning [16] worked with potential flow assumptions to show that an analytical solution can be obtained to estimate this outflow. Here the actuator disc is represented by a doublet pressure source, which determines the flowfield everywhere. The final outflow velocity induced by a single turbine in the local disc coordinate system, denoted by $\bullet'$, is given as:

$$u_i' = \frac{1}{2} a V_\infty \frac{R^2 x_i'}{\left(\sum_{i=1}^{3} x_i'^2\right)^{3/2}} \text{ with } x_i' = \{x'y'z'\} \text{ and } u_i' = \{u'v'w'\} \tag{1}$$

,where a is the axial induction factor and R the disc radius. The former is estimated by momentum theory ($C_T = 4a(1-a)$) [17], where the thrust coefficient (C_T) is taken from a non-corrected simulation. Note that applying this correction is to a certain extent equivalent to increasing the domain size. No correction is needed for unrestricted domain methods.

The following paragraph addresses the second important factor regarding the discritisation of the domain and its influence on the results. As previously mentioned the changes in the C_P to be investigated were assumed to be relatively small, thus already at the first grid iteration, the resolution was aimed to be high. For wake investigations setting the number of points per diameter (n_{rot}) to 8, results in an acceptably low error [18]. Here it was initially set to 32, instead. In table 1 a summary of all grid parameters is presented. A higher grid level derived from halving the inner box spacing Δb.

Table 1. Mesh parameters.

Mesh	n_{rot} $[D^{-1}]$	Δb $[D]$	n_r	n_z	Cells $\times 10^6$
coarse	32	0.0313	32	128	2.05
fine	64	0.0156	64	256	8.21

Since the intention of this paper is to investigate the variation of C_P along a row of turbines, its sensitivity to changes in the domain size and grid level was analysed to evaluate the uncertainty in the simulations. The minimum and maximum yaw (θ) settings were chosen as evaluation points, as these were expected to yield the most extreme simulation solutions, making grid and domain errors more noticeable.

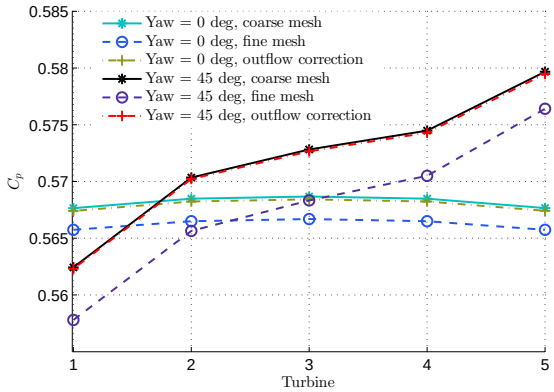

Figure 4. Evolution of C_P along a row of turbines for a coarse, fine and coarse mesh with outflow correction.

In figure 4 the evolution of C_P with turbine number is presented for the fine, coarse and coarse mesh with the outflow correction at the two extreme yaw positions. All curves agree in terms of their overall trend, though there is a visible offset between the solutions of the coarse and fine meshes. A numerical summary of the grid and domain errors is presented in table 2. The errors are calculated by taking the non-corrected coarse mesh solution as base and then calculating the resulting percentage difference in C_P at each turbine. As the aim of this study is to access relative changes in C_P across the row of turbines any absolute offsets are acceptable as long as they stay constant across the row. This implies that its standard deviation ($\sigma(\Delta C_P)$) has to be small. Between the fine and coarse meshes the largest error in predicting the overall trend was 0.1 %. This is acceptable for proving a significant change in C_P and therefore the coarse mesh was sufficiently resolved. The outflow correction had an even smaller impact, thus showing that the domain was acceptably large.

Table 2. Grid and domain errors calculated with the coarse mesh solution for C_P as base.

	θ [°]	$\langle \Delta C_P \rangle$ [%]	$\sigma(\Delta C_P)$ [%]
Grid	0	0.344	0.00636
	45	0.738	0.11200
Outflow	0	0.0433	0.000928
	45	0.0272	0.005070

2.4. Turbine orientation and location correction

The power coefficient for each turbine is not independent of its grid location. Therefore single turbine calculations are needed at each turbine location. Furthermore yawing the turbines inside the numerical domain (see figure 2) changes the way the body forces from the actuator disc are implemented inside the flow domain, thus making single turbine calculations at each yaw setting necessary. The resulting C_P values are then used to normalise the simulations:

$$\Delta C_P|_{i,j} = \frac{C_P|_{i,j} - C_{P_{single}}|_{i,j}}{C_{P_{single}}|_{i,j}} \times 100 \quad (2)$$
$$\text{,with } i = \{1, \ldots, 5\}, j = \{0, 15, \ldots, 45\}$$

3. Results

3.1. Power evolution

Figure 5 shows the variation in the global power coefficient across the row of turbines for the four inflow settings. These results are summarised in figure 6 in terms of their respective mean, minimum and maximum at each inflow angle. For a yaw of 0° the result's overall trend agrees well with those of McTavish [6]. McTavish also found an increased mean power production and a rise towards the centre of the row. A direct comparison is not possible as his lateral spacing was only 1.5D, half of what is used in this simulation. Yawing the inflow changes the behaviour markedly. Whereas the middle turbine (3) shows an increase in the power production close to the mean value, the upstream turbines (1-2) are losing their gain in power in line with an increase in yaw. For the first turbine losses are observed from a yaw of 15° onwards. The losses upstream are counteracted by almost equally sized increases on the downstream side (4-5). The existing balance between the losses upstream and gains downstream is underlined by the mean of all turbines being practically independent of yaw (see figure 6).

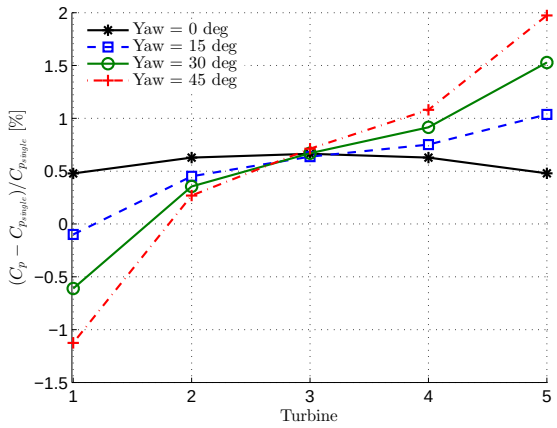

Figure 5. Percentage change in the power coefficient for different yaw angles.

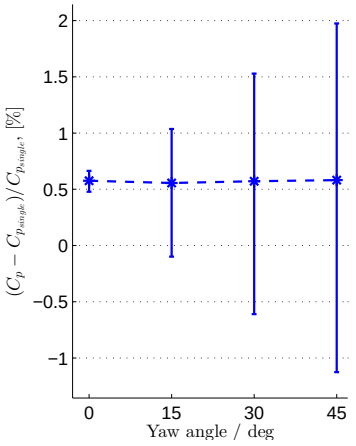

Figure 6. Summary of mean, minimum and maximum values of the results in figure 5 as a function of yaw angle.

3.2. The flowfield

The changes in the power coefficient along a row of turbines presented in the previous section can be directly linked to the emerging flow phenomena.

The main factors that are interacting and causing these flow alterations are the blockage, both on a local and global scale, and the acceleration of the flow between wind turbines and neighbouring wakes. The overall flow alterations are best explained via the extreme example of

$\theta = 45°$. Contours of the free-stream normalised axial velocity component (v_a) for this case are shown in figure 7. All wind turbines taken together act as one large flow obstruction and thus cause the emergence of a 'global' blockage effect or, equivalently, induction zone. Its presence is clearly visible in figure 7, where the flow is decelerating over the entire length of the wind farm. Notably at a yaw of 45° this deceleration is visibly reduced along the row of turbines.

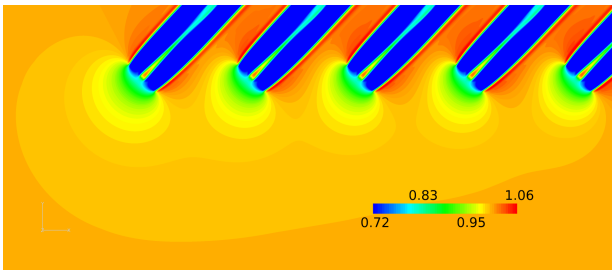

Figure 7. Normalised axial velocity contours (v_a) at a yaw angle (θ) of 45°.

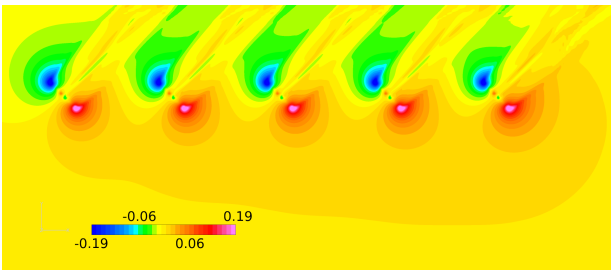

Figure 8. Normalised cross flow velocity contours (u) at a yaw angle (θ) of 45°.

This can be partly attributed to the local blockage from each turbine. As the flow approaches the turbine furthest upstream (1) the local induction reduces the mass flow forcing some of the flow to be diverted around it and thus towards turbine 2. There some of the flow is channelled through the space between the neighbouring wake and the turbine, hence causing the flow to accelerate, reducing the size of the local induction zone of turbine 2. This is also reflected by the axial velocity v_a distributions along the disc for turbines 3 and 5 shown in figure 9. This flow diversion continues all along the row of turbines leading to a continues build up of mass flow, as not all the excess flow escapes in-between turbines and wakes. This build up is a clear feature in the cross flow velocity contours in figure 8. It is this effect that leads to a decrease in the global induction zone along the row of turbines, as the flow accelerates. Note that the axial forcing from the turbines, defined by the thrust coefficient C_T, is actually increasing towards turbine 5. This shows that it is indeed the acceleration causing the decrease in the global induction zone. The process described in the paragraph above is aggravated by an increase in θ, as the distance between the turbines and neighbouring wakes decreases. This reduces the mass flow in-between turbines and wakes, causing an increase in the cross flow. Linked to this decrease in distance is a stronger induction felt by turbine 1 (see figure 9). The increased induction at turbine 1 and the subsequent increase in v_a along the row can be better understood by conceiving the row of turbines as a partially permeable flat plate.

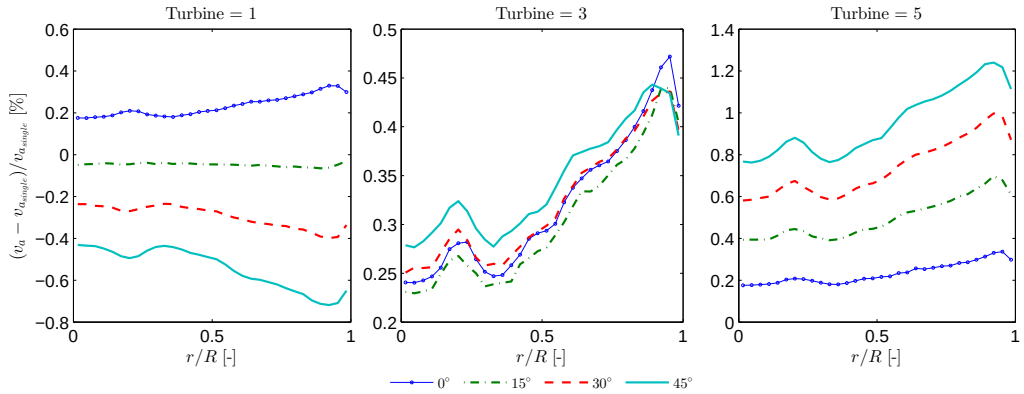

Figure 9. Azimuthally averaged axial velocity v_a distributions at the rotor disc at each yaw configuration.

4. Conclusion

The blockage effect and its impact on power production were assessed for a scenario similar to that of a wind turbines testing site using CFD. Extensive attention was paid to uncertainty reduction by assessing the influence of the numerical methodology on the results. Detrimental to a reliable investigation of this rather small effect, was selecting a sufficiently large domain. As an outcome the blockage ratio was significantly lower than deemed usually acceptable at 0.165 %. It is generally recommended to use similar ratios for domain restricted methods or alternatively applying corrections.

The blockage effect for laterally aligned wind turbines significantly alters the upstream flow, leading to marked changes in individual power coefficients. An inflow orthogonal to the row of turbines only had limited impact, causing a mean increase in the power coefficient across all turbines of 0.57 %. The different turbines' C_P values encompassed a range of 0.18 %. Yawing the inflow in respect to the line of alignment did not greatly affect the mean, in contrast to this the range of C_P extended in line with turbine rotation up to 3.1 % at 45°.

This was attributed to local and global blockage effects. Global blockage increased with turbine rotation, making the row of turbines adopt flow characteristics similar to those of a flat plate, diverting increasing amounts of mass flow down the row of turbines. Furthermore a stronger induction zone appeared at the upstream turbine causing a decrease in power, whereas downstream reacceleration lead to increases, peaking at the last turbine (2.0 % at 45°).

For wind turbine testing sites the accuracy with which a power performance evaluation can be carried out is of utmost importance. Even relatively small changes in the individual power coefficients, registered in this study, might prove significant. Nevertheless to make specific recommendations for real world applications, a more realistic flow, including an atmospheric boundary layer should be implemented and the actual measurement procedure be included.

Acknowledgments

This work was performed inside the UniTTe project (unitte.dk), which is financed by The Innovation Fund Denmark, grant number 1305-00024B. Further to the authors R. Wagner (DTU Wind Energy) contributed to this work through her valuable insights into power curve validation procedures. Computational resources were provided by the Risø DTU central computing facility.

References

[1] Mitraszewski K, Hansen K, Nygaard N and Rethoré P E Wall effects in offshore wind farms *Torque 2012*
[2] Bahaj A, Molland A, Chaplin J and Batten W 2007 *Renewable Energy*
[3] Turnock S R, Phillips A B, Bank J and Nicholls-Lee R 2011 *Ocean Engineering*
[4] Nishino T, Richard and Wilden H 2012 *J. Fluid Mech.*
[5] Medici D, Ivanell S, Dahlberg J A and Alfredsson P 2011 *Wind Energy*
[6] McTavish S, Rodrigue S, Feszty D and Nitzsche F 2014 *Wind Energy* DOI: 10.1002/we.1806
[7] Sørensen N 1995 *General purpose flow solver applied to flow over hills* Ph.D. thesis RisøNational Laboratory
[8] Michelsen J 1994 Basis3d - a platform for development of multiblock pde solvers Tech. rep. Dept. of Fluid Mechanics, Technical University of Denmark, DTU
[9] Michelsen J 1994 Block structured multigrid solution of 2d and 3d elliptic pdes Tech. rep. Dept. of Fluid Mechanics, Technical University of Denmark, DTU
[10] Patanker S and Spalding D 1972 *International Journal of Heat and Mass Transfer*
[11] Leonard B 1979 *Computer Methods in Applied Mechanics and Engineering*
[12] Rethoré P E and Sørensen N 2012 *Wind Energy*
[13] Menter F R 1993 *AIAA Journal*
[14] Jonkerman J, Butterfield S, Musial W and Scott G 2009 Definition of a 5-mw reference wind turbine for offshore system development Tech. rep. NREL
[15] Rethoré P E, van der Laan P, Troldborg N, Zahle F and Sørensen N 2014 *Wind Energy*
[16] 1976 *Aerodynamic Theory: A General Review of Progress* (Peter Smith) chap Devision M: Influence of the propeller on other parts of the airplane structure
[17] 2008 *Aerodynamics of Wind Turbines* 2^{nd} *Ed.* (Earthscan)
[18] van der Laan P, Sørensen N N, Rethoré P E, Mann J, Kelly M C, Troldborg N, Schepers J G and Machefaux E 2014 *Wind Energy*

ARTICLE 2

USING A CYLINDRICAL VORTEX MODEL TO ASSESS THE INDUCTION ZONE IN FRONT OF ALIGNED AND YAWED ROTORS

CONFERENCE ARTICLE

Conference Proceedings

EWEA Annual Event, Paris, France, 2015 DTU Orbit

Co-author

This paper is only one of many papers published by Emmanuel Branlard during his PhD at DTU Wind Energy. The main contribution towards this paper are the CFD simulations verifying his vortex model. The results of this paper strongly motivated following a vortex-based approach in the development of a simple induction zone model (see article 10).

Using a cylindrical vortex model to assess the induction zone in front of aligned and yawed rotors

Emmanuel Branlard, Alexander R. Meyer Forsting

DTU, Wind Energy, Denmark

February 19, 2016

Abstract

Analytical formulae for the velocity field induced by a cylindrical vortex wake model are applied to assess the induction zone in front of aligned and yawed rotors. The results are compared to actuator disk (AD) simulations for different operating conditions, including finite tip-speed ratios. The mean relative error is estimated in the induction zone and found to be below 0.4% for the aligned flows tested and below 1.3% for the yawed test cases. The computational time required by the analytical model is in the order of thousands of times less than the one required by the actuator disk simulation.

1 Introduction

The interest in the flow behaviour inside the induction zone, which develops in front of a wind turbine rotor, has re-emerge over the last decade. Simley compared lidar measurements with Computational Fluid Dynamics (CFD) simulations [14]. A better knowledge of the induction zone can improve control strategies. In recent work, the possibility that the wind turbine influences the turbulence characteristics in the induction zone has been investigated [4]. Based on analyses of the turbulence spectrum, it appeared that the approximation that the turbulence characteristics remained unaffected by the turbine was fair upstream of the turbine. The standards recommend a distance of 2.5 diameters to locate a meteorological mast and measure the representative free-stream velocity [10]. The possible effect of the turbine induction at this location can be quantified as mentioned in previous work by the authors [2].

The current paper uses the cylindrical rotor model of Joukowski [11] to determine the velocity field developing in the induction zone. The model was recently applied by the authors to aligned [2] and yawed conditions [3], where closed form expressions or semi-empirical expressions can be obtained for the entire flow field, respectively. Superposing such models can add further detail to the flow [5].

The paper briefly presents the analytical models needed to assess the velocity field upstream of the rotor. Results are then compared to CFD - actuator disk (AD) simulations in aligned and yawed conditions.

2 Model for the velocity field in the induction zone

2.1 Presentation of the model

The vortex cylinder (VC) model represents an actuator disk and its wake by assuming a prescribed support of vorticity in line with the cylindrical model of Joukowski [11]. The rotor and

its wake are assumed to be contained within a cylinder. The cylinder axis forms an angle χ with respect to the normal of rotor disk in case of a yawed inflow. This angle is referred to as the "skew" angle and is usually higher than the yaw angle [7]. The term "aligned flow" will be used when $\chi = 0$. When the circulation is constant along the span of the rotor disk, the model is said to be an "elementary" model. The model for a radial variation of circulation is detailed in subsection 2.4. The azimuthal variation of circulation is not accounted for in the current study. That the assumption of constant circulation produces satisfying results has been proven by many Blade Element Momentum (BEM) codes relying on this simplification for their yaw models [9, 6]. The elementary model consists of the following components of vorticity: a root vortex, a semi-infinite vortex cylinder with tangential γ_t and longitudinal vorticity γ_l, and a bound vortex disk with radial vorticity γ_b. The elementary cylindrical vortex model considered and the coordinate system used are shown in Figure 1. The generation of this vortex system

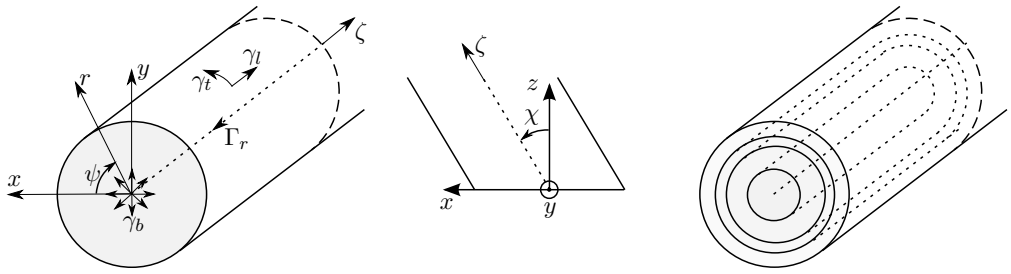

Figure 1: Vortex model and coordinate system. (a) Elementary system. (b) Positive definition of the skew angle χ. (c) Concentric superposition of elementary systems.

behind an actuator disk is discussed by van Kuik [16]. For simplicity, the current models neglects wake expansion. This assumption is discussed in detail in [5]. The notation $u_{\bullet,\diamond}$ will refer to the $\bullet$-component of the velocity induced by the vortex element $\diamond$, where $\bullet \in \{r, \psi, z\}$ and $\diamond \in \{r, t, l, b\}$. The velocity field induced by the full vortex system is: $u_r = u_{r,t} + [u_{r,l} + u_{r,r}]$, $u_z = u_{z,t} + [u_{z,l} + u_{z,r}]$, $u_\psi = u_{\psi,l} + u_{\psi,r} + u_{\psi,b} + [u_{\psi,t}]$ where the terms in square brackets are zero in the aligned case. The following notations are further introduced: Γ_{tot} is the total circulation of the rotor, R is the rotor radius, and h is the pitch of the helical wake formed by the combination of the two tip-vorticity components γ_t and γ_l.

2.2 Formulae in the aligned case for the elementary model

The different strengths of the root vortex, the bound vorticity, the tangential and longitudinal vorticity are respectively [2]:

$$\boldsymbol{\Gamma}_r = -\Gamma_{\text{tot}}\, \boldsymbol{e}_z, \qquad \boldsymbol{\gamma}_b(r) = \frac{\Gamma_{\text{tot}}}{2\pi r}\, \boldsymbol{e}_r, \qquad \boldsymbol{\gamma}_t = -\frac{\Gamma_{\text{tot}}}{h}\, \boldsymbol{e}_\psi, \qquad \boldsymbol{\gamma}_l = \frac{\Gamma_{\text{tot}}}{2\pi R}\, \boldsymbol{e}_z, \tag{1}$$

The expressions of the different components were obtained by direct integration of the Biot-Savart law as [2]:

$$
\begin{aligned}
u_r(r,z) &= -\frac{\gamma_t}{2\pi}\sqrt{\frac{R}{r}}\left[\frac{2-\mathrm{k}^2(r,z)}{\mathrm{k}(r,z)}K\left(\mathrm{k}^2(r,z)\right)-\frac{2}{\mathrm{k}(r,z)}E\left(\mathrm{k}^2(r,z)\right)\right]\\
u_z(r,z) &= \frac{\gamma_t}{2}\left[\frac{R-r+|R-r|}{2|R-r|}+\frac{z\mathrm{k}(r,z)}{2\pi\sqrt{rR}}\left(K\left(\mathrm{k}^2(r,z)\right)+\frac{R-r}{R+r}\Pi\left(\mathrm{k}^2(r,0),\mathrm{k}^2(r,z)\right)\right)\right] \qquad (2)\\
u_\psi(r,z) &= \begin{cases} -\Gamma_{\mathrm{tot}}/4\pi r, & r<R \text{ and } z=0 \quad \text{,or,} \quad r=R \text{ and } z>0\\ -\Gamma_{\mathrm{tot}}/2\pi r, & r<R \text{ and } z>0\\ 0, & \text{otherwise}\end{cases}
\end{aligned}
$$

where E, K and Π are the complete elliptic integrals of the first, second and third kind respectively, where the elliptic parameter k is given by

$$
\mathrm{k}^2(r,z)=\frac{4rR}{(R+r)^2+z^2}, \qquad n_1=\frac{2r}{r+\sqrt{r^2+z^2}}, \qquad n_2=\frac{2r}{r-\sqrt{r^2+z^2}}. \qquad (3)
$$

and where n_1 and n_2 are used below. The different components forming the tangential velocity are:

$$
u_{\psi,l}(r,z)=\frac{\gamma_l}{2}\frac{R}{r}\left[\frac{r-R+|R-r|}{2|R-r|}+\frac{z\mathrm{k}(r,z)}{2\pi\sqrt{rR}}\left(K\left(\mathrm{k}^2(r,z)\right)-\frac{R-r}{R+r}\Pi\left(\mathrm{k}^2(r,0),\mathrm{k}^2(r,z)\right)\right)\right] \qquad (4)
$$

$$
u_{\psi,r}(r,z)=-\frac{\Gamma_{\mathrm{tot}}}{4\pi r}\left[1+\frac{z}{\sqrt{r^2+z^2}}\right] \qquad (5)
$$

$$
u_{\psi,b}(r,z)=\frac{\Gamma_{\mathrm{tot}}}{4\pi}\Big\{\frac{1}{r}\left[\frac{z}{\sqrt{r^2+z^2}}-\frac{|z|}{z}\right]-\frac{1}{\pi z}\sqrt{\frac{r}{R}}\frac{z^2}{r^2}\,\mathrm{k}\left[K(\mathrm{k}^2)+T_1\,\Pi(n_1,\mathrm{k}^2)-T_2\,\Pi(n_2,\mathrm{k}^2)\right]\Big\} \qquad (6)
$$

$$
T_1=\frac{\left(\sqrt{r^2+z^2}-r\right)(r+R)-z^2}{2z^2}, \qquad T_2=\frac{\left(\sqrt{r^2+z^2}+r\right)\left(\sqrt{r^2+z^2}+R\right)}{2z^2}, \qquad (7)
$$

2.3 Formulae in the yawed case for the elementary model

The different strengths of the root vortex, the bound vorticity, the tangential and longitudinal vorticity are respectively [3]:

$$
\boldsymbol{\Gamma}_r=-\Gamma_{\mathrm{tot}}\,\boldsymbol{e}_z, \qquad \boldsymbol{\gamma}_b(r)=\frac{\Gamma_{\mathrm{tot}}}{2\pi r}\,\boldsymbol{e}_r, \qquad \boldsymbol{\gamma}_t=-\frac{\Gamma_{\mathrm{tot}}}{h/\cos\chi}\,\boldsymbol{e}_\psi, \qquad \boldsymbol{\gamma}_l=\frac{\Gamma_{\mathrm{tot}}}{2\pi R}\,\boldsymbol{e}_\zeta \qquad (8)
$$

Velocities induced by the tangential vorticity The velocity induced by the tangential vorticity was first studied by Coleman [9], then extended by Castles and Durham [8] and recently generalized by Branlard and Gaunaa [3]. The velocity is obtained using an analytical integration over z and a numerical integration over ψ to give:

$$
\begin{aligned}
u_{\bullet,t}(r,\psi,z) &= \frac{\gamma_t}{4\pi}\int_0^{2\pi}\frac{2\left(a'_\bullet\sqrt{c}+b'_\bullet\sqrt{a}\right)}{\sqrt{a}\left(2\sqrt{ac}+b\right)}\,d\theta' \qquad (9)\\
\{a'_z,\ b'_z\} &= R\left\{R-r\cos(\theta'-\psi),\ m\cos\theta'\right\}\\
\{a'_r,\ b'_r\} &= R\left\{z\cos(\theta'-\psi),\ -\cos(\theta'-\psi)\right\}\\
\{a'_\psi,\ b'_\psi\} &= R\left\{z\sin(\theta'-\psi),\ -\sin(\theta'-\psi)\right\}\\
\{a,\ b,\ c\} &= \left\{R^2+r^2+z^2-2rR\cos(\theta'-\psi),\ 2mR\cos\theta'-2mr\cos\psi-2z,\ 1+m^2\right\}
\end{aligned}
$$

where the symbol $\bullet$ stands indifferently for r, ψ, z and where $m = \tan\chi$. In the rotor plane, and for $\psi = 0$ the integration over the azimuthal variable can be carried on analytically. An analytical formula was given by Coleman et al. [9] for the velocity inside the rotor and by the first author for the velocity outside of the rotor [1]:

$$u_{z,t}(r > R, \psi = 0, z = 0) = \frac{\gamma_t}{2}(1 + K_i + K_o) \tag{10}$$

$$K_i(r, \chi) = 2F_t(r, \chi)\tan\frac{\chi}{2}$$

$$K_o(r, \chi) = -\frac{r\sqrt{1+m^2}}{2m^2\left(r^2 - R^2\right)}\left(\frac{r\left(\sqrt{C-B}+\sqrt{B+C}\right)}{\sqrt{r^2+m^2R^2}} + \frac{\sqrt{C-B}-\sqrt{B+C}}{\sqrt{1+m^2}}\right)$$

with $F_t(r, \chi) = \frac{K_i(r,\chi)}{2\tan\frac{\chi}{2}} \approx r/2R$ and

$$B = 2r\sqrt{(1+m^2)(r^2+m^2R^2)}, \quad C = (2+m^2)r^2 + m^2R^2$$

The exact expression for K_i is given in the article of Coleman et al. Equation 10 can be used to verify the numerical integration performed in Equation 9 for the axial induction. The azimuthal variation of the axial velocity is modelled based on the value at the fore-aft diameter as:

$$u_{z,t}(r < R, \psi, z = 0) \approx \frac{\gamma_t}{2}\left[1 + K_i(r)\cos(\psi)\right] \tag{11}$$

$$u_{z,t}(r > R, \psi, z = 0) \approx \frac{\gamma_t}{2}\left[(1 + K_o(r))\cos(2\psi) + K_i(r)\cos\psi\right] \tag{12}$$

The model values are exact for $\psi = 0°$ and $\psi = 90°$.

Other components In the current paper, yawed simulations will be performed for an infinite tip-speed ratios so that only the tangential component of vorticity contributes to the flow. The induced velocities originating from other components were already derived in previous work [3] and will be tested against actuator disk simulations in the future.

2.4 Extension to a varying circulation along the span

The velocity field of a rotor with varying circulation along its span is obtained using a superposition of the velocity fields given in the previous sections. The superposition of cylinders is illustrated in Figure 1c. The determination of the cylinder strengths from the thrust distribution is done according to previous work published on this topic [5].

3 Results

Actuator disk simulations were carried out using the in-house 3D flow solver EllipSys3D, developed by Michelsen and Sørensen [13, 15]. Results from these simulations are used as a reference to assess the quality of the velocity field obtained from the analytical model.

3.1 Aligned case, without swirl

The results presented in this paragraph were performed for a constant thrust coefficient prescribed along the span. Further, the actuator disk is not rotating. This which is similar to $\lambda = \infty$ for which only the tangential vorticity component is present. In the absence of swirl, a constant thrust coefficient implies a constant circulation distribution. As a result of this,

one vortex cylinder is enough to model the flow. For ease of comparison, the value of γ_t was obtained by extracting the induced velocity at the middle of the rotor plane from the Actuator disk simulation. Indeed according to the vortex cylinder model, $u(r = 0, z = 0) = \gamma_t/2$. The axial and radial velocities along the rotor's axis $x = 0$ and along the rotor radius $z = 0$ are shown in Figure 2 for two different C_T values. The coefficients of determination R^2 between the

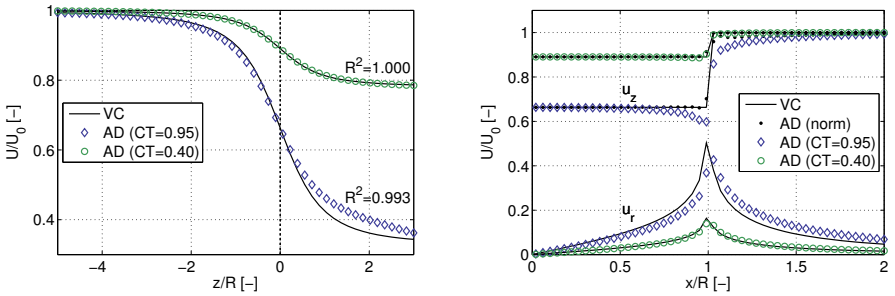

(a) (b)

Figure 2: Axial and radial velocities along the rotor's axis (left) and along the rotor radius (right) for two different C_T values.

curves are also shown in the figure. It is reminded that along the z axis, Equation 2 reduces to (see e.g. [2]):

$$u_z(r = 0, z) = \frac{\gamma_t}{2}\left[1 + \frac{z}{\sqrt{R^2 + z^2}}\right] \tag{13}$$

The figure shows that the AD and VC results are in strong agreement for low values of the thrust coefficient, where the omission of the wake expansion is indeed justifiable. Discrepancies arises at higher thrust coefficients. In particular, the axial induction obtained from the AD simulations are not constant over the rotor span as opposed to what is predicted by the VC theory. On the other hand, the velocity norm on the rotor plane is close to constant. These observations were also presented by van Kuik and Lignarolo [17].

The full velocity fields for the challenging case of $C_T = 0.95$ are compared for the numerical and analytical model in Figure 3.

3.2 Aligned case with swirl

Simulations including swirl cannot be carried out with a constant thrust coefficient along the span, as it would result in infinite tangential velocities at the root [5]. In line with the work of Madsen et al. [12], the thrust coefficient is prescribed to a constant C_{T_0} along most of the span and drops linearly to zero from the radial position $r/R = 0.11$ towards the root. For convenience the subscript 0 is dropped in the rest of the document. For the VC model, the circulation is determined by solving the following equation for k at each radial position [5]:

$$k(r)\left(1 + \frac{k(r)}{4\lambda_r^2}\right) - C_{t,in}(r) = 0 \tag{14}$$

The vortex cylinder strengths are then determined using the pitch angle of the helix [5]. An example of the axial velocity contours obtained for $C_T = 0.4$ is shown in Figure 4. The two models strongly agree in the induction zone, and predict the high velocity core towards the root

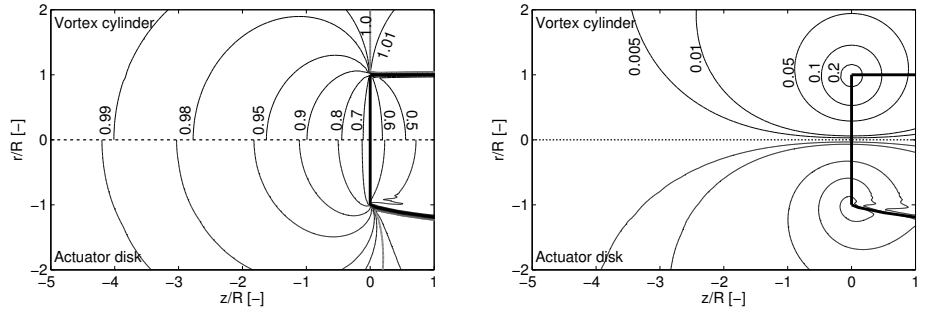

(a) (b)

Figure 3: Contours of axial (left) and radial (right) velocities normalized by the free stream for a thrust coefficient $C_T = 0.95$ and for both the actuator disk and vortex cylinder model. The lack of wake expansion in the vortex cylinder model is the main source of discrepancy between the two models.

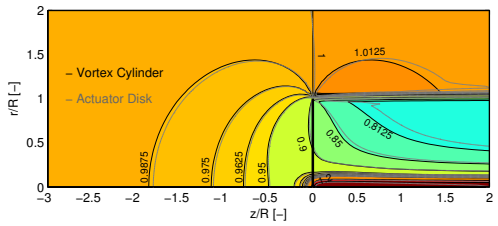

Figure 4: Axial velocity contours for an aligned flow with swirl $C_T = 0.4$, $\lambda = 2$. The contours for the vortex cylinder are plotted in black while the ones from the actuator disk are plotted in gray.

of the blade. Progressively downstream of the rotor the discrepancies keep increasing, due to the wake expansion present in the CFD simulation.

A parametric study is performed to quantify the error of the axial induction predicted by the vortex cylinder model for different operating conditions (C_T, λ). Results are reported in Table 1. The induction zone was defined as the rectangular area delimited by $r, z \in [-0.9R, 0.9R] \times$

Table 1: Relative error in axial velocity in the induction zone for different operating conditions.

	$C_T = 0.4$				$C_T = 0.95$			
	$\lambda = 2$	$\lambda = 6$	$\lambda = 10$	$\lambda = \infty$	$\lambda = 2$	$\lambda = 6$	$\lambda = 10$	$\lambda = \infty$
Mean	0.1%	0.1%	0.1%	0.0%	0.1%	0.2%	0.3%	0.4%
Max	0.2%	0.2%	0.2%	0.2%	1.8%	2.5%	2.7%	3.3%

$[-3R, 0R]$. The vortex cylinder singularity towards $R = 1$ was avoided in this manner. A regularized vortex cylinder formulation can also be used to avoid this singularity [1]. The error is highest, as expected, for high thrust coefficients, due to the lack of wake expansion in the vortex model. Overall the induction zone is predicted with an average accuracy of 0.4%.

3.3 Yawed case

Simulations of a yawed rotor without swirl are presented in this paragraph. The actuator disk simulations were run for a yaw angle of $\theta_{\text{yaw}} = 30°$. The loading on the actuator disk was prescribed using a constant thrust coefficient. The vortex cylinder model assumed a constant circulation along the span. The skew angle required by the vortex cylinder model is determined using the following empirical relation [7, p. 105]:

$$\chi = \theta_{\text{yaw}} \left[1 + 0.6\,\overline{a}\right] = \theta_{\text{yaw}} \left[1 + 0.3\left(1 - \sqrt{1 - C_T}\right)\right] \tag{15}$$

where the mean induction was estimated as $\overline{a} = \frac{1}{2}\left(1 - \sqrt{1 - C_T}\right)$. An azimuthal variation of the loading and circulation is expected in a realistic simulation of an actuator disk in yawed inflow. The assumption made here was discussed in subsection 2.1. Figure 5 presents the same axial velocity profiles as Figure 2 but for $\theta_{\text{yaw}} = 30°$. In the left of this figure, the induction is

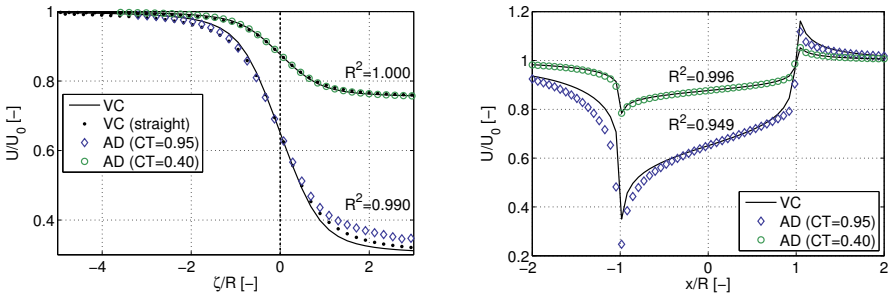

(a) (b)

Figure 5: Axial velocity along the rotor's axis (left) and along the rotor radius (right) for two different values of C_T. The curve labelled 'VC (straight)' corresponds to the evaluation of Equation 13 with $z = \zeta$.

plotted along the wake axis ζ. The curve labelled 'VC (straight)' corresponds to the evaluation of Equation 13 with $z = \zeta$. It is seen that along the wake axis this formula is still of reasonable accuracy even for a yaw angle as large as 30°. The agreement between the AD and VC for the yawed case is slightly less than in the non-yawed case. The induction agrees to a high degree for the thrust coefficient $C_T = 0.4$. The same conclusions are drawn for the axial induction within the rotor plane as plotted in the right of the figure.

Axial velocity contours for two values of the thrust coefficients are shown in Figure 6. The agreements is fair for the low thrust coefficient case, whereas the marked differences in wake expansion observed in the right of the figure for $C_T = 0.95$ lead to visible differences in the velocity contours. These differences are further quantified. The absolute value of the relative error, scaled with the free-stream velocity, between the actuator disk and vortex cylinder models is shown in Figure 7. The induction zone as defined earlier is marked on the figure using a dashed box. The mean and maximum relative error within the induction zone is computed and shown on the figure. The mean relative error in the challenging case of high thrust coefficient $C_T = 0.95$ is 1.3%. The differences are the strongest close to the rotor where the effect of expansion has more impact.

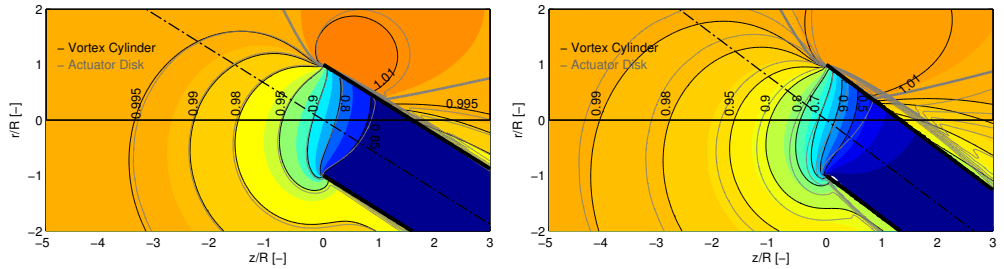

Figure 6: Axial velocity contours obtained with the two models for two values of the thrust coefficients. (left:) $C_T = 0.4$, (right:) $C_T = 0.95$

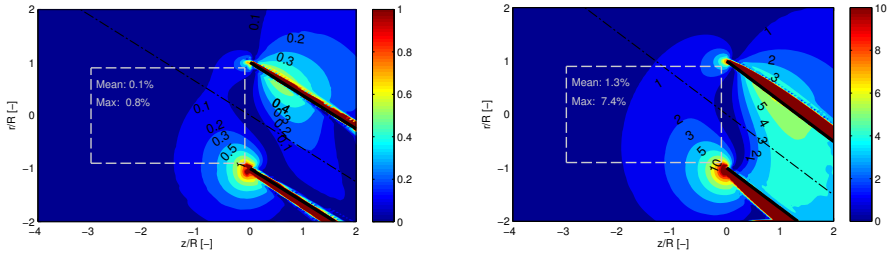

(a) (b)

Figure 7: Absolute value of the relative error in axial induction obtained by the vortex cylinder model compared to the actuator disk simulation for two thrust coefficients. (left:) $C_T = 0.4$, (right:) $C_T = 0.95$. The area marked with a dashed box refers to the "induction zone" for which the mean and maximum error are computed.

3.4 Computational time

The computational time on one CPU of the full velocity field for the vortex cylinder model takes approximately $1s$ using a non-compiled scripting language. The actuator disk simulations were run on 8 CPUs using a compiled language. If these simulations were run on one CPU the simulation times would be 2400s and 6000s for the simulations with swirl and without swirl respectively. In light of this difference of computational time the accuracy obtained by the vortex cylinder model are remarkable.

4 Conclusions

The velocity field from the analytical formulae of the cylindrical vortex wake model agreed to a high degree with the ones obtained from actuator disk simulations. For the aligned flow, a mean relative error of 0.4% was obtained in the induction zone. In the yawed condition tested, a mean relative error of 1.3% was obtained in the induction zone for the challenging case of $C_T = 0.95$ and $\chi = 30°$. The computational time required by the analytical model is in the order of thousands of times less than the one required by the actuator disk simulation. The model can be used for rapid estimates of the induction zone with a remarkable accuracy.

References

[1] Branlard, E. *Analysis of wind turbine aerodynamics and aeroelasticity using vortex-based methods*. PhD thesis, Technical University of Denmark (DTU), Wind Energy Department, 2015.

[2] Branlard, E., and Gaunaa, M. Cylindrical vortex wake model: right cylinder. *Wind Energy 18*, 11 (2015), 1973–1987.

[3] Branlard, E., and Gaunaa, M. Cylindrical vortex wake model: skewed cylinder, application to yawed or tilted rotors. *Wind Energy* (2015), 1–14. we.1838.

[4] Branlard, E., and Gaunaa, M. Impact of a wind turbine on turbulence: un-freezing the turbulence by means of a simple vortex particle approach, 2015. (Submitted to the Journal of Wind Engineering and Industrial Aerodynamics, February 2015).

[5] Branlard, E., and Gaunaa, M. Superposition of vortex cylinders for steady and unsteady simulation of rotors of finite tip-speed ratio. *Wind Energy* (2015), 1–17. we.1899.

[6] Branlard, E., Gaunaa, M., and Machefaux, E. Investigation of a new model accounting for rotors of finite tip-speed ratio in yaw or tilt. *Journal of Physics: Conference Series (Online) 524*, 1 (2014), 1–11.

[7] Burton, T., Sharpe, D., Jenkins, N., and Bossanyi, E. *Wind Energy Handbook*, first ed. J. Wiley & Sons, New-York, N.Y., 2002.

[8] Castles, W., and De Leeuw, J. H. The normal component of the induced velocity in the vicinity of a lifting rotor and some examples of its application. Tech. rep., NACA Report No. 1184, Giorgia Institure of Technology, Atlanta, 1954.

[9] Coleman, R. P., Feingold, A. M., and Stempin, C. W. Evaluation of the induced-velocity field of an idealized helicopter rotor. *NACA ARR No. L5E10* (1945), 1–28.

[10] International Standard IEC. *IEC 61400-12 Power performance measurements of electricity producing wind turbines*. International Electrotechnical Commission, Geneva, 2005.

[11] Joukowski, N. E. Vortex theory of screw propeller, I. *Trudy Otdeleniya Fizicheskikh Nauk Obshchestva Lubitelei Estestvoznaniya 16*, 1 (1912), 1–31. (in Russian). French translation in: Théorie tourbillonnaire de l'hélice propulsive. Gauthier-Villars: Paris, 1929; 1: 1-47.

[12] Madsen, H., Bak, C., Døssing, M., Mikkelsen, R., and Øye, S. Validation and modification of the blade element momentum theory based on comparisons with actuator disc simulations. *Wind Energy 13* (2010), p373–389.

[13] Michelsen, J. A. *Block Structured Multigrid Solution of 2D and 3D elliptic PDE's*. AFM 94-05 - Department of Fluid Mechanics, Technical University of Denmark, 1994.

[14] Simley, E., Pao, L. Y., Gebraad, P., and Churchfield, M. Investigation of the impact of the upstream induction zone on lidar measurement accuracy for wind turbine control applications using large-eddy simulation. *Journal of Physics: Conference Series 524*, 1 (2014), 012003.

[15] Sørensen, N. N. *General Purpose Flow Solver Applied to Flow over Hills*. PhD thesis, Risø National Laboratory., 1995.

[16] van Kuik, G. A. M. On the generation of vorticity by force fields in rotor- and actuator flows. *Renewable Energy 70* (2014), 124–128.

[17] van Kuik, G. A. M., and Lignarolo, L. E. M. Potential flow solutions for energy extracting actuator disc flows. *Wind Energy Online* (2015), 1–16.

ARTICLE 3

A NUMERICAL STUDY ON THE FLOW UPSTREAM OF A WIND TURBINE IN COMPLEX TERRAIN

CONFERENCE JOURNAL ARTICLE

Journal of Physics: Conference Series 753 (2016) DOI

The Science of Making Torque from Wind (TORQUE), Munich, Germany, October 2016

Main author

Nikola Vasiljevic and Nikolas Angelou *et al.*, both at DTU Wind Energy, performed the first measurement campaign combining short- and long-range multi-lidar systems [54] in May 2015. They measured the flow over a double ridge and around a wind turbine erected on one of them simultaneously. Their experiment motivated simulating the flow around the wind turbine at this site, to study any influence the extreme terrain might have on the induction zone. The simulations were based on the WAsP-CFD approach developed by Andreas Bechmann [35]. The mesh generation required special attention, due to the complexity of the terrain. A preliminary comparison with the measurements was presented at ECCOMAS 2016 and a publication with a more detailed comparison might follow in the future.

A numerical study on the flow upstream of a wind turbine in complex terrain

A R Meyer Forsting[1], A Bechmann[1], N Troldborg[1]

[1] DTU Wind Energy, Department of Wind Energy, Technical University of Denmark, Risø Campus, DK-4000 Roskilde, Denmark

E-mail: alrf@dtu.dk

Abstract. The interaction of a wind turbine with the upstream flow-field in complex and flat terrain is studied using Reynolds-averaged Navier-Stokes (RANS) simulations with a two equation turbulence closure. The complex site modelled is Perdigão (Portugal), where a turbine is located on one of two parallel running ridges. Simulating various wind directions with and without rotor, the impact of the rotor on the flow-field upstream is determined. This is compared and related to simulations with sheared and uniform inflow. The induction zones forming for these two inflows agree to such an extent, that shear could be interpreted as linear perturbation to the uniform inflow solution. However, for complex terrain this is not the case, as it is highly dependant on flow features caused by the topography and their interaction with the rotor. Separation in the lee of the ridge plays a crucial role, as it dictates the wind turbine wake trajectory which in turn governs the orientation of the induction zone.

1. Introduction

The flow coming towards a wind turbine rotor is continuously decelerated by the rotor's thrust force acting on it. The thrust is in turn a result of the aerodynamic forces acting over the rotor blades. The area over which this effect acts is also referred to as the induction zone. Medici *et al.* [1] found through RANS computations and wind tunnel measurements, that the influence of the turbine extends up to 6 rotor radii (R) upstream. Field measurements with wind lidars confirmed the presence of the decelerating region in front of the rotor, though the exact extent of it is disputed with Asimakopoulos *et al.* [2] putting it $7R$ upstream and Slinger *et al.* [3] at $3R$. The IEC standards for power performance measurements [4] on the other hand assume the turbine to have a negligible effect beyond $4R$ upstream. Therefore this value also acts as guideline for industry.

Existing literature tried to quantify the induction zone solely in flat terrain, thus we address a situation where the topography considerably impacts the flow-field upstream of the rotor. Using RANS simulations in connection with an actuator disc (AD) representation of the rotor, we assess the difference in the induction zone in complex topography from flat terrain and uniform inflow. As a representative test case the site of the New European Wind Atlas (NEWA) at Perdigão (Portugal) is taken - here a turbine is located on top of one of two parallel ridges as shown in figure 1.

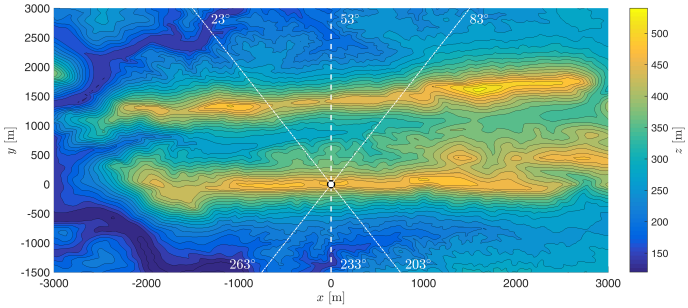

Figure 1. Height contours of the parallel ridges at Perdigão (Portugal). The wind turbine location (o) and the investigated wind direction sectors are marked.

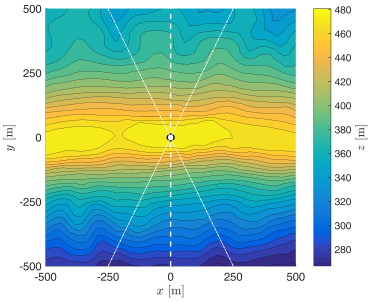

Figure 2. Height contours of the immidiate area sourrounding the wind turbine (o).

2. Computational method

2.1. Numerical setup

Changing the topography around a wind turbine is similar to altering the inflow profile to a rotor. Therefore simulations are preformed for uniform and sheared inflow profiles as well as for several wind directions at the Perdigão site. As the induction zone is governed by the rotor thrust, the comparability of the different inflow scenarios is driven by applying exactly the same thrust coefficient C_T in each simulation. This condition is met with an actuator disc representation of the rotor with prescribed forces. The normal force acting over a sectional area ΔA of the disc is given by

$$F_{\{N,\Delta A\}} = \frac{1}{2}\rho_\infty V^2_{\{\infty,\Delta A\}} C_T \Delta A \tag{1}$$

Here the free-stream velocity $V_{\{\infty,\Delta A\}}$ acting over the area ΔA is determined by extracting the velocity at ΔA from a rotor-less simulation as shown in Figure 3. Ultimately subtracting the

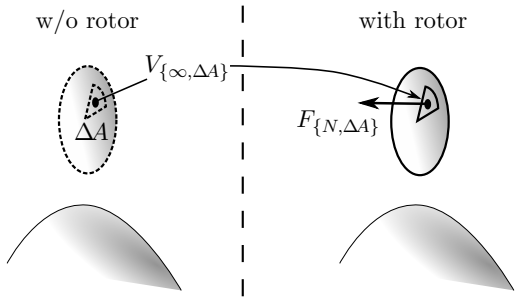

Figure 3. Method for determining the axial force $F_{\{N,\Delta A\}}$ for each section of the actuator disc by extracting velocities from a rotor-less simulation.

rotor-less flow-field from the one with rotor $\vec{V}_R - \vec{V}$ isolates the influence of the induction zone $\Delta\vec{V}$. Forces are calculated for different thrust coefficients C_T, namely 0.36, 0.64 and 0.89, to investigate the sensitivity of the induction zone to this parameter. The simulations are performed by solving the incompressible steady-state Reynolds-averaged Navier-Stokes (RANS) equations

under neutral stratification. By omitting Coriolis and assuming neutral stratification the wind field becomes Reynolds number independent. The employed turbulence model, a modified $k-\epsilon$ [5] formulation, captures turbulence at both, terrain and rotor scales. The rough logarithmic velocity profile models the near ground flows [6]. The friction velocity is prescribed at the inlet boundary with $z_0 = 0.1$ and $u^\star = 0.4$. Additionally the wind direction is specified at the Perdigão site. The wind directions are selected to cover 60° sectors, divided by 15° steps centred about the directions orthogonal to the rotor ridge, equivalent to 53° and 233°.

2.2. Flow solver
The in-house finite volume code EllipSys3D solves the incompressible RANS equations over a discretised block-structured domain [7–9] with collocated variables. Solving convective terms using the QUICK scheme [10] and the SIMPLE method [11] for the pressure-linked terms of the Navier-Stokes equations. A modified Rhie-Chow algorithm [12, 13] avoids decoupling velocity and pressure in the presence of discrete body forces originating from an actuator disc (AD).

2.3. Actuator disc
In the computational domain the prescribed rotor forces are distributed over a permeable disc using an actuator disc model [14]. The disc itself consists of a polar grid with 33 points in the radial and 180 points in the annual direction. The intersections between the disc and computational grid determine in which cell the forces are applied.

2.4. Numerical domains

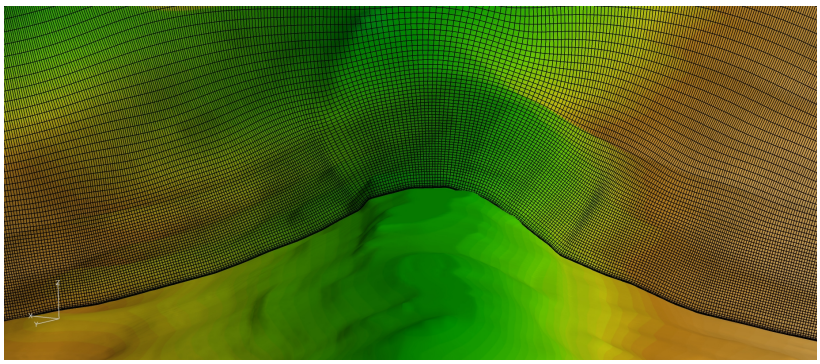

Figure 4. Impression of the Perdigão computational mesh along the transect of the ridge, passing through the turbine location.

2.4.1. Uniform & sheared inflow A box domain with side lengths of 25 radii (R) is created for both inflow cases. This minimises domain blockage ($\pi/25^2 = 0.5\%$). For uniform inflow the actuator disc is located at the domain centre and surrounded by a finely meshed box with $2.5R$ side lengths. Using a grid spacing of $R/16$ for the inner mesh surrounding the rotor, has yielded sufficiently accurate results in previous studies [15–17] for structured box domains in uniform and sheared inflow. The same finely meshed box surrounds the rotor in sheared inflow. However the rotor centre is shifted to 78 m above ground, equivalent to the hub height of the turbine at Perdigão. The wall cell is set to 0.06 m and grows from a height of z_0 [7] hyperbolically in the vertical direction until reaching the equispaced fine box mesh at 16.5 m above ground. For both

grids the mesh spacing increases hyperbolically towards the outer domain edges starting from the finely meshed zones. The front, sides and top boundaries of the domain fulfil the Dirichlet and the rear the Neumann condition. The bottom face for uniform inflow is also of a Dirichlet type, whereas it becomes a no-slip boundary with a roughness length of $z_0 = 0.1$ in sheared inflow.

2.4.2. Perdigão The turbine location acts as origin to an O-type mesh with a radius of 17 km. This meshing methodology allows to specify variable wind directions without changing the grid. A finely meshed rectangular box surrounds the actuator disc with $8R$ side length (see figure 4). The inner mesh resolution matches that of the uniform and sheared domains. From the centrally located fine mesh the grid grows hyperbolically outwards, whilst following the terrain surface. The domain height is set to 10 km and discretised with 129 points. The in- and outflow boundaries are applied circumferentially to the O-mesh. The outflow region is defined as the arc resulting from a 90° sector centred about the inflow direction. The velocities at the top and the inlet boundaries of the domain are prescribed, whereas at the outflow the velocity has zero-gradient. The roughness length is deduced from lidar canopy measurements taken at the site. The surface roughness as well as the topography is smoothed towards the edges to arrive at reference far-field quantities.

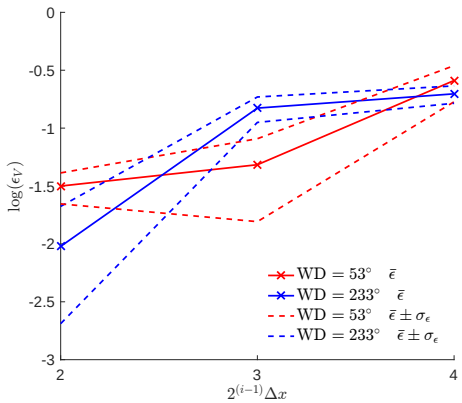

Figure 5. Error evolution in V with grid level relative to the finest mesh with spacing Δx. The error is shown for the two main wind directions and calculated for an area upstream of the rotor.

2.4.3. Mesh sensitivity The mesh spacings defining the grid surrounding the rotor at Perdigão are equivalent to those in the sheared inflow grid. However, the area it covers is larger incorporating a box with $8R$ side lengths. The area of interest studied in this paper extends $5R$ upstream and $1.2R$ radially outwards from the rotor centre. The discritisation error is calculated over this area for each grid level i with spacing $2^{(i-1)}\Delta x$, where Δx represents the highest resolution and V the velocity magnitude:

$$\epsilon_V = |\frac{V_i - V_1}{V_1}| \qquad \text{for } -5 < x/R < 0;\ \{y, z\}/R < |1.2| \tag{2}$$

In complex terrain the error is highly depended on wind direction, due to the differing terrain interacting with the wind field. Therefore the error is shown for both main wind directions, 53°

and 233°, in figure 5. Convergence is achieved for both directions, though for 53° the gain in accuracy from using the finest grid is larger.

3. Results

3.1. The induction zone in uniform and sheared inflow

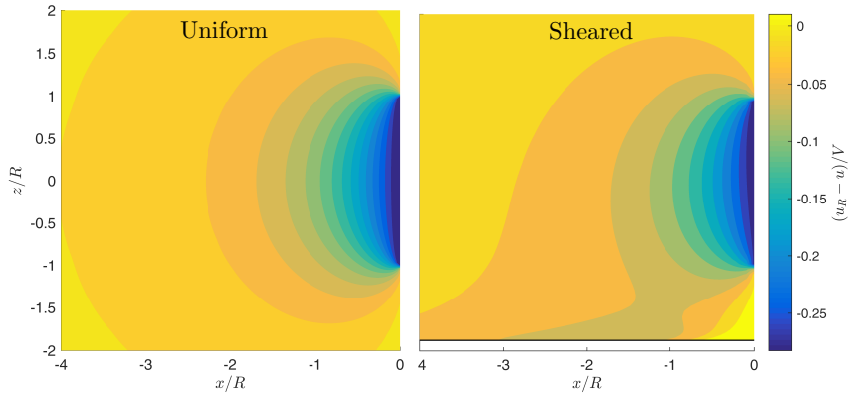

Figure 6. Contours of the normalised difference in the axial velocity component between the undisturbed and rotor simulation for uniform and sheared inflow with $C_T = 0.89$. The ground is marked with a balck line in the sheared contours.

In figure 6 the change in the axial velocity component is shown in the presence of a rotor with $C_T = 0.89$ for uniform and sheared inflow. The change is normalised by the velocity magnitude of the rotor-less flow-field. The rotor is centred at (0,0). The induction zones are very similar, except for the area close to the ground. Here the flow inside the boundary layer experiences additional deceleration upstream and acceleration just below the rotor. This difference originates from the stronger blockage emerging from to the constriction between rotor and ground. The deceleration reduces with C_T, but the overall shape of the induction zone stays unchanged. The other components are small relative to the velocity magnitude ($v \approx 0.01V$) and barely change from uniform to sheared inflow.

3.2. The induction zone in complex inflow

In complex terrain the change in the flow-field caused by the rotor can be much more drastic depending on the effective topography. The latter changes markedly with wind direction as shown in figures 1 and 2. Even small differences in the topography can have a large effect on the induction zone, which is exemplary shown for wind directions 218° and 263° with $C_T = 0.89$. For these directions the terrain gradient is larger leading up to the turbine than towards the other side. In figure 7 each row presents the results for one of these directions. The first two columns show the axial velocity component for undisturbed and rotor influenced flow-fields, respectively. In the final two columns contours of the normalised change in the axial velocity component are presented. Comparing the undisturbed flows, the much larger separation region downstream of the ridge for a wind direction of 218° is noticeable. The separation is marked in light blue. Interestingly the transects for each direction are very similar, though. Once the rotor is introduced into the flow-field the separation bubble is pushed downwards, such that it almost disappears from the area shown for 263°. Furthermore the acceleration at the hill top

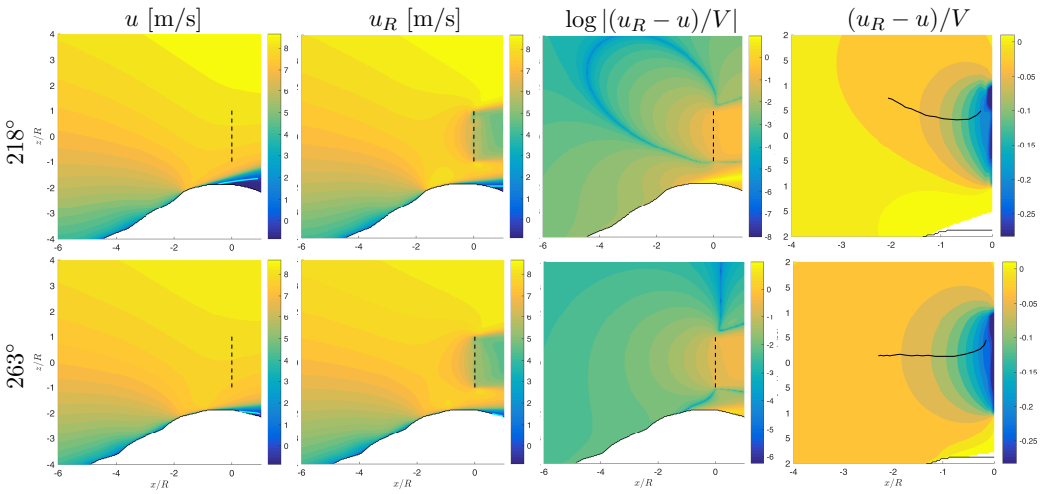

Figure 7. Contours in each row correspond to solutions for the axial velocity component for wind directions 218° and 263°, respectively, and $C_T = 0.89$. From left to right: Undisturbed flow; flow-field with rotor; difference between the former two with log-scale, zoomed difference with black line indicating maximum deficit as function of x.

is strengthened. A more quantitative representation of the change in the flow-field originating from the presence of the rotor is given in the 3^{rd} column of figure 7. It clearly shows that the rotor has an extremely different impact on the flow depending on wind direction and can interact heavily with the ridge flow. This is especially noticeable for 218°. Finally examining an area of equal size to the one shown for uniform and sheared inflows in the last column, not much change in the upstream flow deceleration can be found for 263° compared to the uniform or sheared cases. However, at 218° the induction zone points upwards instead. The direction of the induction zone is shown by the black line, which tracks the maximum deficit upstream of the rotor. To identify the reason for a change in the orientation of the induction zone the maximum deficit has been tracked for all wind directions. In figure 8 the mean induction zone orientation

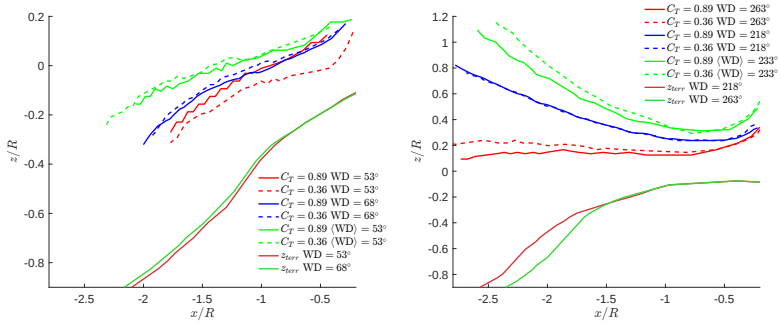

Figure 8. Evolution of maximum deficit in stream-wise velocity component, for $C_T = 0.36, 0.89$ and each sector - left = 53° and right = 233°. The extremes and their corresponding terrain transects are given additionally to the mean for each sector.

as well as its extremes are shown for the sectors centred around 53° and 233°. Furthermore the transect for each extreme is shown as reference. For the sector centred around 53° the tendency is similar across all directions and the induction zone points slightly downwards. For the other sector the location of the maximum deficit covers a greater range over all wind directions. On average the induction zone points upwards, however. Apparently the induction zone does not follow the terrain and its direction is insensitive to changes in thrust. It is in fact the interaction of the rotor wake with the ridge flow that governs the shape of the induction zone. For a wind direction of 218° a large separation bubble forms downstream of the ridge, which pushes the wake upwards which in turn leads to an upwards pointing induction zone. The correspondence of wake and induction zone directions agrees with the results of Brandlard *et al.* [18], who found the same behaviour for yawed rotors. Determining the induction zone in complex terrain is therefore immensely challenging, as it relies on predicting separation in complex topography correctly.

3.3. Change in the induction with non-uniform inflow

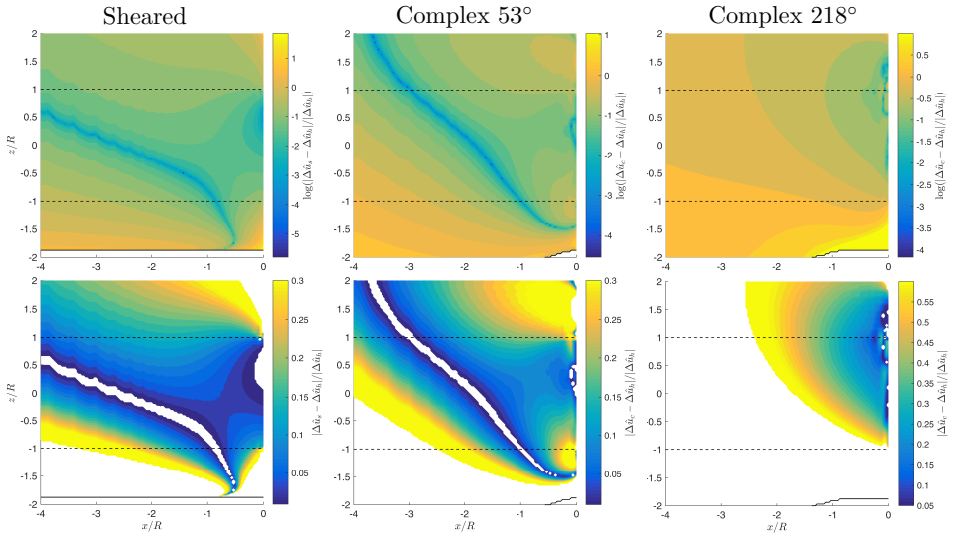

Figure 9. Contours of the normalised absolute difference in the induction zone relative to uniform inflow.

The rotor's influence on the flow-field has been previously isolated by taking the normalised difference between the rotor and undisturbed flow-field ($\Delta\hat{u} = (u_R - u)/V$). The change in the induction zone resulting from non-uniform inflow can subsequently be determined by taking the absolute difference of these quantities $|\Delta\hat{u}_{\{s,c\}} - \Delta\hat{u}_h|$, where s = sheared, c = complex and h = homogeneous/uniform. By dividing the absolute difference by $\Delta\hat{u}_h$ the change from uniform inflow is normalised. Contours of the normalised absolute difference for sheared and different complex inflow scenarios are shown in figure 9. The first row depicts the difference on a log scale. The lower does not, but excludes some data lying far beyond the color range. Unsurprisingly the largest differences are mostly concentrated towards the lower part of the flow-field, close to the ground and towards the rotor edges. In case of sheared inflow the difference to uniform is remarkably low. This would most likely diminish further in-line with the roughness length. The equivalence between the uniform and sheared induction zone has been hinted at by Simley *et al.*

[19]. They measured the flow upstream of a full-scale wind turbine with a triple-lidar system in vertical and horizontal planes. The induction zones of both planes showed great similarity, when normalised by the hub-height wind speed or the shear profile, respectively. In complex inflow the differences are amplified compared to the sheared scenario. Nevertheless for a wind direction of 53° the contours are clearly related to those for sheared inflow. This is not the case for 218°. The large difference to uniform inflow arises from the upwards pointing induction zone, that ultimately stems from the large separation region in the lee of the ridge. Figure 10 shows the dependency of the normalised absolute difference on wind direction. For each complex terrain simulation the mean and extrema of an area bounded by $-2 < x/R < -0.25$ and $-0.85 < z < 0.85$ are determined for $C_T = \{0.36, 0.89\}$. Note that the two wind directions depicted in figure 9 are representative of the extrema in the mean value. Interestingly there is no clear dependency on thrust and despite the shallower terrain upstream of the rotor for the wind sector centred around 53°, their values are on par with those of the other sector.

Ultimately it seems that the induction zone acts as a linear perturbation to the flow-field in sheared inflow, whereas in complex inflow the interaction is highly non-linear.

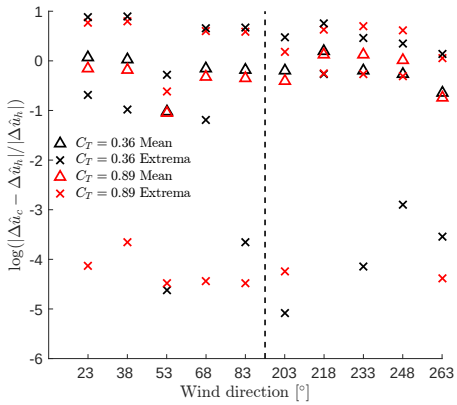

Figure 10. Dependency of the normalised absolute difference on wind direction. For each complex terrain simulation the mean and extrema of an area bounded by $-2 < x/R < -0.25$ and $-0.85 < z < 0.85$ are shown for differing values of C_T.

4. Conclusion

To the author's knowledge this is the first study on the induction zone in complex terrain. By comparing the induction zone between uniform, flat and complex inflow the influence of topography on the induction zone is assessed. There is generally strong agreement between the wind turbine induction zones forming with uniform and sheared inflow, whilst in complex terrain the topographically caused flow features play a crucial role. The speed-up effect in conjunction with separation forming downstream of the ridge can influence the shape of the induction zone. The latter influences the wake trajectory, which ultimately determines the orientation of the induction zone. Neither Coriolis nor stratification different from neutral have been considered in these simulations. Both can have an extensive influence on the wind turbine wake and separation and thus on the induction zone. Nevertheless the results of this study serve as a first indication of the dominating factors governing the rotor induction zone in complex terrain. A future study

should systematically investigate different commonly encountered topographies. Consequently the uncertainty in the induction zone model should be determined as a function of the terrain.

Acknowledgments
This work was performed inside the UniTTe project (unitte.dk), which is financed by The Innovation Fund Denmark, grant number 1305-00024B.

References

[1] Medici D, Ivanell S, Dahlberg J A and Alfredsson P 2011 *Wind Energy* **14** 691–697
[2] Asimakopoulos M, Clive P and abd R Boddington G M 2014 Offshore compression zone measurement and visualisation *Proceedings of the European Wind Energy Assosciation 2014 Annual Event*
[3] Slinger C, Leak M, Pitter M and Harris M 2013 Relative power curve measurements using turbine mounted, continous-wave lidar *Proceedings of the European Wind Energy Assosciation 2013 Annual Event*
[4] *IEC 61400-12-1:2005, Power performance measurements of electricity producing wind turbines.*
[5] van der Laan P, Sørensen N N, Réthoré P E, Mann J, Kelly M C, Troldborg N, Schepers J G and Machefaux E 2014 *Wind Energy*
[6] Tennekes H and Lumley J 1974 *A first course in turbulence* (MIT Press)
[7] Sørensen N 1995 *General purpose flow solver applied to flow over hills* Ph.D. thesis Risø National Laboratory
[8] Michelsen J 1994 Basis3d - a platform for development of multiblock pde solvers Tech. rep. Dept. of Fluid Mechanics, Technical University of Denmark, DTU
[9] Michelsen J 1994 Block structured multigrid solution of 2d and 3d elliptic pdes Tech. rep. Dept. of Fluid Mechanics, Technical University of Denmark, DTU
[10] Leonard B 1979 *Computer Methods in Applied Mechanics and Engineering*
[11] Patanker S and Spalding D 1972 *International Journal of Heat and Mass Transfer*
[12] Réthoré P E and Sørensen N 2012 *Wind Energy*
[13] Troldborg N, Sørensen N, Réthoré P E and van der Laan M 2015 *Computers & Fluids*
[14] Réthoré P E and Sørensen N 2013 *Wind Energy*
[15] Meyer Forsting A R, Troldborg N and Gaunaa M 2016 *Wind Energy* ISSN 1099-1824 we.1991 URL `http://dx.doi.org/10.1002/we.1991`
[16] Meyer Forsting A and Troldborg N 2015 *Journal of Physics: Conference Series (Online)* **625** ISSN 1742-6596
[17] Troldborg N, Zahle F, Réthoré P E and Sørensen N 2013 *Wind Energy* 10.1002/we.1757
[18] Branlard E and Meyer Forsting A 2015 *Using a cylindrical vortex model to assess the induction zone infront of aligned and yawed rotors* (European Wind Energy Association (EWEA))
[19] Simley E, Angelou N, Mikkelsen T, Sjöholm M, Mann J and Pao L Y 2016 *Journal of Renewable and Sustainable Energy* **8**

ARTICLE 4

A FINITE DIFFERENCE APPROACH TO DESPIKING INSTATIONARY VELOCITY DATA - TESTED ON A TRIPLE-LIDAR

CONFERENCE JOURNAL ARTICLE

Journal of Physics: Conference Series 753 (2016) DOI

The Science of Making Torque from Wind (TORQUE), Munich, Germany, October 2016

Main author

Multi-lidar measurements taken in the induction zone of a full-scale turbine were available in 2015 and presented a great opportunity for model validation. Filtering the velocity data without eliminating critical amounts proved extremely difficult for these multi-lidar measurements and resulted in the development of a new despiking algorithm. The measurements were filtered using this algorithm and subsequently allowed validating the CFD model [article 9] presented in section 2.1.

A finite difference approach to despiking in-stationary velocity data - tested on a triple-lidar

A R Meyer Forsting[1], **N Troldborg**[1]

[1] DTU Wind Energy, Department of Wind Energy, Technical University of Denmark, Risø Campus, DK-4000 Roskilde, Denmark

E-mail: alrf@dtu.dk

Abstract. A novel despiking method is presented for in-stationary wind lidar velocity measurements. A finite difference approach yields the upper and lower bounds for a valid velocity reading. The sole input to the algorithm is the velocity series and optionally a far-field reference to the temporal variation in the velocity. The new algorithm is benchmarked against common despiking algorithms using a dataset acquired by three synchronised lidars in the upstream area of a full-scale wind turbine rotor and an artificially created space-time series with controlled spike contamination. By accounting for variations in space and time, this approach yields improvements in spike detection for in-stationary lidar measurements of about 25% over other more established stationary methods. Furthermore it proofs to be robust even for large numbers of spikes.

1. Introduction

Lidars have been developing into important measurement instruments for the wind industry over the last decade, as they have proven to give accurate measurements and are more versatile than any other classic wind measurement system. As their prices are continuing to drop and their accuracy steadily improves, their market penetration can be expected to increase. Nevertheless the measurement principle of laser Doppler anemometry itself poses serious challenges regarding signal processing. Atmospheric conditions, hard targets, electric noise as well as perturbations in the optical system can heavily influence measurement quality. The various post-processing steps lying in-between the raw Doppler spectra and the final radial velocity usually reject spurious data. However, scanning lidars, like the short-range WindScanners [1], continuously change their focus location to measure velocities over an entire two-dimensional plane, thereby increasing the probability of spikes penetrating into the velocity signal. Undetected and processed these spikes can seriously contaminate the velocity signal; in the worst case making it futile. Avoiding any loss of accuracy and data misinterpretation therefore requires a robust despiking algorithm. Detecting and processing spikes is a widely discussed topic, which has not yet been satisfactorily resolved. The existing despiking methods' performance largely depends on the purpose of the processed data. In the related field of acoustic Doppler velocimetry it has been shown that the 3D phase space method, originally proposed by Goring and Nikora [2] and later modified by Wahl [3], is highly efficient [4] for turbulent flow data. Nevertheless the latter method is only valid for stationary measurements, whereas the scanning lidar measurements are moving spatially. Vickers and Mahrt [5] developed methods for detecting in-stationary flux measurement problems. However, their approach does not directly incorporate the influence of the spatial

movement. Therefore in this paper we present a finite-difference based despiking algorithm, that is derived from considering derivatives in both dimensions, space and time. It is tested and benchmarked against other common despiking methods for an extensive dataset acquired by three synchronised lidars in the upstream area of a wind turbine rotor and on an artificially created signal.

2. Finite difference despiking method

The in-stationary measurements represent a discretised form of the function $u(\mathbf{x}, t)$ in space and time. Considering a point x_i in one-dimensional space and t^n in time, the value of the function can be expressed as $u_i^n = u(x_i, t^n)$. Defining $\Delta\bullet$ as the interval of a quantity $\bullet$, the point can be expressed as $x_i = i\Delta x$ and $t^n = n\Delta t$. Each consecutive in-stationary measurement point can be thought of as a step in time and space away from the previous point as shown in Figure 1.

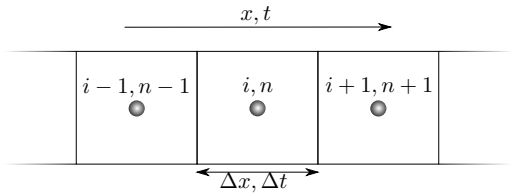

Figure 1. Discrete measurement points of quantity u.

Using Taylor expansion around x_i^n, expressions for u_{i-1}^{n-1} and u_{i+1}^{n+1} can be established, where the partial derivative of $u(x,t)$, $\partial u/\partial\bullet$ is denoted by $u_\bullet$:

$$u(x_i + \Delta x, t^n + \Delta t) = u_{i+1}^{n+1} = u_i^n + \Delta x u_x|_i^n + \Delta t u_t|_i^n + \mathcal{O}(\Delta x^2, \Delta t^2) \quad (1)$$

$$= u_{i+1}^n + \Delta t u_t|_i^n + \mathcal{O}(\Delta x^2, \Delta t^2) \quad (2)$$

$$u(x_i - \Delta x, t^n - \Delta t) = u_{i-1}^{n-1} = u_i^n - \Delta x u_x|_i^n - \Delta t u_t|_i^n + \mathcal{O}(\Delta x^2, \Delta t^2) \quad (3)$$

$$= u_{i-1}^n - \Delta t u_t|_i^n + \mathcal{O}(\Delta x^2, \Delta t^2) \quad (4)$$

The first derivative in space can be estimated by a central difference.

$$u_x|_i^n \approx \frac{u_{i+1}^n - u_{i-1}^n}{2\Delta x} \quad (5)$$

Rearranging equations 2 and 4 and inserting them into the central difference scheme in equation 5 the derivative becomes

$$u_x|_i^n \approx \frac{u_{i+1}^{n+1} - u_{i-1}^{n-1} - 2\Delta t u_t|_i^n}{2\Delta x} \quad (6)$$

The exact time derivative of u at x_i^n is unknown. Instead it can be approximated by measurements of u in homogeneous far-field flow, where u is solely a function of time. Denoting the maximum possible fluctuation in u with time as f and including wind field evolution, the time derivative becomes

$$u_t|_i^n \approx \pm f(t) \quad (7)$$

Note that the fluctuation can either be positive or negative, which stops the u_t terms from cancelling in the following operation. Inserting equation 7 into 6 and 1 or 3, as well as replacing the spatial derivative in the latter, a final approximation of u_i^n can be found

$$u_i^n = \frac{u_{i+1}^{n+1} + u_{i-1}^{n-1}}{2} \pm 2\Delta t f(t) \quad (8)$$

Note that u_i^n in fact becomes a mid-point approximation with an additional term including the fluctuation in u over time. If the measured velocity at x_i^n exceeds the bounds of the estimated value determined by equation 8, then it is marked as spike. There are many options for estimating f. However, for it to capture the temporal fluctuations of the wind field it should be directly linked to the time derivative of the velocity. We propose, based on other common despiking methods, to determine the bounds of an expected fluctuation by the mean of the signal plus α standard deviations. Note that the magnitude of the derivative needs to be taken in this process. Depending on the length of the reference signal, it should be considered to adapt the period length over which these statistics are computed. Hence, in the benchmarking in section 5.2 $f(t)$ becomes

$$f(t) \approx \langle |u_{t,\infty}(t - t_s < t < t + t_s)| \rangle + \alpha \sigma_{|u_{t,\infty}|}(t - t_s < t < t + t_s) \tag{9}$$

Here t_s is the time it takes the measurement instrument to revisit the same point in space, equivalent to 15 s for the triple-lidar and α is a constant. The latter is set to 3.0, such that 99.7% of all data are contained within its range, assuming $u_{t,\infty}$ is normally distributed.

2.1. Replacing the free-stream reference

A free-stream reference might at times not exist, such that a replacement for $u_{t,\infty}$ in equation 9 is needed. In fact it could be replaced by the measured signal itself, such that $u_{t,\infty} = u_t$. However, to avoid spikes from contaminating $f(t)$ the median is used instead, setting $\hat{u}_t = \text{median}(|u_t|)$:

$$f(t) \approx \hat{u}_t(t - t_s < t < t + t_s) + \alpha \sigma_{\hat{u}_t}(t - t_s < t < t + t_s) \tag{10}$$

3. Despiking methods for benchmarking

The method is benchmarked against three other common despiking methods. A simple acceleration thresholding (AT), 3D phase space (PS) [2] method and one using the interquartile range (IQ). The AT method accentuates the high-frequency content of the signal by determining its time derivative $\partial u/\partial t$ and dynamically determines a threshold over which a point is identified as spike. For this particular application certain ratios were tuned manually to ensure only local extrema were removed. Clearly this method relies heavily on careful calibration with respect to the measurement scenario and cannot easily be applied universally. Goring and Nikora [2] tried to reduce the parameters governing despiking methods by combining different approaches. They propose to compute the first and second derivatives of a signal and assume any spikes to lie outside an ellipsoid in phase-space. The ellipsoid's axes itself are determined by multiplying the standard deviations of the signal and its second derivative by the Universal threshold [6]. The simple IQ method defines outliers to fall 1.5 times the inter quartile range above or below the upper and lower quartiles, respectively. Finally the method developed by Vickers and Mahrt [5] (MW) employs moving averages and standard deviations on which it bases its threshold criterion. The threshold is first set to 3.5 standard deviations and then increased by 0.1 until no more spikes are detected. The temporal window over which the statistics are calculated is set to 180s, which was determined to be optimal.

4. Test cases

4.1. Real

Both, real field measurements and an artificially created space-time series are used for testing the different methods. Ten hours of measurements by a triple-lidar system [7, 8], the so called short-range WindScanner [1], in the upstream area of a wind turbine test the robustness of the algorithms. The stall controlled Nordtank NTK 500 wind turbine with a 41 diameter is located at the DTU Risø campus, just off the Roskilde Fjord (N 55° 41' 04", E 012° 05' 48"). A met

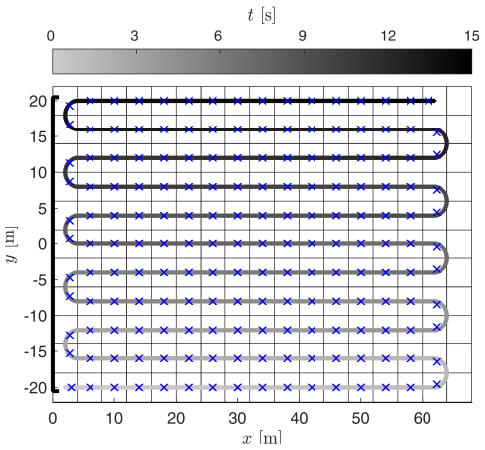

Figure 2. Measurement trajectory performed by a triple-lidar system in a horizontal plane at hub height in the upstream area of a wind turbine. The rotor centre is located at (0,0) and the cell-averaged data points are shown as x.

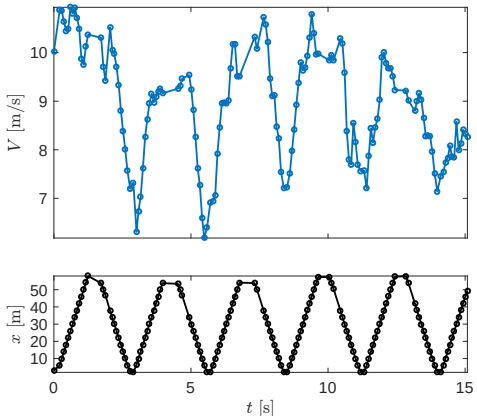

Figure 3. Resulting space-time series from triple-lidar measurements following the trajectory in figure 2.

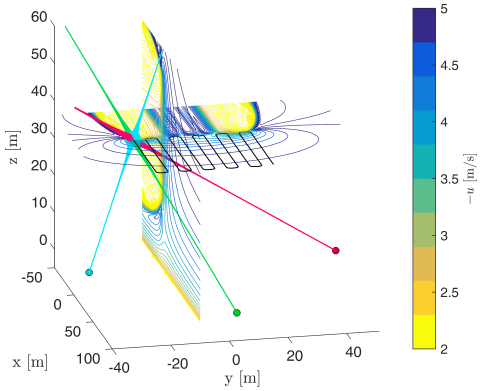

Figure 4. CFD-RANS simultation of the flow upstream of the turbine with $V_\infty = 5$ m/s sampled using a numerical triple-lidar. The lidar beams' thickness indicates the weighting of the velocities.

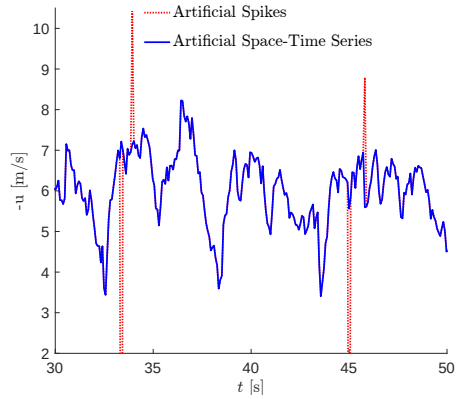

Figure 5. Computationally created triple-lidar space-time series.

mast equipped with sonics, cups and vanes at several heights was located 92 m upstream of the turbine along the prevailing wind direction of 283°. The three lidars' focal points followed the trajectory shown in figure 2 simultaneously, such that they completed one horizontal scan at hub height (34 m) in 15 s. The continuous measurements are averaged over each grid cell shown in figure 2 to reduce the noise in the Doppler spectra. The noise filtering method by Angelou *et al.* [9] is subsequently applied to the spectra, determining the line-of-sight velocities. The three

lidar velocity signals allow to compute the velocity vectors in each cell. A similar campaign with a triple-lidar was performed by Simley *et al.* [10] giving a more complete description of the experimental method. In figure 3 an example of the resulting space-time series is shown. The data points closer to the rotor are affected by the rotor induction or blockage, explaining their lower velocities. The resulting troughs in the velocity are easily mistaken as spikes and thus provide a challenging test case, especially on days with large turbulence intensity. An overview of the dataset is given in the first six columns of table 1. It covers average wind speeds from $2.88 - 9.85$ m/s and turbulence intensities from $9.31 - 18.2\%$.

Table 1. The first seven columns summarise the triple-lidar measurement periods compromising a total of 10 hours of data. The last four show the percentage of each dataset rejected by the respective despiking method. The meteorological conditions are given by: mean wind speed, turbulence intensity and wind direction. The length of its dataset is given in both, minutes and datapoints.

#	Date [d/m]	$\bar{V}_\infty$ [m/s]	TI [%]	WD [°]	T [min]	Length [$\times 10^3$]	AT [%]	PS [%]	IQ [%]	FD [%]
1	06/08	3.89	18.2	297	28.5	21.3	0.77	3.42	2.02	1.32
2	20/08	9.85	15.9	260	22.7	17.0	0.51	1.60	0.96	0.26
3	21/08	7.31	14.1	247	27.7	20.7	0.79	4.59	0.77	0.44
4	25/08	6.06	13.6	249	26.2	19.6	1.00	3.45	0.62	0.50
5	27/08	5.54	14.4	285	23.1	17.3	1.25	2.37	0.31	0.91
6	25/09	9.64	12.6	271	28.3	21.2	0.17	1.38	0.48	0.22
7	27/09	8.07	14.9	275	86.6	63.8	0.29	1.13	0.05	0.29
8	02/10	6.04	15.3	274	27.4	20.5	0.82	8.97	2.14	3.20
9	29/10	2.88	9.31	270	198	148	8.88	0.00	13.1	2.00
10	30/10	3.10	9.34	274	168	126	3.63	0.00	2.64	6.86

4.2. Artificial

An artificially created space-time series can be contaminated with spikes at will, thus creating a controlled benchmarking environment, where the true solution is known. For this purpose numerical flow-fields are computed using Computational Fluid Dynamics (CFD). The computational method is described in detail in previous publications of the authors [11–13]. Steady-state simulations are performed for free-stream wind speeds between $5 - 12$ m/s. Their solutions are subsequently sampled by a numerical triple-lidar, including the effect of volume averaging. This achieved by sampling the CFD flow-field along the entire length of the lidar beam and weighting the velocities according to a function. For the triple-lidar system it is equivalent to the one given by Simley *et al.* [10]. Note that the beam is assumed to have zero thickness. The numerical triple-lidar follows the experimental trajectory as shown in figure 4. As in the experiments all velocities falling into one cell (figure 2) are first averaged for each lidar and only afterwards combined to give the velocity vector. Finally for each free-stream velocity a numerically determined velocity vector is given for each cell. During the field experiment described in the previous section measurements from the met mast served as free-stream reference. To create the artificial space-time series the free-stream velocity data is taken from the #3 dataset, which is 28 minutes long. Interpolating for each measured free-stream velocity between the CFD solutions, taking into account the spatial variation of the triple-lidar measurements in time, the artificial space-time series with 22440 data points is created. An extract of which is presented in figure 5.

The spikes are injected into the artificial series by randomly selecting points, which are subsequently multiplied by certain factors. These are determined by a normal distribution centred around $3.5 \cdot \sigma_u/\bar{u}$ with a standard deviation of $\sigma_u/\bar{u}$. Here u denotes the space-time series of the artificially created axial velocity component, $\bar{u}$ its mean. To identify the sensitivity of each despiking method, the sign of the factors are either all positive, negative or randomly mixed. To create statistically viable results, 100 spiked time series are created on which the despiking methods are tested.

5. Results

5.1. Real space-time series

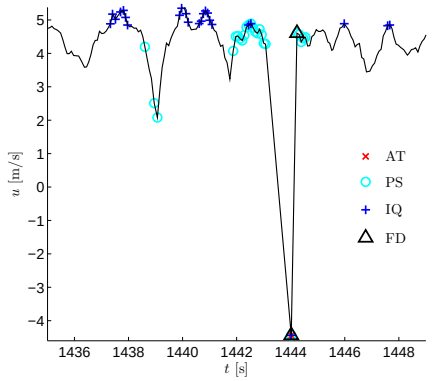

Figure 6. Extract from dataset #5 streamwise velocity time series and spikes detected by: AT (x) = Acceleration Thresholding, PS (o) = 3D Phase Space, IQ (+) = Inter Quartile Range, FD (△) = Finite Difference algorithm.

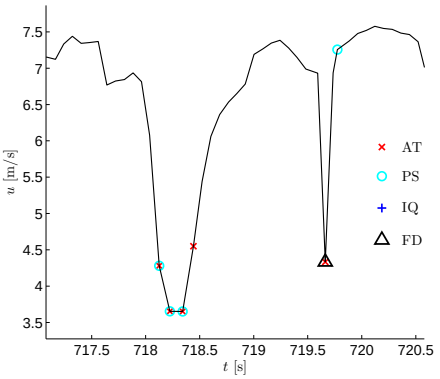

Figure 7. Extract from dataset #8 streamwise velocity time series and spikes detected by each despiking method.

Demonstrations of the spikes detected by selected methods are shown in figures 6 and 7. They highlight the advantage of using the finite difference based algorithm for detecting spikes over the existing methods. All algorithms detect the obvious spike in figure 6 at $t = 1444$ s, but both the IQ and the PS methods remove a vast amount of valid data. In figure 7 these methods miss the spike at $t = 719.7$ s completely. Furthermore this figure enforces the difficulty for the algorithms to solely identify spikes, as both AT and PS remove valid readings. The last four columns of table 1 list the percentage of each dataset identified as spikes by the different methods. Clearly all four methods reject quite different amounts. Nevertheless except for a few datasets AT, FD and IQ seem to agree well, whereas PS rejects more points. It fails for the last two sets, but this might be related to the sheer length of the dataset over which some large-scale effects might have occurred. It should also be noted that the turbine was barely running during those days, as the wind speeds were on average below cut-in.

5.2. Artificial space-time series

In this section all despiking tools presented throughout the paper are compared by testing them on the 100 spiked time series. This includes two finite-difference methods with differing formulations of f, following equations 9 and 10. The one without a free-stream reference is

denoted "FD w/o ref". Firstly the four despiking methods are tested on the uncontaminated artificial 2-D series. Remarkably the new FD methods correctly identified none of the points as spikes. For the AT, PS, IQ and MW the points marked as spikes as percentage of the total are 0.70%, 0.79%, 0.23% and 0.46%, respectively. This is result can be deemed acceptable, especially with a turbulence intensity of 14.1 % that day.

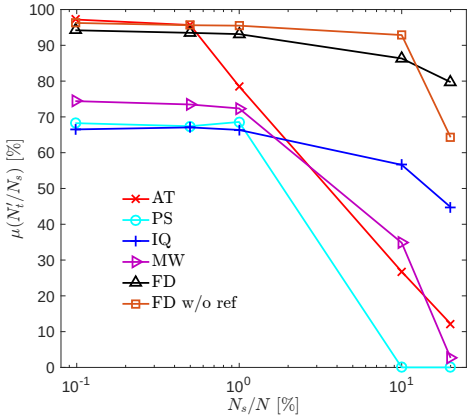

Figure 8. Mean detection rate of true spikes.

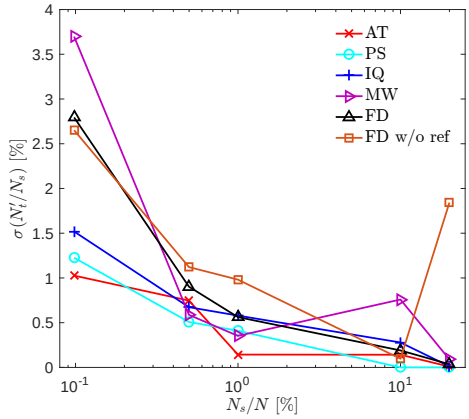

Figure 9. Standard deviation of true spikes detected.

The behaviour of the tools is tested for different spike contamination rates. The latter is defined as the ratio between the number of artificial spikes injected over the total number of data points N_s/N. The ratios were $0.1, 0.5, 1, 10, 20\%$. In figure 8 the percentage of the injected spikes detected N_t'/N_s by each method is shown as a function of the contamination rate. Note that the sign of the spike factor is random. The quantities $N'_{\{t,f\}}$ denote the number of true and false spikes marked by each method, respectively. The spike detection universally reduces with spike contamination. However, whereas the IQ and FD algorithms perform stably, all other despikers' performances deteriorate past a low contamination of 1%. Whilst the detection rate of AT tumbles towards zero, the PS algorithm fails to identify any true spikes any longer. The best performance for this measure has the FD method with free-stream reference, identifying on average 89% across all rates. However, the other FD method without a free-stream reference is actually outperforming it until the contamination rate passes 10%. That all methods except FD exhibit large performance drops above a certain contamination rate is related to the high-frequency content increasing with contamination. This ultimately obscures the existence of spikes, as the standard deviation and median of the signal is giving larger spike thresholds. FD on the other hand only relies on the free-stream standard variation and thus is not affected. Figure 9 presents the standard deviation of the true spikes found across all spiked series. It decreases rapidly with increasing contamination rate, except for FD w/o ref for the largest number of spikes. The larger standard deviation at low contamination rates is related to the sensitivity of the despiking tools to the position of the spikes. With fewer spikes this is more visible.

Another measure of performance is the ratio between the true spikes found and the total amount of points marked as spikes $N_t'/(N_t' + N_f')$. This essentially measures whether the algorithm is rejecting the right data. The results are plotted in figure 10. Here the FD methods are the only ones showing constant performance, however they are much worse than the other

methods, except PS. However, the results can easily misinterpreted, as in fact AT, MW and IQ are almost not flagging any points as spike any longer beyond a contamination of 1%. The reason for the FD methods performing worse lies in the mid-point approximation that involves the neighbouring cells. Is a spike a neighbour, a valid point might be identified as spike. This is the case in figure 6. As before the standard deviation decreases with contamination as shown in figure 11. This occurs for similar reasons mentioned before.

Lastly, to test the sensitivity of the algorithms with respect to the sign of the spikes, solutions were obtained for solely positive and negative spike factors. Unsurprisingly all methods are showing some sensitivity, as negative spikes are harder to identify in-between the troughs in the velocity series, caused by the rotor induction. Similarly, it is challenging to identify spikes inside the trough itself. Nevertheless the FD methods perform well with the mean detection rate changing by maximally 2.1% (w/o ref) and 8.4%. AT follows with 11% and MW performs worst with 30%. The other methods fall in-between.

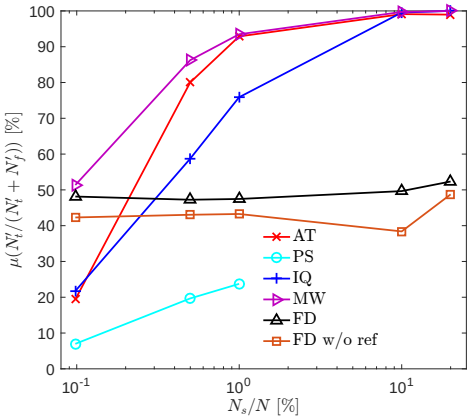

Figure 10. Mean of the ratio between true spikes and total points marked as spikes.

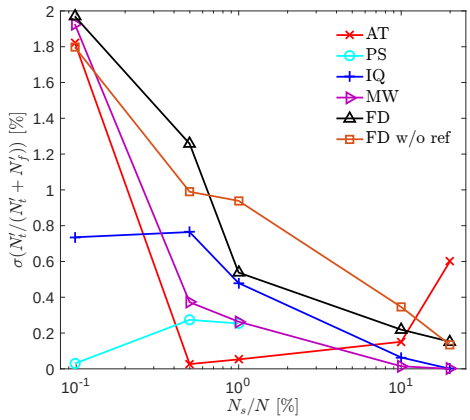

Figure 11. Standard deviation of the ratio between true spikes and total points marked as spikes.

6. Conclusion

The novel finite difference based despiking algorithm accounts for the in-stationary nature of scanning lidar velocity measurements. This allows it to outperform other methods, which have established themselves for despiking stationary velocity time series. Its mean detection rate lies above 70% for spike contamination rates between $0.1-20\%$ and reaches up to 100%. Furthermore its performance is constantly high, whereas all other tested methods fail past a contamination of 1%. It does remove more data then necessary, however. An interesting and simple alternative for despiking in-stationary data seems to be the inter quartile range. It has not performed as well as the new algorithm, but still found about 60% of all spikes. Especially without any information on the free-stream velocity fluctuation, needed in the proposed method, the inter quartile range could be advantageous. In the future it would be interesting to apply the new algorithm to more datasets, thus testing its robustness.

Acknowledgments
This work forms part of UniTTe (www.unitte.dk), financed by The Innovation Fund Denmark (1305-00024B). Special thanks to Nikolas Angelou and Andrea Vignaroli from DTU Wind Energy for providing the lidar datasets and Michael Harris from ZephIR Lidar for the valuable input on commercial approaches to lidar signal processing.

References

[1] Mikkelsen T K 2015 Windscanner.dk, a new danish remote sensing-based infrastructure for wind energy nd turbulence research: Design, establishment and operation 2009-2014 Tech. rep. DTU Wind Energy, Technical University of Denmark
[2] Goring D G and Nikora V I 2002 *Journal of Hydraulic Engineering* **128** 117–126
[3] Wahl T L 2007 *Journal of Hydraulic Engineering*
[4] Mori N, Suzuki T and Kakuno S 2007 *Journal of Engineering Mechanics*
[5] Vickers D and Mahrt L 1997 *J. of Atmos. Oceanic Tech.* **14** 512–526
[6] Donoho D L and Johnstone I M 1994 *J. Atmos. Sci.* **155** 377–389
[7] Angelou N and Sjöholm M 2015 *UniTTe WP3/MC1: Measuring the inflow towards a Nordtank 500kW turbine using three short-range WindScanners and one SpinnerLidar* DTU Wind Energy E (DTU Wind Energy)
[8] Vignaroli A 2015 *UniTTe- Nordtank Measurement Campaign (Turbine and Met Masts)* DTU Wind Energy E (DTU Wind Energy)
[9] Angelou N, Abari F F, Mann J, Mikkelsen T and Sjöholm M 2012 Challenges in noise removal from doppler spectra acquiered by continous-wave lidar *Proceedings of the 26th International Laser Radar Conference*
[10] Simley E, Angelou N, Mikkelsen T, Sjöholm M, Mann J and Pao L Y 2016 *Journal of Renewable and Sustainable Energy* **8**
[11] Meyer Forsting A R, Troldborg N and Gaunaa M 2016 *Wind Energy* ISSN 1099-1824 we.1991 URL `http://dx.doi.org/10.1002/we.1991`
[12] Meyer Forsting A and Troldborg N 2015 *Journal of Physics: Conference Series (Online)* **625** ISSN 1742-6596
[13] Troldborg N, Zahle F, Réthoré P E and Sørensen N 2013 *Wind Energy* 10.1002/we.1757

ARTICLE 5

DYNAMICS OF THE INTERACTION BETWEEN THE ROTOR AND THE INDUCTION ZONE

CONFERENCE JOURNAL ARTICLE

Journal of Physics: Conference Series 753 (2016) DOI

The Science of Making Torque from Wind (TORQUE), Munich, Germany, October 2016

Co-author

The work of this publication was initiated by Mahmood Mirzaei from DTU Wind Energy. A multitude of CFD simulations were performed for his analysis and necessitated some changes in the AD model of EllipSys3D.

Dynamics of the interaction between the rotor and the induction zone

Mahmood Mirzaei, Alexander R. Meyer Forsting and Niels Troldborg
DTU Wind Energy, Technical University of Denmark, Frederiksborgvej 399, 4000 Roskilde, Denmark

E-mail: {mmir, alrf, niet}@dtu.dk

Abstract. Traditionally met masts are used for power and load verifications. They are normally placed 2-4 rotor diameters ahead of the turbine. However in complex terrain this can lead to complex analysis of the effect of the terrain on the flow field. A nacelle mounted lidar can provide a better tool for wind field measurements in all terrains. Provided that the measurement is close enough to the rotor disc, the uncertainty in the flow field measurement can be reduced significantly. Therefore any complex terrain calibration and changes in the wind direction can be avoided. However, close distance lidar measurements are affected by the presence of the wind turbine, due to its induction zone. In this work, the dynamic coupling between changes in the wind turbine operating point and the velocities inside the induction zone is studied. Reynolds-Averaged Navier-Stokes (RANS) simulations are used to investigate this interaction. Thereafter, system identification is used to fit first order dynamic models to the simulation results. The parameters of the model are given for the turbine induction zone. These results possibly reduce the uncertainty in lidar measurements, arising from wind turbine blockage.

1. Introduction

Lidar sensors prove to be very helpful in the wind energy industry for different reasons. They can be used for yaw corrections [3], pitch control [12] and power and loads verifications [2]. Nevertheless, there are different issues with lidar measurements. One of the issues is the difficulty of wind speed measurements very close to the rotor disc (e.g. less than one rotor diameter). Close range measurements are being used in order to minimize the uncertainty due to the terrain etc. on the wind field measurements. In this case the effect of the induction zone of the rotor is prominent in the measurements. In [14] the authors have used SOWFA [1] for Large Eddy Simulations (LES) of a wind turbine model in a wind field in order to investigate the effect of the induction zone on lidar measurements. The authors have compared the simulation measurements in terms of mean wind velocity and turbulence intensity in the steady state conditions. Another investigation of the induction zone effect is presented in [13] where the wind field in the induction zone of a Vestas V27 is investigated.

In this work we address the problem with close range measurements where the lidar measurements are close enough to be affected by the induction of the rotor. Specifically, we will investigate the dynamic effect of the induction zone on the lidar measurements. We will show that changes in the operating point of the turbine affects the wind speed in the induction zone. Moreover, we will find the appropriate dynamic model that represents this behavior. The

results of this work can be used to reduce the uncertainty in the wind speed measurements close to the rotor disc.

2. Simulation setup

2.1. Numerical setup

The simulations are performed solving the incompressible transient Reynolds Averaged Navier-Stokes (RANS) equations with uniform non-turbulent inflow, at a Reynolds number of 1.0×10^8 with respect to the rotor radius (R). The finite volume code EllipSys3D solves the RANS equations over a discretized block-structured domain [15, 8, 9] with collocated variables. Solving convective terms using the QUICK scheme [4] and the SIMPLE method [10] for the pressure-linked terms of the Navier-Stokes equations. A modified Rhie-Chow algorithm [11, 16] avoids decoupling velocity and pressure in the presence of discrete body forces originating from an actuator disc (AD). The effect of turbulence on the mean flow is accounted for using Menters k–ω shear-stress transport turbulence model [6]. The turbine rotor is represented by an actuator disc. The loading on the rotor is uniform and only acting normal to the disc. The simulations are converged at an initial thrust coefficient C_{T_i} before at a specific point in time t_0 a change ΔC_T is initiated. The C_T of the rotor at a time t is given by:

$$C_T(t) = \begin{cases} C_{T_i} & \text{for} \quad t \leq t_0 \\ C_{T_i} + \Delta C_T \left(1 - e^{-\frac{t-t_0}{\tau}}\right) & \text{for} \quad t > t_0 \end{cases} \tag{1}$$

where τ determines the speed with which the change is applied. The time step Δt had its upper limit at 0.04 set by the CFL number. Furthermore the ratio of the maximal gradient of $C_T(t)$ to Δt was kept constant in-between the simulations:

$$\frac{\max\left(dC_T/dt\right)}{\Delta t} = \frac{\Delta C_T/\tau}{\Delta t} = \text{constant} \tag{2}$$

2.2. Turbine model

The turbine rotor was represented by an actuator disc. The loading on the rotor was uniform and only acting normal to the disc. The normal force thus acting over a sectional area ΔA of the actuator disc is:

$$F_N = \frac{1}{2}\rho_\infty V_\infty^2 C_T \Delta A \tag{3}$$

Only the thrust coefficient C_T was changed between simulations. Note that approximating the influence of a rotor with only normal forces corresponds to the ideal case where the tip speed ratio tends to infinity.

2.3. Numerical domain

A box domain with side lengths of 25 radii (R) minimises the impact of domain blockage ($\pi/25^2 = 0.5\%$). It contains a finely meshed box that surrounds the actuator disc located at its center as shown in figure 1. The rotor radius is discretized with 33 grid points giving an inner mesh spacing, which previously yielded sufficiently accurate results [7]. From the fine mesh the grid grows hyperbolically outwards. The frontal and side faces of the domain are set as Dirichlet boundaries, whereas and Neumann boundary condition is applied to the rear.

3. Modeling of the Dynamics

In this work, the dynamic effect of the rotor on the upstream induced velocities is modelled via a transfer function. The transfer function describes how the induced velocity respond to a step change in the rotor loading. The transfer function was found to be well represented by the

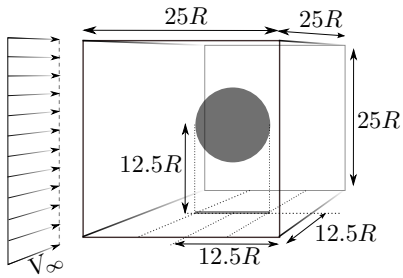

Figure 1: The numerical domain containing the actuator disc with uniform inflow. All dimensions are given in turbine radii.

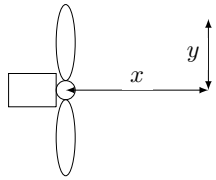

Figure 2: Probe points relative to the wind turbine, the wind turbine is seen from the top

following first order model:

$$H(s) = \frac{k(x,y)}{T(x,y)s+1} \tag{4}$$

The two parameters to be identified are the gain of the system $k(x,y)$ and the time constant $T(x,y)$. These parameters are functions of space with the spatial coordinates x and y defined as shown in Figure 2. In order to illustrate the effect a change in the gain and time constant have on the transfer function, Figure 3 compares the response of the function with the following parameters:

$$H_1(s) = \frac{-0.1347}{1.4610s+1} \tag{5}$$

$$H_2(s) = \frac{-0.0796}{1.4610s+1} \tag{6}$$

$$H_3(s) = \frac{-0.1347}{1.8957s+1} \tag{7}$$

H_1 and H_2 have the same time constant, but different gains. As it is seen in figure 3 they converge towards their respective steady state values with the same rate. However, the steady state values are different due to the different gains. H_1 and H_3 on the other hand converge to the same steady state value with different rates. This is because they have the same gain, but different time constants.

4. Results

System identification [5] is used to find an appropriate model that fits the dynamic changes in the wind speed at the probe point (x,y), as the thrust coefficient changes. Figure 4 includes a sample response used for the system identification and the output of the identified model. This figure shows the changes in the wind speed at $(x,y) = (0.5R, 0)$ as a response to changes in the C_T for $\Delta C_T = 0.8$. The changes are shown as $\Delta V(t) = V(t) - V_0$, in which $V(t)$ is the

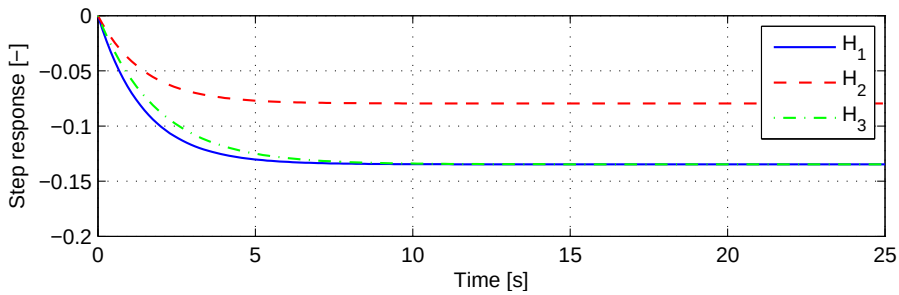

Figure 3: Step response comparison of three systems with different gains and time constant

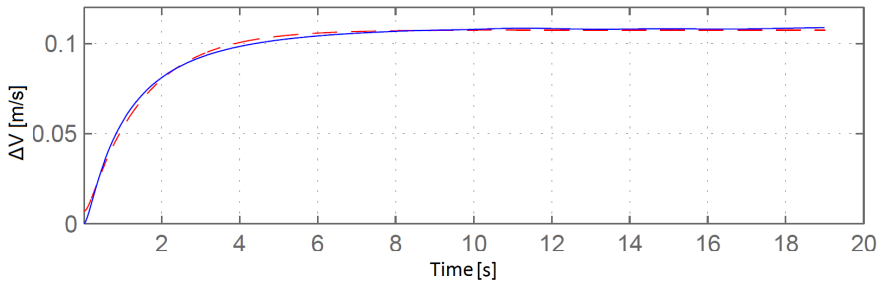

Figure 4: Changes in the wind speed as a result of changes in the C_T value in time, solid-blue is the predictions from CFD and red-dashed is the identified system

wind speed as a function of time and V_0 is the initial wind speed. System identification [5] is used to find an appropriate model that fits the dynamic changes in the wind speed at the probe point (x, y), as the thrust coefficient changes. Figure 4 includes a sample response used for the system identification and the output of the identified model. This figure shows the changes in the wind speed at $(x, y) = (0.5R, 0)$ as a response to changes in the C_T for $\Delta C_T = 0.8$. The changes are shown as $\Delta V(t) = V(t) - V_0$, in which $V(t)$ shows the wind speed in time and $V(0)$ is the wind speed at initial time. The same identification procedure is used for the parameters of the transfer functions for the whole grid of $x-y$. The contour curve of the two parameters are given in figures 5 and 6. Figure 5 shows as x increases the amplitude of the gain of the transfer function decreases. This is natural, as when the probe point moves away from the rotor disc, the effect of the induction zone is reduced. Figure 6 shows that the dynamics, modeling changes in the CT, become slower as x increases. The figure shows that close to the turbine fast changes in the C_T have a prominent effect on the wind speed. As the measurement point moves away from the turbine, the fast changes are filtered and only slow changes in the C_T value can be observed.

5. Conclusions

In this paper the dynamic effect of changes in the operating point of the wind turbine on the wind speed measurements using lidars is investigated. It is observed that changes in the turbine operating point affect the upstream wind speed, and that the effect occurs dynamically. First order systems are used to capture this interaction. For each probe point or lidar measurement point upstream the wind turbine a model of the dynamic effect is identified and parameters of

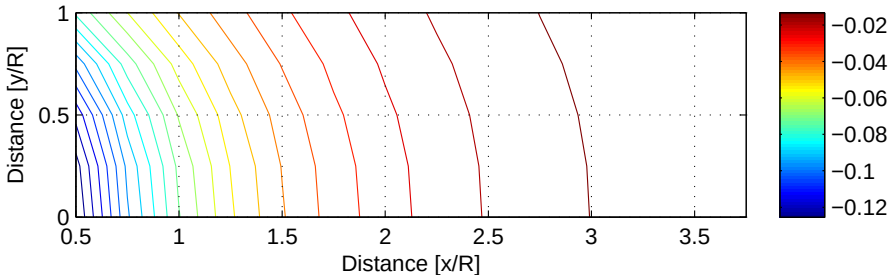

Figure 5: Gain of the transfer function $k(x, y)$

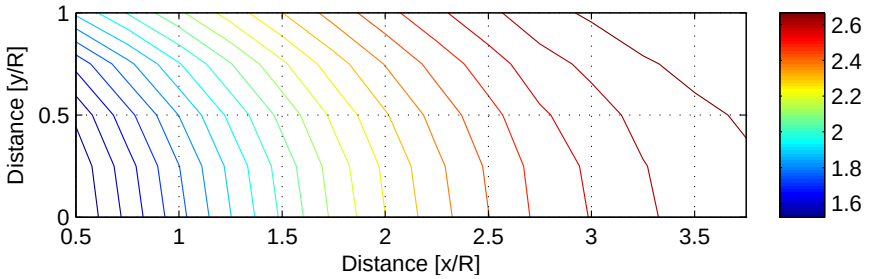

Figure 6: Time constant of the transfer function $T(x, y)$

the model determined. The results can be used to correct for the dynamic effect of the induction zone on the wind speed measurements. Furthermore, it allows to improve the estimation of the free stream wind speed by lidar measurements close to the rotor disc.

References

[1] M. Churchfield and S. Lee. NWTC information portal (SOWFA), 2012.
[2] N. K. Dimitrov and B. S. Lazarov. Reducing wind turbine load simulation uncertainties by means of a constrained gaussian turbulence field. *Proceedings of the 12th International Conference on Applications of Statistics and Probability in Civil Engineering (ICASP12)*, pages –, 2015.
[3] P. A. Fleming, A. K. Scholbrock, A. Jehu, S. Davoust, E. Osler, A. D. Wright, and A. Clifton. Field-test results using a nacelle-mounted lidar for improving wind turbine power capture by reducing yaw misalignment. *Journal of Physics. Conference Series*, 524(1), 2014.
[4] B. Leonard. A stable and accurate convective modelling procedure based on quadratic upstream interpolation. *Computer Methods in Applied Mechanics and Engineering*, 1979.
[5] L. Ljung. *System identification / Theory for the user.* Prentice Hall, Upper Saddle River, N.J., 1999.
[6] F. R. Menter. Zonal two equation $k - \omega$ turbulence models for aerodynamic flows. *AIAA Journal*, 1993.
[7] A. Meyer Forsting and N. Troldborg. The effect of blockage on power production for laterally aligned wind turbines. *Journal of Physics: Conference Series (Online)*, 625, 2015.
[8] J. Michelsen. Basis3D - a platform for development of multiblock PDE solvers. Technical report, Dept. of Fluid Mechanics, Technical University of Denmark, DTU, 1994.
[9] J. Michelsen. Block structured multigrid solution of 2D and 3D elliptic PDE's. Technical report, Dept. of Fluid Mechanics, Technical University of Denmark, DTU, 1994.
[10] S. Patanker and D. Spalding. A calculation procedure for heat, mass and momentum transfer in three-dimensional parabolic flows. *International Journal of Heat and Mass Transfer*, 1972.
[11] P.-E. Réthoré and N. Sørensen. A discrete force allocation algorithm for modelling wind turbines in computational fluid dynamics. *Wind Energy*, 2012.
[12] D. Schlipf and M. Kühn. Prospects of a collective pitch control by means of predictive disturbance

compensation assisted by wind speed measurements. In *Proceedings of the German Wind Energy Conference, DEWEK*, 2008.

[13] E. Simley, N. Angelou, T. K. Mikkelsen, M. Sjöholm, J. Mann, and L. Y. Pao. Characterization of wind velocities in the upstream induction zone of a wind turbine using scanning continuous-wave lidars. *Journal of Renewable and Sustainable Energy, J Renew Sustain Ener, J. Renew. Sustain. Energy*, 8(1), 2016.

[14] E. Simley, L. Y. Pao, P. Gebraad, and M. Churchfield. Investigation of the impact of the upstream induction zone on lidar measurement accuracy for wind turbine control applications using large-eddy simulation. *Journal of Physics. Conference Series*, 524(1), 2014.

[15] N. Sørensen. *General purpose flow solver applied to flow over hills*. PhD thesis, Risø National Laboratory, 1995.

[16] N. Troldborg, N. Sørensen, P.-E. Réthoré, and M. van der Laan. A consistent method for finite volume discretization of body forces on collocated grids applied to flow through an actuator disk. *Computers & Fluids*, 2015.

ARTICLE 6

MODELLING LIDAR VOLUME-AVERAGING AND ITS SIGNIFICANCE TO WIND TURBINE WAKE MEASUREMENTS

CONFERENCE JOURNAL ARTICLE

Journal of Physics: Conference Series 854 (2017) DOI

Wake Conference, Visby, Sweden, May 2017

Main author

The effect of lidar volume-averaging is often ignored when comparing lidar measurements and computational results. In the validation of the CFD model [article 9] it is included by sampling the computed flow-field with a numerical lidar. This paper details the numerical implementation in EllipSys3D and studies its effect with respect to wake measurements.

IOP Conf. Series: Journal of Physics: Conf. Series **854** (2017) 012014 doi:10.1088/1742-6596/854/1/012014

Modelling lidar volume-averaging and its significance to wind turbine wake measurements

A R Meyer Forsting[1], N Troldborg[1], A Borraccino[1]

[1] DTU Wind Energy, Technical University of Denmark, Risø Campus, DK-4000 Roskilde, Denmark

E-mail: alrf@dtu.dk

Abstract. Lidar velocity measurements need to be interpreted differently than conventional in-situ readings. A commonly ignored factor is "volume-averaging", which refers to lidars not sampling in a single, distinct point but along its entire beam length. However, especially in regions with large velocity gradients, like the rotor wake, can it be detrimental. Hence, an efficient algorithm mimicking lidar flow sampling is presented, which considers both pulsed and continous-wave lidar weighting functions. The flow-field around a 2.3 MW turbine is simulated using Detached Eddy Simulation in combination with an actuator line to test the algorithm and investigate the potential impact of volume-averaging. Even with very few points discretising the lidar beam is volume-averaging captured accurately. The difference in a lidar compared to a point measurement is greatest at the wake edges and increases from 30% one rotor diameter (D) downstream of the rotor to 60% at $3D$.

1. Introduction

Lidars rely on the reflection of emitted light from aerosols back to the receiver to measure wind speed. To determine the velocity at the desired measurement location, the beam can be focused (continous-wave) or the backscattered signal split by the time of flight (pulsed). In both cases there are reflections from aerosols away from the desired probe location. Lidars therefore sample the flow velocity all along their beams, albeit with a spatial filter. This is also commonly referred to as "volume-averaging" or "range-weighting". Schematically this is shown in Figure 1 with the weighting function $W(r)$ acting in the local beam coordinate system with $r = |\mathbf{x} - \mathbf{x}_L|$ and peaking at the probe location F. The measured line-of-sight velocity v_{los} at a point in space $\mathbf{x}_F$ is thus given by the convolution of the radial velocities sampled along the beam and the weighting function

$$v_{los}(\mathbf{x}_F) = -\int_0^\infty \mathbf{e}(\mathbf{x}_F, \mathbf{x}_L) \cdot \mathbf{V}(r) W(r)\, \mathrm{d}r \tag{1}$$

Here $\mathbf{e}(\mathbf{x}_F, \mathbf{x}_L)$ represents the beam direction unit vector. The difference between the point and lidar measurement, $\Delta v_r = v_{los} - (-\mathbf{e}(\mathbf{x}_F, \mathbf{x}_L) \cdot \mathbf{V}(\mathbf{x}_F))$, therefore depends on the combination of flow-field and weighting function. This implies that large flow gradients and/or broad weighting functions can lead to significant Δv_r. In wind energy and the atmospheric sciences lidars are becoming ever more popular, especially in model validation, but usually their data are still treated as conventional point measurements. However, with the currently available lidar technology the effect of volume-averaging can be non-negligible, especially in areas of large

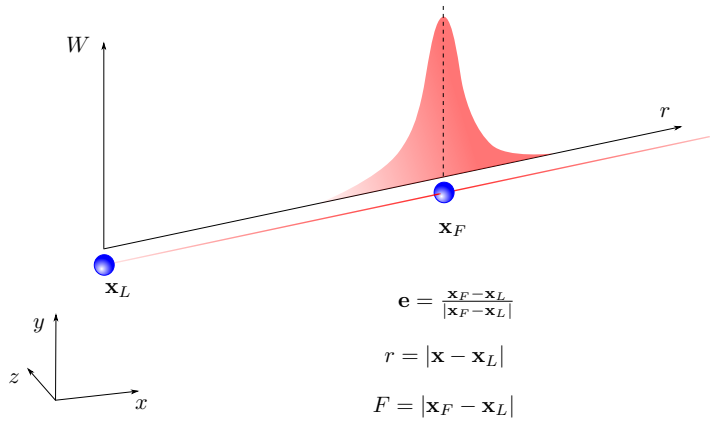

Figure 1. Lidar range weighting of the sampled velocities along the beam. The beam originates from $\mathbf{x}_L$ to measure at $\mathbf{x}_F$. The weighting function acts in the local beam coordinate system.

velocity gradients like the wind turbine wake. Furthermore, continous-wave (CW) and pulsed lidars possess very distinct weighting functions. The large domains of numerically generated flow-fields readily provide $\mathbf{V}(r)$, so only the weighting function remains to be implemented to arrive at a numerical estimate of $v_{los}(\mathbf{x}_F)$. These in turn are valuable to experimentalists using lidars, as they give insight into the magnitude of Δv_r given some measurement setup. This allows optimising the setup and estimating uncertainties, as done by Churchfield *et al.* [1] for a wake experiment with a CW lidar. Simley *et al.* [2] implemented a numerical version of the latter to study the errors from lidar measurements and their implications for feed-forward turbine control. Similarly, Mirocha *et al.* [3] used a virtual pulsed lidar to compare measurements and simulations. Despite presenting the respective weighting functions, there are no details given regarding the actual beam discretisation.

The aim of this paper is to increase the awareness of volume-averaging in lidar measurements, with a focus on wake measurements, and providing a guide for implementing numerical lidars in post-processing. For this purpose computational fluid dynamics (CFD) simulations of the wind turbine wake in flat terrain using an actuator line (AL) are sampled over large regions using numerical, nacelle-based CW and pulsed lidars.

2. Lidar modelling

The fundamental part underlying a numerical implementation of a lidar is the approximation of the weighting function and its efficient discretisation. The former is well established for each respective lidar technology (refer to the references for more detail):

- Continous-wave [4]

$$W_C(r) = \frac{1}{\pi} \frac{z_R}{z_R^2 + (r - F)^2} \quad \text{with} \quad z_R = \frac{\lambda F^2}{\pi \alpha_0^2} \tag{2}$$

- Pulsed [5, 6]

$$W_P(r) = \frac{1}{2\Delta p} \left\{ \mathrm{Erf}\left[\frac{(r - F) + \Delta p/2}{r_p} \right] - \mathrm{Erf}\left[\frac{(r - F) - \Delta p/2}{r_p} \right] \right\}$$
$$\text{with} \quad \mathrm{Erf}(x) = \frac{2}{\sqrt{\pi}} \int_0^x \exp(-t^2)\, \mathrm{d}t \quad \text{and} \quad r_p = \frac{\Delta l}{2\sqrt{\ln(2)}} \tag{3}$$

Here $\lambda, \alpha_0, \Delta p, \Delta l$ are lidar specific constants, usually provided by the manufacturer, and denote laser wavelength, effective telescope radius, range-gate length and lidar beam full width at half maximum, respectively. In figure 2 the influence of these parameters on the lidars' weighting functions are shown. The baseline parameters, which are used throughout the paper, are taken from the ZephIR Dual Mode (CW) and Avent 5-beam Demonstrator (pulsed) (see table 1) and $F = 100$ m. Both functions are symmetric about the probe location F, independent of the choice of parameters. The pulsed weighting function is broader than the one for the continous-wave lidar at this probe location, but it is independent of F. The continous-wave lidar's weighting function on the other hand broadens rapidly with increasing F, as $z_R \propto F^2$. This has some important implications regarding the discretisation of each weighting function, as in a real measurement scenario the only parameter changing is F. Hence, the CW weighting function needs to be re-discretised for each F, whereas the one for a pulsed lidar can be determined once and shifted along r according to F.

Table 1. Lidar parameters used throughout this paper.

CW	α_0	28×10^{-3} m
(ZephIR Dual Mode)	λ	1565×10^{-9} m
Pulsed	Δl	24.75 m
(Avent 5-beam Demo)	Δp	38.4 m

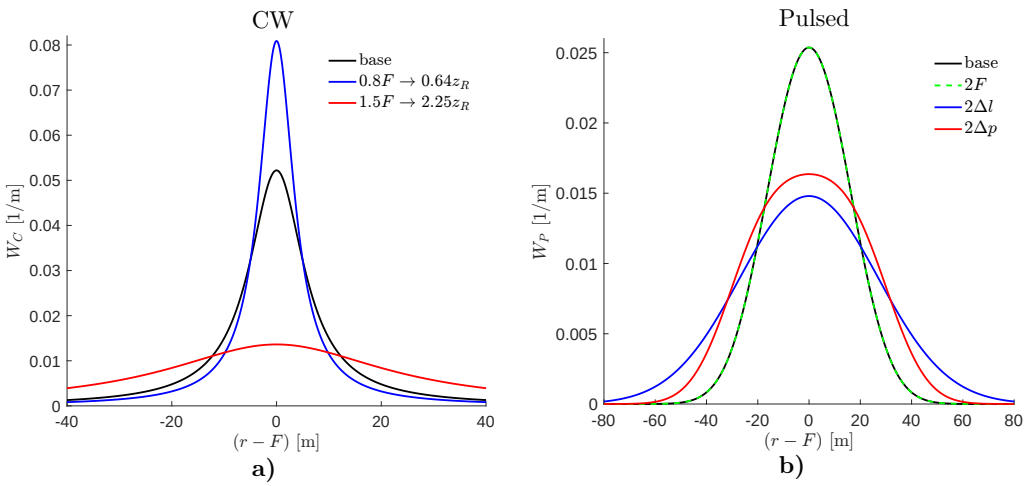

Figure 2. Idealised lidar weighting functions for $F = 100$ m and with baseline parameters given in table 1: a) Continous-wave, equation (2); b) Pulsed, equation (3).

2.1. Discretisation of weighting functions

In discrete space equation (1) becomes

$$v_{los}(\mathbf{x_F}) = \frac{\sum_{i=1}^{n_W} \mathbf{e}(\mathbf{x}_F, \mathbf{x}_L) \cdot \mathbf{V}(r_i) W(r_i)}{\sum_{i=1}^{n_W} W(r_i)} \tag{4}$$

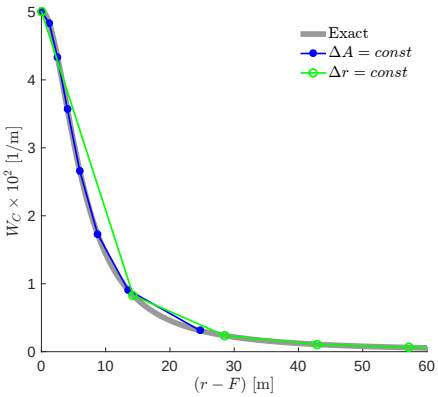

Figure 3. Continous-wave lidar weighting function as defined in equation (2) with $F = 100$ and discretised with either linear spacing in ΔA or Δr each with $n_W = 15$. Lidar parameters: $\lambda = 1565 \times 10^{-9}$ m; $\alpha_0 = 28 \times 10^{-3}$ m.

where n_W denotes the number of points used to discretise the lidar beam. It is directly linked to the numerical efficiency of estimating $v_{los}(\mathbf{x}_F)$, as it determines the number of locations at which $\mathbf{V}$ needs to be evaluated by some costly interpolation. Using a linear point distribution in r the convergence of v_{los} is poor, as the functions are not sampled sufficiently in regions where W is large. Instead, the the area under the curve should be conserved to preserve the shape of the function as shown in Figure 2.1 for $n_W = 15$. Adopting this strategy the integral of the respective weighting function needs to be determined:

$$\Delta A = \int_{r_i}^{r_{i+1}} W(r)\,\mathrm{d}r = const \tag{5}$$

with

$$\Delta A = \frac{2A_F}{(n_W - 1)} \quad \text{and} \quad A_F = \int_{-\infty}^{F} W(r)\,\mathrm{d}r \tag{6}$$

Here the symmetry of the weighting functions is used. The discretisation approach of each function differs, due to the nature $\int W(r)$.

2.1.1. Continous-wave Equation (2) has a definite integral

$$\Delta A = \int_{r_i}^{r_{i+1}} W_C(r)\,\mathrm{d}r = \frac{1}{\pi}\left[\tan^{-1}\left(\frac{r-F}{z_R}\right)\right]_{r_i}^{r_{i+1}} \tag{7}$$

It follows that

$$A_F = \int_{0}^{F} W_C(r)\,\mathrm{d}r = \frac{1}{\pi}\tan^{-1}\left(\frac{F}{z_R}\right) \tag{8}$$

Here the lower bound is set to zero instead, as $\int_{-\infty}^{0} W_C(r)\,\mathrm{d}r \approx 0$. By rearranging equation (7) the point distribution can be determined

$$r_{i+1} = z_R \tan\left(\tan^{-1}\left(\frac{r_i - F}{z_R}\right) - \Delta A\pi\right) + F \tag{9}$$

The best starting location is $r_1 = F$ and the sampling points only need to be evaluated for one side and reflected in $r - F$.

2.1.2. Pulsed The error function has no definite integral, requiring a numerical approach. As W_P is independent of F, the discretisation should be performed only once for $s = r - F$. The shape of the weighting function requires choosing a certain cut-off value $w_{\min}$ until which the weighting function is discretised. The corresponding point $s_{\min}$ can be determined numerically down to a certain tolerance. Consequently s can be discretised linearly with a high resolution in the region $0 \leq s \leq s_{\min}$ to evaluate $\mathbf{w}^+ = W_P(\mathbf{s}^+)$. Some quadrature rule can then be used to determine $\mathbf{A}^+(\mathbf{s}^+)$, which is summed to determine A_F and consequently ΔA (see equation 6). Lowering the level of discretisation reduces computational time as less interpolation is performed in the flow domain. The final discretised weighting function should be sampled at each s_i corresponding to an area $i\Delta A$, which can be interpolated from $\mathbf{A}^+(\mathbf{s}^+)$. Reflecting $\mathbf{w}(\mathbf{s})$ in 0 gives the fully discretised W_P and to recover the beam coordinate system $\mathbf{r} = \mathbf{s} + F$.

2.2. Domain boundary exceeding beams
Depending on the probe location and the beam direction, some part of the lidar beam may lie outside the computational domain. Additionally, pulsed lidars give weight to velocities sampled at $r < 0$, when $F < 2\Delta l$. One solution to obtain an estimate of v_{los}, despite missing parts of the weighting function, is to scale the weights with regard to the total inside the domain

$$\tilde{W}(r) = \frac{W(r)}{\int_0^{r_\Omega} W(r)\,\mathrm{d}r} \tag{10}$$

Here r_Ω denotes the intersection of the beam with the domain boundaries. In a real measurement scenario it is not unusual that $\int_0^{r_\Omega} W(r)\,\mathrm{d}r \neq 1$, which corresponds to a beam intersecting hard targets like towers, turbines, ground etc. Usually these measurements are outright rejected by the lidar signal processing software, as hard targets show up as anomalies in the Doppler spectra. Similarly, a pulsed lidar cannot measure at around $F < 2\Delta l$ for technical reasons (internal reflections etc. [7]). Therefore numerical estimates of v_{los} for which $\int_0^{r_\Omega} W(r)\,\mathrm{d}r < 1$ should be treated with caution.

3. Computational method

3.1. Flow solver and modelling approach
The finite-volume solver, EllipSys3D, discretises the Navier-Stokes equations over a block-structured domain [8–10]. The SIMPLE algorithm [11] solves the pressure-linked terms of the Navier-Stokes equations and a modified Rhie-Chow algorithm the pressure equation [12]. Time-stepping is achieved through an iterative, second-order scheme. The turbulence is either modelled by a Reynolds-averaged Navier-Stokes (RANS) formulation with a Menter k–ω shear-stress transport closure [13] or by solving the filtered Navier-Stokes equations with a sub-grid scale (SGS) model by Ta Phouc [14]. Switching between models is determined by a limiter function as defined by Strelets [15]. This also determines whether the QUICK [16] (RANS) or a fourth-order CDS scheme (LES) discretises the convective terms. The rotor forces are introduced by an actuator line [17, 18].

3.2. Siemens SWT 2.3-93
The turbine is a commercial product by Siemens Wind Power with a rated power of 2.3 MW and a three-bladed rotor with 93 m diameter. The hub is located 80 m above. At a hub height wind speed of 8 m/s it performs 15 rotations per minute and $C_T = 0.81$.

3.3. Numerical domain
A box domain with 25 radii (R) side length reduces the blockage from the turbine ($\pi/25^2 = 0.5\%$). The bottom boundary is a no-slip wall and the top, side and rear boundary conditions follow the shear profile (Dirichlet). The AL is located centrally, at a hub height of 80 m, and is surrounded by a finely meshed box with 2.5 R side length and a grid spacing of $R/32$. This resolution is sufficient for accurate wake simulations using an AL [19, 20]. The wall cell of the structured mesh is set to 0.05 m and grows [8] hyperbolically in the vertical direction until reaching the equispaced finely meshed box. From there the mesh spacing increases hyperbolically towards the outer domain edges.

3.4. Numerical setup
The hub height velocity was 8 m/s and the inflow profile followed the power law with an exponent of 0.3. The kinematic viscosity and air density were set to 1.789×10^{-5} kg/m/s and 1.225 kg/m^3, respectively. Neither nacelle nor tower were modelled. The smearing factor of the AL is set to twice the grid spacing as suggested by Troldborg *et al.* [19].

The flow was sampled with a CW and pulsed lidar situated at the rotor centre. The parameters of the lidars were those given in table 1. The probe locations $\mathbf{x}_F$ lay in a vertical ($x - z$) and horizontal ($x - y$) plane passing through the rotor centre. The spacing between probe locations was $D/50$ in both directions.

4. Results

4.1. The mean flow-field
The developing mean flow-field is shown in Figure 4. The large C_T of 0.81 induces strong velocity gradients and peak deficit. The wake is asymmetric, due to the interaction of shear with wake rotation. The rotor blocks the incoming flow, leading to deceleration in the wall-bound regions upstream and re-acceleration downstream. This flow-field presents a challenging test case for lidars with its large velocity gradients.

4.2. Beam discretisation & v_{los} convergence
The convergence of the line-of-sight velocity Δv_{los} with respect to the number of points discretising the lidar beam is investigated over the region outlined in Section 3.4. Here the residual error is defined as

$$\epsilon^i = \frac{v_{los}^i - v_{los}^{i\text{-}1}}{v_{los}^{i\text{-}1}} \tag{11}$$

with i representing the discretisation level. For the vertical plane sampled by a CW lidar and $n_W = 19$ the residuals are shown in Figure 5. Only probe locations where the entire beam lies inside the domain ($\int_0^{r_\Omega} W(r)\,\mathrm{d}r = 1$) are presented. Close to the rotor v_{los} has converged further than downstream in the wake. This is linked to the CW lidar's weighting function: it is very acute close to the rotor but stretches quickly, necessitating more points for an accurate representation. Furthermore, close to large velocity gradients, as at the wake edge, the exact point distribution starts to play an important role. Figure 6 summarises the change of the v_{los} residual with n_W over the vertical plane for both lidars. Convergence is of second order for the CW and nearly third order for the pulsed lidar. Therefore even with few points discretising the beam the effect of volume-averaging can be captured. Note that beyond $n_W > 100$ the beam

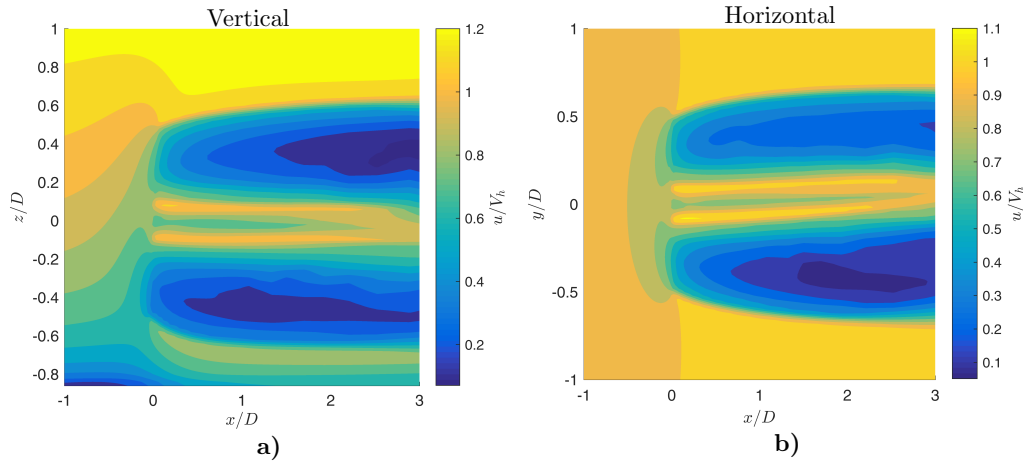

Figure 4. Contours of the time-averaged streamwise velocity component normalised by the hub height velocity $V_h = 8$ m/s in the a) vertical b) horizontal plane through the rotor centre.

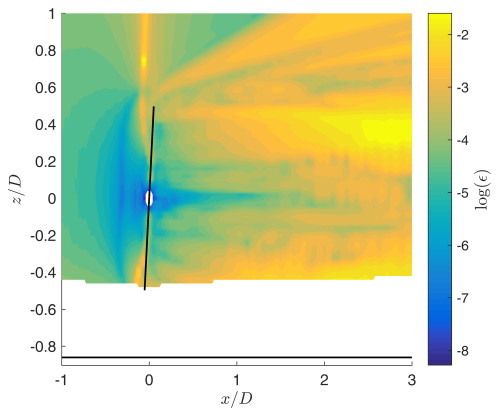

Figure 5. Contours of the v_{los} residual for the CW lidar with $n_W = 19$ discretising the beam. Regions where $\int_0^{r_\Omega} W(r)\,\mathrm{d}r \neq 1$ are removed.

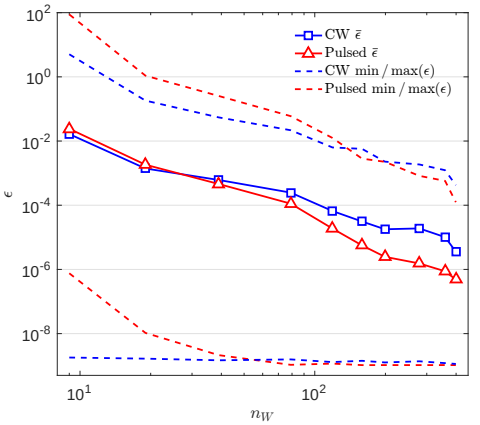

Figure 6. Evolution of the line-of-sight velocity v_{los} residual with number of beam points n_W. Mean and extreme values are determined over a vertical plane ($-3 \leq x/D \leq 3, y/D = 0, -0.86 \leq z/D \leq 1$).

discretisation becomes finer than that of the flow-field and the residuals continue to fall due to interpolation in the flow domain.

4.3. The effect of volume-averaging

To investigate the effect of volume-averaging the flow-field sampled by lidars are compared to point-like measurements, such that

$$\Delta\tilde{v}_{los} = \frac{v_{los}^{\text{lidar}} - v_{los}^{\text{point}}}{v_{los}^{\text{point}}} \tag{12}$$

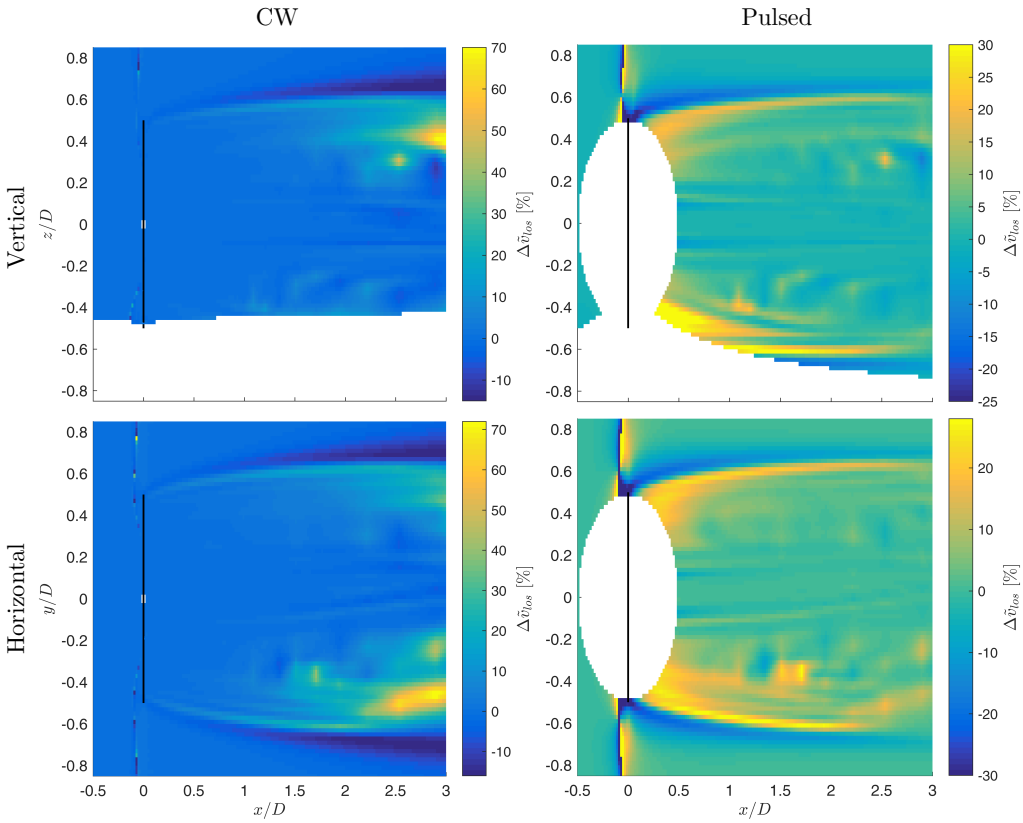

Figure 7. Time-averaged relative difference in the line-of-sight velocity $\Delta\tilde{v}_{los}$ measured by a CW (left) and pulsed (right) in a vertical (top) and horizontal plane (bottom) with respect to point-like velocities.

Time-averaged contours of this quantity are shown in Figure 7 for both planes and lidars. Note that here the beam was discretised with $n_W = 200$ and again probe locations where $\int_0^{r_\Omega} W(r)\,\mathrm{d}r \neq 1$ are excluded. Unsurprisingly, for both lidars the difference to point-like measurements are most prominent around the wake edges, due to the large velocity gradients. However, whereas the CW sampled velocities present nearly no volume-averaging close to the rotor, the pulsed system suffers greatest in this region. The inverse is true the further the probe locations move downstream. This is clearly related to the CW lidar's weighting function spreading quickly with F^2. The pulsed lidar's weights are unchanged with distance, but close to the rotor the beam cuts the wake edge nearly orthogonally.

This results in a relatively small v_{los} and in combination with sampling along a large velocity gradient introduces substantial amounts of volume-averaging. The large difference encountered in the rotor plane also stems from sampling the flow perpendicular to the mean flow direction. To give a more quantitative impression of volume-averaging in the wake, Figure 8 compares the difference in the line-of-sight velocities at different longitudinal stations between lidars. Upstream the velocity profile is nearly unchanged, except close to the ground, whereas in the wake there are significant alterations, mostly leading to larger measured velocities. This is most prominent around the wake edges.

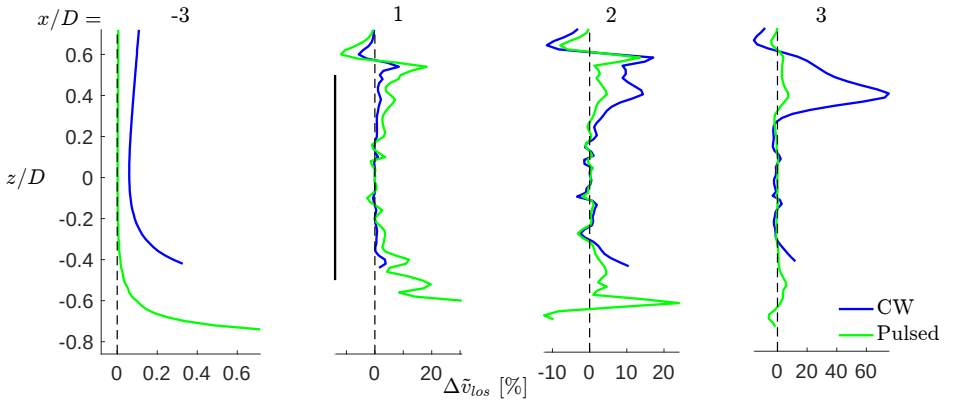

Figure 8. Time-averaged difference in the measured line-of-sight to point-like velocities along z at changing locations along the centreline.

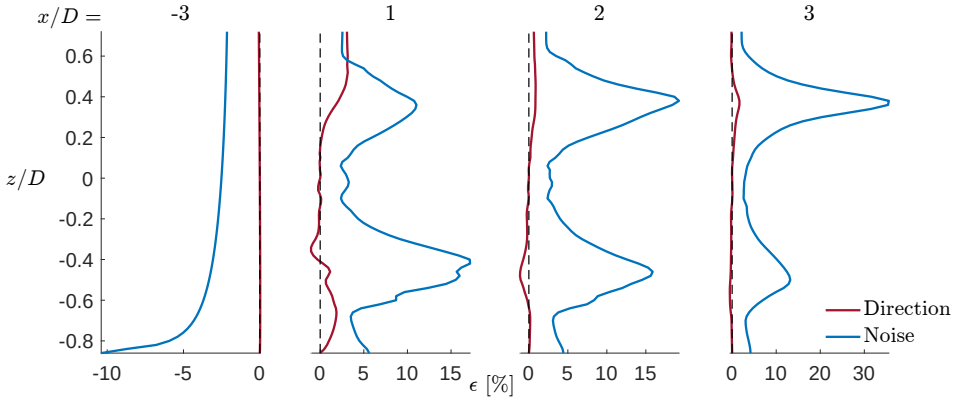

Figure 9. Directional and noise errors (only positive) along the same lines as Figure 8.

However, as discussed by Simley *et al.* [21], there are various other errors impacting lidar measurements, namely directional bias, signal noise and flow evolution. Here the directional bias refers to the error incurred by estimating the streamwise velocity from line-of-sight measurements ("cyclops dilemma"). Random measurement noise is unavoidable and introduces uncertainty in the measured velocities by disturbing the Doppler spectra. Both errors were computed for the transects already shown in Figure 8 following the definition of Simley *et al.*, which assumes a maximum noise error of $\pm$ 0.2 m/s. They are presented in Figure 9, which highlights that signal noise is the more significant of both. Referring to Figure 8, noise plays a detrimental role with respect to the total error, as it is of the same magnitude as the volume-averaging effect. Upstream it is in fact the only significant error source. Nevertheless, it should be kept in mind that the noise level needs to be reassessed for each measurement campaign, as it can vary significantly [21]. Therefore, the impact from noise presented here cannot be generalised.

5. Conclusion

Lidar volume-averaging can be readily implemented in existing flow simulation tools, as it is solely an additional post-processing step. An efficient and accurate method for discretising the lidar beam weighting function is presented, that allows lidar sampling at each time step at limited computational cost. Wake measurements are affected by volume-averaging especially at the wake edges, due to the large velocity gradients being smeared out. However the type of lidar, CW or pulsed, determines the region in which it is most prominent: close to the rotor the CW shows nearly none, whereas the pulsed lidar's velocity might reach 30% of a point-like measurement; the opposite is true beyond 200 m downstream. The lidar measurement location and type therefore determine whether volume-averaging should be incorporated into simulation data post-processing. As there are many variables determining the lidar line-of-sight velocity it is, however, hard to make a general statement regarding the significance of volume-averaging.

Acknowledgments

This work was performed inside the UniTTe project (unitte.dk), which is financed by The Innovation Fund Denmark, grant number 1305-00024B. Computational resources were provided by the Risø DTU central computing facility. Furthermore, we would like to thank Siemens Wind Power and the lidar manufacturers ZephIR and Avent.

References

[1] Churchfield M, Wang Q, Scholbrock A, Herges T, Mikkelsen T and Sjöholm M 2016 *Journal of Physics: Conference Series* **753**
[2] Simley E, Pao L Y, Frehlich R, Jonkman B and Kelley N 2012 Analysis of wind speed measurements using continous wave lidar for wind turbine control *49th AIAA Aerospace Sciences Meeting* AIAA 2011-263 (Orlando, Flordia, US)
[3] Mirocha J D, Rajewski D A, Marjanovic N, Lundquist J K, Kosovic B, Draxl C and Churchfield M J 2016 *Journal of Physics: Conference Series* **753**
[4] Sonnenschein C M and Horrigan F A 1971 *Applied Optics* **10**
[5] Banakh V A and Smalikho I N 1997 *Atmos. Oceanic Opt.* **10** 957–965
[6] Sonnenschein C M and Horrigan F A 1997 *J. Atmos. Oceanic Technol.* **14** 54–75
[7] Vasiljevic N, Courtney M and Mann J 2014 *A time-space synchronization of coherent Doppler scanning lidars for 3D measurements of wind fields* Ph.D. thesis DTU Wind Energy
[8] Sørensen N 1995 *General purpose flow solver applied to flow over hills* Ph.D. thesis Risø National Laboratory
[9] Michelsen J 1994 Basis3d - a platform for development of multiblock pde solvers Tech. rep. Dept. of Fluid Mechanics, Technical University of Denmark, DTU
[10] Michelsen J 1994 Block structured multigrid solution of 2d and 3d elliptic pdes Tech. rep. Dept. of Fluid Mechanics, Technical University of Denmark, DTU
[11] Patanker S and Spalding D 1972 *International Journal of Heat and Mass Transfer*
[12] Réthoré P E and Sørensen N 2012 *Wind Energy* **15** 915–926
[13] Menter F R 1993 *AIAA Journal*
[14] Phouc T 1994 *Modèles de sous maille appliqués aux écoulmements instationnaires décollés* (LIMSI)
[15] Strelets M 2001 Detached eddy simulation of massively separated flows 39th *AIAA Aerospace Sciences Meeting and Exhibit* AIAA Paper 2001-0879 (Reno,NV)
[16] Leonard B 1979 *Computer Methods in Applied Mechanics and Engineering* **19** 59–98
[17] Srensen J N and Shen W Z 2002 *Journal of Fluids Engineering* **124** 393–399
[18] Mikkelsen R 2003 *Actuator Disc Methods Applied to Wind Turbines* Ph.D. thesis Technical University of Denmark
[19] Troldborg N, Sørensen J and Mikkelsen R 2009 *Actuator Line Modeling of Wind Turbine Wakes* Ph.D. thesis Technical University of Denmark
[20] Meyer Forsting A and Troldborg N 2015 *Journal of Physics: Conference Series (Online)* **625** ISSN 1742-6596
[21] Simley E, Pao L Y, Frehlich R, Jonkman B and Kelley N 2014 *Wind Energy* **17** 413–433

ARTICLE 7

COMPARISON OF OPENFOAM AND ELLIPSYS3D ACTUATOR LINE METHODS WITH (NEW) MEXICO RESULTS

CONFERENCE JOURNAL ARTICLE

Journal of Physics: Conference Series 854 (2017) DOI

Wake Conference, Visby, Sweden, May 2017

Co-author

This paper is the outcome of the External Stay at ÉTS in Montréal and was written and initiated by Jörn Nathan, a PhD student of Prof. Christian Masson, who was hosting the stay. All data and written content associated with EllipSys3D were provided for this publication. The outcome of this work was the validation and verification of the AL model in EllipSys3D.

Comparison of OpenFOAM and EllipSys3D actuator line methods with (NEW) MEXICO results

J Nathan[1], A R Meyer Forsting[2], N Troldborg[2] and C Masson[1]
[1]ÉTS Montral, Mechanical Engineering, Montréal H3C 1K3, Canada
[2]Technical University of Denmark, Department of Wind Energy, 4000 Roskilde, Denmark

E-mail: joern.nathan.1@ens.etsmtl.ca

Abstract. The Actuator Line Method exists for more than a decade and has become a well established choice for simulating wind rotors in computational fluid dynamics. Numerous implementations exist and are used in the wind energy research community. These codes were verified by experimental data such as the MEXICO experiment. Often the verification against other codes were made on a very broad scale. Therefore this study attempts first a validation by comparing two different implementations, namely an adapted version of SOWFA/OpenFOAM and EllipSys3D and also a verification by comparing against experimental results from the MEXICO and NEW MEXICO experiments.

1. Introduction

In order to circumvent the modeling of the boundary layers attached to the wind rotor blades by representing their full geometry numerically, the Actuator Line Method[1] (ALM) has become a well established alternative for more than a decade. Numerous implementations exist and are used in the wind energy research community. Often those codes were compared to experimental results such as the MEXICO experiment, which is a wind tunnel experiment with a three-bladed rotor (with a radius of $R = 4.5\,m$) conducted at the German-Dutch wind tunnels (DNW). By placing pressure sensors on the blades and using particle image velocimetry (PIV) pertinent information about the near-wake could be obtained. After some amelioration of the setup a second round of the experiment was conducted, called NEW MEXICO. For more technical details see [2] and [3].

This work picks two of the most widely used implementatons, namely EllipSys3D[4] and the SOWFA[1] project[5] in OpenFOAM. Despite the fact that some adaptions have been made to the original SOWFA code by the authors, it will be referenced as SOWFA througout the article. This work tries to presents the ability to well reproduce near wake phenomena without modeling the boundary layer on the blades and at the same time show the models limitations due to its underlying assumptions.

First there will be brief comparison of similarities and differences between the two frameworks in section 2 alongside with a description of the numerical setup. Then there will be a discussion of the results by comparing the two numerical methods against each other and against the experimental data from the MEXICO and NEW MEXICO experiment in section 3. The

[1] This implementation is part of SOWFA (Simulator fOr Wind Farm Applications) by National Renewable Energy Laboratory.

examined cases include the cases for the reference velocities $U_\infty = \{10, 15, 24\}\, m/s$ and for the comparison with the experiment the PIV sheets and force measurements are used. Finally some concluding remarks will be given in section 4.

2. Numerical method

2.1. Numerical framework

Both implementations have been done within a CFD framework based on the control volume method with variables located at cell center and a Rhie-Chow[6] like correction. For a more in-depth description of the underlying CFD methods see [7] and [8].

In both cases the rotor is modeled by a force inserted as a momentum sink in the Navier-Stokes equations and distributed by a Gaussian distribution in order to avoid non-physical spikes in the velocity field around the affected cells. While SOWFA specifies a cut-off length for the 3D Gaussian curve in order to recover approximately 99.9% when integrated, the cut-off length of EllipSys3D is significantly larger to contain an even higher percentage. These two different cut-off lengths do not seem to have a significant impact on the simulation results.

Velocities are sampled in a very similar manner. While EllipSys3D uses explicitly trilinear interpolation to obtain the sampled velocity at the actuator point, SOWFA relies on correcting the cell center value by the velocity gradient. In the present case this gradient is obtained by linear interpolation and hence both sampling methods behave the same way.

While there are efforts to modify the orignal 2D airfoil coefficient data such as[9], the present work wants to use the ALM as an a priori tool. Hence the ALM is relying on the original airfoil data obtained from wind tunnel experiments of an infinite wing. As the centrifugal forces of the rotating blades keep the boundary layer attached longer than on a non-rotating wing [10], the angle of attack (AOA) for the maximum c_L is expected to be shifted towards higher values. Therefore it is expected that this ALM will lead to discrepancies between simulation and experiment for AOAs beyond the angle where stalling occurs in the airfoil data.

A tip correction is applied on the calculated forces. Without the tip correction, the forces where much higher than predicted by experiment. This is most probably due to the under-resolved tip vortex resulting in a weaker down-wash than in the experiment. By conducting the same simulation at different resolutions around the rotor, a higher induction in the tip region can be noticed. In order to compensate for this effect a Glauert tip correction is applied. This resulted also in a better agreement with the experimental data.

2.2. Numerical setup

The computational domain is cubic with an edge length of $20R$ with R as the rotor radius and the rotor positioned at the domain center. In both cases the cells in the vicinity of the rotor are cubic with the size $\Delta x = R/32$ and are stretched towards the domain boundaries in the case of EllipSys3D. Within SOWFA several refinement zones are applied each time halfing the cell edge length. Therefore the mesh of EllipSys3D consists of 7.1e6 cells while the mesh of the SOWFA case consists of $1.9e6$ cells.

For both cases the velocity boundary condition are given by a uniform inflow velocity of $\mathbf{U} = (U_\infty, 0, 0)$ and a zero gradient at the outlet. The lateral boundaries are set as symmetric.

As both simulations are Large Eddy Simulations, the subgrid-scale models are the dynamic Lagrangian method based on[11] for the SOWFA case and a DES model using a limiter to switch between $k - \omega$ SST and LES[12] for the EllipSys3D case. But as there is no inflow turbulence and the helical vortex structure does not break up within the examined region, not a lot of turbulence modeling has to be done. When comparing to a very coarse DNS by deactivating the sub-grid scale model, no significant difference is found.

The SOWFA case uses a discretisation scheme for the convection term that blends 75% of second order central differencing with 25% linear upwind differencing, which is a second

order upwinding scheme, where the face value is corrected by the gradient in the upwind cell. EllipSys3D applies QUICK in RANS regions and central differencing of fourth order in LES regions using the same limiter as for DES model.

For parametrisation of the ALM the Gaussian distribution parameter is set at $\epsilon = 2\Delta x$ and 40 actuator points are used to represent one blade.

3. Results

The first interesting observation is the similarity in sampled velocities and AOAs as shown in figure 1 and figure 2. The directions in figure 2 are based on a local coordinate system on the blade. Despite the existence of steep velocity gradients due to the bound vorticity both frameworks obtain very similar values. This even holds for the relative small value of the

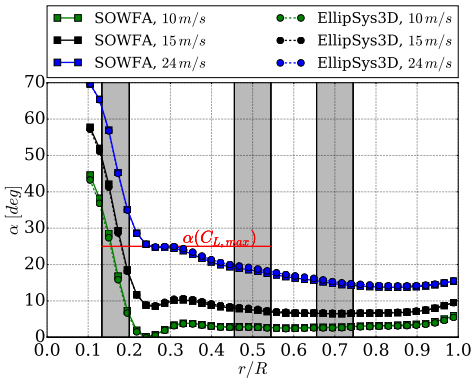

Figure 1. Angle of attack α for each actuator point along the blade. The grey zones represent transition between different airfoil types and the red line (—) the AOA for which the inbound airfoil data indicates stalling.

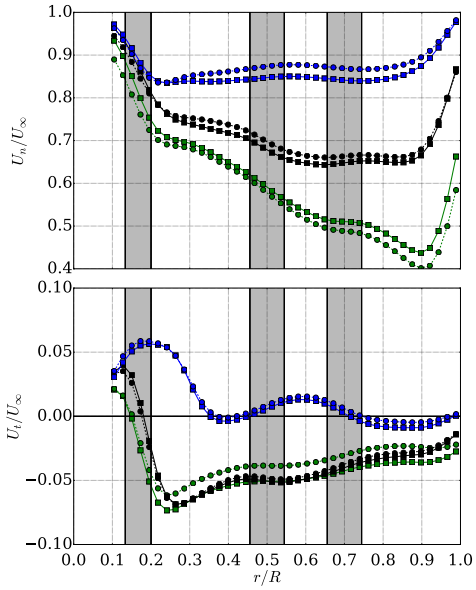

Figure 2. Normalized normal velocity and tangential velocity component U_n/U_∞ and U_t/U_∞ for each actuator point along the blade. The grey zones represent transition between different airfoil types. (see legend in figure 1)

tangential velocity component.

When looking at the AOAs in figure 1 it can be seen that for the radial position $r/R < 0.3$ at $U_\infty = 24\,m/s$ it exceeds the angle after which stalling occurs according to the 2D airfoil data. For the other cases and airfoil sections the AOA always remains below the critical angle. Hence the ALM with the unaltered airfoil data breaks for the aforementioned case and the calculated forces will not match the ones obtained experimentally. In figure 3 the body forces associated with rotating blades can be seen. Again the directions are based on a local coordinate system on the blade. For $U_\infty = 10\,m/s$ and $15\,m/s$ exists a very good agreement, while the forces are not correctly evaluated for the high velocity case. A sudden drop in both forces can be seen. This is stemming from the fact that beyond a certain AOA no experimental data is available

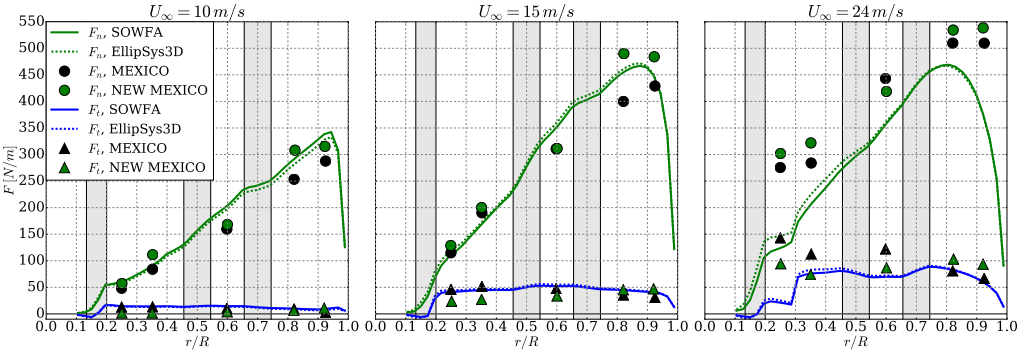

Figure 3. Comparion between the evaluated normal and tangential blade forces F_n and F_t by SOWFA and EllipSys3D against the experimental results of MEXICO and NEW MEXICO over the radial position.

and the void was filled by using the flat plate assumption. Therefore the airfoil data has a sharp drop in the lift coefficient at this point. Another interesting observation is that the forces for the MEXICO experiment are lower than for the NEW MEXICO experiment. This is probably due to the fact that the experiments were conducted with a slightly lower inlet velocity. Again the SOWFA and the EllipSys3D case are very similar even in the case where the models break down.

Due to the slight difference in the blade forces both frameworks produce a relatively similar flow field as shown in figure 4. In the following visualisations the flow field data is based on the domain coordinate system with x in flow direction, r parallel to the rotor plane and lying in the PIV sheet and t as the tangential direction normal to the PIV sheet. The blade position is expressed by the angle Ψ whereas $\Psi = 0$ means that the first blade is pointing upwards. It can be seen that neither SOWFA nor EllipSys3D can simulate distinct vortices shed in the case of turbulent wake state ($U_\infty = 10\,m/s$), but instead a continuous vortex is shed from the rotor. This is due to the rather coarse resolution of $R/32$. With higher inlet velocities a vortical structure can be noticed.

When looking at the radial profiles of the axial, normal and tangential velocity components U_x, U_r and U_t in figure 5 and figure 6, it can be seen that in general both frameworks are underestimating the velocity deficit in the ultimate rotor vicinity ($x/R = \pm 0.13$) compared to the experimental results but the overall trend is very well maintained. An exception is the high velocity case ($U_\infty = 24\,m/s$) where the models deficit becomes appearant. The high gradient of the radial velocity component in the tip region seems to be smeared out by the numerical simulation as can be seen in figure 6. This is most probably due to the numerical schemes and the mesh discretisation, which is expected to ameliorate when using a finer resolved mesh around the rotor. This would not only lead to a better resolution of the vortical structures, but due to the fixed force distribution parameter $\epsilon = 2\Delta x$ also to a more realistic distribution of the force in the tip region. The same applies to the tangential velocity component in the root region.

The axial profiles of the velocity components can be seen figure 7 and figure 8 and again both codes reproduce very similar results in the near wake further away from the rotor. While for the inbound position only data from NEW MEXICO experiments for $U_\infty = 15\,m/s$ are available, we can look at a bigger picture for the outbound position shown in figure 8. Again simulation results are very close to experimental data from the NEW MEXICO experiment, while overestimating with respect to MEXICO results due to reasons already mentioned. For

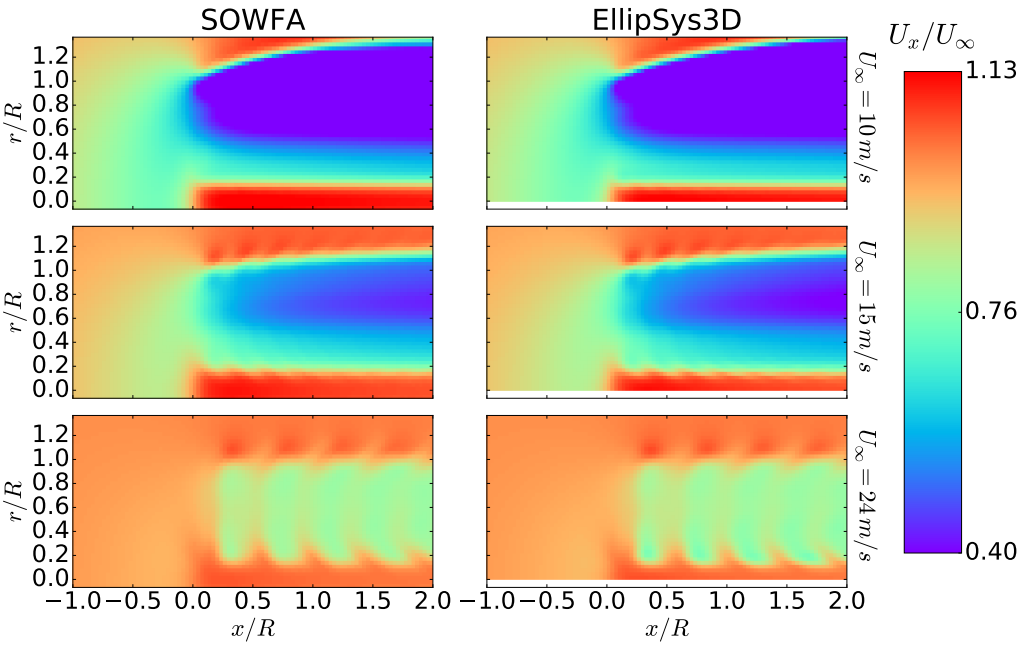

Figure 4. Planes of normalized axial velocity component U_x/U_∞ for all three cases for SOWFA and EllipSys3D. The rotor is situated at $x/R = 0$ and the velocity field is phase averaged for the rotor position $\Psi = 0^o$.

the high velocity case ($U_\infty = 24\,m/s$) the vortex sheets shed from the blades become visible by the oscillations in the axial velocity component U_x.

When looking at the vortex properties as examined in [13] in figure 9 and figure 10. it can be seen that there is a good general agreement despite the coarse resolution of the grid around the rotor ($\Delta x = R/32$). In figure 9 the vortex locations were calculated based on a rotor position of $\Psi = 0^o$ while the experimental was taken for $\Psi = 30^o$, which is the moment when the blade crosses the PIV sheet. Despite the fact that the origins of the vortices might not coincide as stated in [13] and the wake deficit was lower than in the experiments, the simulations appear to represent well the vortex propagation. This can also be seen by looking at figure 9 and comparing the axial locations of the vortices compared to the experimental results. Differences between the two simulations as seen in figure 9 stem from discrete representation of the vortices. In a more refined mesh both curves are expected to be closer.

In order to evaluate the vortex strength the circulation for each vortex is calculated. For obtaining the circulation of the vortices the vorticity magnitude ω in the plane at $\Psi = 0^o$ is integrated over a square with the edge length R_S weighted by the area. When looking at the evolution of vortex circulations in figure 10 it can be seen that the circulation remains almost constant througout the examined region, despite the fact that a constant integration radius R_S was used in order to evaluate the total circulation Γ. In figure 10 the total circulation can be seen in dependence of the square edge size R_S. At around $R_S/R = 0.113$ the saddle point can be perceived. Upto this point the integration only includes vorticity due to the examined vortex. Beyond that R_S also the vorticity of the neighbouring vortices is taken into account hence the steeper increase in circulation.

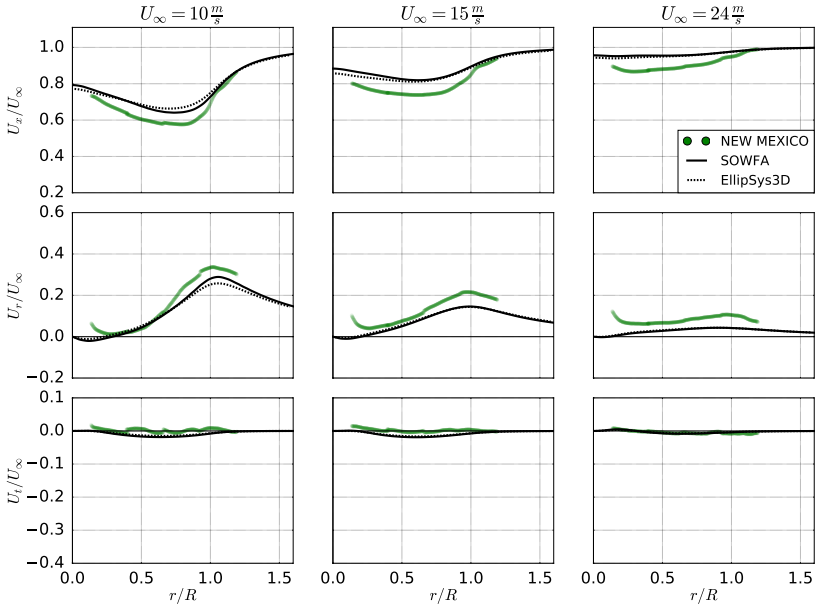

Figure 5. Radial profile of phase averaged ($\Psi = 0^o$) velocity components for different flow cases at upstream ($x/R = -0.13$) position.

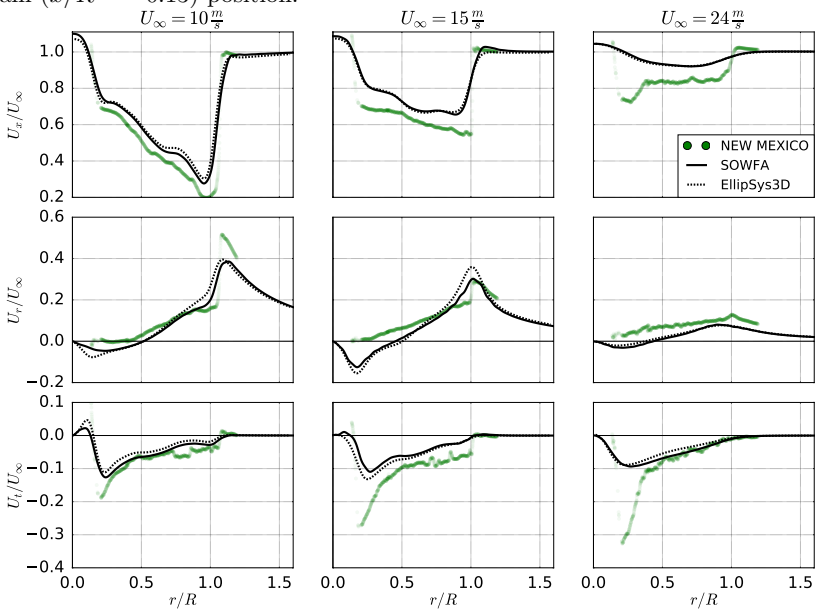

Figure 6. Radial profile of phase averaged ($\Psi = 0^o$) velocity components for different flow cases at downstream ($x/R = 0.13$) position.

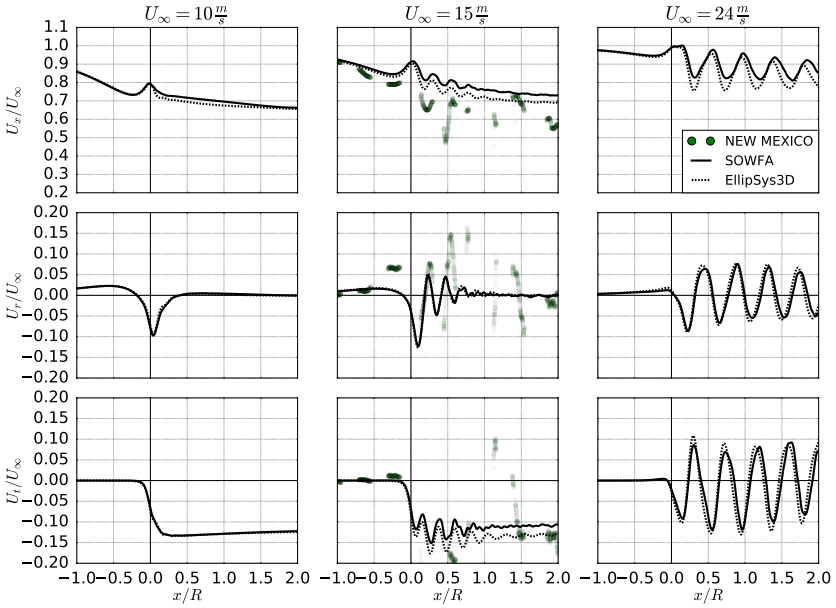

Figure 7. Axial profile of phase averaged ($\Psi = 0^o$) velocity components for different flow cases at inbound ($r/R = 0.22$) blade position.

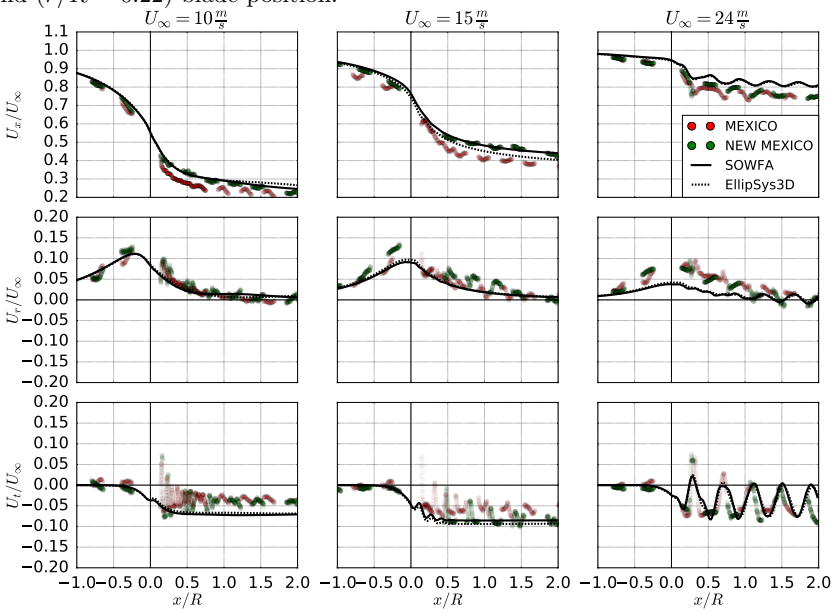

Figure 8. Axial profile of phase averaged ($\Psi = 0^o$) velocity components for different flow cases at outbound ($r/R = 0.67$) blade position.

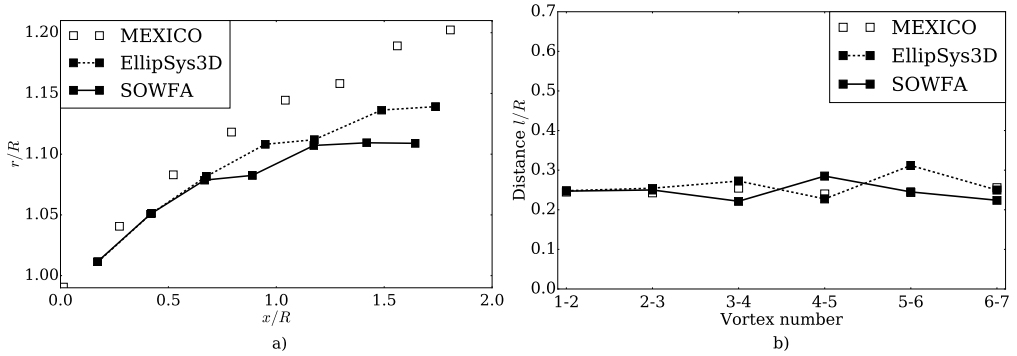

Figure 9. Normalized vortex locations (a) and distances (b) for $U_\infty = 15\,m/s$.

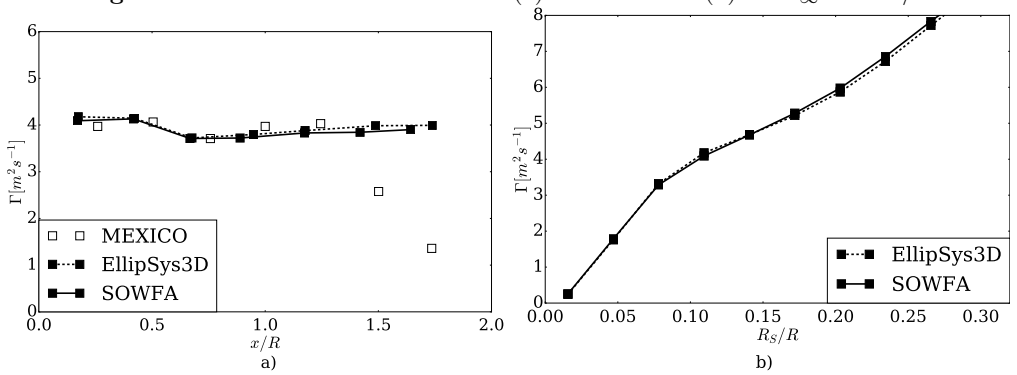

Figure 10. Circulation of vortices (a) and integration radius R_S/R (b) for $U_\infty = 15\,m/s$.

4. Conclusion

The two examined frameworks, EllipSys3D and SOWFA, compare very well in the near wake of the rotor used in the MEXICO and NEW MEXICO experiment. When comparing them against experimental data it can be seen that they predict well the experimental results from the NEW MEXICO experiment while there is an overprediction compared to MEXICO results due to the inlet velocity mismatch in this experiment. Even vortex properties matched among the simulations and predicted the same trend as in the MEXICO experiment, although the resolution in the rotor vicinity might be too coarse for well resolving the helicoidal vortex structure.

Both frameworks obtain very similar velocites and AOAs, and fail at the moment where 3D effects start to dominate. As this occurs only for a very high velocity at the inbound region, it is very encouraging for using only non-altered airfoil data in the presented case.

Future work could be to conduct simulations with a finer resolved region around the rotor and also to find a suitable method for including 3D effects in order to reproduce well the results for the high velocity case. Furthermore the influence of a turbulent inflow could be examined as well.

Acknowledgments

This work is partially supported the Canadian Research Chair on the Nordic Environment Aerodynamics of Wind Turbines, the Natural Sciences and Engineering Research Council

(NSERC) of Canada, the Innovation Fund Denmark (grant number 1305-00024B) and DTU Risø central computing facilities. Thanks for the great work done by Matthew Churchield and colleagues at National Wind Technology Center, Boulder, CO, by establishing the open source framework SOWFA. The data used have been supplied by the consortium which carried out the EU FP5 project Mexico: 'Model rotor EXperiments In COntrolled conditions'. The consortium received additional support to perform the New Mexico measurements from the EU projects ESWIRP and INNWIND.EU.

References

[1] Sørensen, J. N. and Shen, W. Z., 2002. Numerical Modeling of Wind Turbine Wakes. *Journal of Fluids Engineering*, 124(2), pp. 393.

[2] Schepers, J. G. and Snel, H., 2007, *Model Experiments in Controlled Conditions, Final report*, Report, ECN-E-07-042, Energy Research Center of the Netherlands, ECN.

[3] Schepers, J.G., Boorsma K. et al., 2014, *Final report of IEA Task 29, Mexnext (Phase 2)*, Report, ECN-E-14-060, Energy Research Center of the Netherlands, ECN.

[4] Troldborg, N., 2008, *Actuator Line Modeling of Wind Turbine Wakes*, PhD Thesis, Technical University of Denmark, Copenhagen.

[5] Churchfield M J, Lee S, Michalakes J and Moriarty P J 2012 A numerical study of the effects of atmospheric and wake turbulence on wind turbine dynamics *Journal of Turbulence* 13

[6] Rhie, C.M. and Chow, W.L., 1983. Numerical study of the turbulent flow past an airfoil with trailing edge separation, *AIAA journal*, 21(11), pp. 1525–1532.

[7] Sørensen, N. N., 1995, *General Purpose Flow Solver Applied to Flow over Hills*, PhD thesis, Technical University of Denmark, Copenhagen.

[8] Jasak, H., 1996, *Error analysis and estimation in the Finite Volume method with applications to fluid flows*, PhD Thesis, Imperial College, University of London.

[9] Shen, W. Z., Zhu, W. J., and Sørensen, J. N., 2012, Actuator line/NavierStokes computations for the MEXICO rotor: comparison with detailed measurements, *Wind Energy*, 15(5), pp. 811–825.

[10] Vermeer, L. J., Sørensen, J. N., and Crespo, A., 2003, Wind turbine wake aerodynamics, *Progress in Aerospace Sciences*, 39(67), pp. 467–510.

[11] Meneveau, C., Lund, T. and Cabot, W., 1996, A Lagrangian dynamic subgrid-scale model of turbulence, J. Fluid Mech, vol 319, pp. 353–385.

[12] Troldborg, N., Zahle, F., Rthor, P.-E. and Sørensen, N. N., 2015, Comparison of wind turbine wake properties in non-sheared inflow predicted by different CFD rotor models, *Wind Energy*, 18(7), pp. 1239–1250.

[13] Nilsson, K., Shen, W. Z., Sørensen, J. N., Breton, S.-P., and Ivanell, S., 2015, Validation of the actuator line method using near wake measurements of the MEXICO rotor, *Wind Energy*, 18(9), pp. 499–514.

ARTICLE 8

THE FLOW UPSTREAM OF A ROW OF ALIGNED WIND TURBINE ROTORS AND ITS EFFECT ON POWER PRODUCTION

JOURNAL ARTICLE

Wind Energy, Vol. 20, No. 1, 2017, pp. 63-77 DOI

Main author

This journal article expands article 1 by a more detailed flow analysis and presents a simple vortex model that nearly reproduces the CFD results. It furthermore includes a physical explanation for the changes in the induced velocities upstream of a row of wind turbines, which is aided by the vortex model. Following this paper a real power measurement scenario was investigated and the results presented at the Wind Europe Summit 2016.

Wind Energy

WIND ENERGY
Wind Energ. 2017; **20**:63–77
Published online 16 May 2016 in Wiley Online Library (wileyonlinelibrary.com). DOI: 10.1002/we.1991

RESEARCH ARTICLE

The flow upstream of a row of aligned wind turbine rotors and its effect on power production

Alexander Raul Meyer Forsting, Niels Troldborg and Mac Gaunaa

Department of Wind Energy Technical University of Denmark Frederiksborgvej 399 4000 Roskilde Denmark

ABSTRACT

A row of wind turbine rotors with a mutual spacing of three diameters is simulated using both Reynolds averaged Navier-Stokes (RANS) simulations and a simple inviscid vortex model. The angle between the incoming wind and the line connecting the turbines is varied between 45 and 90 degrees. The simulations show that the power production of the turbines deviate significantly compared with a corresponding isolated turbine even though there is no direct wake-turbine interaction at the considered wind directions. Nevertheless, both models indicate marked alterations in the upstream flow, which directly link to the turbines' power adjustments. Thus, turbines which are placed laterally relative to the prevailing wind (as seen at various test sites) have, at least numerically, a mutual effect on each other. Therefore, they might not necessarily produce the same power as a stand-alone turbine.

KEYWORDS
blockage; induction zone; power production; CFD; vortex

Correspondence
A. R. Meyer Forsting, Department of Wind Energy, Technical University of Denmark, Frederiksborgvej 399, 4000 Roskilde, Denmark.
E-mail: alrf@dtu.dk

Received 16 October 2015; Revised 17 February 2016; Accepted 4 April 2016

1. INTRODUCTION

Typical wind turbine test sites consist of a number of turbine stands, which are commonly spaced approximately three rotor diameters (D) apart and placed along a line perpendicular to the prevailing wind as sketched in Figure 1. These test sites are frequently used for validating the power curve of new turbine designs by relating their power output with the incoming wind speed measured by an upstream located met mast. In order to avoid wake effects from neighbouring turbines, such measurements should, according to the IEC standards for power curve measurements,[1] only be carried out when the wind direction is less than approximately 45° off the direction perpendicular to the wind turbine row. It is assumed that for these wind directions the turbines do not affect the power production of each other, inferring that their power output is equivalent to that of an isolated turbine. The validity of this assumption was to some extent verified numerically by Troldborg and Gaunaa[2] for two turbines operating side-by-side in uniform inflow. Their simulations showed that the turbines' power at a given thrust coefficient (C_T) was fairly insensitive to turbine spacing with uniform inflow. More specifically they found that for a spacing of $1.25D$, the power increased by less than 0.8% compared with a corresponding isolated turbine with $C_T = 0.89$. This increase was even smaller for lower C_T values. They argued that assuming independence between two laterally closely spaced rotors is as valid as the assumption of radial independence between stream tubes used in 1-D momentum theory.

However, more recently McTavish *et al.*[3] conducted wind tunnel studies showing that the power production of three downscaled wind turbines positioned $2D$ apart along a line perpendicular to the incoming wind could be augmented by about 3% compared with a corresponding stand alone turbine. With an inter-turbine spacing of $1.25D$ it increased by 7%. They attributed this observation to constricted wake expansion and to a speed-up between the turbines, which caused an increased thrust. They argued that this beneficial effect could be utilized to increase the total power yield of new wind farms. In their measurements the tunnel blockage, defined as the ratio of the rotor swept area and the wind tunnel cross-sectional

area, was 5%, which could have affected the results. Nevertheless, they later confirmed their findings through simulations with the free-vortex code GENUVP.[4] In these simulations there were no external boundaries and hence, no tunnel blockage. Mitraszewski *et al.*[5] showed that the variations in power are not limited to simulations and wind tunnel experiments by analysing the power production along the outer rows of turbines in the Horns Rev 1 wind farm. Along this row, the individual turbine power output relative to the mean of the entire wind park varied up to $\pm 5\%$. The aforementioned studies call for further investigations into how closely spaced turbines may affect each other. Especially, it should be expected that the turbines' mutual interaction increases with a wind direction non-orthogonal to the alignment axis, as it effectively corresponds to a reduction in the lateral spacing between the turbines. At a sufficiently large angle between the wind direction and the alignment axis, their interaction will obviously be dominated by wakes. Nevertheless, it is well know that a wind turbine causes a reduced flow velocity up to $3D$ upstream,[6] questioning whether the inter-turbine interaction should be reduced solely to wakes, as it is commonly done. The upstream induction is evidently less pronounced than the wake; however, it is expected that this blockage effect may have some effect on the velocities (and hence the power) found at neighbouring turbines.

There is a lack of current literature investigating alterations in power production and the flow-field upstream of multiple turbines over an isolated turbine. Furthermore, it only addresses inflows which are perpendicular to the alignment axis of the turbines. Therefore, this study determines numerically the flow around five aligned wind turbines for different inflow angles and directly links it to any changes in turbine power output. Firstly, a CFD-RANS model with an actuator disc (AD) representation of the NREL 5-MW rotor is used to investigate the flow-field in Section 3.1, followed by a presentation of the respective power changes in Section 3.2.1. To enhance the physical interpretation of the flow-field and to demonstrate the reproducibility of these results, a simple vortex model is introduced and compared with CFD for constantly loaded rotors, hence eliminating specific rotor effects, in Section 3.2.2. In the following discussion, both model results are compared and interpreted with regards to changes in power and the flow-field. The CFD and vortex model are presented in Section 2.

1.1. Problem definition

The turbine arrangement chosen in this investigation is very generic, consisting of five rotors with a single axis passing through all their centres. The inter rotor spacing was set to $3D$, which agrees with spacings used at wind turbine test sites currently in use (Table I). The angle between the line of wind turbines and the main wind direction (θ) was varied from 0° to 45° in 15° steps. The turbines yawed in-line with the inflow as shown in Figure 1. The numerical setup itself was

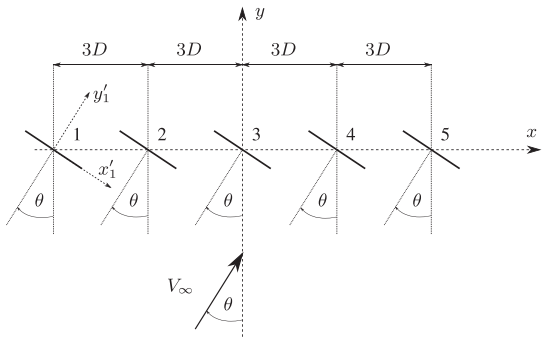

Figure 1. Schematic of the wind turbines' arrangement and reaction to changing inflow directions. Furhter to the wind park corrdinate system a representative local rotor coordinate system is shown for rotor no. 1.

Table I. Overview of some wind turbine test sites currently in use and their specifications regarding inter-turbine spacing and maximally allowed rotor diameters.

Test Site	Country	No. of turbine stands	Inter-stand spacing [m]	Max. rotor diameter [m]	Ratio spacing to rotor diameter
DTU Høvsøre	DK	5	300	130	2.3
DTU Østerild	DK	7	600	210 - 250	2.9 - 2.4
NREL	USA	4	240 - 500	-	-
ECN	NL	2 & 3	500 & 400	125	4.0 - 3.2

Wind Energ. 2017; **20**:63–77 © 2016 John Wiley & Sons, Ltd.
DOI: 10.1002/we

strongly simplified to facilitate the identification of the fundamental physical phenomena underlying the rotor interaction. Hence, the inflow was set to be uniform at 8 m/s, without turbulence. Furthermore, the solution was assumed to be time invariant and the ground was not modelled. Of the turbines only the rotors were modelled as actuator discs (AD), whereas, the turbine tower and the nacelle were ignored. Simplifying the turbine in this way was not expected to impact the results, as the flow on the investigated scale is dominated by the rotors. Note that the turbines are numbered as specified in Figure 1 and have their own local coordinate systems denoted by $\bullet_i'$ with $i = \{1, ..., 5\}$, centred at the rotor hub.

2. COMPUTATIONAL METHOD

2.1. CFD

2.1.1. Flow solver.

The flow field is solved via the in-house developed finite volume code EllipSys3D. It solves the incompressible Reynolds Averaged Navier-Stokes (RANS) equations over a discretized block-structured domain [7–9] using a collocated grid formulation. The SIMPLE algorithm[10] computes the pressure-linked terms of the Navier-Stokes equations, whereas the QUICK scheme[11] determines the convective terms. To avoid velocity-pressure decoupling in the presence of discrete body forces, originating from an actuator disc (AD), a modified Rhie-Chow algorithm [12–14] is applied to the convective term. The turbulence was incorporated via the Menter $k-\omega$ shear-stress transport model.[15]

2.1.2. Turbine model.

The turbine rotor was represented by an actuator disc. The discrete body forces acting over the disc are either determined iteratively from the local blade velocities and airfoil data or are predefined. In the former type of force allocation the airfoil data and geometry of the NREL 5-MW[16] with a 126 m diameter rotor was used. At the set wind speed of 8 m/s, the rotor performs 9.21 rotations per minute (RPM).

To arrive at a more general description of the laterally induced blockage, simulations were also performed with constantly loaded discs. The global thrust coefficient C_T of a single NREL turbine at $V_\infty = 8$ m/s equalled 0.798, which was subsequently applied to the constantly loaded discs. The normal force thus acting over a sectional area ΔA of the actuator disc is:

$$F_N = \frac{1}{2}\rho_\infty V_\infty^2 C_T \Delta A \tag{1}$$

with $\rho_\infty = 1.225$ kg/m^3 and R equalling the rotor radius. Note that approximating the influence of a rotor with only normal forces corresponds to the ideal case where the tip speed ratio tends to infinity.

2.1.3. Numerical domain.

The numerical domain is discretized by a structured O-type meshing methodology, containing a centrally located equispaced box mesh. The latter encompasses the row of turbines. The mesh layout and its dimensions are specified in Figures 2 and 3. All dimensions are scaled by the rotor diameter D. The inflow and outflow boundaries are applied circumferentially to the O-mesh. The outflow region is defined as the arc resulting from a 90° sector centred around the inflow direction.

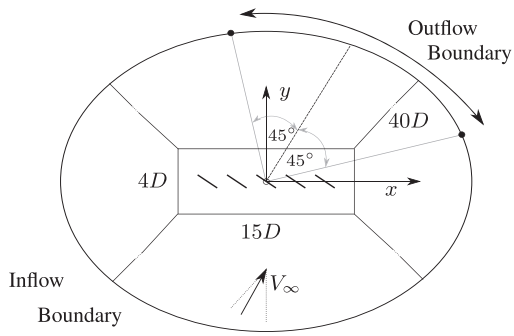

Figure 2. Top view of the numerical domain. All dimensions are scaled by the turbine diameter D. Note that the boundaries are a function of the inflow angle.

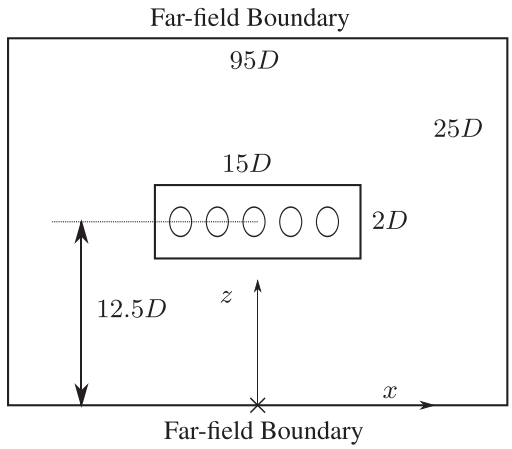

Figure 3. Frontal view of the numerical domain.

The velocities at the top, bottom and the inlet boundaries of the domain are prescribed (Dirichlet), whereas at the outflow the velocity has zero-gradient (v. Neumann). The mesh spacing inside the central box is $D/32$ in all directions. From there the mesh grows hyperbolically outwards in the radial and z directions, where the dimension of the first cell matches that of the inner box. The number of grid spaces along the radial and z directions are 32 and 128, respectively. The total number of cells is 2.05×10^6.
Note that the relatively large numerical domain causes the domain blockage to be negligible.

For a full domain and mesh sensitivity analysis refer to the previous work by the authors.[17]

2.2. Vortex model

The vortex model used in the present work is based on the method originally proposed by Øye[18] and is described in more detail in Appendix A. The basis of this model is formed by a rotor with uniform circulation along each blade, where the product of total circulation on the rotor and rotational speed remains constant, as the former tends to zero and the latter to infinity. This corresponds to simulating a constant loaded disc where the thrust coefficient, c.f. equation (A.3) is:

$$C_T = \frac{\Gamma \Omega}{\pi V_\infty^2} \tag{2}$$

where Γ is the total circulation of all blades, Ω the rotational speed and V_∞ the free-stream velocity.
The wake of each turbine is modelled using discrete vortex rings in the near wake and a semi-infinite vortex cylinder in the far-wake. In the first part of the near wake the rings are allowed to expand while in the last part the ring radius is kept constant. In this paper, the initial 30 rotor radii of the wake are simulated with vortex rings with a streamwise spacing of 0.1 rotor radii. In the first 29 rotor radii the rings can expand freely while their radius is fixed in the last part.

3. RESULTS

3.1. The flow-field

Figures 4 and 5 show streamwise velocity contours for inflow angles of 0° and 45°, respectively. Both are xy-planes extracted at hub height and simulated with CFD using the NREL 5-MW turbine model. The contours reveal the emergence of a 'global' induction zone along the entire turbine row, as they start to act as one single flow obstruction. Unsurprisingly, this global effect is symmetric about the central turbine for a perpendicular inflow, hence, it extents furthest upstream of the central turbine. A more quantitative insight into the induction zone is given in Figure 6, which presents normalized streamwise velocity profiles extracted along lines parallel to each rotor plane, one up- and another downstream. Generally the velocities profiles extracted at each rotor are close to indistinguishable, only at the outer edges of the row does the velocity exceed the one in-between the rotors.

Wind Energ. 2017; **20**:63–77 © 2016 John Wiley & Sons, Ltd.
DOI: 10.1002/we

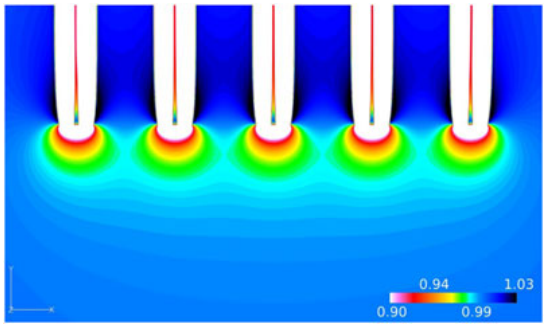

Figure 4. Normalized streamwise velocity contours (v'/V_∞) in the *xy*-plane at an inflow angle (θ) of 0° and with the NREL 5-MW turbine model.

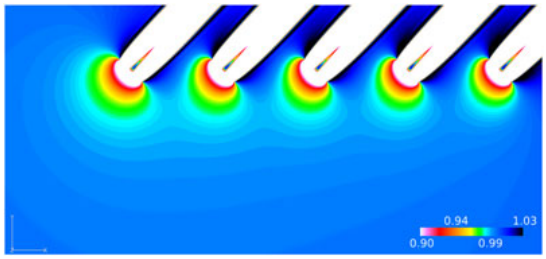

Figure 5. Normalized streamwise velocity contours (v'/V_∞) in the *xy*-plane at an inflow angle (θ) of 45° and with the NREL 5-MW turbine model.

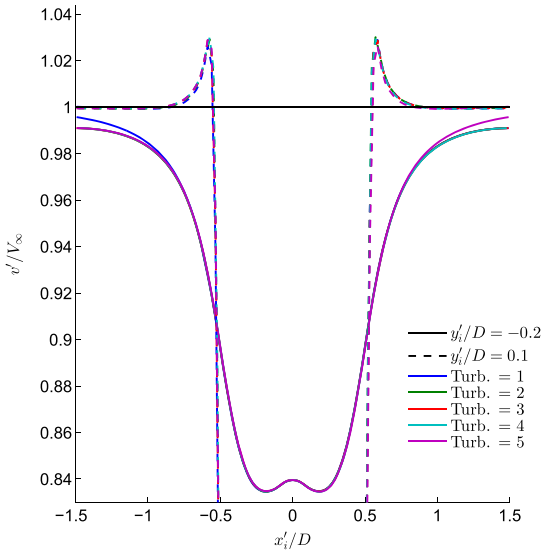

Figure 6. Normalized streamwise velocity profiles (v'/V_∞) extracted along two lines parallel to each rotor plane at $y'/D = \{-0.2, 0.1\}$. The inflow angle (θ) is 0°. The profiles are shown as function of the local rotor coordinate systems $\bullet_i'$ with $i = \{1, ..., 5\}$.

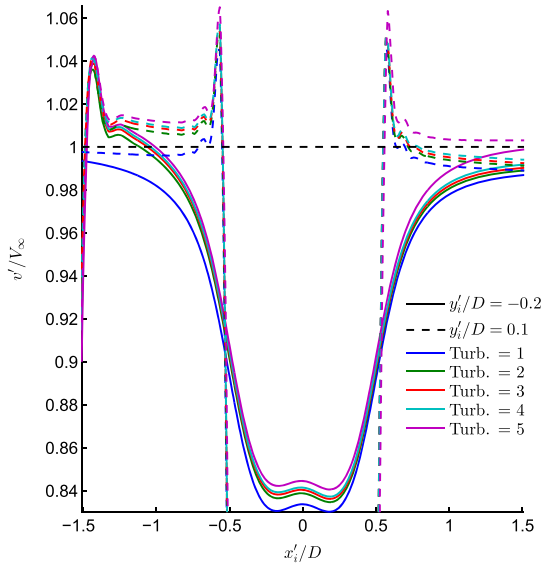

Figure 7. Normalized streamwise velocity profiles (v'/V_∞) extracted along two lines parallel to each rotor plane at $y'/D = \{-0.2, 0.1\}$. The inflow angle (θ) is 45°. The profiles are shown as function of the local rotor coordinate systems $\bullet'_i$ with $i = \{1, ..., 5\}$.

Changing the wind direction brakes the symmetry and the upstream rotor (rotor no. 1 in Figure 1) starts to experience the strongest velocity deficit. The flow velocity starts to recover as it moves down the row of turbines along the x direction. Figure 7 presents the velocity profiles in the local rotor coordinate systems ($\bullet'_i$) along the upstream lines $y'_i/D = -0.2$. They underline the aforementioned re-acceleration and show that the maximal velocity deficit decreases with increasing x/rotor number. This effect is amplified in-line with increasing the inflow angle.

In-between the individual induction zones the flow is accelerated, as the flow approaching each rotor decelerates. This is clearly visible in Figure 6. Passing the rotor plane ($y'_i > 0$) the flow exceeds the free-stream value. This channelling aggravates with increasing inflow angle, as the cross-sectional area normal to the flow direction is further constrained by the wake of the neighbouring turbine. Consequently, a non-symmetric local induction zone forms, as the flow accelerates towards the wake. The side that is influenced most by the upstream wake is found for $x'_i < 0$ in Figure 7. Rotor no. 1 is missing this phenomenon, as it does not experience a wake. Directly comparing the velocity profiles of the two inflow cases, the velocities found for $x'_i < 0$ are always greater for the angled inflow, except for turbine no. 1. For $\theta = 45°$ the maximum deficit exceeds that of $\theta = 0°$.

3.2. Power evolution

3.2.1. NREL 5-MW.

In Figure 8 the percentage change of the computationally determined power produced by each NREL 5-MW turbine is shown for all four inflow angles. The change in power for each rotor is calculated with respect to a corresponding isolated rotor:

$$\Delta P = \frac{P - P_{single}}{P_{single}} \tag{3}$$

Note that turbine no.1 is upstream i.e. on the far left in Figure 5. A summary of the results in Figure 8 is given in Table II. A flow perpendicular to the row ($\theta = 0°$) is shown to increase the power output universally by 0.58% compared with an isolated turbine. This global rise and the gain towards the central turbine is in line with the work of McTavish *et al.*[4] Using half the lateral spacing compared with this study (1.5D) he found larger gains in power of up to 8% for the central turbine. Even when matching all parameters of his numerical simulations, in particular the turbine thrust coefficient C_T and lateral spacing, we only found an increase of 3% using our set-up. This discrepancy is most likely related to the markedly different rotor designs and numerical methods employed. Nevertheless the trend is clear.

Wind Energ. 2017; **20**:63–77 © 2016 John Wiley & Sons, Ltd.
DOI: 10.1002/we

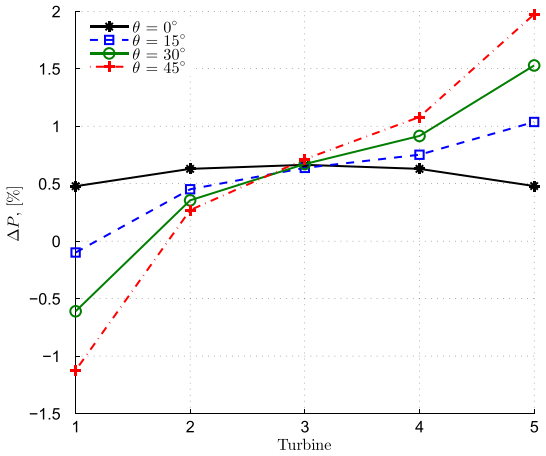

Figure 8. Percentage change in power extracted by each NREL 5-MW turbine at different inflow angles determined using CFD-RANS.

Table II. Summary of mean ($\langle\bullet\rangle$), minimum, maximum and range of the results in Figure 8, where $\Delta\mathbf{P} = \{\Delta P_1, ..., \Delta P_5\}$.

θ [°]	$\langle\Delta\mathbf{P}\rangle$ [%]	min($\Delta\mathbf{P}$) - $\langle\Delta\mathbf{P}\rangle$ [%]	max($\Delta\mathbf{P}$) - $\langle\Delta\mathbf{P}\rangle$ [%]	range($\Delta\mathbf{P}$) [%]
0	0.576	−0.0881	0.0977	0.186
15	0.556	−0.481	0.654	1.14
30	0.572	−0.956	1.18	2.14
45	0.582	−1.39	1.71	3.10

The change in power across the turbines is altered significantly once the inflow is yawed, except for the central turbine, where ΔP is about constant for any θ. All curves start to demonstrate an anti-symmetry about the central turbine for $\theta \neq 0°$. The losses upstream translate to additional gains downstream, which is underlined by a quasi constant mean power rise of approximately 0.57% across the rotors (Table II). The range in ΔP increases rapidly with inflow angle and reaches 3.1% for $\theta = 45°$.

3.2.2. Comparison CFD - vortex model.

To verify that the results found in the previous section are not rotor dependant and are reproducible using very simplified models, a constantly loaded disc is simulated using the CFD and vortex model. Comparing Figures 8 and 9 underlines that the overall behaviour of the solution does not change by altering the rotor loading. The magnitude of the percentage changes in power has dropped relative to the NREL simulations, but still shows a net rise in power for the constantly loaded discs. In Figure 9 the y-axis of the vortex solutions (on the right) is shifted upwards by 0.4%, as it consistently under-predicts the power relative to CFD. Nevertheless the scale is left unchanged, which essentially demonstrates that both methods agree on the changes in power upstream and downstream relative to the central turbine.

4. DISCUSSION

The overall rise in power and the significant changes in the individual turbine power production can be related to the emerging flow-field. As mentioned in Section 3.1 the flow is accelerated in-between turbines and along the row of turbines when the inflow is not orthogonal to the row of rotors. Almost equal to the acceleration along the turbines is the stronger deceleration in front of the upstream turbines. It is this balance that ensures that power production for the entire row is essentially unchanged by alterations in the inflow angle. Furthermore, it underlines that global changes in the induction zone are determining the individual power output, instead of local ones. Decreasing the distance between turbine and neighbouring wake with increasing inflow angle, does not seem to accelerate the flow sufficiently to noticeably impact the power evolution along the row.

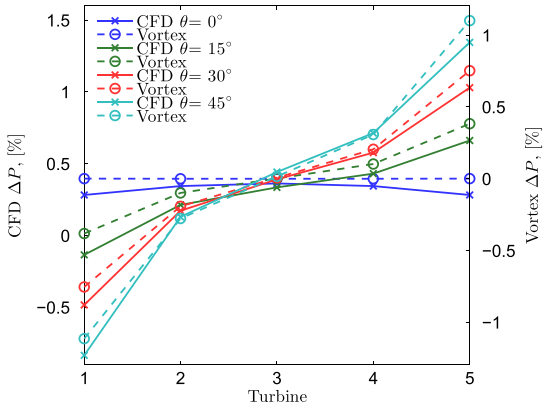

Figure 9. Comparison of the percentage changes in the power for different inflow angles θ between CFD-AD simulations and the vortex model. They are presented with respect to two independent y-axes, but equal scaling. The axes are shifted by 0.4% to each other.

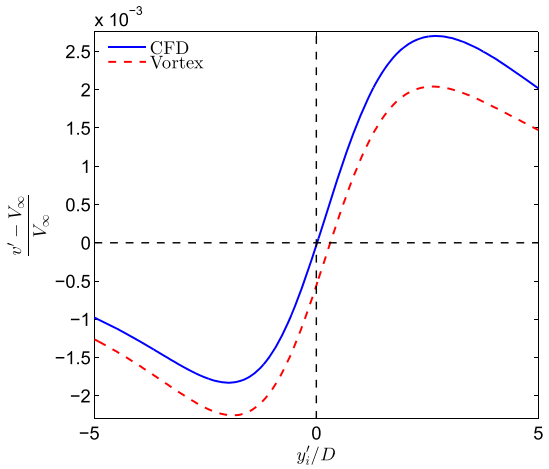

Figure 10. Axially induced velocity along the local y_i' rotor coordinate systems of two imaginary rotors with their centres located at $x/D \pm 3$ predicted by the CFD and vortex model by a rotor located at $x/D = 0$ and an inflow angle θ of 0°. Note that, due to symmetry, the induced velocities overlap at both imaginary rotor locations.

In fact the features found in the ensuing flow-field itself can be explained considering the wake induced velocities. Figure 10 shows the axially induced velocity by an isolated, constantly loaded rotor centred at $x/D = 0$ along the local y-axis of two imaginary rotors centred at $x/D \pm 3$ (i.e. lines that would coincide with the centreline of a neighbouring turbine) at an inflow angle of zero degrees. Note that the induced velocities found at both imaginary rotor locations $x/D \pm 3$ are equivalent, due to symmetry. Both CFD and the vortex model predict positive induced velocities downstream and negative velocities upstream of the rotor plane. In the CFD simulation, the velocities induced downstream are larger than the ones upstream. The opposite is the case for the vortex model, although similar to the comparison in Section 3.2.2 it is mainly an offset differentiating both methods. In fact the vortex velocities are very similar to those of the CFD model only shifted by 5×10^{-4} downwards. In general, the positive induced velocities found for $y/D > 0$ signify that if there was a turbine placed at $x/D \pm 3$, its wake would be advected more quickly under the neighbouring turbine's influence. This would in turn reduce the negative velocity induced by the wake in front of the turbine and diminish the local blockage, hence increase power.

Wind Energ. 2017; **20**:63–77 © 2016 John Wiley & Sons, Ltd.
DOI: 10.1002/we

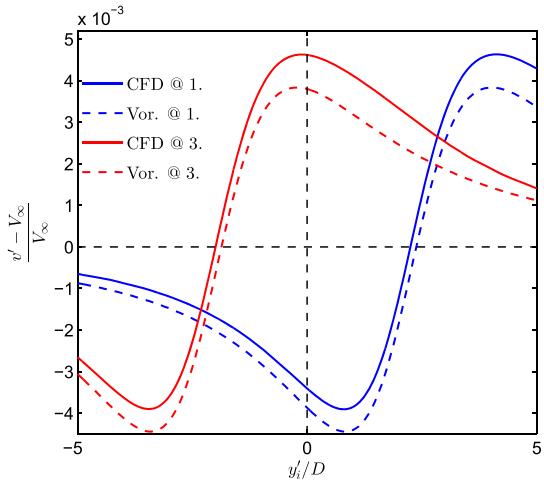

Figure 11. Axially induced velocity along y_i', the local rotor coordinate systems of two imaginary rotors centred at locations $x/D \pm 3$, predicted by the CFD and vortex model by a single rotor centred at $x/D = 0$ and an inflow angle θ of 45°. The imaginary rotors are numbered according to Figure 12, where rotor no. 2 is inducing the velocities presented here.

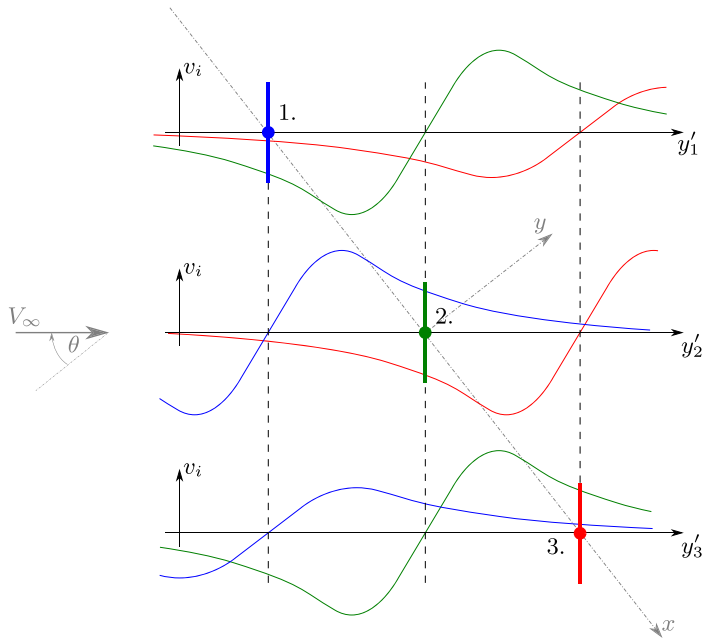

Figure 12. Schematic of three aligned turbines at a non-zero inflow angle and their axially induced velocities, v_i, along each turbine's local x_i'-axis. The profiles are colour coded by the turbine that caused their appearance. The x- and y-axis or alternativley the alignement coordinate system is underlayed.

Figure 11 shows the induced velocities of an isolated turbine at an inflow angle of $\theta = 45°$ along the centreline of two imaginary turbine locations, up- and downstream of an isolated rotor at $x/D \pm 3.0$ (equivalent to rotors no. 1 and 3 in Figure 12). The most obvious feature is that the imaginary rotor upstream ($x/D = -3$) would experience negative induced velocities at the rotor and only far downstream in the wake positive velocities, whereas the rotor downstream ($x/D = 3$) and its wake encounter solely positive velocities. Furthermore, the magnitude of the induced velocities are larger than for a zero inflow angle, as the distance between the centrelines of the neighbouring turbines is reduced. Similarly, to the vortex results at zero inflow angle, its induced velocity profiles are systematically lower than those from the CFD simulations.

In the context of a wind farm, the results presented in Figures 10 and 11 entail an interplay of induced velocities from all turbines. The axial velocities induced by the neighbouring rotors along each turbine's centreline are schematically shown for three aligned rotors for a non-zero inflow angle in Figure 12. The contribution from turbines no. 2 and 3 are not only negative at the position of turbine no.1, but also decelerate its wake. Therefore, the blockage at this turbine is further strengthened. Contrarily turbines no. 1 and 2 only induce positive velocities at turbine no. 3 and accelerate its wake, reducing its blockage. As the magnitude of the induced velocities in front and behind each rotor plane are identical in this figure, they cancel at the central rotor plane. Nevertheless, its wake experiences some deceleration. Figure 12 should really just be taken as a crude visualization of the rotor interactions, as the actual interplay between the wakes and their induced velocities is far more complex, especially when introducing wake rotation and tangentially induced velocities.

As mentioned earlier, in the CFD simulations and the vortex model the magnitude of the induced velocities downstream of the rotor plane do not coincide with those upstream. The shift between the induced velocities predicted by the CFD and vortex model (Figures 10 and 11) in fact explains the shift in the percentage power changes found in Figure 9. Whereas CFD always predicts positive induced velocities everywhere downstream of the rotor plane, the vortex model only predicts these a little further downstream. The diminishing effect of an accelerated wake on the blockage is thus offset by a negative velocity at the rotor in case of the vortex model, which nullifies ΔP. The CFD simulations on the other hand predict a stronger acceleration of the wake and the induced velocity at the rotor is zero, thus there is a net gain in power.

The difference in induced velocities shown in Figure 10 is partly related to the wake expansion predicted by each method. As shown in Figure 13, the wake is expanding more rapidly using the vortex method. This is most likely due to some non-linear effects influencing the interplay of wakes that are not captured by the vortex method as its wakes are inherently axisymmetric. This impacts the induced velocities and in turn wake expansion. In Figure 13 the evolution of the wake radius of the outermost turbine (no. 5) from a CFD simulation at $\theta = 0°$ is shown. The inner side of the wake is expanding less than the outer part, because of the channelling of the flow in-between turbines. This kind of wake straightening towards the inner turbines was also observed numerically and experimentally by McTavish *et al.*.[4] Additionally to the wake straightening, their free expansion in the vertical plane results in slightly elliptical wakes in the CFD computations opposing the assumption of axisymmetry. The wake radii determined for the CFD calculations are estimated from mass conservation, although this might not be a very accurate representation, it demonstrates that the wake radii differ between methods, which

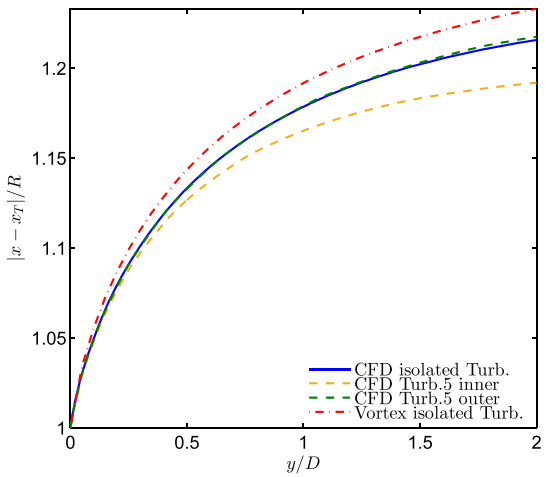

Figure 13. Radial wake expansion for an isolated turbine predicted by CFD simulations and vortex method at $\theta = 0°$, as well as the inner and outer wake expansion in x for turbine 5. All turbines had uniform loading.

.

Wind Energ. 2017; **20**:63–77 © 2016 John Wiley & Sons, Ltd.
DOI: 10.1002/we

might explain some of the discrepancies between the CFD and vortex model. Yet another explanation might be related to the numerical implementation of the actuator disc and grid resolution. Whereas, the forces in the vortex method act over an infinitesimally thin disc, they act over several grid cells in the computational mesh of the CFD simulations, potentially influencing the rate of wake expansion.[19] Furthermore, despite minimizing the domain blockage in the CFD simulations, it cannot be excluded as a potential source causing the offset.

Nevertheless, overall the discrepancies between the models are minute considering that a very simplistic vortex approach was used. It underlines that the vortex model includes all the most important physical attributes for studying the problem at hand.

5. CONCLUSION

The blockage induced by a row of five wind turbine rotors and its impact on power production was determined from numerical simulations with a CFD and vortex model for varying inflow angles.

Noticeable changes in the individual turbine power were found for both methods in the range of -1% to 2%, where the change in power increased in-line with the inflow angle. The two models agree on the overall trends, although the CFD results predict a constantly larger power than the vortex model. The offset was determined to lie at approximately 0.5%. The CFD model predicts a relatively constant average increase in the power across all turbines with inflow angle at about 0.57%, whereas, the vortex model predicts no change, meaning that the losses at one turbine are balanced out by another. The exact reason for this discrepancy could not be determined. Nevertheless, the turbines are influencing each other in a consistent manner across the numerical model, which indicates that noticeable changes in power, at least numerically, do exist at test sites. The changes in power are linked to the turbine wakes inducing velocities at the other turbine locations. This in turn affects the velocity at the rotor plane directly and indirectly by affecting the advection velocity of the wakes, that will determine the thrust exerted by each rotor on the incoming flow.

Future work should study the effect of the ground, including a more realistic flow with an atmospheric boundary layer. The exact power curve measurement procedures should also be included to assess the actual impact of our findings on real world measurements. Furthermore, the cause for the discrepancy between the vortex and CFD model should be analysed in more detail, potentially with a vortex particle code. At a later stage, it might be possible to compare the results with measurements from real test sites, although it will be challenging to isolate the effect of upstream blockage from field measurements.

ACKNOWLEDGEMENTS

This work was performed as part of the UniTTe project (unitte.dk) led by DTU Wind Energy and financed by The Innovation Fund Denmark (1305-00024B). Further to the authors R. Wagner (DTU Wind Energy) contributed to this work through her valuable insights into power curve validation procedures. Computational resources were provided by the Risø DTU central computing facility.

APPENDIX A. A SIMPLE VORTEX MODEL INCLUDING WAKE EXPANSION

The model used in the present work is a modified version of the model proposed by Øye.[18] In the following the basics of the model will be briefly described.

A.1. Rotor circulation and loads

The model considers an idealized wind turbine where each blade is represented by a line with a constant circulation of Γ_b. The flow field is assumed incompressible, irrotational and inviscid so the forces per unit span of the the rotating lines is given by the the Kutta-Joukowski relation:

$$\boldsymbol{f}_b = \rho \boldsymbol{V}_{\mathrm{rel}} \times \Gamma_b \tag{A.1}$$

where $\boldsymbol{V}_{\mathrm{rel}}$ is the local velocity relative to the blade and ρ denotes density. The local force per unit area in the radial, tangential (driving force) and axial direction, respectively then becomes

$$\boldsymbol{F} = \begin{bmatrix} F_r \\ F_\theta \\ F_z \end{bmatrix} = \frac{N_b \boldsymbol{f}_b dr}{2\pi r dr} \frac{\rho \Gamma \Omega}{2\pi} \begin{bmatrix} 0 \\ (V_\infty + W_z)/(\Omega r) \\ 1 - W_\theta/(\Omega r) \end{bmatrix} \tag{A.2}$$

Here, $\Gamma = n_b\Gamma_b$ is the total circulation of all n_b blades, Ω is the rotor rotational velocity, r is the radius where the forces are evaluated and V_∞ is the free stream velocity, which is assumed to be parallel to the rotor axis. W_z and W_θ are the induced velocities in the axial and tangential directions at the rotor plane, respectively.
In the following, we now assume that the rotational speed of the rotor tends to infinity and the total circulation to zero, such that their product becomes a finite value. In that case, only the axial force component remains and equation (A.2) simplifies to:

$$F_z = \frac{\rho\Gamma\Omega}{2\pi} \tag{A.3}$$

Note that in order to retain a finite value of the rotor force, the product $\Gamma\Omega$ needs to be finite, i.e. $\Gamma \to 0$.

A.2. Modelling the wake

The present model is a so-called vortex model. Thus, the velocity is determined from the vorticity in the wake using the Biot-Savart law. Because the vortex strength is constant along each blade, vorticity will only be trailed from the roots and tips. Because the incoming wind is further assumed to be uniform and aligned with the rotor axis, the root vortices merge to a single axial vortex of strength Γ, while the tip vortices forms a circular tube of vorticity with increasing radius as the wake expands. However, a consequence of the infinitely high rotational speed is that the strength of the root vortex tends to zero (as shown above), i.e. there is no wake rotation and that the density of the tip vorticity sheet only has a tangential component, $\gamma_t = d\Gamma/dz$. The value of γ_t is most easily obtained by acknowledging that the vortex strength between two windings of the tip vortex produced by one of the blades is Γ, i.e.:

$$\gamma_t(z) = \frac{\Gamma\Omega}{2\pi V_a(z)} \tag{A.4}$$

where V_a is the axial velocity at which the tip vortices are transported.

As in the original model by Øye[18] the near wake, where the wake is expanding, is modelled using discrete vortex rings, while the far wake, is modelled using a half-infinite circular vortex cylinder with constant γ_t and radius, see Figure A.1. When the induction from each vortex ring as well as from the cylinder is known, then the total induced velocity W everywhere is determined by simply adding all contributions together.

A.2.1. Modelling the near wake

The near wake is modelled using discrete vortex rings, where each ring are allowed to expand freely. The velocity induced by a vortex ring in a point P is:[18]

$$w_z(r,z) = \frac{\Gamma_i}{2\pi\sqrt{(r+R)^2+z^2}}\left(\frac{R^2-r^2-z^2}{(r-R)^2+z^2}\cdot E(k^2(z)) + K(k^2(z))\right) \tag{A.5}$$

$$w_r(r,z) = \frac{\Gamma_i}{2\pi\sqrt{(r+R)^2+z^2}}\frac{z}{r}\left(\frac{r^2+R^2+z^2}{(r-R)^2+z^2}E(k^2(z)) - K(k^2(z))\right) \tag{A.6}$$

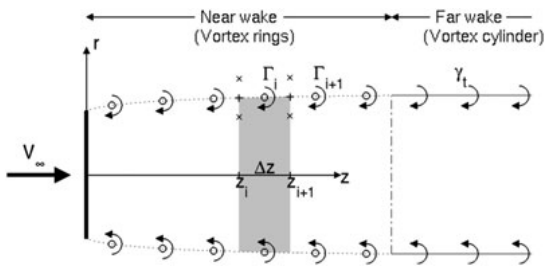

Figure A.1. Model of near and far wake with discrete vortex rings and a vortex cylinder, respectively.

Wind Energ. 2017; **20**:63–77 © 2016 John Wiley & Sons, Ltd.
DOI: 10.1002/we

with

$$k^2(z) = \frac{4Rr}{(r+R)^2 + z^2}$$

where r and z are the radial and axial coordinates, respectively of P relative to the ring center, Γ_i is the strength of the ring and R is the radius of the ring, which is equal to the local wake radius. Finally, E and K are the complete elliptic integral of first and second kind, respectively.
As shown in Figure A.1, each ring represents a segment of the wake of length Δz and because the ring is positioned in the center of the segment its strength is

$$\Gamma_i = \frac{1}{2}\left(\gamma_t(z_i) + \gamma_t(z_{i+1})\right)\Delta z \tag{A.7}$$

In order to get the vortex density, we need to determine V_a. As suggested by Øye[18] we assume that V_a is the average of the velocity on each side of the wake surface. Thus for a downstream position z_i, we get:

$$V_a(z_i) = V_\infty + \frac{1}{2}\left(W_z(R_w(z_i) + \Delta r, z_i)) + W_z(R_w(z_i) - \Delta r, z_i))\right) \tag{A.8}$$

where Δr is a small distance selected by the modeller (indicated with a "×" in Figure A.1) and W_z is the total induced velocity from all vortex rings as well as from the vortex cylinder, representing the far wake.
The local wake radius is computed from the continuity equation and the fact that the wake surface is a streamtube, which implies that the flow through the rotor disc is the same as through each wake cross-section. Thus, the local wake radius at $z = z_i$ is

$$R_w(z_i) = R\sqrt{\frac{V_\infty + \bar{W}_z(0)}{V_\infty + \bar{W}_z(z_i)}} \tag{A.9}$$

where R is the radius of the rotor and $\bar{W}_z$ is the average induced velocity over the wake cross-section at $z = z_i$ downstream of the rotor, i.e.

$$\bar{W}_z(z_i) = \frac{1}{\pi R_w(z_i)^2}\int_0^{2\pi}\int_0^{R_w(z_i)} W_z(r,\theta,z_i) r dr d\theta \tag{A.10}$$

Here, the dependency of W_z on azimuth position θ is explicitly shown because the present model is also used for computing multiple turbines next to each other where the velocity in the wake is not axisymmetric. Since the induced velocity depends on γ_t, which in turn depends on V_a and the local wake radius the equations (A.7)–(A.10) need to be solved iteratively to determine the the strength and radius of the vortex rings.

A.2.2. Modelling the far wake

Going downstream from the rotor the wake gradually stops expanding and therefore the far wake is modelled with a half infinite cylinder of constant γ_t and radius, both equal to the values of the last section in the near wake. Øye suggested to approximate the contribution from the cylinder to the total induction as the induction along its centreline. Here, we instead use the full velocity field induced by the cylinder, which in a point P is:[20]

$$w_r(r,z) = -\frac{\gamma_t}{2\pi}\sqrt{\frac{R}{r}}\left[\frac{2-k^2(z)}{k(z)}K\left(k^2(z)\right) - \frac{2}{k(z)}E\left(k^2(z)\right)\right] \tag{A.11}$$

$$w_z(r,z) = \frac{\gamma_t}{2}\left[\frac{R-r+|R-r|}{2|R-r|} + \frac{zk(z)}{2\pi\sqrt{rR}}\left(K\left(k^2(z)\right) + \frac{R-r}{R+r}\Pi\left(k^2(0), k^2(z)\right)\right)\right] \tag{A.12}$$

where r and z is the radial and axial position of P relative to the center of the cylinder front, R is the radius of the cylinder which is equal to the far wake radius and Π is the complete elliptic integral of the third kind. The solution for the velocity near at the axis of the cylinder is:

$$w_r(0,z) = 0; \qquad w_z(0,z) = \frac{\gamma_t}{2}\left[1 + \frac{z}{\sqrt{R^2+z^2}}\right] \tag{A.13}$$

For $r = R$ the axial induction is

$$w_z(R,z) = \frac{\gamma_t}{4} + \frac{\gamma_t}{2}\frac{zk(z)}{2\pi\sqrt{rR}}K\left(k^2(z)\right) \tag{A.14}$$

A.3. Model set-up

The accuracy of the above model depends on the chosen streamwise extent of the near wake, the spacing between the vortex rings, Δz, the distance Δr used to compute the transport velocity, equations (A.8), and the method used for computing $\bar{W}_z(z)$.

In this paper we use $\Delta z = \Delta r = R/10$ as suggested by Øye.[18] Here, the near wake length is here set to $30R$, which is significantly longer than the $5R$ used by Øye. The extended near wake length is necessary to accurately capture the mutual effect, the near wake of each turbine has on each other. In the simulation of a single turbine Øye [18] assumes that the velocity at 70% radius is representative of the average velocity at each cross-section, i.e. $\bar{W}_z(r,z) = W_z(0.7R_w, z)$. Here, we instead approximate $\bar{W}_z(z)$ by computing the integrals in equation (A.10) using the trapezoid rule with a discretization of $dr = R_w/10$ and $d\theta = \pi/2$. Thus the average velocity over the entire cross-section is estimated as the average of the integrated velocity at four azimuthal positions corresponding to the two vertical and horizontal directions. The use of several azimuthal positions is intended to take into account that the flow is not axisymmetric when considering several turbines next to each other.

REFERENCES

1. *IEC 61400-12-1:2005. Power performance measurements of electricity producing wind turbines*.
2. Troldborg N, Gaunaa M, Mikkelsen RF. Actuator disc simulations of influence of wind shear and ground proximity on power production of wind turbines. In *Proceedings of the V European Conference on Computational Fluid Dynamics, ECCOMAS 2010*, Pereira J. C. F. Sequeira A. Pereira J.M.C. (eds): Lisbon, 2010.
3. McTavish S, Rodrigue S, Feszty D, Nitzsche F. An investigation of in-field blockage effects in closely spaced lateral wind farm configurations. *Renewable Energy* 2013; **59**: 128–135.
4. McTavish S, Feszty D, Nitzsche F. An experimental and computational assessment of blockage effects on wind turbine wake development. *Wind Energy* 2014; **17**: 1515–1529.
5. Mitraszewski K, Hansen KS, Nygaard NG, Réthorè PE. Wall effects in offshore wind farms. *Torque 2012* 2012.
6. Medici D, Ivanell S, Dahlberg J, Alfredsson PH. The upstream flow of a wind turbine: blockage effect. *Wind Energy* 2011; **14**: 691–697.
7. Sørensen NN. General purpose flow solver applied to flow over hills, *Ph.D. Thesis*, RisøNational Laboratory, 1995.
8. Michelsen JA, Basis3d - a platform for development of multiblock pde solvers. *Technical Report*, Department of Fluid Mechanics, Technical University of Denmark, DTU, 1994.
9. Michelsen JA, Block structured multigrid solution of 2d and 3d elliptic pdes. *Technical Report*, Department of Fluid Mechanics, Technical University of Denmark, DTU, 1994.
10. Patanker SV, Spalding DB. A calculation procedure for heat, mass and momentum transfer in three-dimensional parabolic flows. *International Journal of Heat and Mass Transfer* 1972; **15**: 1787–1806.
11. Leonard BP. A stable and accurate convective modelling procedure based on quadratic upstream interpolation. *Computer Methods in Applied Mechanics and Engineering* 1979; **19**: 59–98.
12. Réthoré PE, Sørensen NN. A discrete force allocation algorithm for modelling wind turbines in computational fluid dynamics. *Wind Energy* 2012; **15**: 915–926.
13. Réthoré PE, Sørensen NN. Verification and validation of an actuator disc model. *Wind Energy* 2013; **17**(6): 919–937.
14. Troldborg N, Sørensen N, Réthoré PE, van der Laan M. A consistent method for finite volume discretization of body forces on collocated grids applied to flow through an actuator disk. *Computers & Fluids* 2015; **119**: 197–203.
15. AIAA Paper 93-2906. AIAA Fluid Dynamics Conference, Orlando, FL; United States, 24th; 6-9 Jul. 1993.
16. Jonkerman J, Butterfield S, Musial W, Scott G, Definition of a 5-mw reference wind turbine for offshore system development. *Technical Report*, NREL, 2009.
17. Meyer Forsting A, Troldborg Niels. The effect of blockage on power production for laterally aligned wind turbines. *Journal of Physics: Conference Series (Online)* 2015; **625**: 012029.
18. Øye S. A simple vortex method. *Proceedings of the Third IEA Symposium on the Aerodynamics of Wind Turbines*. Institute of Physics Publishing, Harwell, 1990; 4.1–4.15.

19. Troldborg N, Zahle F, Réthoré PE, Sørensen NN. Comparison of wind turbine wake properties in non-sheared inflow predicted by different computational fluid dynamics rotor models. *Wind Energy* 2015; **18**(7): 1239–1250.
20. Branlard E, Gaunaa M. Cylindrical vortex wake model: right cylinder. *Journal of Wind Energy* 2015; **18**(11): 1973–1987.

ARTICLE 9

VALIDATION OF A CFD MODEL WITH A SYNCHRONIZED TRIPLE-LIDAR SYSTEM IN THE WIND TURBINE INDUCTION ZONE

JOURNAL ARTICLE

Wind Energy, Vol. 20, 2017, pp. 1481-1498 DOI

Main author

This journal publication is the backbone of the thesis, as it validates the CFD model with lidar measurements taken in the induction zone of a full-scale wind turbine. A new validation method was developed for this purpose. Various measurement uncertainties are quantified and propagated throughout all data processing steps. This is the first validation covering such dimensions and the first to use multi-lidar data. The complexity of the measurements, the associated uncertainties and their propagation extended the review process.

WIND ENERGY

WIND ENERGY
Wind Energ. 2017; **20**:1481–1498
Published online 14 March 2017 in Wiley Online Library (wileyonlinelibrary.com). DOI: 10.1002/we.2103

RESEARCH ARTICLE

Validation of a CFD model with a synchronized triple-lidar system in the wind turbine induction zone

A. R. Meyer Forsting, N. Troldborg, J. P. Murcia Leon, A. Sathe, N. Angelou and A. Vignaroli

Department of Wind Energy, Technical University of Denmark, Frederiksborgvej 399, 4000, Roskilde, Denmark

ABSTRACT

A novel validation methodology allows verifying a CFD model over the entire wind turbine induction zone using measurements from three synchronized lidars. The validation procedure relies on spatially discretizing the probability density function of the measured free-stream wind speed. The resulting distributions are reproduced numerically by weighting steady-state Reynolds averaged Navier-Stokes simulations accordingly. The only input varying between these computations is the velocity at the inlet boundary. The rotor is modelled using an actuator disc. So as to compare lidar and simulations, the spatial and temporal uncertainty of the measurements is quantified and propagated through the data processing. For all velocity components the maximal difference between measurements and model are below 4.5% relative to the average wind speed for most of the validation space. This applies to both mean and standard deviation. One rotor radius upstream the difference reaches maximally 1.3% for the axial component. © 2017 The Authors. *Wind Energy* Published by John Wiley & Sons, Ltd.

KEYWORDS
validation; lidar; CFD; blockage effect; upstream flow; induction zone; uncertainty quantification

Correspondence
A. R. Meyer Forsting, Department of Wind Energy, Technical University of Denmark, Frederiksborgvej 399, 4000 Roskilde, Denmark.
E-mail: alrf@dtu.dk

Received 21 December 2015; Revised 8 February 2017; Accepted 13 February 2017

NOMENCLATURE

$\mathbf{V}$	velocity vector $\mathbf{V} = \{u, v, w\}$
$\mathbf{x}$	position vector $\mathbf{x} = \{x, y, z\}$
$\mathcal{N}(\mu, \sigma)$	normal distribution with mean μ and standard deviation σ
$V_\infty^{\min}, V_\infty^{\max}$	boundaries of validation space
$f(\bullet;\bullet)$	probability density function (pdf), semi-colon separates sample-space and function variables
i	triple-lidar data point index
j	triple-lidar cell index
k	index of wind speed bin
p	participation factor (equation (18))
θ	misalignment angle between rotor and triple-lidar reference frame
σ_ϕ	standard deviation of a quantity ϕ
$\bar{\phi}$	mean of a quantity ϕ
n_ϕ	total number of points discretizing ϕ
$\bullet_{\mathrm{CFD}}$	quantity derived from CFD simulations
$\bullet_{3l}$	quantity derived from triple-lidar measurements
$\bullet_\infty$	free-stream reference
$\bullet'$	triple-lidar coordinate system

1. INTRODUCTION

Power generating wind turbines exert a thrust force on the incoming flow, inducing a deceleration in the upstream region close to the rotor. The area in which this effect is noticeable is commonly referred to as the induction zone. The IEC standards for power performance measurements[1] assume this region to have a negligible effect beyond four radii (R) upstream, such that velocity measurements at hub height beyond this distance should give a reliable indication of the free-stream velocity on which to base a turbine's power curve. This free-stream velocity is an artificial construct as it is defined as the velocity that would have been measured at the rotor centre if there was no turbine. Measuring the power curve reference velocity at least $4R$ away from the turbine to avoid the induction zone, might however violate the very definition of the free-stream. Especially when considering the large rotor dimensions reached nowadays ($R > 80$ m), the flow evolution over this distance and the resulting time lag might decorrelate the measured wind field and the one interacting with the wind turbine. This is also the case for turbines in complex surroundings, which include mountainous terrain, forest or wind farms. Measuring closer to the turbine and thus inside the induction zone would partly offset the uncertainty from flow evolution. Replacing met masts with nacelle-mounted lidars would allow such measurements without disturbing the flow approaching the turbine. Wagner *et al.*[2] established that this is a viable approach to power curve validation. Nacelle lidars are furthermore tracking the wind direction, potentially decreasing the time for acquiring a full power curve, as more wind sectors become available. Likewise, it can become an input to preview-based control strategies, enabling the turbine to dynamically adapt to the incoming wind field, as suggested by Schlipf *et al.*[3] Nevertheless, measuring inside the induction zone and predicting the wind field evolution requires a robust model capturing the flow upstream of a turbine accurately. Medici *et al.*[4] compared a linear vortex model with wind tunnel measurements and a computational fluid dynamics (CFD) simulation. They extracted the flow-field of three small-scale wind turbine models from laser particle image velocimetry and hot wire measurements. The final inter-comparison along the turbines axis of symmetry showed matching trends. Howard and Guala[5] similarly compared wind tunnel experiments and the simple vortex sheet model but furthermore included lidar field measurements. This work was spatially extended by Simley *et al.*,[6] measuring with a synchronized triple-lidar system over half a turbine rotor. Similar to the work of Medici *et al.*,[4] these studies showed agreeing trends, but the model's validity was not proven. Simley's work involving the triple-lidar system formed the basis for a measurement campaign in the inflow region of a 500 kW wind turbine in the summer of 2014 as part of the UniTTe project (www.unitte.dk). This lidar system captured all three velocity components over a large area, providing a unique dataset for model validation. In this paper, a probabilistic methodology for validating a high-fidelity CFD model with this dataset is presented. The inherently variable nature of the wind requires special treatment, such that the boundary conditions of the field experiment can be matched in the numerical simulations.

Failing to incorporate the variability of the wind speed ultimately leads to similarly inconclusive results regarding model validity as those of Medici[4] and Howard[5] as shown in Figure 1.

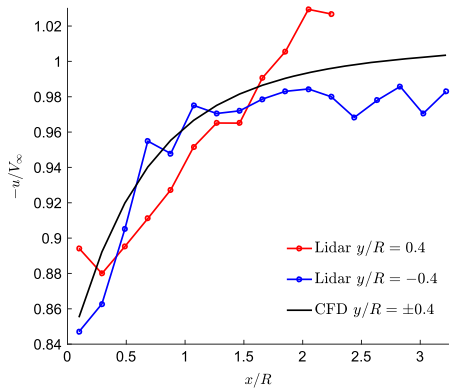

Figure 1. Axial velocity evolution upstream of wind turbine along two lines perpendicular to the rotor. The turbine is located at $x/R = 0$. The lidar data were averaged over a 30 min period with a free-stream velocity of 10.3 m/s. This velocity was set as inlet condition to the steady-state CFD (RANS-AD) simulation. [Colour figure can be viewed at wileyonlinelibrary.com]

Wind Energ. 2017; **20**:1481–1498 © 2017 The Authors. *Wind Energy* Published by John Wiley & Sons, Ltd.
DOI: 10.1002/we

These results underwent exactly the same post-processing as the data presented in Section 6 of this paper, excluding the probabilistic validation procedure. Instead, the lidar data were averaged over a 30 min period and compared with a CFD simulation at the free-stream velocity of 10.3 m/s. Again, the results in Figure 1 follow the same trend: as the flow approaches the turbine ($x \to 0$), the axial velocity component (u) diminishes, owing to the turbine-induced blockage. However, whereas the line $y/R = -0.4$ appears to match the numerical simulations, the other line shows strong disagreement with regards to the nature of this deceleration. This figure only serves as an example of a phenomenon registered across all measurements and is not limited to temporal averages. Any kind of sorting and averaging introduces some bias into model validation, by making the validation space a function of the sorting process. This encourages tuning the sorting parameters and limiting the validation space, which jeopardizes proper model validation. Note that the development of a validation procedure that utilizes data to its full extent also became a necessity owing to the scarcity of measurements. Apart from the validation method, several post-processing levels of the triple-lidar data are needed that propagate the measurement uncertainty. The complexity of the numerical simulations was reduced by employing a steady-state Reynolds Averaged Navier-Stokes (RANS) model and representing the rotor by an actuator disc. Validating this high-fidelity model is expected to allow the development of less computationally expensive methods.

2. VALIDATION METHODOLOGY

The validation approach relies on incorporating the inherently variable nature of field measurements into the numerical model. This is achieved by treating the boundary conditions of the experiment stochastically, in particular the estimated free-stream velocity, as it essentially determines the thrust exerted by the turbine. The free-stream velocity is a theoretical quantity that describes the velocity at the rotor centre as if there was no turbine. Therefore, it is only a function of time $V_\infty(t)$. Assuming that the rotor thrust, and with it the induction zone, is fully determined by the instantaneous free-stream velocity, the velocity field upstream can be expressed as a function of free-stream velocity, space and time $\mathbf{V}(V_\infty, \mathbf{x}, t)$. A measurement instrument with infinite spatial and temporal resolution would sample exactly this velocity. Assuming that this device periodically revisits the same probe locations after a time Δt_s, the following relationship can be established: $(x(t_0 + l\Delta t_s), y(t_0 + l\Delta t_s)) = (x_0, y_0)$, where l denotes the period number. This point will have seen free-stream velocities of $V_\infty(t_0 + l\Delta t_s)$. If the device's probe location moves in time, then with $\Delta t < \Delta t_s$, a new measurement location is obtained $(x(t_0 + \Delta t + l\Delta t_s), y(t_0 + \Delta t + l\Delta t_s)) = (x_{\Delta t}, y_{\Delta t})$. Equally, the free-stream velocity would be sampled with a time shift $V_\infty(t_0 + \Delta t + l\Delta t_s)$. Therefore each measurement point in $\mathbf{x}$ has its own free-stream time series that depends on the number of periods l as shown in Figure 2. Finally, grouping all measurements for each point in space over time, the free-stream velocity and the measured velocities can be expressed with probability density functions $f(V_\infty; \mathbf{x})$ and $f(\mathbf{V}; \mathbf{x})$. Note that f is a function of $\mathbf{x}$, but a density over the sample-space variables to the left of the semi-colon. This notation is used throughout the paper.

Two free-stream pdfs and their approximation by a histogram with n_{V_∞} number of free-stream velocity bins are shown schematically in Figure 3. Each bin represents one CFD simulation with a deterministic boundary condition given by V_∞. By weighting the CFD solutions $\mathbf{V}_{\mathrm{CFD}}(V_\infty, \mathbf{x})$ according to $f(V_\infty; \mathbf{x}), f(\mathbf{V}; \mathbf{x})$ can be reconstructed numerically. Mean and

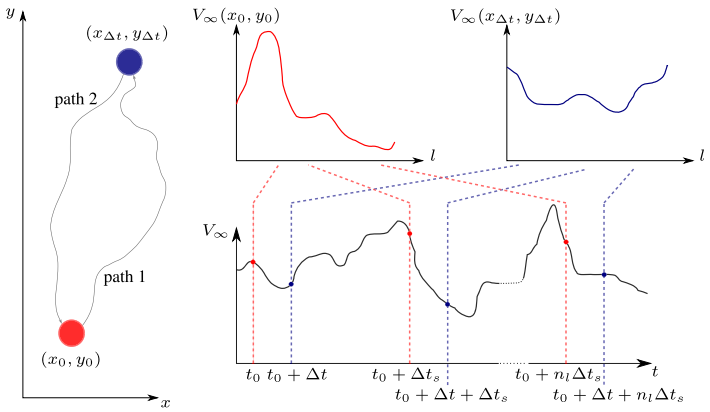

Figure 2. Sampling of the free-stream velocity V_∞ at two different points in time and space. [Colour figure can be viewed at wileyonlinelibrary.com]

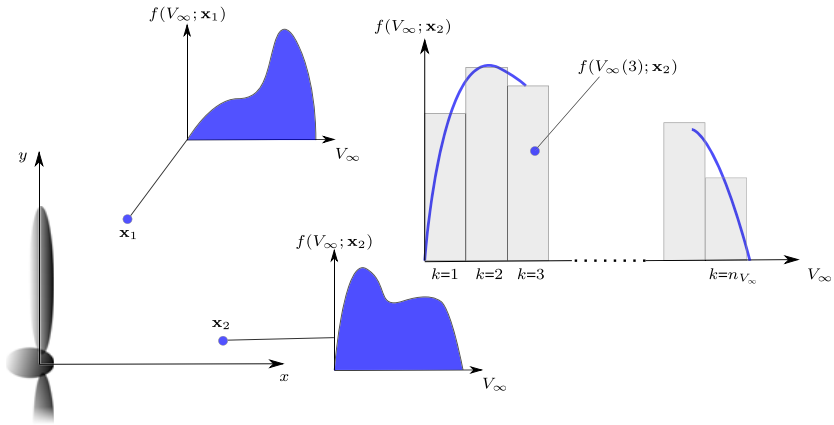

Figure 3. Probability density functions of the free-stream velocity at two measurement locations in the induction zone and their discretization by a histogram with n_{V_∞} number of bins. [Colour figure can be viewed at wileyonlinelibrary.com]

variance of the resulting $f(\mathbf{V}_{\mathrm{CFD}};\mathbf{x})$ are given by

$$\bar{\mathbf{V}}_{\mathrm{CFD}}(\mathbf{x}) = \sum_{k=1}^{n_{V_\infty}} f(V_\infty(k);\mathbf{x})\,\mathbf{V}_{\mathrm{CFD}}(V_\infty(k),\mathbf{x}) \tag{1}$$

$$\sigma^2_{\mathbf{V}_{\mathrm{CFD}}}(\mathbf{x}) = \sum_{k=1}^{n_{V_\infty}} f(V_\infty(k);\mathbf{x})[\mathbf{V}_{\mathrm{CFD}}(V_\infty(k),\mathbf{x}) - \bar{\mathbf{V}}_{\mathrm{CFD}}(\mathbf{x})]^2 \tag{2}$$

These measures can be compared directly with the corresponding ones of $f(\mathbf{V};\mathbf{x})$ to evaluate the validity of the CFD model. The centre of each k^{th} bin is given by

$$V_\infty(k) = V_\infty^{\min} + \frac{V_\infty^{\max} - V_\infty^{\min}}{n_{V_\infty}}\left(k - \frac{1}{2}\right) \tag{3}$$

In this equation, $k = 1, 2, \ldots, n_{V_\infty}$, where $V_\infty^{\min}$ and $V_\infty^{\max}$ represent the boundaries of free-stream velocities over which the validation is performed. The reconstruction of a distribution from a histogram is also known as the *simple histogram method*. This method originated from simulating dispersion with steady-state RANS and is commonly used to incorporate the stochastic variability of wind direction over time.[7,8] The advantage of combining time-invariant solutions is the possibility of using simpler RANS models in combination with an actuator disc for numerically solving the flow. A more accurate model would not necessarily yield any better results, as the larger uncertainty in the model inputs would conceal any gain in accuracy in the outputs. The fundamental improvement this method provides is the independence of the validation from any kind of data sorting process—usually done in time and/or for wind speeds—which increases the confidence in the validation itself. Additionally, it allows for the use of all acquired data at once and avoids splitting measurements into smaller subsets, thus using the available data fully. Another important feature is the complete decoupling of experimental and numerical methods, as the numerical model does not use any other input from the measurements apart from the free-stream velocity. As a consequence, the model is not fitted to the measurements; instead, the boundary conditions are matched. Note that an essential part to this methodology is the estimation of the free-stream time series, which will be discussed in Section 4.4.

3. DATA PROCESSING OVERVIEW

A triple-lidar captures complex flow patterns over large areas, bringing with it added complexity in its data analysis, especially in terms of uncertainty quantification. This is reflected in the coming sections. Therefore, Figure 4 shows the connection between different processes that correspond to certain sections of this paper. The processes are either associated with the triple-lidar or the CFD model and grouped accordingly into Sections 4 and 5.

Wind Energ. 2017; **20**:1481–1498 © 2017 The Authors. *Wind Energy* Published by John Wiley & Sons, Ltd.
DOI: 10.1002/we

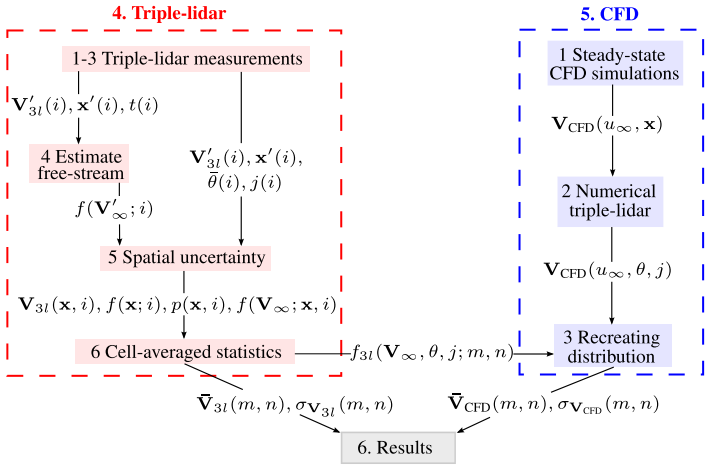

Figure 4. Validation process chain. Each process is outlined in the section denoted by the number in each block. [Colour figure can be viewed at wileyonlinelibrary.com]

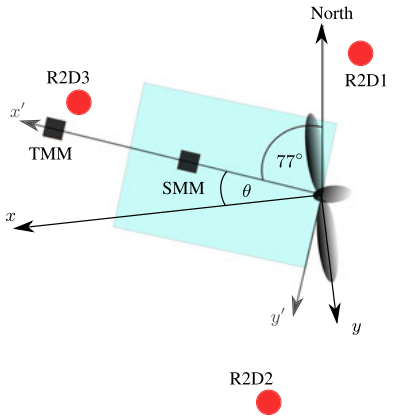

Figure 5. Schematic of the experimental setup. ●= lidars; ■ = met masts (T = tall, S = short); shaded rectangle = lidar scanning area. The triple-lidar measurements are misaligned with the rotor by θ. [Colour figure can be viewed at wileyonlinelibrary.com]

4. TRIPLE-LIDAR

4.1. Experimental setup

4.1.1. Measurement layout.

The Nordtank NTK 500 wind turbine is located at the southern edge of the DTU Risø campus, just off the Roskilde Fjord (N 55° 41′ 04″, E 012° 05′ 48″). The triple-lidar coordinate system had the turbine's base at its origin. Its x-axis was aligned with the prevailing wind direction of 283°, passing through both the tall and short met masts (TMM/SMM). Coming from this direction, the flow passes from fjord to land, up a gentle slope. The overall layout is pictured schematically in Figure 5. The exact coordinates of all instruments are listed in Table I. The TMM was equipped with several instruments along its entire height of 57 m, whereas the SMM only had a sonic anemometer at its tip of 30.5 m. The triple-lidar scanning pattern sliced the induction zone horizontally at hub height (36 m), covering the entire rotor diameter. The prescribed scanning trajectory thus encompassed a plane of 64 m × 40 m ($3.1R \times 2.0R$) and took 15 s to complete, as shown in Figure 6. The

Table I. Coordinates of instrument locations.

	x' [m]	y' [m]	z' [m]
NTK	0.00	0.00	0.00
R2D1	−0.94	−34.6	0.60
R2D2	−1.01	49.6	2.09
R2D3	78.7	5.40	−0.75
SMM	46.8	0.12	−1.61
TMM	92.00	−0.23	−3.03

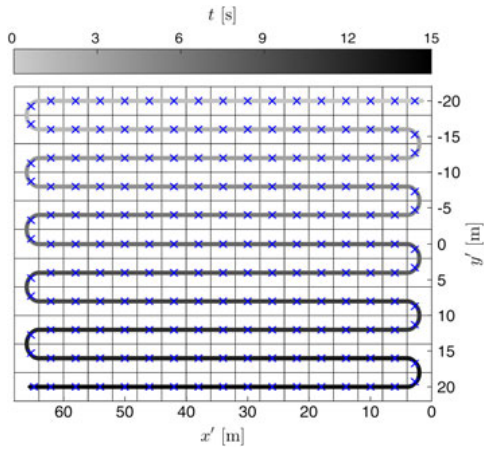

Figure 6. Triple-lidar grid and sampling path. x = Cell - averaged points. [Colour figure can be viewed at wileyonlinelibrary.com]

trajectory was fixed during the entire experiment and was thus misaligned with the rotor at times by an angle θ. As in the measurements performed by Simley,[6] the lidars were positioned, such that their line-of-sight would intersect the main wind vector far from perpendicular and minimize their probe volumes.

4.1.2. Nordtank NTK 500/41.

The stall-regulated turbine is equipped with three 20.5 m blades and has a hub height of 36 m. The turbine is operational between wind speeds of 4 and 25 m/s and maximally generates 500 kW. Under these conditions, the rotor performs approximately 27.0 rotations per minute (rpm). Strain gauges and accelerometers are located at several points along the main shaft, blades and tower. For a more detailed description of the sensory equipment and the turbine, see Hansen *et al.*[9] All sensors, including the yaw sensor, were calibrated prior to the experiment.[10]

4.2. Doppler spectra processing

The lidars sample the backscattered light signal at 100 MHz and compute 2×10^5 Doppler spectra per second by fast Fourier transformation. Each spectrum is split into 256 frequency bins, with a Nyquist frequency of 50 MHz the bin width corresponds to $\Delta f = 195$ kHz. The velocity step for each bin is directly related to it by $\Delta v_{los} = \frac{1}{2}\Delta f \lambda = 0.153$ m/s, where $\lambda = 1.56$ μm represents the laser wavelength. So as to increase the signal-to-noise ratio, all 1.6×10^4 Doppler spectra falling into one 4 m ×4 m cell were averaged (Figure 6). As a result, only a single v_{los} remained per lidar and cell. An ideal scan therefore contained 187 data points. The exact procedure to derive velocities from lidar Doppler spectra, including various filtering operations, is outlined in detail by Angelou *et al.*[11,12] The volume-averaged estimates of the velocity components in each cell can be found from the v_{los} in combination with the beam direction unit vectors as described by Simley.[6] Despite the filtering operations at a spectral level some erroneous measurements remained in the velocity data. A gradient-based spike detection algorithm[13] was used in combination with manual filtering, removing on average 2% and maximally 3% of the data points. Denoting the triple-lidar by 3l and the measurement point index by i, the velocity vector at location $\mathbf{x}'(i)$ and time $t(i)$ is $\mathbf{V}'_{3l}(i)$.

Wind Energ. 2017; **20**:1481–1498 © 2017 The Authors. *Wind Energy* Published by John Wiley & Sons, Ltd.
DOI: 10.1002/we

4.3. Lidar measurement summary

Over 11 days, 11.5 h of data were acquired. The turbine was operational during 5 h of these measurements, and only those were considered in the following analyses, totalling 197×10^3 valid triple-lidar points. A summary of the meteorological conditions during each 30 min measurement period is presented in Table II. For further background, information on the measurement campaign and its methods consult the UniTTe reports[10,14] and for a full description of the triple-lidar measurement system refer to Mikkelsen.[15]

4.4. Estimating the free-stream velocity probability density function

Usually velocity data from the TMM would be considered representative of the free-stream. However, its signal suffers from decorrelation with some of the cells in the triple-lidar grid. With a strong cross-flow, relative to the experimental setup, a gust encountered at the TMM for instance might not be encountered by any of the triple-lidar cells. Another important factor is the varying time-lag between the met mast and the triple-lidar velocity signal. Therefore, the triple-lidar data themselves are used to determine the spatial and temporal variation of the free-stream velocity. The idea is to derive the free-stream conditions in all 187 grid cells of each triple-lidar scan from measurements taken furthest from the rotor; as there, the induced velocities are lowest. As the estimation process is in itself uncertain the free-stream velocity is treated as a stochastic process. Thus, each triple-lidar data point is associated with a unique free-stream velocity pdf. An added benefit over a deterministic approach is that it mediates the impact of assumptions made in the validation methodology.

Table II. Summary of the usable 30 min triple-lidar measurement periods with a total of 1117 trajectory scans comprising 197×10^3 valid triple-lidar points.

#	Date [dd/mm]	Start time [hh:mm]	$\bar{V}_\infty$ [m/s]	TI [%]	WD [°]
1	06/08	08:16	3.89	13.6	298
2	20/08	12:26	10.3	10.6	255
3	21/08	10:17	7.39	14.0	246
4	25/08	10:40	6.06	13.8	249
5	27/08	08:03	5.39	13.2	292
6	25/09	09:35	9.59	11.3	271
7	27/09	12:11	9.49	14.1	275
8	27/09	13:50	8.43	11.1	274
9	27/09	15:28	8.16	12.1	277
10	02/10	14:01	2.64	9.96	282

The values in the *4th*–*6th* column were determined from the large met mast at hub height and denote: mean wind speed, turbulence intensity and wind direction. Note that the scanning trajectory was fixed and aligned with a wind direction of 283°.

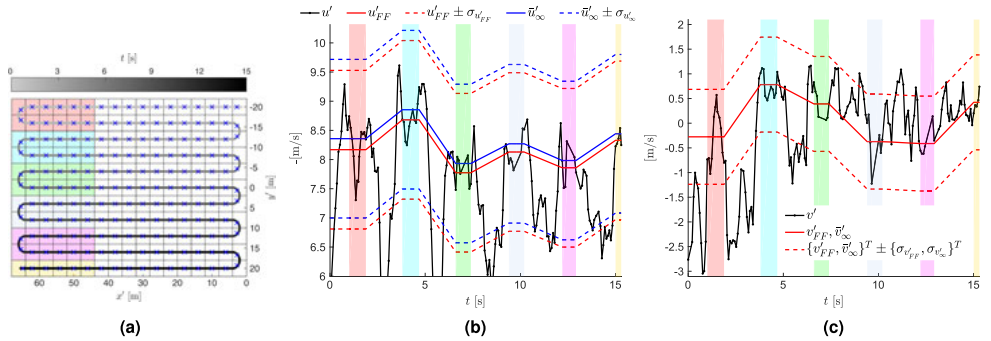

Figure 7. A visual representation of the far-field velocity estimation. (a) Triple-lidar scan trajectory with colour coded averaging areas; (b) Axial velocity *u* for a triple-lidar scan shown in (a) with various far-field estimates and same colour coded averaging areas; (c) As (b) only for the radial velocity component *v*. [Colour figure can be viewed at wileyonlinelibrary.com]

The latter implicitly assumes that the free-stream velocity in one cell instantaneously determines the thrust and thus the upstream flow-field. However, with a stochastic representation weight is given to a range of free-stream velocities softening the instantaneity requirement. Similarly, it could be interpreted as a variation of the free-stream velocity along the radial direction. The method for approximating the pdf is outlined in the following subsections and supported by Figure 7.

4.4.1. Velocity far from rotor.

The triple-lidar measures solely six times during a single scan far from the rotor (Figure 7(a)), making a continuous far-field estimate for all 187 cells difficult. Essentially, it corresponds to estimating the signal from a second triple-lidar scanning simultaneously along $x \approx 3R$. The approach here relies on establishing averaging areas far from the rotor, shown in different colours in Figure 7(a). All velocity measurements falling into one of these areas are averaged and assumed to be representative of the far-field conditions in each respective averaging area. Here, spatially averaging avoids bias from a single point estimate. The estimated mean far-field velocity $\mathbf{V}'_{\mathrm{FF}} = \{u'_{\mathrm{FF}}, v'_{\mathrm{FF}}, w'_{\mathrm{FF}}\}$ is thus constant over these areas, which is shown in Figure 7(b) and 7(c) for the axial and radial velocity components. By interpolating between these regions, all cells are attributed a far-field velocity. Note that cells lying in front of the first averaging area (red) in time are assigned its average value.

4.4.2. Uncertainty from wind variability.

As the rotor induction zone might interact with the ambient turbulence, the standard deviation is also estimated in the far-field. For each of the cells falling into the coloured averaging areas, the standard deviation is determined over each of the continuous 30 min triple-lidar acquisition periods. The average of all their standard deviations is then taken as the final standard deviation of the far-field velocity $\sigma_{\mathbf{V}'_{\mathrm{FF}}} = \{\sigma_{u'_{\mathrm{FF}}}, \sigma_{v'_{\mathrm{FF}}}, \sigma_{w'_{\mathrm{FF}}}\}$. Note that this signifies that each of the ten 30 min triple-lidar measurement periods has only one far-field standard deviation associated with it. It does not vary in space, as this has shown to be insignificant. The resulting far-field estimates are again shown in Figure 7(b) and 7(c).

4.4.3. Estimating the induced velocity.

The axial velocity induced by the rotor is still significant at the position where the triple-lidar far-field velocity is estimated. The latter should be corrected by the rotor induced velocity to obtain a better estimate of the 'true' free-wind speed. The induced velocity is estimated by calculating the induction of a cylindrical vortex sheet trailed from the rotor tip and extending infinitely far downstream. Along the centreline of such a vortex system, the induced velocity is given by:[4]

$$u_I = \frac{1}{2}\left(1 - \sqrt{1 - C_T}\right) u_\infty g(x) \tag{4}$$

$$g(x) = \left(1 - \frac{x}{\sqrt{R^2 + x^2}}\right) \tag{5}$$

where C_T is the thrust coefficient. The aforementioned expression for the induced velocity is uncertain owing to the crude assumptions behind the model as well as the uncertainties in predicting C_T and u_∞. In order to quantify this uncertainty, the measured C_T of the NTK 500 is first approximated by the following expression:

$$C_T = 1 - (b_2 u_\infty + b_1)^2 \tag{6}$$

where $b_2 = 0.055$ s/m and $b_1 = 0.079$ are determined using least-squares fitting. A detailed discussion of the measured thrust curve is given in Section 6.1. Figure 8 shows a good fit over the wind speed range for which measurements are available. For us to avoid an iterative process, the dependence of u_I on u_∞ is removed by assuming $u_\infty \approx u'_{\mathrm{FF}}$. The combined equations (4)-(6) yield

$$u_I = (c_2 u'_{\mathrm{FF}} + c_1) u'_{\mathrm{FF}} g(x) \tag{7}$$

where $c_2 = -\frac{1}{2} b_2 = -0.028$ s/m and $c_1 = \frac{1}{2}(1 - b_1) = 0.46$. Assuming $u_\infty \approx u'_{\mathrm{FF}}$ causes the term between brackets in equation (7) to increase and the one outside to decrease and therefore should not affect the estimate of u_I significantly. Next, it is assumed that u'_{FF}, c_1 and c_2 are independent random variables. Linearizing around the most likely u_I then yields:

Wind Energ. 2017; **20**:1481–1498 © 2017 The Authors. *Wind Energy* Published by John Wiley & Sons, Ltd.
DOI: 10.1002/we

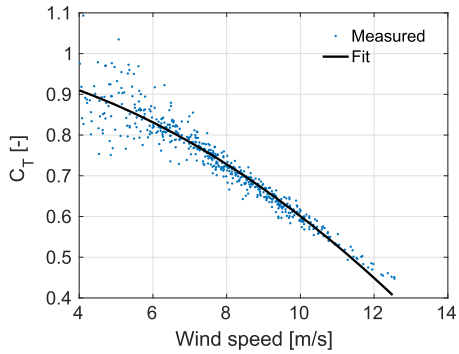

Figure 8. Comparison of measured C_T and the fit given by equation (6). [Colour figure can be viewed at wileyonlinelibrary.com]

$$\sigma_{u_I}^2 = \left(\frac{\partial u_I}{\partial u'_{\mathrm{FF}}}\right)^2 \sigma_{u'_{\mathrm{FF}}}^2 + \left(\frac{\partial u_I}{\partial c_1}\right)^2 \sigma_{c_1}^2 + \left(\frac{\partial u_I}{\partial c_2}\right)^2 \sigma_{c_2}^2 \tag{8}$$

where $\sigma_{c_2} = 6.7 \cdot 10^{-4}$ s/m and $\sigma_{c_1} = 6.0 \cdot 10^{-3}$ are determined by the least square procedure. The standard deviation of u'_{FF} is in the order of 1 m/s that is significantly higher than σ_{c_2} and σ_{c_1}. Thus, the last two terms in equation (8) can be neglected, i.e.

$$\left(\frac{\sigma_{u_I}}{\sigma_{u'_{\mathrm{FF}}}}\right)^2 \approx \left(\frac{\partial u_I}{\partial u'_{\mathrm{FF}}}\right)^2 = \left((2c_2 u'_{\mathrm{FF}} + c_1) g(x)\right)^2$$

At $x \approx 3R$, the function $g(x) \approx 0.05$ and hence $\sigma_{u_I}^2 \approx \left((-2.8 \cdot 10^{-3} u'_{\mathrm{FF}} + 0.023)\sigma_{u'_{\mathrm{FF}}}\right)^2$. Thus, the uncertainty in the estimated u_I is only a small fraction of the variability of u'_{FF}.

4.4.4. Forming the free-stream pdf.

Finally all contributions from the last sections can be combined to form the basis of the free-stream pdf

$$\bar{\mathbf{V}}'_\infty = \begin{bmatrix} \bar{u}'_\infty \\ \bar{v}'_\infty \\ \bar{w}'_\infty \end{bmatrix} = \begin{bmatrix} u'_{\mathrm{FF}} + u_I \\ v'_{\mathrm{FF}} \\ w'_{\mathrm{FF}} \end{bmatrix} \quad \sigma_{\mathbf{V}'_\infty} = \begin{bmatrix} \sigma_{u'_\infty} \\ \sigma_{v'_\infty} \\ \sigma_{w'_\infty} \end{bmatrix} = \begin{bmatrix} \sqrt{\sigma_{u'_{\mathrm{FF}}}^2 + \sigma_{u_I}^2} \\ \sigma_{v'_{\mathrm{FF}}} \\ \sigma_{w'_{\mathrm{FF}}} \end{bmatrix} \tag{9}$$

Their time-series are shown Figure 8(b) and 8(c). The free-stream pdf of each i^{th} data point in the triple-lidar coordinate system thus becomes

$$f(\mathbf{V}'_\infty; i) = \mathcal{N}\left(\bar{\mathbf{V}}'_\infty(i), \sigma_{\mathbf{V}'_\infty}(i)\right) \tag{10}$$

Here, $\mathcal{N}$ defines a Gaussian distribution.

4.5. Spatial uncertainty in triple-lidar data

The induction zone is only a function of the rotor frame of reference, however even with the rotor following the wind the triple-lidar measurements followed a fixed pattern (Section 4.1). The yaw sensor of the NTK 500/41 provided an indication of the mean misalignment between the measured and rotor coordinate system $\bar{\theta}$. Nevertheless, the turbine controller employs a yaw margin to avoid wearing down the yaw system, introducing uncertainty in the misalignment angle. The rotor and triple-lidar coordinate systems are related via the transformation matrix $T(\theta)$ such that $\Psi = T(\theta)\Psi'$.

$$T(\theta) = \begin{bmatrix} \cos(\theta) & \sin(\theta) \\ -\sin(\theta) & \cos(\theta) \end{bmatrix} \tag{11}$$

Therefore, the uncertainty in θ propagates to the location of the measurements and their velocity components in Ψ. The uncertainty in the misalignment is modelled via $\mathcal{N}(\bar{\theta}(i), \sigma_\theta)$, a Gaussian distribution with $\sigma_\theta = 5°$, based on the calibration report[10] and work by Kragh *et al.*[16] The resulting mean misalignment is shown in Figure 9 with $\pm\sigma_\theta$ for all triple-lidar data

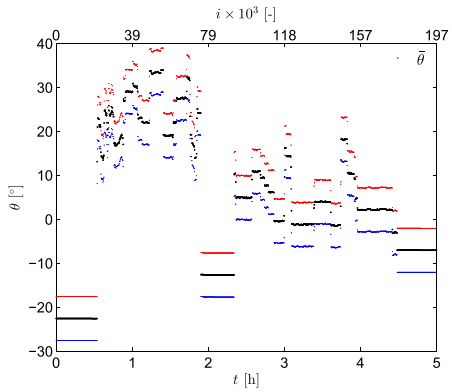

Figure 9. Triple-lidar-rotor misalignment for all triple-lidar data points. The lower axis indicates the cumulative time, the upper the data point index. Coloured points indicate σ_θ boundaries about the mean. [Colour figure can be viewed at wileyonlinelibrary.com]

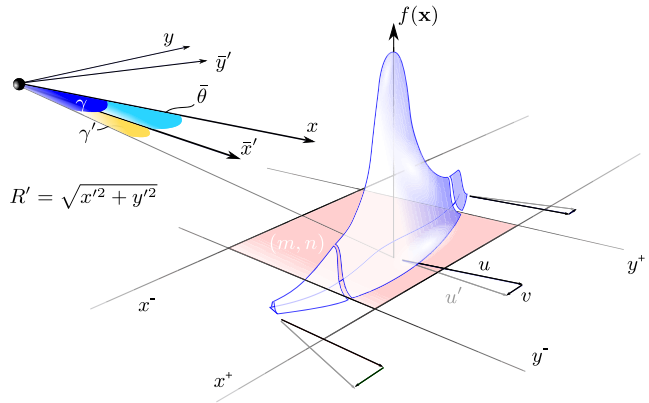

Figure 10. Spatial weighting of a single triple-lidar data point. [Colour figure can be viewed at wileyonlinelibrary.com]

points. Defining $\gamma = -\tan^{-1}(y/x)$ and $\gamma'(i) = -\tan^{-1}(y'(i)/x'(i))$, the pdf for each data point i in the rotor coordinate system becomes

$$f(\gamma; i) = \mathcal{N}(\left[\bar{\theta}(i) + \gamma'(i)\right], \sigma_\theta) \tag{12}$$

Furthermore, the triple-lidar cell-averaged data should not be perceived as discrete points in space, owing to the uncertainty in the scan trajectory. The standard deviation in $R'(i) = \sqrt{x'(i) + y'(i)}$ was 0.11 m. Again, the pdf was modelled as a normal

$$f(R; i) = \mathcal{N}(R'(i), \sigma_{R'}) \tag{13}$$

, where $R = \sqrt{x^2 + y^2}$. Finally, the total spatial uncertainty is

$$f(\mathbf{x}; i) = f(\gamma; i) f(R; i) \tag{14}$$

A visual representation of a single data point's pdf and the different angles defined earlier is given in Figure 10. It further demonstrates the effect of the uncertainty in the reference frame misalignment on the rotor velocity components, indicated by the arrows. Here, a u' component with a misalignment $\bar{\theta}$ gives rise to both velocity components in the rotor reference frame. The uncertainty in θ furthermore changes the velocity components in space. The entire rotor velocity field under

Wind Energ. 2017; **20**:1481–1498 © 2017 The Authors. *Wind Energy* Published by John Wiley & Sons, Ltd.
DOI: 10.1002/we

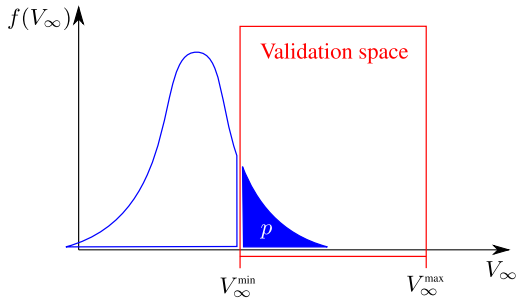

Figure 11. Evaluation of the participation of a single triple-lidar measurement at some point in space. Note $\bar{V}_\infty(i) < V_\infty^{\min}$. [Colour figure can be viewed at wileyonlinelibrary.com]

uncertainty in the misalignment angle can be computed from the triple-lidar signal

$$\begin{bmatrix} u_{3l}(\gamma,i) & \bar{u}_\infty(\gamma,i) & \sigma_{u_\infty}(\gamma,i) \\ v_{3l}(\gamma,i) & \bar{v}_\infty(\gamma,i) & \sigma_{v_\infty}(\gamma,i) \end{bmatrix} = T(\gamma-\gamma'(i)) \begin{bmatrix} u'_{3l}(i) & \bar{u}'_\infty(i) & \sigma_{u'_\infty}(i) \\ v'_{3l}(i) & \bar{v}'_\infty(i) & \sigma_{v'_\infty}(i) \end{bmatrix} \tag{15}$$

$$\begin{bmatrix} w_{3l}(\gamma,i) \\ \bar{w}_\infty(\gamma,i) \\ \sigma_{w_\infty}(\gamma,i) \end{bmatrix} = \begin{bmatrix} w'_{3l}(i) \\ \bar{w}'_\infty(i) \\ \sigma_{w'_\infty}(i) \end{bmatrix} \tag{16}$$

Note that $\theta(\mathbf{x},i) = \gamma - \gamma'(i)$. This finally gives a rotor velocity field for each data point $\mathbf{V}_{3l}(\mathbf{x},i)$ but also a spatially varying free-stream pdf.

$$f(\mathbf{V}_\infty;\mathbf{x},i) = \mathcal{N}(\bar{\mathbf{V}}_\infty(\mathbf{x},i), \sigma_{\mathbf{V}_\infty}(\mathbf{x},i)) \tag{17}$$

The velocity range over which the validation is performed is linked to the turbine's operating wind speeds. This implies that some triple-lidar measurements only participate in the comparison by a factor given as

$$p(\mathbf{x},i) = \int_{V_\infty^{\min}}^{V_\infty^{\max}} f(V_\infty;\mathbf{x},i)\mathrm{d}V_\infty \tag{18}$$

Figure 11 shows the participation of a single triple-lidar point with a free-stream pdf where $\bar{V}_\infty(i) < V_\infty^{\min}$.

4.6. Cell-averaged statistics

Finally, all triple-lidar data can be gathered in space and time forming a pdf. The spatial integration of the uncertainty is performed numerically by discretizing the x–y plane with a spacing $\Delta x = \Delta y = 0.04$ m over 0 m$\leq \Delta x \leq 68$ m and -22 m$\leq y \leq 22$ m. The upper and lower spatial boundaries of each grid cell (m,n) (Figure 10), denoted by the superscripts $^+$ and $^-$, followed from the original triple-lidar grid shown in Figure 6. Over a discretized cell, the spatial coordinates become

$$\Delta x = \frac{x^+(m,n) - x^-(m,n)}{n_x} \qquad \Delta y = \frac{y^+(m,n) - y^-(m,n)}{n_y}$$
$$x_r = x^-(m,n) + (r-\frac{1}{2})\Delta x \qquad y_s = y^-(m,n) + (s-\frac{1}{2})\Delta y$$

Here, $n_\bullet$ denotes the total number of points discretizing each dimension. Consequently, the mean and variance of a triple-lidar velocity pdf $f(\mathbf{V}_{3l};m,n)$ in a cell (m,n) are given by

$$\bar{\mathbf{V}}_{3l}(m,n) = \frac{\sum_{r=1}^{n_x}\sum_{s=1}^{n_y}\left(\sum_{i=1}^{n_{3l}} \mathbf{V}_{3l}(\mathbf{x}_{rs},i) f(\mathbf{x}_{rs};i) p(\mathbf{x}_{rs},i)\right)}{\sum_{r=1}^{n_x}\sum_{s=1}^{n_y}\left(\sum_{i=1}^{n_{3l}} f(\mathbf{x}_{rs};i) p(\mathbf{x}_{rs},i)\right)} \tag{19}$$

$$\sigma^2_{\mathbf{V}_{3l}}(m,n) = \frac{\sum_{r=1}^{n_x}\sum_{s=1}^{n_y}\left(\sum_{i=1}^{n_{3l}}\left[\mathbf{V}_{3l}(\mathbf{x}_{rs},i)-\bar{\mathbf{V}}_{3l}(m,n)\right]^2 f(\mathbf{x}_{rs};i)p(\mathbf{x}_{rs},i)\right)}{\sum_{r=1}^{n_x}\sum_{s=1}^{n_y}\left(\sum_{i=1}^{n_{3l}} f(\mathbf{x}_{rs};i)p(\mathbf{x}_{rs},i)\right)} \tag{20}$$

The free-stream distributions in each cell needed for the CFD reconstruction is more complex compared with the one presented in Section 2, owing to the intrinsic cell-averaging of the triple-lidar data. The triple-lidar acquires spectra along some path $\mathbf{x}'(t)$ (Figure 6) at a misalignment of $\theta(t)$ - assuming it is exactly known—which are subsequently averaged over a grid cell j to determine a cell velocity (Section 4.1). The latter can be expressed in terms of the 'true' wind field $\mathbf{V}(V_\infty,\mathbf{x},t)$, ignoring volume-averaging

$$\mathbf{V}_{3l}(i) = \frac{1}{\delta t(j(i))}\int_{t(i)-\delta t(j(i))/2}^{t(i)+\delta t(j(i))/2} \mathbf{V}(\overbrace{T(\theta(t))V'_\infty(t)}^{V_\infty(t)},\overbrace{T(\theta(t))\mathbf{x}'(t)}^{\mathbf{x}(t)},t)\mathrm{d}t \tag{21}$$

The limits of the integral are given by the time of the measurement and the time span the triple-lidar focal point rests in a particular grid cell. This implies that each lidar measurement does not solely depend V_∞ but also on the triple-lidar grid cell j and misalignment θ. Hence, for recreating the measurements from the true wind field (or equivalently the CFD solution), an estimated pdf needs to capture these additional dependencies. Noting that the spatially weighted free-stream pdf $f(\mathbf{V}_\infty;\mathbf{x},i)f(\mathbf{x};i)$ is linked to $\theta(\mathbf{x},i)$ and $j(i)$ via the data index i, a multi-dimensional joint pdf can be formed from all data that captures these dependencies stochastically

$$f_{3l}(\mathbf{V}_\infty,\theta,j;\mathbf{x}) \tag{22}$$

Treating the pdf as fully discrete and integrating it spatially over the cell (m,n) yields the final pdf used for recreating the measurements, detailed in Section 5.3.

$$f_{3l}(\mathbf{V}_\infty,\theta,j;m,n) = \frac{\sum_{r=1}^{n_x}\sum_{s=1}^{n_y} f_{3l}(\mathbf{V}_\infty,\theta,j;\mathbf{x}_{rs})}{\sum_{r=1}^{n_x}\sum_{s=1}^{n_y}\sum_{k=1}^{n_{V_\infty}}\sum_{l=1}^{n_\theta}\sum_{r=1}^{n_j} f_{3l}(\mathbf{V}_\infty,\theta,j;\mathbf{x}_{rs})} \tag{23}$$

Note that the normalization should be performed for each velocity component individually.

5. COMPUTATIONAL METHOD

5.1. CFD simulations

5.1.1. Numerical setup.

The simulations were performed using incompressible steady-state RANS with sheared inflow and an actuator disc representation of the rotor.[17] The kinematic viscosity and air density were kept constant at 1.789×10^{-5} kg/m/s and 1.225 kg/m^3, respectively. Neither nacelle nor tower were modelled. Only the velocity prescribed at the inlet boundary $\mathbf{V}_\infty$ changed between calculations. It was varying with height according to a rough logarithmic velocity profile (log-law), where the roughness length z_0 was determined from fitting the profile to wind speeds measured at three different heights of the TMM, resulting in $z_0 = 0.055$. This corresponds to the terrain category of the site for the wind directions of interest, i.e. *farmland with open appearance*.[18] The friction velocity followed from specifying the free-stream velocity at hub height $\mathbf{V}_{\infty,h}$. It corresponds to the velocity of the *kth* bin used to discretise f_{3l}, as given in equation (3). The small magnitude and large uncertainty in v_∞ and w_∞ meant that only u_∞ was used as input to the simulations, such that $\mathbf{V}_{\infty,h} = \{u_\infty(k),0,0\}$. The crudity of the numerical representation was not expected to undermine the accuracy of the numerical results, as this numerical setup also yields accurate results for the wake deficit of a rotor.[19,20] The wake deficit is, as the induction zone, governed by the turbine's thrust.

5.1.2. Flow solver.

The in-house finite volume code EllipSys3D solves the incompressible RANS equations over a discretised block-structured domain.[21–23] The QUICK scheme[24] is applied to the convection-diffusion equation. It is third order accurate by using quadratic interpolation over three nodes. The SIMPLE algorithm[25] solves the pressure-linked terms by coupling the

Wind Energ. 2017; **20**:1481–1498 © 2017 The Authors. *Wind Energy* Published by John Wiley & Sons, Ltd.
DOI: 10.1002/we

Navier–Stokes equations in an iterative manner. The discrete body forces from the actuator disc are hindered by a modified Rhie-Chow algorithm from decoupling velocity and pressure.[26,27] The Menter $k-\omega$ shear-stress transport closes the RANS equations.[28]

5.1.3. Numerical domain.

A box domain with side lengths of 25 radii (R) was created, minimizing the impact of domain blockage ($\pi/25^2 = 0.5\%$). The actuator disc was located at the NTK hub height (Figure 12) and was surrounded by a finely meshed box with $2.5R$ side lengths. The inner mesh resolution followed from discretizing the rotor radius with 33 grid points, which has been shown in previous studies to yield sufficiently accurate results.[19,29] From the fine mesh, the grid grew hyperbolically towards the edges of the domain. The front, sides and top boundaries of the domain were prescribed according to the specified shear profile (Dirichlet), while the outlet was a Neumann boundary. The bottom face was set as no-slip boundary with a roughness length of $z_0 = 0.055$.

5.2. Numerical triple-lidar

For us to make the simulation results more comparable with the measured data, the simulated flow was sampled by a numerical triple-lidar. Each of the three continuous-wave lidars in fact probes the flow-field along the entire length of its laser beam and not in a single point. This phenomenon is also referred to as volume averaging or range weighting. A detailed modelling approach is given by Simley *et al.*[6] The numerical triple-lidar followed the same measurement trajectory as the real one shown in Figure 6, and the sampled velocities are spatially averaged in similar fashion. Furthermore, the

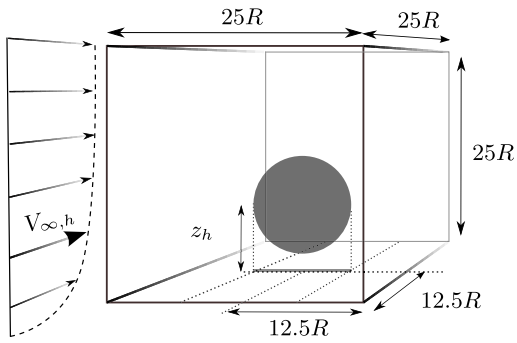

Figure 12. The numerical domain containing the actuator disc with sheared inflow and a free-stream velocity at hub height $V_{\infty,h} = u_\infty(k)$. All dimensions are given in turbine radii ($R = 20.5$ m).

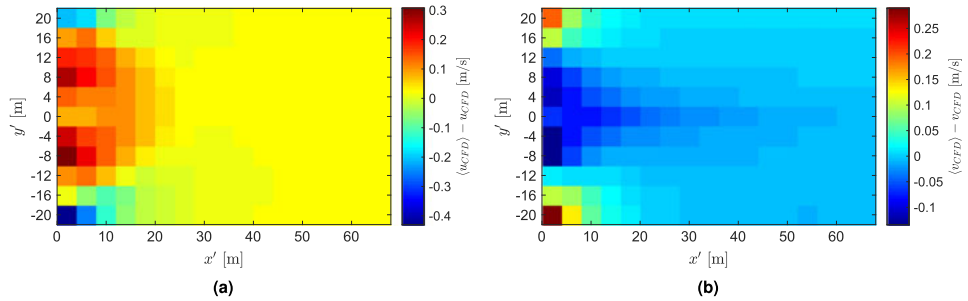

Figure 13. The difference between volume-averaged and point-like sampled a) axial b) radial CFD velocity fields. The results are furthermore cell-averaged. The free-stream velocity at hub heigth is 5 m/s, $\theta = 0$ and the sheared inflow followed a log-law. [Colour figure can be viewed at wileyonlinelibrary.com]

fixed measurement coordinates necessitate sampling the flow over trajectories at various angles θ (Figure 5) to the rotor coordinate system. This was performed in-between $-44°$ and $54°$ in $1°$ steps. This impacts the final comparison, as with a non-zero θ the flow is no longer sampled at right angles to the rotor plane. Finally, the CFD velocity field is a function of the free-stream velocity u_∞, the misalignment angle θ and j, the grid cell index, i.e. $\mathbf{V}_{\mathrm{CFD}}(u_\infty, \theta, j)$. For a free-stream velocity at hub height of 5 m/s and $\theta = 0$, the difference between numerical triple-lidar velocities and point-like velocity data is shown in Figure 13. Close to the rotor $x < 1.5R$ volume-averaging becomes significant, as gradients are smeared out by the lidar's range-weighting.

5.3. Recreating the free-stream velocity distribution

Discretizing $f_{3l}(\mathbf{V}_\infty, \theta, j; m, n)$ over the sample-space, the modelled statistics can be computed in combination with the CFD results extracted by the numerical triple-lidar. To clearly mark lidar and CFD contributions, they are denoted by $\bullet_{3l}$ and $\bullet_{\mathrm{CFD}}$.

$$\bar{\mathbf{V}}_{\mathrm{CFD}}(m,n) = \sum_{k=1}^{n_{u\infty}} \sum_{l=1}^{n_\theta} \sum_{r=1}^{n_j} f_{3l}\left(u_\infty(k), \theta(l), j(r); m, n\right) \mathbf{V}_{\mathrm{CFD}}\left(u_\infty(k), \theta(l), j(r)\right) \tag{24}$$

$$\sigma^2_{\mathbf{V}_{\mathrm{CFD}}}(m,n) = \sum_{k=1}^{n_{u\infty}} \sum_{l=1}^{n_\theta} \sum_{r=1}^{n_j} f_{3l}\left(u_\infty(k), \theta(l), j(r); m, n\right) \left[\mathbf{V}_{\mathrm{CFD}}\left(u_\infty(k), \theta(l), j(r)\right) - \bar{\mathbf{V}}_{\mathrm{CFD}}(m,n)\right]^2 \tag{25}$$

These equations only differ from those presented in Section 2 by the added variables θ, j and using u_∞. Also note that for consistency $V_\infty(i) = u_\infty(i)$ in equation (18) to calculate the participation of the triple-lidar measurements. The effect of $v_{\infty,3l}$ is included in the CFD results by assuming that the induction zone behaves linearly to sufficiently small radial and vertical velocity components

$$\begin{bmatrix} \bar{v}_{\mathrm{CFD},2} \\ \bar{w}_{\mathrm{CFD},2} \end{bmatrix} = \begin{bmatrix} \bar{v}_{\mathrm{CFD},1} + \bar{v}_{\infty,3l} \\ \bar{w}_{\mathrm{CFD},1} + \bar{w}_{\infty,3l} \end{bmatrix} \qquad \begin{bmatrix} \sigma^2_{v_{\mathrm{CFD},2}} \\ \sigma^2_{w\mathrm{CFD},2} \end{bmatrix} = \begin{bmatrix} \sigma^2_{v_{\mathrm{CFD},1}} + \sigma^2_{v_{\infty},3l} \\ \sigma^2_{w_{\mathrm{CFD},1}} + \sigma^2_{w_{\infty},3l} \end{bmatrix} \tag{26}$$

Here, the subscript $_1$ denotes the result from equations (24) and (25), and $_2$ the final value that will be compared with the triple-lidar measurements.

6. RESULTS AND DISCUSSION

6.1. The thrust curve

As an initial validation of the computational method, the experimental and numerical global thrust coefficients were compared. The experimental data were derived from the tower bending moments as proposed by Réthoré.[30] The detailed

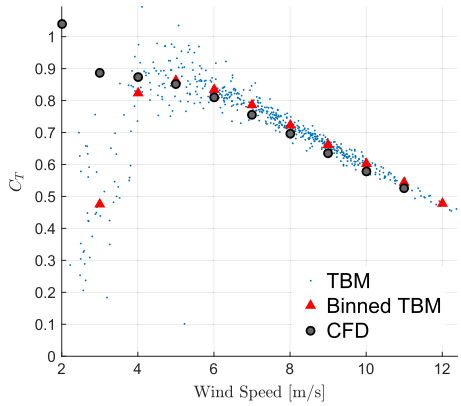

Figure 14. Thrust curves generated from tower bending moments (TBM) and RANS simulations with the actuator disc method. The wind speed is equivalent to the free-stream velocity at hub height. [Colour figure can be viewed at wileyonlinelibrary.com]

Wind Energ. 2017; **20**:1481–1498 © 2017 The Authors. *Wind Energy* Published by John Wiley & Sons, Ltd.
DOI: 10.1002/we

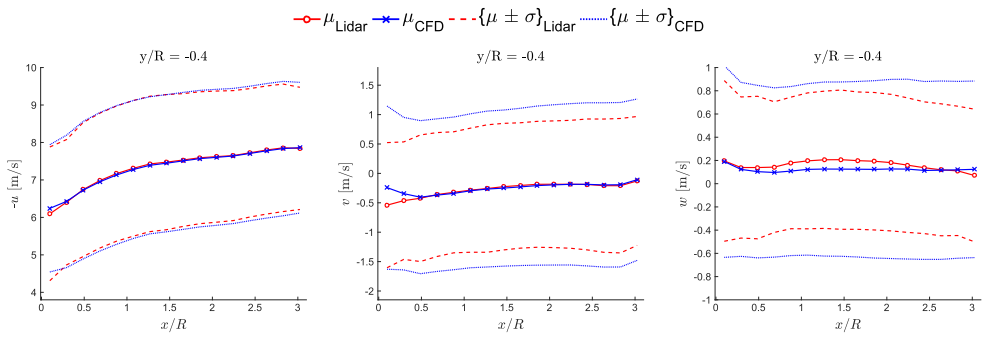

Figure 15. Comparison between mean μ and standard deviation σ of triple-lidar (o-) and CFD (x-) for all three velocities components $\{u, v, w\}$ along the line $(x/R,\ y/R = -0.4)$. [Colour figure can be viewed at wileyonlinelibrary.com]

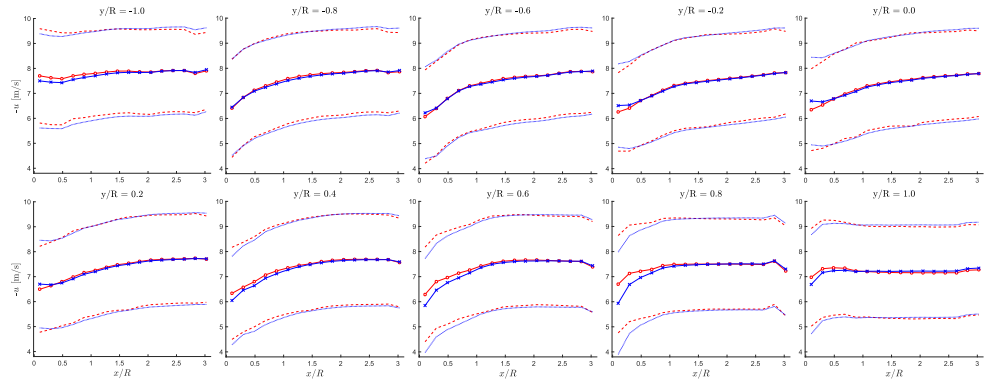

(a) Axial velocity component

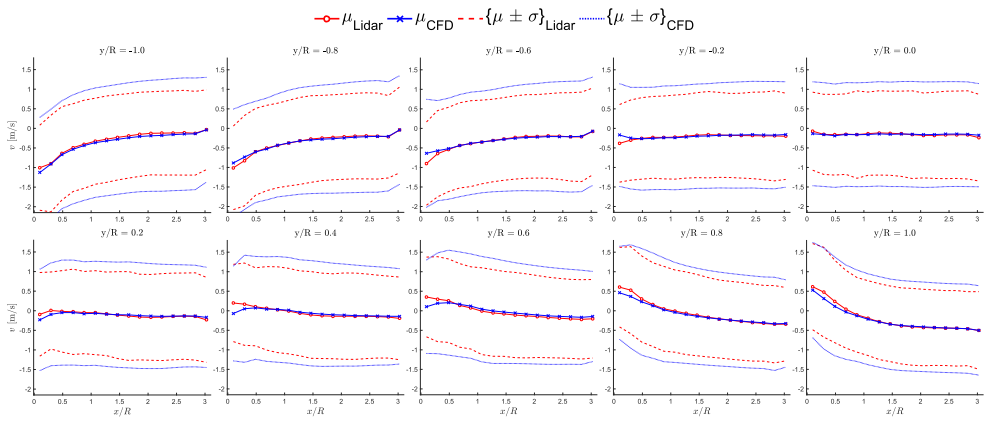

(b) Radial velocity component

Figure 16. Comparison between mean and standard deviation of triple-lidar(o-) and CFD (x-) along lines with constant y/R. [Colour figure can be viewed at wileyonlinelibrary.com]

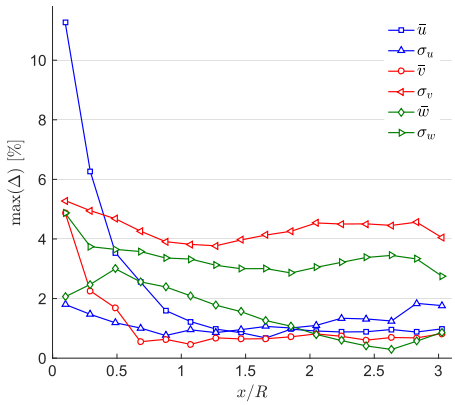

Figure 17. Maximal absolute difference across the rotor induction zone between triple-lidar and CFD statistics, normalised by the mean of the free-stream velocity in each cell. [Colour figure can be viewed at wileyonlinelibrary.com]

method can be found in the campaign report.[10] Figure 14 demonstrates that the CFD simulations are in good agreement with the measurements over a large wind speed range. The best agreement was found for wind speeds > 5 m/s, as below this threshold, the turbine is barely running. This also causes the large scatter in the measurements. Figure 14 essentially verifies the RANS model for predicting the global thrust coefficient, under the condition that the free-stream velocity is matched. Consequently, the range of free-stream velocities in equation 3 over which the pdfs were discretized was set to $4.75 \text{ m/s} \leq u_\infty \leq 11.75$ m/s and with $n_{u_\infty} = 14$ the free-stream bin width was 0.5 m/s. Therefore, the CFD simulations were performed with 14 inlet velocities of $4.75 + 0.5(k - 0.5)$ m/s with $k = 1, \ldots, n_{u_\infty}$.

6.2. Comparison in the induction zone

Here, mean and standard deviations determined in Sections 4.6 and 5.3 for the triple-lidar measurements and CFD simulations are compared. Figure 15 shows these measures for all three velocity components along the line $(x/R, y/R = -0.4)$. These results are representative of the main features found across the entire validation space. The comparisons of u and v over the full rotor area are given in Figures 16a and 16b, respectively. Only when mean and standard deviation agree are the pdfs matching. This is the case for the u-component until close to the rotor, whereas for the radial velocity v, it is solely the mean. Its computed that standard deviation is larger. This over-prediction of σ_{v_∞} is directly linked to the free-stream estimate (equation 26), as $\sigma_{v_\infty} = \sigma_{v_\infty,3l}$, except for $x/R < 0.5$. Consequently, this difference is linked to estimating the inputs and cannot be attributed to model inaccuracies. The evolution of the vertical velocity w away from the rotor is not reproduced, as the simulations were performed for flat terrain. The maximal difference across the rotor between triple-lidar and CFD statistics are given in Figure 17 for all three velocity components. The results are normalized by $\bar{V}_\infty$ in each cell. Except for σ_{v_∞} and statistics of w, the difference lies below 1.5% for $1 < x/R < 3$. It is really just for $x/R < 0.5$ that differences start to diverge. This might be related to the missing nacelle and tower in the simulations or the triple-lidar hitting hard targets.

7. CONCLUSION

Using a probabilistic approach that captures the variability of the wind field interacting with the rotor and the uncertainties in the field experiment allows to bring model and measurements in great accordance. The difference between triple-lidar and CFD statistics across the entire rotor induction zone lies below 4.5% up to half a radius upstream of the turbine relative to the measured free-stream velocity. For the axial component, it remains below 2% for $x/R > 0.8$, which translates into a maximal nominal difference of 0.14 m/s. This difference should be judged with respect to potential measurement errors. The minimal recorded standard deviation during a triple-lidar measurement period was almost double this figure at 0.26 m/s. The Doppler spectral resolution of the lidars lies at 0.15 m/s and a 1° error in the lidar beam angle would incur the same velocity difference. Essentially, this renders model and measurement errors indistinguishable, validating the model within the measurement error bounds. Close to the rotor its validity is more questionable, however, as both model and

Wind Energ. 2017; **20**:1481–1498 © 2017 The Authors. *Wind Energy* Published by John Wiley & Sons, Ltd.
DOI: 10.1002/we

measurements are suffering from errors in this region. The large uncertainties in the model inputs required a probabilistic approach to the validation, which obscures whether the model functions for specific scenarios. Here, field measurements are probably not the right choice, as neither inputs nor errors can be controlled. Wind tunnel measurements allow more control over the inputs and might allow to evaluate the performance of the model under different atmospheric conditions but might introduce scaling errors.

ACKNOWLEDGEMENTS

This work is part of the Unified Turbine Testing (UniTTe) project funded by The Innovation Fund Denmark (1305-00024B). Special thanks are due to the Test & Measurements section, in particular the WindScanner team, at DTU Wind Energy for their generous support as well as to R. Meyer Forsting for editing this document. Furthermore we would like to thank the anonymous reviewers for their valuable contribution. The computational resources were provided by the Risø DTU central computing facility.

REFERENCES

1. *IEC 61400-12-1:2005, power performance measurements of electricity producing wind turbines*.
2. Wagner R, Pedersen TF, Courtney M, Antoniou I, Davoust S, Rivera RL. Power curve measurement with nacelle mounted lidar. *Wind Energy* 2014; **17**: 1441–1453. DOI: 10.1002/we.1643.
3. Schlipf D, Fleming P, Haizmann F, Scholbrock AK, Hofsäß M, Wrigth A, Cheng PW. Field testing of feedforward collective pitch control on the cart2 using a nacelle-based lidar scanner. *Journal of Physics: Conference Series* 2012; **555**: 012090, DOI: 10.1088/1742-6596/555/1/012090.
4. Medici D, Ivanell S, Dahlberg JA, Alfredsson PH. The upstream flow of a wind turbine: blockage effect. *Wind Energy* 2011; **14**: 691–697. DOI: 10.1002/we.451.
5. Howard KB, Guala M. Upwind preview to a horizontal axis wind turbine: a wind tunnel and field-scale study. *Wind Energy* 2015; **19**: 1371–1389. DOI: 10.1002/we.1901.
6. Simley E, Angelou N, Mikkelsen T, Sjöholm M, Mann J, Pao LY. Characterization of wind velocities in the upstream induction zone of a wind turbine using scanning continuous-wave lidars. *Journal of Renewable and Sustainable Energy* 2016; **8**. DOI: 10.1063/1.4940025.
7. Quinn AD, Wilson M, Reynolds AM, Couling SB, Hoxey RP. Modelling the dispersion of aerial pollutants from agricultural buildings - an evaluation of computational fluid dynamics (CFD). *Computers and Electronics in Agriculture* 2001; **30**: 219–235.
8. Tang W, Huber A, Bell B, Schwarz W. Application of CFD simulations for short-range atmospheric dispersion over open fields and within arrays of buildings. *AMS 14th Joint Conference on the Applications of Air Pollution Meteorology with the A&WMA*, Atlanta, GA, 2006.
9. Hansen KS, Pedersen KH, Paulsen US. Online wind turbine measurement laboratory. *EWEC*. Athens, Greece, 2006.
10. Vignaroli A. *UniTTe- Nordtank Measurement Campaign (Turbine and Met Masts)*, DTU Wind Energy E. DTU Wind Energy I, 2016. no. 0363.
11. Angelou N, Mann J, Sjöholm M, Courtney M. Direct measurement of the spectral transfer function of a laser based anemometer. *Review of Scientific Instruments* 2012; **83**: 033111.
12. Angelou N, Abari FF, Mann J, Mikkelsen T, Sjöholm M. Challenges in noise removal from doppler spectra acquiered by continous-wave lidar. *Proceedings of the 26th International Laser Radar Conference*, Porto Heli, Greece, 2012.
13. Meyer Forsting AR, Troldborg N. A finite difference approach to despiking in-stationary velocity data - tested on a triple-lidar. *Journal of Physics: Conference Series (Online)* 2016; **753**. DOI: 10.1088/1742-6596/753/7/072017.
14. Angelou N, Sjöholm M. *UniTTe WP3/MC1: Measuring the inflow towards a Nordtank 500 kW turbine using three short-range WindScanners and one SpinnerLidar*, DTU Wind Energy E. DTU Wind Energy, 2015, no. 0093.
15. Mikkelsen TK. *WindScanner.dk - a new Remote Sensing based Research Infrastructure for on- and offshore Wind Energy Research*. National Telford Institute Advanced Research Workshop: Aberdeen, United Kingdom, 2013.
16. Kragh KA, Hansen MH, Mikkelsen T. Precision and shortcomings of yaw error estimation using spinner-based light detection and ranging. *Wind Energy* 2013; **16**: 353–366.
17. Réthoré PE, Sørensen NN. Verification and validation of an actuator disc model. *Wind Energy* 2013; **17**: 919–937.
18. Troen I, Petersen EL. *European Wind Atlas*. Risø National Laboratory: Roskilde, Denmark, 1989.

19. Troldborg N, Zahle F, Réthoré PE, Sørensen NN. Comparison of wind turbine wake properties in non-sheared inflow predicted by different cfd rotor models. *Wind Energy* 2013; **18**: 1239–1250.
20. van der Laan P, Sørensen NN, Réthoré PE, Mann J, Kelly MC, Troldborg N, Schepers JG, Machefaux E. An improved $k-\epsilon$ model applied to a wind turbine wake in atmospheric turbulence. *Wind Energy* 2014; **18**: 889–907.
21. Sørensen NN. General purpose flow solver applied to flow over hills, *Ph.D. Thesis*, Risø National Laboratory, 1995.
22. Michelsen JA, *Basis3d – a platform for development of multiblock pde solvers. Technical Report,* Technical Report AFM 92-05, Dept. of Fluid Mechanics, Technical University of Denmark, DTU, Lyngby, DK, 1994.
23. Michelsen JA, *Block structured multigrid solution of 2d and 3d elliptic pdes. Technical Report,* Technical Report AFM 94-05, Dept. of Fluid Mechanics, Technical University of Denmark, DTU, Lyngby, DK, 1994.
24. Leonard BP. A stable and accurate convective modelling procedure based on quadratic upstream interpolation. *Computer Methods in Applied Mechanics and Engineering* 1979; **19**: 59–98.
25. Patanker SV, Spalding DB. A calculation procedure for heat, mass and momentum transfer in three-dimensional parabolic flows. *International Journal of Heat and Mass Transfer* 1972.
26. Réthoré PE, Sørensen NN. A discrete force allocation algorithm for modelling wind turbines in computational fluid dynamics. *Wind Energy* 2012; **15**: 915–926.
27. Troldborg N, Sørensen NN, Réthoré PE, van der Laan MP. A consistent method for finite volume discretization of body forces on collocated grids applied to flow through an actuator disk. *Computers & Fluids* 2015; **119**: 197–203.
28. Menter FR. Zonal two equation $k-\omega$ turbulence models for aerodynamic flows. *AIAA Journal* 1993.
29. Meyer Forsting AR, Troldborg N. The effect of blockage on power production for laterally aligned wind turbines. *Journal of Physics: Conference Series (Online)* 2015; **625**: 012029. DOI: 10.1088/1742-6596/625/1/012029.
30. Réthoré PE. Thrust and wake of a wind turbine: relationship and measurements, *Master's Thesis*, Technical University of Denmark, 2007.

Wind Energ. 2017; **20**:1481–1498 © 2017 The Authors. *Wind Energy* Published by John Wiley & Sons, Ltd.
DOI: 10.1002/we

ARTICLE 10

A SIMPLE MODEL OF THE WIND TURBINE INDUCTION ZONE DERIVED FROM NUMERICAL SIMULATIONS

JOURNAL ARTICLE

Wind Energy, 2017, 1-10 DOI

Co-author

This journal article details the development of a simple vortex model with the aid of the validated CFD model [article 9]. It allows the commercial application of lidar measurements in the induction zone.

Received: 17 October 2016 | Revised: 8 May 2017 | Accepted: 27 July 2017

DOI: 10.1002/we.2137

WILEY

RESEARCH ARTICLE

A simple model of the wind turbine induction zone derived from numerical simulations

Niels Troldborg | **Alexander Raul Meyer Forsting**

DTU Wind Energy, Department of Wind Energy, Technical University of Denmark, Risø Campus, DK-4000 Roskilde, Denmark

Correspondence
Niels Troldborg, DTU Wind Energy, Department of Wind Energy, Technical University of Denmark, Risø Campus, DK-4000 Roskilde, Denmark.
Email: niet@dtu.dk

Funding information
The Innovation Fund Denmark, Grant/Award Number: 1305-00024B; Risø DTU

Abstract

The induction zone in front of different wind turbine rotors is studied by means of steady-state Navier-Stokes simulations combined with an actuator disk approach. It is shown that, for distances beyond 1 rotor radius upstream of the rotors, the induced velocity is self-similar and independent of the rotor geometry. On the basis of these findings, a simple analytical model of the induction zone of wind turbines is proposed.

KEYWORDS

actuator disk, induction zone, RANS, wind turbine

1 | INTRODUCTION

In the last decade, the behaviour of the flow formed upstream of a wind turbine has received increasing interest. A better understanding of this so-called induction zone could improve both lidar-based control strategies[1-5] and wind turbine power/loads assessments. In the former case, the aim is to use upstream wind measurements to predict the wind disturbance that will interact with the turbine. In the latter, it is to establish the correlation between power/loads and the free-stream velocity, ie, the velocity there would have been at the turbine position if it had not been there.[6,7] Here, the interest in the induction zone lies in potentially using measurements close to the turbine to estimate the free-stream velocity, which is one of the objectives of the UniTTe project (www.unitte.dk).

Medici et al[8] used wind tunnel measurements to investigate the induction zone of different model wind turbines and compared the results to actuator line simulations. In addition, the results were compared to an analytical expression of the centre line induction obtained from a simple linear vortex cylinder model. The numerical predictions of the upstream velocity were in good agreement with each other but were consistently slightly higher than in the measurements. The reason for this is most likely that a different rotor was used in the simulations than in the measurements and, therefore, the rotor thrust was not the same.

Howard and Guala [9] compared wind tunnel experiments and full-scale lidar measurements in the field with the same analytical expression as used by Medici et al.[8] They found reasonably good agreement between the model and wind tunnel measurements but poor agreement with the field data. The observed discrepancies were attributed to differences in the wind turbine controller, Reynolds number, and inflow conditions.

Branlard and Forsting[10] used an analytical cylindrical vortex wake model to study the induction zone in front of a rotor and compared the results to Navier-Stokes actuator disk (AD) simulations. The predictions were in excellent agreement with each other for a wide range of operating conditions including situations where the rotor was yawed.

Simley et al[11] studied the upstream induction zone of a wind turbine using synchronized continuous wave lidars. They found that the standard deviation of the longitudinal velocity component is relatively unaltered as the wind approaches the rotor, whereas the standard deviation of the vertical and lateral component increased slightly. These conclusions were partly supported by Branlard et al[12] who used a vortex particle method to show that the spectral characteristics of the longitudinal velocity component only changes marginally throughout the induction zone of a wind turbine rotor.

The main objective of the present work is to study the generic features of the induction zone of a wind turbine operating in simple inflow conditions and to derive an analytical model that describes the relation between the stream-wise velocities in the induction zone to the free-stream velocity. Considering that, most often, wind turbine owners do not have detailed knowledge about the wind turbine, such a model should be simple and independent of its specific blade design. To achieve this, we perform AD Navier-Stokes simulations of the induction zone upstream of different wind turbine rotors operating in steady uniform inflow.

2 | METHOD

The Navier-Stokes simulations were performed using the incompressible Reynolds-averaged Navier-Stokes (RANS) solver EllipSys3D.[13–15] This code solves the finite volume discretized equations in general curvilinear coordinates using a collocated grid arrangement to facilitate complex mesh geometries.

The coupled momentum and pressure-correction equations were solved using the SIMPLE[16] algorithm, the convective terms were discretized using the QUICK scheme,[17] and turbulence was modelled using the k-ω SST model.[18]

The wind turbine rotors were represented using the AD model by Réthoré et al.[19] The AD forces were applied in the computational domain by using a modified Rhie-Chow algorithm[20,21] to avoid odd/even pressure decoupling.

The computations were performed in a cubic grid with a side length of 100 rotor radii (R) and with 160 cells in each direction. The turbine was centred at $(x, y, z) = (0, 0, 0)$, and the axis of rotation was aligned with the x-axis (flow direction) as shown in Figure 1. In the region around the turbine (see Figure 1), the grid cells were cubic with a side length of R/32. Outside of this region, the grid cells were stretched away towards the boundaries. The used grid resolution has previously been shown sufficient for resolving both the wake[22] and the induction zone.[23]

The boundary conditions were as follows: A uniform velocity U_∞ was applied at the inlet ($x = -50R$), zero velocity gradient at the outlet ($x = 50R$), symmetry conditions at the lower and upper boundaries ($z = \pm 50R$), and periodic conditions on the sides ($y = \pm 50R$).

The AD was represented with a polar grid of 194 radial and 180 angular elements. The loading applied to each differential area was either determined from aerofoil data and the local flow conditions at the disk or was prescribed uniformly according to a specified thrust coefficient.

The specifications of the simulated wind turbines are summarized in Table 1. These turbines were chosen because they cover most of the range of turbines that are in operation today.

Each of the wind turbines in Table 1 was simulated at uniform free-stream velocities, U_∞, in the range from 5 to 24 m/s with increments of 1 m/s, ie, 20 simulations per wind turbine. For each wind speed, the pitch and rotational speed of the individual turbines were set according to specification provided by the manufacturers or presented elsewhere in the literature (see references in Table 1). Neither the tower nor nacelle were included in the simulations.

Besides these simulations, a uniformly loaded disk with a thrust coefficient of 0.36, 0.51, 0.64, 0.70, 0.75, 0.80, and 0.89, respectively, was also simulated. Thus, a total of 107 simulations were performed as part of the present work.

In all simulations of the turbines listed in Table 1, the air density and dynamic viscosity was set to $\rho = 1.225\ kgm^{-3}$ and $\mu = 1.784 \cdot 10^{-5}\ kgm^{-1}s^{-1}$, respectively. The simulations on the uniformly loaded AD all assumed $V_\infty = 1\ ms^{-1}$, $R = 1\,m$, $\rho = 1\,kgm^{-3}$, and $\mu = 2 \cdot 10^{-7}\ kgm^{-1}s^{-1}$ so that

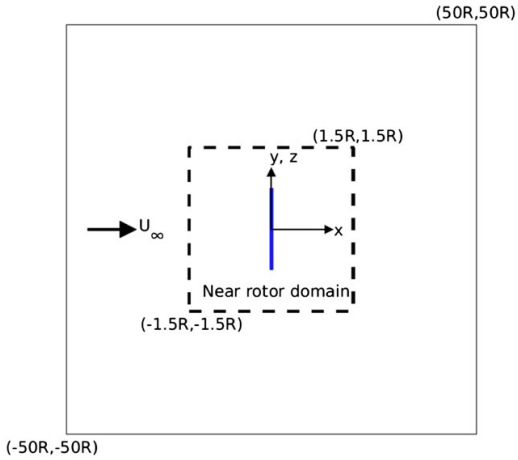

FIGURE 1 Sketch of computational domain with the actuator disk shown as a blue line [Colour figure can be viewed at wileyonlinelibrary.com]

TABLE 1 Overview of wind turbine rotors used in the present study

Turbine	Radius, m	Rated power, MW	Power control
NTK [24]	20.5	0.5	Stall regulated
NM80 [25]	40.0	2.0	Pitch regulated
SWT-2.3-93 [26]	46.5	2.3	Pitch regulated
NREL 5MW [27]	63.0	5.0	Pitch regulated
DTU 10MW [28]	89.2	10.0	Pitch regulated

the Reynolds number based on rotor diameter was $Re = 10^7$ at all C_T. The Reynolds number, $Re = 10^7$, was chosen because it reflects the range experienced by real wind turbines.

3 | SIMULATION RESULTS

The main parameter governing both the induction zone and the wake of a wind turbine is the thrust coefficient, C_T. In the following, we distinguish between the global and the local thrust coefficient defined as

$$C_T = \frac{T}{\frac{1}{2}\rho\pi R^2 V_\infty^2}, \tag{1}$$

$$C_{T,loc} = \frac{\frac{dT}{dA}}{\frac{1}{2}\rho V_\infty^2}, \tag{2}$$

where T is the total thrust force acting perpendicular to the rotor disk and dT/dA is the local thrust force per unit area acting on a differential area dA of the disk. Figure 2 shows the computed variation of C_T as a function of wind speed for each rotor. The C_T curves of all the pitch-regulated rotors are rather similar despite their large difference in size.

Figure 3 compares the spanwise distribution of $C_{T,loc}$ for each rotor at a global thrust coefficient of $C_T = 0.8$. Note, from Figure 2, that this condition occurs at different free-stream velocities for each turbine. Furthermore, $C_T = 0.8$ is the highest that the SWT-2.3-93 turbine operates at in the entire wind speed range and hence this condition represents the highest C_T reached by all turbines. As seen, the distributions of $C_{T,loc}$ vary significantly between the different rotors.

Figure 4 shows the radial variation of the stream-wise velocity, U, at various positions upstream of the rotors in the case where they all operate at $C_T = 0.8$. For distances of 1 R and beyond, the predicted profiles are quite close to each other despite the very large differences in the actual load distribution. Hence, beyond 1 R upstream, the induction profiles seem to be rather insensitive to the rotor design. However, a clear trend is that the deepest velocity deficit is associated to the rotor with the highest maximum $C_{T,loc}$.

Next, we extract the stream-wise velocity field upstream of all rotors operating at the same C_T and average them together to obtain $\langle U \rangle$.

Figure 5 shows $\langle U \rangle$ along the rotor centre line at $C_T = 0.8$. The error bars indicate the standard deviation σ_U of the $\langle U \rangle$-curve and thus represent the scatter between the simulations of the different rotors. The figure reveals that the scatter of the mean curve as expected diminishes as the distance to the rotor increases. Note that the increasing velocity close to the rotor plane is a consequence of excluding the nacelle in the simulations.

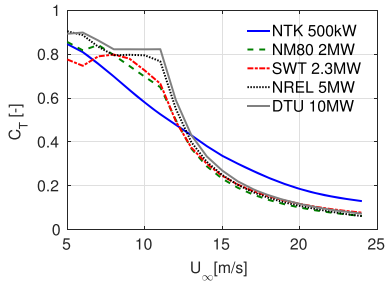

FIGURE 2 Computed C_T curves for all wind turbine [Colour figure can be viewed at wileyonlinelibrary.com]

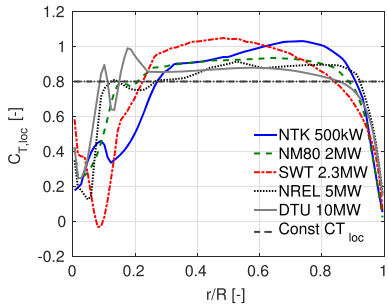

FIGURE 3 Radial variation of $C_{T,loc}$ at $C_T = 0.8$ [Colour figure can be viewed at wileyonlinelibrary.com]

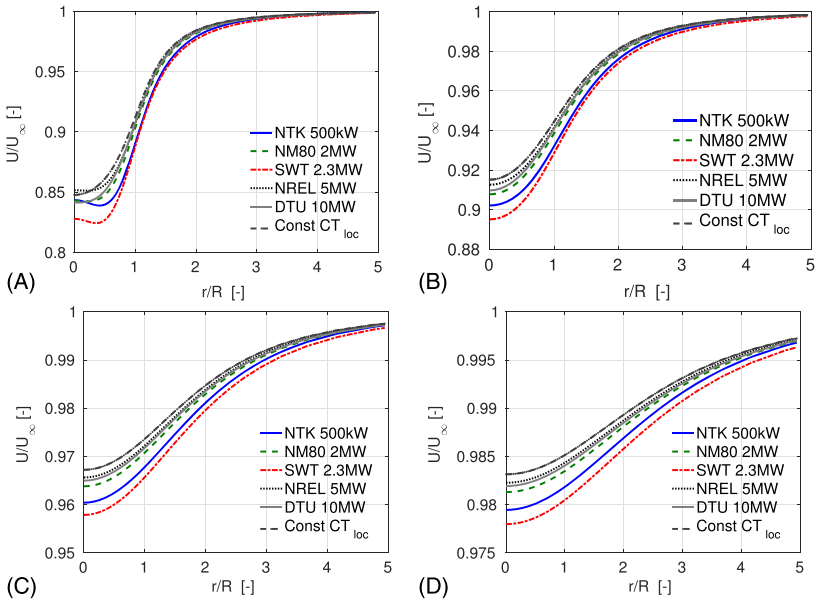

FIGURE 4 Axial velocity profiles upstream of the rotors operating at $C_T = 0.8$. A, x=−0.5 R; B, x=−1.0 R; C, x=−2.0 R; and d, x=−3.0 R [Colour figure can be viewed at wileyonlinelibrary.com]

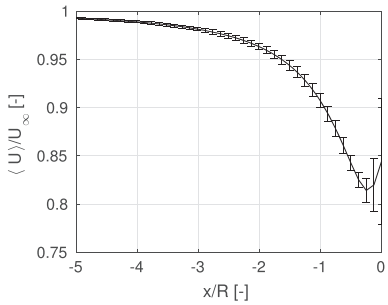

FIGURE 5 Mean axial velocity along centreline at $C_T = 0.8$

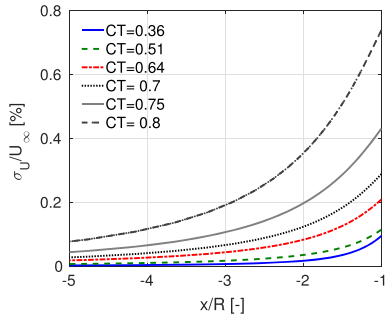

FIGURE 6 Standard deviation of the mean centreline velocity [Colour figure can be viewed at wileyonlinelibrary.com]

Figure 6 shows how the standard deviation of $\langle U \rangle$ varies along the centreline for various C_T. As expected, σ_U decreases with decreasing C_T. As seen, σ_U is below 0.8% of the free-stream velocity in the shown region and thus confirms that the velocity induced by the different rotor is similar for $x < -R$.

3.1 | Self-similarity

Figures 4 and 6 showed that the induction profiles are insensitive to the rotor design to within 0.8% when the stream-wise distance to the rotor is greater than 1 R. In the following, we will investigate whether the induction profiles can also be considered self-similar, ie, if the shape of the profiles stays unchanged with upstream position. Therefore, we define a scaled induction field, $f(r,x)$ and a characteristic half width $r_{1/2}(x)$:

$$f(r,x) = \frac{U_\infty - U(r,x)}{U_\infty - U(0,x)} = \frac{a(r,x)}{a(0,x)}, \tag{3}$$

$$a(r_{1/2}(x),x) = \frac{1}{2}a(0,x), \tag{4}$$

where $a(r,x) = 1 - U(r,x)/U_\infty$ is the local axial induction factor while $r_{1/2}(x)$ is the radial position where the induction is half of the centreline induction.

The scaled induction field and $r_{1/2}(x)$ are calculated for each of the 107 RANS simulations, ie, for all tested rotors at all wind speeds/operational conditions.

Figure 7 shows the average of all the scaled induction fields at various upstream positions. As seen, the scaled induction profiles start to collapse onto a single curve from 1 R upstream and beyond. Therefore, the induction zone can be considered self-similar after this point irrespective of the rotor and rotor loading.

Figure 8 shows the standard deviation of the the f profiles, σ_f. The standard deviation is in the order of 1% and lower when the upstream distance to the rotor is more than 1 R and therefore confirms that, beyond this point, the mean scaled induction profile is very representative for all rotors at all operational conditions.

Figure 9 shows the upstream variation of $\bar{r}_{1/2}(x)$, ie, its average over all 107 RANS simulations. The error bars indicate the standard deviation of the predicted curve. In the region from $x < -R$, the standard deviation does not exceed 13% of the rotor radius. The rather low standard deviation indicates that $r_{1/2}(x)$ can be considered independent of the rotor design and operational conditions.

4 | PARAMETRIZATION OF INDUCTION ZONE

In the previous section, we showed that the axial induced velocity can be considered self-similar for upstream positions of $x < -R$. In the following, we will use this finding to derive a simple analytical expression for the axial velocity upstream of a wind turbine. In the self-similar region, the scaled induction profile is only a function of $r/r_{1/2}$ (see Figure 7) and, therefore, the axial velocity here can be expressed as

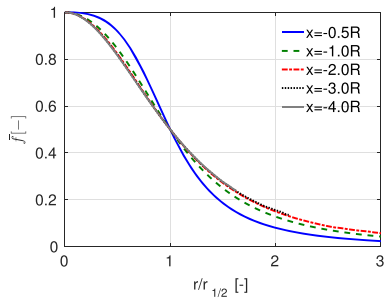

FIGURE 7 Average scaled induction profiles at different upstream positions [Colour figure can be viewed at wileyonlinelibrary.com]

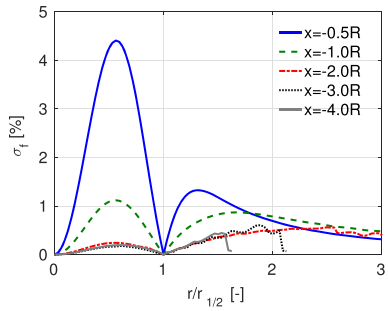

FIGURE 8 Standard deviation of scaled induction profiles at different upstream positions [Colour figure can be viewed at wileyonlinelibrary.com]

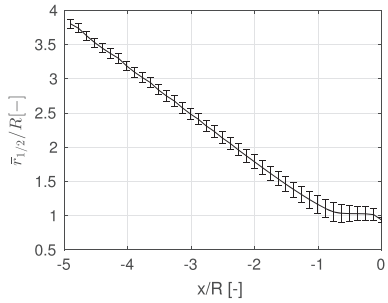

FIGURE 9 Upstream variation of the average characteristic half width

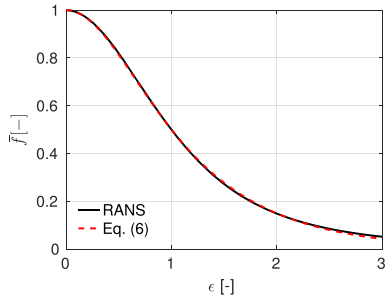

FIGURE 10 Comparison of the self-similar $f(\epsilon)$ profile computed from Reynolds-averaged Navier-Stokes (RANS) and Equation 6 [Colour figure can be viewed at wileyonlinelibrary.com]

$$\tilde{U}(\tilde{r},\tilde{x}) = 1 - a(0,\tilde{x})f(\epsilon), \tag{5}$$

where we have introduced the dimensionless variables:

$$\tilde{U}(r,x) = \frac{U(r,x)}{U_\infty}, \quad \epsilon = \frac{r}{r_{1/2}(x)}, \quad \tilde{r}_{1/2}(x) = \frac{r_{1/2}(x)}{R}, \quad \tilde{r} = \frac{r}{R}, \quad \tilde{x} = \frac{x}{R}.$$

Hence, in the self-similar region, $\tilde{U}(\tilde{r},\tilde{x})$ can be fully characterized by establishing functional forms of $f(\epsilon)$, $a(0,\tilde{x})$ and $\tilde{r}_{1/2}(\tilde{x})$.

Figure 10 shows that the computed $f(\epsilon)$ is well represented by the function:

$$f(\epsilon) = sech^{\alpha}(\beta\epsilon), \tag{6}$$

with $\alpha = \frac{8}{9}$ and $\beta = \sqrt{2}$.

The functional form of $f(\epsilon)$ is inspired by the uniform turbulent viscosity solution to the self-similar plane jet,[29] while the coefficients α and β are found from least-squares fitting.

The centre line induction is represented by the following expression derived from a simple vortex model [12]:

$$a(0,\tilde{x}) = a_0\left(1 + \frac{\tilde{x}}{\sqrt{1+\tilde{x}^2}}\right), \tag{7}$$

where a_0 is the axial induction factor at the rotor plane, which we here compute as

$$a_0 = \frac{1}{2}(1 - \sqrt{1-\gamma C_T}), \tag{8}$$

where γ is a constant. The simple vortex model [12] predicts the same a_0 as in 1D momentum theory,[30] ie, $\gamma = 1$. However, we propose to use $\gamma = 1.1$ because it generally leads to better agreement with the RANS predictions in the region $x < -R$. An example of this is shown in Figure 11. The value $\gamma = 1.1$ was determined in the following way: First, the centre line induction upstream of each rotor was extracted at the same C_T and averaged together to obtain $\langle a(0,x)\rangle$, ie, the rotor averaged centre line induction as a function of C_T. Then Equation 7 was fitted to each of these centre line induction curves in the region $x < -R$ to obtain the best fit of a_0 for different values of C_T (the blue curve in Figure 12). Finally, Equation 8 was fitted to this curve to obtain the best fit of γ. Figure 12 shows how $\gamma = 1.1$ improves the agreement with RANS for all C_T.

To derive an expression for $\tilde{r}_{1/2}(\tilde{x})$, we use the continuity equation from which we have

$$\frac{d}{d\tilde{x}}\int_0^\infty a(\tilde{r},\tilde{x})\tilde{r}d\tilde{r} = 0 \iff a(0,\tilde{x})\tilde{r}_{1/2}^2(\tilde{x})\int_0^\infty f(\epsilon)\epsilon d\epsilon = constant. \tag{9}$$

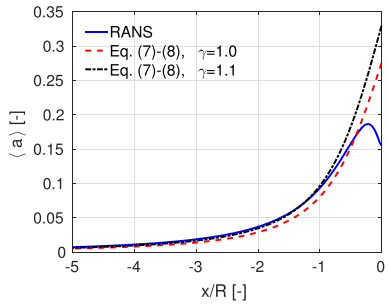

FIGURE 11 Centre line induction factor at $C_T = 0.8$ predicted by Reynolds-averaged Navier-Stokes (RANS) and Equations 7 to 8 for different γ [Colour figure can be viewed at wileyonlinelibrary.com]

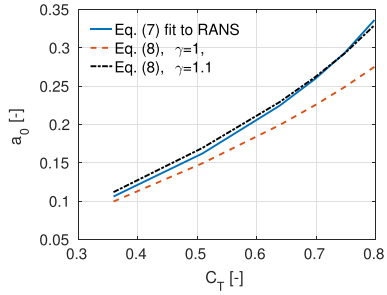

FIGURE 12 Best fit of a_0 in Equation 7 to Reynolds-averaged Navier-Stokes (RANS) in comparison to predictions of Equation 8 for different γ [Colour figure can be viewed at wileyonlinelibrary.com]

In the self-similar region, the last integral becomes constant, and, hence, the product $a(0,\tilde{x})\tilde{r}_{1/2}^2(\tilde{x})$ is also constant. Combining this with Equation 7 and using the fact that $\tilde{r}_{1/2}(\tilde{x})$ is independent of C_T (and therefore also a_0), see Figure 9, we get the following:

$$\tilde{r}_{1/2}^2(\tilde{x}) = \frac{\sigma}{1+\frac{\tilde{x}}{\sqrt{1+\tilde{x}^2}}} = \sigma\left(1-\frac{\tilde{x}}{\sqrt{1+\tilde{x}^2}}\right)(1+\tilde{x}^2), \tag{10}$$

where σ is a constant. Far upstream, Equation 10 becomes

$$\tilde{r}_{1/2}^2(\tilde{x}) = 2\sigma(1+\tilde{x}^2) for\, x \to -\infty, \tag{11}$$

Close to the rotor, the velocity is not fully self-similar and, therefore, the analysis leading to Equation 11 is not valid. To better represent $\tilde{r}_{1/2}(\tilde{x})$ close to the rotor, we therefore add a constant δ to the right-hand side:

$$\tilde{r}_{1/2}^2(\tilde{x}) = 2\sigma(1+\tilde{x}^2)+\delta, \tag{12}$$

Defining new constants $\lambda = 2\sigma$ and $\eta = 1+\delta/\lambda$, we finally get

$$\tilde{r}_{1/2}(\tilde{x}) = \sqrt{\lambda(\eta+\tilde{x}^2)}. \tag{13}$$

Using least squares fitting of Equation 13 to the computed $r_{1/2}$ shown in Figure 9, we obtain $\lambda = 0.587$ and $\eta = 1.32$. Figure 13 compares the $\tilde{r}_{1/2}$ determined from Equation 13 with the mean RANS predictions. As seen, the fit is excellent for $x < -R$.

4.1 | Performance of the simple model

To evaluate the performance of the proposed analytical model (Equations 5-8 and 13), Figure 14 compares its predictions of the stream-wise velocity upstream of the rotor with the average RANS results at $C_T = 0.8$. Comparing with Figure 4, it is seen that the predictions of the proposed model is well inside the spread between the different RANS simulations. The maximum deviation from the mean RANS prediction is found to be below 0.7% of the free-stream velocity in the entire region $x < -R$.

To further quantify the performance of the model, we compute the maximum absolute deviation between the simple model and the RANS simulations over all individual rotors and C_T. Figure 15 shows this error as function of distance to the rotor at different C_T values. Note that the maximum

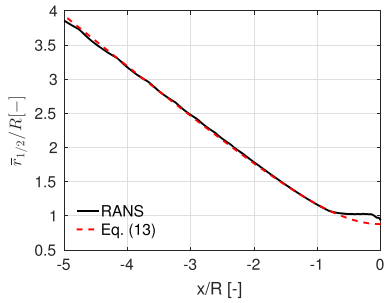

FIGURE 13 Comparison of $r_{1/2}$ predicted by Reynolds-averaged Navier-Stokes (RANS) and Equation 13 [Colour figure can be viewed at wileyonlinelibrary.com]

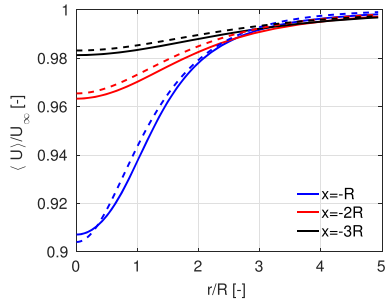

FIGURE 14 Comparison of stream-wise velocity predicted by Reynolds-averaged Navier-Stokes (full lines) and the simple analytical model (dashed lines) at $C_T = 0.8$ [Colour figure can be viewed at wileyonlinelibrary.com]

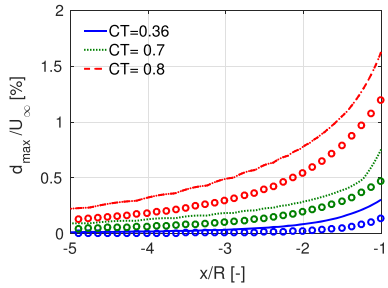

FIGURE 15 Lines: maximum absolute deviation (d_{max}) between the simple model and all RANS simulations; circles: d_{max} between the mean and individual Reynolds-averaged Navier-Stokes simulations. Colours indicate C_T [Colour figure can be viewed at wileyonlinelibrary.com]

deviation may occur at different radial positions for each stream-wise position. The corresponding maximum deviation between the mean and individual RANS simulations at fixed values of C_T is shown as circles in the figure and thus is a measure of the maximum spread in the flow between the rotors. As seen, the deviations follow the same trend but, in general, the deviation to the simple model is slightly higher (below 0.4%). Given that a simple model that is independent of the specific rotor blade geometry never can be expected to get lower maximum deviation than the spread in the simulations on which it is based, we conclude that our model is sufficiently accurate.

5 | DISCUSSION

The numerical setup adopted here is indeed simple and not very representative of the "real" world. However, our work shows that, under these simple conditions, the induced velocity in the region greater than 1 R upstream of any turbine can be well characterized through knowledge of the global thrust coefficient. This was not known before, and, if it had not been the case, then there would be no hope for finding a simple parametrization in more realistic inflow.

The induction zone model proposed here has the nice feature of consisting of 3 independent parts: a model for its shape, a model of its depth, and a model of its width. Thus, the performance of the model could easily be improved by introducing more advanced parametrizations of each of these parts. However, given that the accuracy of the model is already very close to the inherent spread in the RANS simulations (see Figure 15), we do not find it necessary to introduce more parameters into the model.

The presented analytical model has only 2 unknowns, namely, the global thrust coefficient C_T and the free-stream velocity V_∞. If these unknowns are provided, then the model can predict the velocity everywhere more than 1 R upstream of any wind turbine. Alternatively, the model could be used for estimating C_T and V_∞ on the basis of wind speed measurements close to the rotor. In practice, 3 different strategies could be used for this purpose depending on how much is known about the rotor: (1) Measure the velocity in two or more points upstream of the rotor, and use these to determine the 2 unknowns. (2) Use the total thrust, T, of the rotor together with at least one measurement upstream to estimate V_∞ and hence also C_T. (3) Use a known C_T curve together with measurements in at least one point upstream of the rotor to estimate the V_∞.

The first strategy benefits from not requiring any knowledge about the turbine except for its radius. The second strategy can be adopted if measurements are available of the thrust (eg, from strain gauges). The third strategy needs a prior knowledge of C_T as a function of free wind speed. Such a curve is sometimes provided by the manufacturers. Alternatively, one could simply assume a given behaviour of C_T as a function of free-stream velocity. Such approach is justified because the C_T curve behaviour of pitch regulated turbines often is similar as is also evident from this study (see Figure 2).

Obviously, the use of the analytical model for predicting the free-stream velocity and C_T in more realistic settings will be subject to additional uncertainty that are most likely more dominant than the uncertainties associated with deriving the present model. How large these uncertainties are in comparison to those associated with using, eg, a met mast far upstream of the rotor remains to be answered.

6 | CONCLUSION

The induction zone upstream of 6 different wind turbine rotors have been studied using RANS simulations, and the following general features have been found:

- The induction zone forming upstream of rotors operating at the same thrust coefficient is rather insensitive to the load distribution for distances beyond 1 rotor radius (R) upstream. However, the deepest velocity deficit is generated by the rotor having the highest local C_T.
- The induction zone can be considered self-similar for distances more than 1 R upstream of the rotor.

On the basis of the above findings, a simple analytical model of the stream-wise velocity upstream of a wind turbine was proposed. The model is applicable for any rotor in the region more than 1 R upstream of the rotor plane. In the valid region, the standard deviation between the model and the average of the RANS simulations is less than 0.7% of the free-stream velocity while the corresponding maximum difference to any of the RANS simulations never exceeds 1.7%. The latter difference should be seen in proportion to a spread between the individual RANS simulations, which maximizes at about 1.3%. Therefore, it is concluded that the proposed model is sufficiently accurate.

ACKNOWLEDGEMENTS

This work is part of the UniTTe project (unitte.dk), which is financed by The Innovation Fund Denmark (1305-00024B). The computational resources were provided by the Risø DTU central computing facility.

ORCID

Niels Troldborg http://orcid.org/0000-0003-4508-4837
Alexander Raul Meyer Forsting http://orcid.org/0000-0002-3133-1860

REFERENCES

1. Schlipf D, Fleming P, Haizmann F, Scholbrock A, Hofsäß M, Wright A, Cheng PW. Field testing of feedforward collective pitch control on the CART2 using a nacelle-based lidar scanner. *J Phys: Conf Series. TORQUE*. 2014;2012:555.
2. Schlipf D, Schlipf DJ, Kuehn M. Nonlinear model predictive control of wind turbines using LIDAR. *Wind Energy*. 2013;16:1107-1129.
3. Simley E, Pao LY. Evaluation of a wind speed estimator for effective hub-height and shear components. *Wind Energy*. 2016;19:167-184.
4. Simley E, Pao LY, Frehlich R, Jonkman B, Kelly N. Analysis of light detection and ranging wind speed measurements for wind turbine control. *Wind Energy*. 2014;17:413-433.
5. Simley E, Pao LY, Gebraad P, Churchfield M. Investigation of the impact of the upstream induction zone on LIDAR measurement accuracy for wind turbine control applications using large-eddy simulation. *J Phys: Conf Series. TORQUE 2014*. 2014;524:524.
6. Wagner R, Courtney MS, Pedersen TF. Uncertainty of power curve measurement with a two-beam nacelle-mounted lidar. *Wind Energy*. 2015;19:1269-1287.
7. Wagner R, Pedersen TF, Courtney M. Power curve measurement with a nacelle mounted lidar. *Wind Energy*. 2014;17:1441-1453.
8. Medici D, Ivanell S, Dahlberg JÅ, Alfredsson PH. The upstream fl ow of a wind turbine: blockage effect. *Wind Energy*. 2011;14:691-697.
9. Howard KB, Guala M. Upwind preview to a horizontal axis wind turbine: a wind tunnel and field-scale study. *Wind Energy*. 2015;19:1371-1389.

10. Branlard E, Forsting ARM. Using a cylindrical vortex model to assess the induction zone infront of aligned and yawed rotors. In Proceedings of EWEA Offshore 2015 Conference, Copenhagen, Denmark; 2015.
11. Simley E, Angelou N, Mikkelsen T, Sjöholm JM, Pao LY. Characterization of wind velocities in the upstream induction zone of a wind turbine using scanning continuous-wave lidars. *Renewable Sustainable Energy*. 2016;8:8.
12. Branlard E, Mercier P, Machefaux E, Gaunaa M, Voutsinas S. Impact of a wind turbine on turbulence: un-freezing turbulence by means of a simple vortex particle approach. *Wind Eng Ind Aerodyn*. 2016;151:37-47.
13. Michelsen JA. Basis3D—a platform for development of multiblock PDE solvers. Technical report AFM 92-05, Technical University of Denmark, Lyngby, 1992.
14. Michelsen JA. Block structured multigrid solution of 2D and 3D elliptic PDEs. Technical Report AFM 94-06, Technical University of Denmark, 1994.
15. Sørensen NN. General purpose flow solver applied to flow over hills, Technical University of Denmark, PhD thesis, 1995.
16. Patankar SV, Spalding DB. A calculation procedure for heat, mass and momentum transfer in three-dimensional parabolic flows. *Int J Heat Mass Transfer*. 1972;15:1787-1972.
17. Leonard BP. A stable and accurate convective modelling procedure based on quadratic upstream interpolation. *Comp Meth Appl Mech Engrng*. 1979;19:59-98.
18. Menter FR. Zonal two equation k-ω turbulence models for Aerodynamic flows. *AIAA J*. 1993;93-2906.
19. Réthoré P-E, van der Laan P, Troldborg N, Zahle F, Sørensen NN. Verification and validation of an actuator disc model. *Wind Energy*. 2013;17:919-937.
20. Réthoré P-E, Sørensen NN. A discrete force allocation algorithm for modelling wind turbines in computational fluid dynamics. *Wind Energy*. 2012;15:915-926.
21. Troldborg N, Sørensen NN, Réthoré P-E, van der Laan P. A consistent method for finite volume discretization of body forces on collocated grids applied to flow through an actuator disk. *Comput Fluids*. 2015;119:197-203.
22. Troldborg N, Sørensen JN, Mikkelsen R. Numerical simulations of wake characteristics of a wind turbine in uniform inflow. *Wind Energy*. 2010;4:86-99.
23. Meyer Forsting AR, Troldborg N, Murcia Leon JP, Angelou N, Sathe A, Vignaroli A. Validation of a CFD model with a synchronized triple- lidar system in the wind turbine induction zone. *Wind Energy*. 2017;20:1481-1498. https://doi.org/10.1002/we.2103
24. Petersen SM. Konceptundersøgelse nordtank ntk måling af effektkurve. Technical Report Risø-I-799(DA), Risø National Laboratory, 1994.
25. Hansen MH, Fuglsang P, Thomsen K. Aeroelastic modeling of the NM80 turbine with HAWC. Technical Report Risø-I-2017(EN), Risø National Laboratory, Technical University of Denmark, 2004.
26. del Valle Granado I. SWT-2.3.93, Aeroelastic Model, Aerodynamics. Technical Report LD-000-0299-00, Siemens Wind Power A/S, 2014.
27. Jonkman J, Butterfield S, Musial W, Scott G. Definition of a 5-MW reference wind turbine for offshore system development. Technical report NREL/TP-500-38060, NREL, 2009.
28. Bak C, Bitsche R, Yde A, *et al. Light Rotor: The 10-MW Reference Wind Turbine*. Copenhagen: EWEA; 2012.
29. Pope SB. *Turbulent Flows*. Cambridge University Press; 2000.
30. Glauert H. *Airplane Propellers*, Durand WF (ed.), Aerodynamic Theory, vol. IV. The Dover Edition UK, 1963.

How to cite this article: Troldborg N, Meyer Forsting AR. A simple model of the wind turbine induction zone derived from numerical simulations. *Wind Energy*. 2017;1–10. https://doi.org/10.1002/we.2137

THE AUTHOR

Alexander grew up in a small village in Northern Germany close to the Dutch border. He completed his school education in Southern England and moved on to study Aeronautical Engineering at Imperial College London. A group project on the optimisation of paraglider airfoils during his exchange year at ISAE, Toulouse, sparked his interest in computational fluid dynamics. A research internship at the DLR (German Aerospace Centre) investigating transonic panel flutter followed. After finishing his degree with a Master thesis on unsteady aerodynamics, he started his PhD at DTU Wind Energy. He is now a Post-doctoral Researcher at the same institution and lives in Copenhagen.

From early on Alexander has been fascinated with aircraft and thus spends substantial time in the air, flying gliders and motorplanes alike. His home base is EDWN, where he is an active gliding instructor.

COLOPHON

This document was typeset using a modified version of the typographical look-and-feel `classicthesis` developed by André Miede. The style was inspired by Robert Bringhurst's seminal book on typography "*The Elements of Typographic Style*". `classicthesis` is available for both LaTeX and LyX:

`https://bitbucket.org/amiede/classicthesis/`

Final Version as of January 19, 2018 (`classicthesis` version 1.0).

This thesis consists of two parts - a synopsis and a collection of journal articles. It is submitted to the Danish Technical University in partial fulfilment of the requirements for the degree of Doctor of Philosophy in Engineering. The work was carried out at the Aerodynamic Design section of the Department of Wind Energy, located at the Risø campus of the Technical University of Denmark. It was co-funded by The Innovation Fund Denmark as part of the UniTTe project under grant number 1305-00024B.

Principal supervisor: Dr. Niels Troldborg
Co-supervisors: Dr. Andreas Bechmann & Dr. Pierre-Elouan Réthoré
Examiners: Prof. Jens N. Sørensen, Prof. Rebecca J. Barthelmie and Dr. David Schlipf

DTU Wind Energy
Technical University of Denmark
Frederiksborgvej 399
DK-4000 Roskilde
www.vindenergi.dtu.dk